UNIVERSIDAD CARLOS III DE MADRID

Universidad
Carlos III de Madrid

NUMERICAL AND ASYMPTOTIC ANALYSES OF LEAN HYDROGEN-AIR DEFLAGRATIONS

Tesis Doctoral

Autor
Daniel Fernández Galisteo

Director
Antonio L. Sánchez Pérez

Leganés, Diciembre 2009

DEPARTAMENTO DE INGENIERÍA TÉRMICA Y DE FLUIDOS
Escuela Politécnica Superior

NUMERICAL AND ASYMPTOTIC ANALYSES OF LEAN HYDROGEN-AIR DEFLAGRATIONS

Autor
Daniel Fernández Galisteo

Director de Tesis
Antonio L. Sánchez Pérez

Leganés, Diciembre 2009

A mi familia

TESIS DOCTORAL

NUMERICAL AND ASYMPTOTIC ANALYSES OF LEAN HYDROGEN-AIR DEFLAGRATIONS

Autor: Daniel Fernández Galisteo

Director de Tesis: Antonio L. Sánchez Pérez

Firma del Tribunal Calificador:

Firma

Presidente:	D. Amable Liñán Martínez
Vocal:	D. Forman Arthur Williams
Vocal:	D. Pedro Luis García Ybarra
Vocal:	D. Vadim Kourdioumov
Secretario:	D. Eduardo Fernández Tarrazo
Suplente:	D. José Luis Castillo Gimeno
Suplente:	D. Marcos Vera Coello

Calificación:

Leganés, diciembre de 2009

. . . no voy a sentirme mal
si algo no me sale bien,
he aprendido a derrapar
y a chocar con la pared.
Que la vida se nos va,
como el humo de ese tren,
como un beso en un portal,
antes de que cuente diez . . .

Fito&Fitipaldis

Agradecimientos

En primer lugar me gustaría agradecer especialmente al Prof. Antonio L. Sánchez todas las horas involucradas en el buen desarrollo de esta tesis, sus comentarios y su ayuda en los problemas encontrados a lo largo del trabajo y la oportunidad que recibí para realizarlo. También me gustaría agradecer al Prof. Forman Williams su estupenda acogida en la Universidad de California, San Diego, durante los veranos que duró esta tesis y su preocupación por lo que allí hacía, y al Prof. Amable Liñán por las intensas charlas que, junto al Prof. Antonio L. Sánchez, me hicieron dar cuenta que las cosas pueden ser complicadas para la mayoría y sencillas para unos pocos.

Tampoco voy a olvidar cómo comenzamos los tres, Pablo, Wil y yo. A Wil quiero agradecer la ayuda en el último momento en el código numérico y a Pablo sus comentarios sobre la vida. A mis especiales compañeros de despacho Mario y, por supuesto, Carol, a la que agradezco muchos buenos momentos de risas, y a los que llegaron después, Ana e Iván. Jorge, por su ayuda este verano con los cálculos numéricos y sus visitas, y a Baldo y Javier U. por facilitar enormemente los veranos en San Diego, no diré más. Sergio por los ánimos, Celia y Jose Antonio. No voy a olvidar a Eduardo e Imma por la ayuda prestada cada vez que requería de ellos. Ni a Mercedes, Nestor, Domingo, Ulpiano, Marcos, Alejandro, Rocio, Cristina, Fernando, Antonio Soria, Luismi, Alberto. También a Javier R. que fué quien me engañó en todo esto con mi primer proyecto y que luego paso a Antonio. En realidad todos ellos forman un gran conjunto.

También muy especialmente agradezco a mis mejores amigos y mi familia estar a su lado.

Resumen

En esta tesis se aborda el estudio teórico de deflagraciones pobres en mezclas de hidrógeno y aire mediante el uso combinado de métodos numéricos y asintóticos, que, a partir de una descripción detallada de las reacciones químicas implicadas, permiten clarificar la estructura interna de las llamas y proporcionan expresiones simplificadas para el ritmo de reacción. Aunque la mayoría de los cálculos se han realizado con valores atmosféricos normales de presión y temperatura inicial, se han considerado otros valores, incluyendo mezclas precalentadas y precomprimidas, así como condiciones de presión subatmosférica y mezclas criogénicas. El rango de dosados investigado va desde el límite pobre de inflamabilidad hasta condiciones estequiométricas, aunque se ha profundizado especialmente en el estudio de llamas cerca del límite de inflamabilidad.

En primer lugar, se considera la descripción de la química. Partiendo de un mecanismo detallado de veintiuna reacciones elementales reversibles se busca el mínimo conjunto de reacciones elementales capaces de describir con precisión las llamas premezcladas de hidrógeno. Se demuestra que un mecanismo corto de siete reacciones elementales, de las que sólo tres de ellas son reversibles, proporciona una buena predicción para la velocidad de propagación de las llamas cuando el dosado es suficientemente pequeño. Se demuestra, además, que añadiendo dos reacciones de recombinación irreversibles al mecanismo de siete pasos se consigue extender la precisión del mecanismo para cubrir el rango completo de condiciones de inflamabilidad en condiciones atmosféricas normales. Los cálculos indican también que un mecanismo corto de ocho pasos, construido a partir del mecanismo corto de siete pasos mediante la adición de la cuarta reacción de intercambio de radicales, mejora las predicciones para los perfiles de O y OH.

Seguidamente, se estudia la propagación de deflagraciones de hidrógeno en condiciones cercanas al límite de inflamabilidad partiendo del mecanismo de siete reacciones elementales. La capa de reacción que controla la velocidad de propagación laminar resulta ser muy delgada y contiene concentraciones muy pequeñas de todas las especies intermedias, de forma que todas ellas se encuentran en estado estacionario, mientras que las especies principales reaccionan según la reacción global irreversible $2H_2 + O_2 \rightarrow 2H_2O$. El análisis

proporciona una expresión explícita de tipo no-Arrhenius para el ritmo de esta reacción global. Este mecanismo reducido de un paso permite en particular el cálculo de los límites de inflamabilidad y de la velocidad de propagación para deflagraciones pobres planas. El estudio incluye un repaso de las implicaciones que los perfiles de radicales tienen en la deflagración, junto con las razones que permiten que las aproximaciones funcionen. El nuevo mecanismo reducido puede ser de utilidad en estudios analíticos y permite su fácil implementación en códigos computacionales para el cálculo de llamas pobres de hidrógeno, disminuyendo los costes de cálculo.

Se estudia a continuación la estructura interna de la capa delgada de reacción de las deflagraciones pobres en mezclas de hidrógeno y aire próximas al límite de inflamabilidad. En el análisis, que emplea siete reacciones elementales para la descripción de la química, se usa el cociente entre las concentraciones de H, que es el radical dominante, y del combustible como parámetro asintótico pequeño, lo que permite obtener una descripción analítica precisa del ritmo de combustión. El análisis revela que la hipótesis de estado estacionario para las especies intermedias, que resulta apropiada en el lado caliente de la capa reactiva, falla, sin embargo, conforme nos acercamos a la temperatura de cruce, donde existe una capa interna delgada en la que el término de transporte difusivo de los radicales es comparable a los de producción y consumo asociados a la química. El análisis de esta región proporciona una corrección relativamente importante al ritmo de combustión. Los resultados obtenidos pueden ser útiles, por ejemplo, para la futura investigación de inestabilidades de llamas en mezclas pobres de hidrógeno.

Finalmente, el estudio se centra en llamas pobres relativamente lejos del límite de inflamabilidad. Bajo estas condiciones, la hipótesis de estado estacionario para el radical H falla y el mecanismo de un paso para la oxidación del hidrógeno debe ser sustituido por un mecanismo reducido de dos pasos, que incluye una reacción de ramificación con una fuerte dependencia con la temperatura $3H_2 + O_2 \rightleftharpoons 2H_2O + 2H$ y una reacción exotérmica de recombinación $H + H \rightarrow H_2$. Se observa que la temperatura de activación de la reacción de ramificación es lo suficientemente grande como para considerar que la producción de radicales ocurre en una capa relativamente delgada a una temperatura ligeramente por encima de la temperatura de cruce (definida como la temperatura a la que el ritmo de ambas reacciones se iguala), mientras que la recombinación de radicales ocurre de forma distribuida aguas arriba y aguas abajo de esta capa delgada en regiones de espesor comparable al de la llama. La estructura resultante se parece en muchos aspectos a la que encontró

Zel'dovich en su análisis de llamas dominadas por reacciones de ramificación, basado en una descripción modelo de dos etapas para la química. El problema que determina la velocidad de propagación de la llama se reduce en primera aproximación a la integración numérica de las ecuaciones de conservación en la regiones exteriores de recombinación, con condiciones de contorno que incluyen condiciones de salto a través de la capa interna de ramificación, que se se encuentra a una temperatura que se determina a partir del análisis de su estructura interna. La solución que se obtiene de este análisis tipo Zeldovich se compara con cálculos numéricos del problema inicial completo, dando resultados satisfactorios en un amplio rango de condiciones de composición, presión y temperatura inicial.

Abstract

Numerical and asymptotic methods are used to address the structure and burning rate of lean hydrogen-air deflagrations with detailed account of the underlying chemical reactions involved. Although most computations are performed for atmospheric normal values of the pressure and initial temperature, subatmospheric and elevated pressures as well as cryogenic and preheated mixtures are also considered. The whole range of compositions ranging from the lean flammability limit to stoichiometric mixtures has been investigated, with particular attention given to near-limit lean flames.

The chemistry description is investigated first. A short mechanism consisting of seven elementary reactions, of which only three are reversible, is shown to provide good predictions of hydrogen-air lean-flame burning velocities. It is also demonstrated that adding only two irreversible direct recombination steps to the seven-step mechanism accurately reproduces burning velocities of the full detailed mechanism for all equivalence ratios at normal atmospheric conditions and that an eight-step detailed mechanism, constructed from the seven-step mechanism by adding to it the fourth reversible shuffle reaction, improves predictions of O and OH profiles.

For conditions near the lean flammability limit all reaction intermediaries have small concentrations in the important thin reaction zone that controls the hydrogen-air laminar burning velocity and therefore follow a steady state approximation, while the main species react according to the global irreversible reaction $2H_2 + O_2 \rightarrow 2H_2O$. An explicit expression for the non-Arrhenius rate of this one-step overall reaction for hydrogen oxidation is derived from the seven-step detailed mechanism, for application near the flammability limit. The one-step results are used to calculate flammability limits and burning velocities of planar deflagrations. Furthermore, implications concerning radical profiles in the deflagration and reasons for the success of the approximations are clarified. The new reduced-chemistry descriptions can be useful for both analytical and computational studies of lean hydrogen-air flames, decreasing required computation times.

The inner structure of the thin reactive layer of hydrogen-air fuel-lean deflagrations close to the flammability limit is investigated next. The analysis, which employes seven elementary reactions for the chemistry description,

uses the ratio of the characteristic radical and fuel concentrations as a small asymptotic parameter, enabling an accurate analytic expression for the resulting burning rate to be derived. The analysis reveals that the steady-state assumption for chemical intermediaries, applicable on the hot side of the reactive layer, fails, however, as the crossover temperature is approached, providing a nonnegligible higher-order correction to the burning rate. The results can be useful, for instance, in future investigations of hydrogen deflagration instabilities near the lean flammability limit.

Finally, conditions away from the flammability limit, including moderately lean and stoichiometric flames, are explored. Under these conditions, the steady-state assumption for H atoms is seen to fail, and the one-step mechanism for hydrogen oxidation must be replaced with a two-step reduced mechanism comprising a thermally sensitive branching reaction $3H_2 + O_2 \rightleftharpoons 2H_2O + 2H$ and an exothermic recombination reaction $H + H \rightarrow H_2$. It is seen that the activation temperature of the branching step is sufficiently large that branching occurs in a relatively thin layer at a temperature slightly above the crossover value, whereas radical recombination occurs in a distributed manner both upstream and downstream from this layer, yielding a flame structure that in many aspects resembles that found by Zel'dovich in his analysis of branched-chain flames with model chemistry. The leading-order solution of the resulting problem determines the flame propagation velocity. The solution involves the numerical integration of the conservation equations in the recombination regions with appropriate jump conditions imposed at the branching sheet, whose temperature is obtained by the analysis of the branching layer. The results compare reasonably well with those of detailed-chemistry computations for varying conditions of composition, pressure and initial temperature.

Contents

CHAPTER

ONE

General introduction

1.1 Hydrogen-air deflagrations

Increased interest in the use of hydrogen has intensified needs for better understanding of its combustion behavior, for reasons of safety as well as in automotive and stationary-power applications [1]. Besides the necessity of being able to describe hydrogen-air ignition characteristics [2], it is especially desirable to focus on deflagrations in fuel-lean hydrogen-air mixtures, notably in hazard contexts, where release of low concentrations of hydrogen may lead to continued flame spread. As computational capabilities advance, increased use is being made of electronic computers to assess different combustion scenarios. With rare exceptions [3], full detailed hydrogen chemistry remains too complex to be used in related computational studies. Reliable reduced chemistry for lean hydrogen-air deflagrations therefore is needed for obtaining predictions computationally that can be applied ultimately for judging how to handle hydrogen in the built environment.

The hydrogen oxidation chemistry, involving only H_2, O_2, H_2O, H, O, OH, HO_2 and H_2O_2, from a global-reaction viewpoint is no more than a six-step mechanism, there being two atom (or element) conservation equations for the eight chemical species. In other words, although there are many more elementary chemical-kinetic reactions, there are only six independent differential equations for species conservation with nonzero chemical source terms. Various mechanisms that are reduced to fewer than six steps have been proposed and tested in the literature. The simplification follows in general from introducing steady-state assumptions for intermediates after shortening the chemical scheme by discarding those elementary reactions that contribute negligibly to the combustion process. These reductions evolved from pioneering investigations of steady-state and partial-equilibrium approximations by Dixon-Lewis [4] and others. A four-step mechanism with H_2O_2 and HO_2 assumed to

be in steady state has been found to be accurate for laminar diffusion flames, for example [5]. For fuel-lean deflagrations, a three-step mechanism has been investigated in which H_2O_2 is absent and O and HO_2 are in steady states [6], and a two-step mechanism in which all reaction intermediates except H obey steady-state approximations has been shown to be reasonable [7]. The resulting two-step description includes an overall branching reaction $3H_2 + O_2 \rightleftharpoons 2H + 2H_2O$, with a rate given mainly by that of the elementary reaction $H + O_2 \rightleftharpoons OH + O$, and an overall recombination reaction $2H \rightarrow H_2$, with a rate given mainly by that of the elementary reaction $H + O_2 + M \rightarrow HO_2 + M$. This simple mechanism was found to provide predictions of flame structure and propagation velocities in reasonable agreement with those obtained with detailed chemistry [7].

Previous theoretical analyses of hydrogen-air flames have investigated the structure and burning rate of hydrogen-air deflagrations. Cryogenic H_2-O_2 deflagrations near the lean and rich flammability limits, of interest in cryogenic rocket engines, were addressed in [6], whereas moderately lean and stoichiometric flames were studied by Seshadri et al [8]. The latter theoretical development, based on the two-step kinetic description previously derived [7], used rate-ratio arguments to develop the asymptotic description of the flame structure and propagation velocity. The results obtained were reasonably accurate and tendencies were correctly predicted, although errors exceeding 50% in propagation velocities were seen under most conditions.

1.2 Chemistry description

1.2.1 Detailed chemical-kinetic mechanisms

The chemistry of hydrogen-air combustion is reasonably well established. Although existing chemical-kinetic mechanisms differ in the rates of some of the reactions, most of them succeed in predicting with good accuracy flame propagation velocities when used in integrations of one-dimensional adiabatic conservation equations with detailed transport descriptions [9]. This is illustrated in Fig. 1.1, which compares results of computations of flame propagation velocities v_l determined with three different detailed chemistry descriptions: the so-called San Diego Mechanism [10], Warnatz mechanism [11], and the recent mechanism proposed by Curran [12] as an improved development from the GRI-mech [13]. As can be seen, for the computations shown, which correspond to a pressure $p = 1$ atm and initial temperature $T_u = 300$ K, the re-

sulting departures are typically smaller than 5%, except near the flammability limit, where relative differences are somewhat larger.

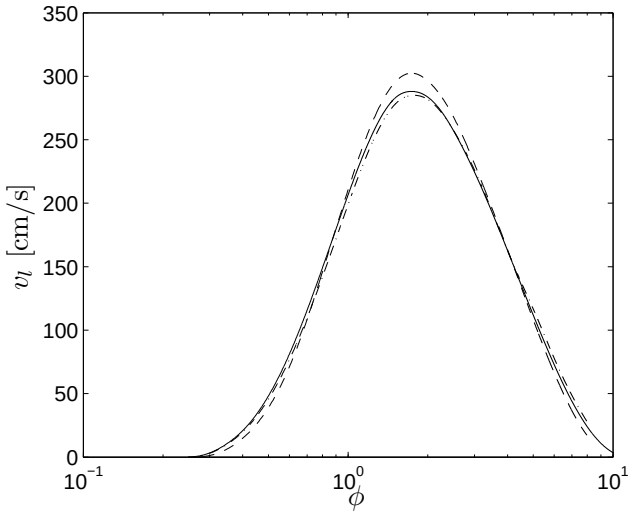

Figure 1.1: The variation with equivalence ratio of the propagation velocity of premixed hydrogen-air flames for $p = 1$ atm and $T_u = 300K$ as obtained from numerical integrations with detailed chemistry (solid curve: San Diego Mechanism [10]; dashed curve: Warnatz [11] and dot-dashed curve: Conaire et al. [12]).

In view of the above comparison, it is clear that different options of comparable accuracy are available for the selection of the detailed starting mechanism. In the following, we shall use the San Diego Mechanism [10], whose 21 reversible steps are shown for completeness in the table of appendix A along with the rate constants of the forward reactions, whereas the reverse rates are to be obtained from the corresponding equilibrium constants. This mechanism was extensively tested recently and, for most conditions, was shown to give excellent predictions of laminar burning velocities [14], as can be seen in Fig. 1.2, which compares numerical results obtained with the COSILAB code [15] with three different sets of experimental data [16–18]. The computations assume adiabatic isobaric planar-flame propagation with pressure $p = 1$ atm and initial temperature $T_u = 300$ K. The agreement between the experimental and numerical results is seen to be excellent when thermal diffusion is taken into account in the numerical description, except for very lean flames with equivalence ratio $\phi < 0.4$, where the numerical integrations tend to under-

predict flame velocities, independent of cross-transport effects of thermal diffusion, suggesting that premixed combustion near the lean flammability limit does not occur in the form of a uniform planar front, a result to be anticipated from concepts of cellular instabilities.

A second set of computations, now with thermal diffusion excluded, is also shown in the figure. In agreement with earlier conclusions [19], the simplified transport description produces somewhat less satisfactory results, leading to overpredictions in flame velocities on the order of 10% for stoichiometric and moderately rich mixtures. This difference is attributable to Soret diffusion of H_2 out of the controlling reaction zone, towards the hot boundary, where the temperature is much higher at these near-stoichiometric conditions. For the fuel-lean mixtures of interest here, however, the temperature of the controlling reaction zone is not very different from the maximum temperature, so that the Soret effect is much less important for planar conditions, and it is seen in Fig. 1.2 that the resulting differences become negligible for lean flames. Since it is possible to focus most directly on the chemistry by excluding transport complexities, thermal diffusion will be omitted in the following development, and therefore the numerical results represented by the thin solid line in Fig. 1.2 will be taken as the basis for comparison with those to be obtained below. Since effects of nonplanar diffusion will not be investigated here, the lean-flame experimental results will not be considered further; they are, however, addressed elsewhere [20].

1.2.2 Short mechanisms

The San Diego Mechanism, of 21 reversible steps, is simplified further by noticing that, for hydrogen-oxygen systems, nine elementary reactions, only three of which are reversible, suffice to describe accurately hydrogen-air laminar burning velocities over the whole range of flammability conditions at pressures sufficiently below the third explosion limit of the hydrogen-oxygen system. This short mechanism includes the seven reactions shown in Table 1.1, together with the recombination reactions $H + H + M \xrightarrow{9f} H_2 + M$ and $H + OH + M \xrightarrow{10f} H_2O + M$, which become important for sufficiently rich mixtures, where the high temperatures lead to large radical concentrations, promoting two-radical reactions. Note that, for simplicity in the presentation, the reaction numbering given in Table 1.1 differs from that used in the appendix A, which corresponds exactly to that of the original reference [10]. Flame velocities computed with these 9 elementary reactions with thermal

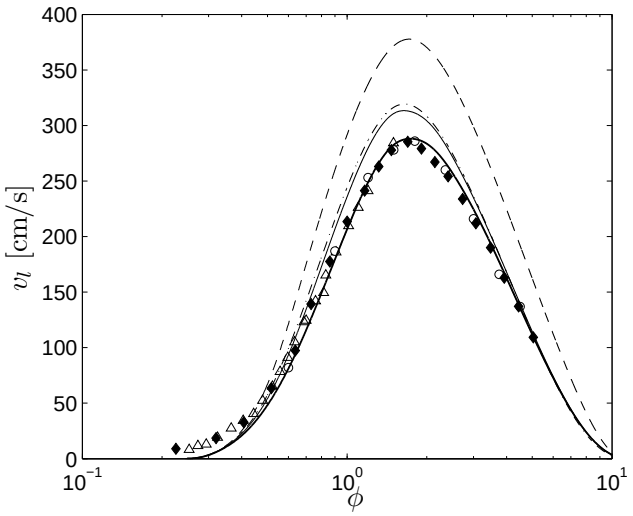

Figure 1.2: The variation with equivalence ratio of the propagation velocity of premixed hydrogen-air flames for $p = 1$ atm and $T_u = 300K$ as obtained from experiments ([16]: diamonds; [17]: triangles; [18]: circles), from numerical integrations with the detailed chemistry and thermal diffusion included (thick solid curve) and with thermal diffusion excluded (detailed mechanism: thin solid curve; 9-step short mechanism: dot-dashed curve; 7-step short mechanism: dashed curve).

diffusion neglected are also included in Fig. 1.2, showing excellent agreement with the detailed-chemistry computations.

For mixtures that are very fuel lean, of interest in the present analysis, radical concentrations take on very small values, causing the direct recombination reactions H + H + M $\stackrel{9f}{\rightarrow}$ H_2 + M and H + OH +M $\stackrel{10f}{\rightarrow}$ H_2O + M, which require three-body collisions involving two radicals, to become very slow compared with reaction $4f$ of Table 1.1 [8]. The chemistry description of 21 steps reduces then for very lean flames to the seven steps shown in Table 1.1, which include the three reversible shuffle reactions 1–3, the irreversible recombination reaction $4f$, and the three irreversible HO_2-consuming reactions $5f$–$7f$. The table shows the rate constants for all reactions, determining their dependence on the temperature T. In calculating the pressure dependence of the reaction-rate constant $k_{4f} = Fk_0/(1 + k_0C_M/k_\infty)$ we have evaluated the falloff factor F from the general expression derived in [21] and present in [15] and in other available codes which in the range of pressures investigated gives values that

differ only by a small amount from those computed with the simpler expression $F = (0.5)^{\{1+[0.8\log(k_0 C_M/k_\infty)]^2\}^{-1}}$ proposed in [22] and in good agreement with the more recent in [23], but not included in most codes, although new developments are now making this available in [15]. Although, like direct recombination, this step $4f$ might be thought to be in the low-pressure limit under normal conditions, falloff was found computationally to be not entirely negligible for it even at $p = 1$ atm, $T_u = 300$ K as can explicitly be seen in appendix B, where a more thorough investigation of the pressure dependence of the reaction $4f$ is presented.

Table 1.1: The 7-step mechanism with rate coefficients in the Arrhenius form $k = AT^n \exp(-T_a/T)$ as given in [14].

Reaction		A[a]	n	T_a [K]
1. $H + O_2 \rightleftharpoons OH + O$[b]	k_f	3.52×10^{16}	-0.7	8590
	k_b	7.04×10^{13}	-0.264	72
2. $H_2 + O \rightleftharpoons OH + H$[b]	k_f	5.06×10^{4}	2.67	3166
	k_b	3.03×10^{4}	2.633	2433
3. $H_2 + OH \rightleftharpoons H_2O + H$[b]	k_f	1.17×10^{9}	1.3	1829
	k_b	1.29×10^{10}	1.196	9412
4f. $H + O_2 + M \rightarrow HO_2 + M$[b]	k_0	5.75×10^{19}	-1.4	0.0
	k_∞	4.65×10^{12}	0.44	0.0
5f. $HO_2 + H \rightarrow OH + OH$		7.08×10^{13}	0.0	148
6f. $HO_2 + H \rightarrow H_2 + O_2$		1.66×10^{13}	0.0	414
7f. $HO_2 + OH \rightarrow H_2O + O_2$		2.89×10^{13}	0.0	-250

[a] Units are mol, s, cm^3, and K.

[b] Chaperon efficiencies are 2.5 for H_2, 16.0 for H_2O, and 1.0 for all other species; Troe falloff with $F_c = 0.5$ [21].

Results of flame computations with the 7-step mechanism of Table 1.1 are represented by the dashed curve in Fig. 1.2. As can be seen, the 7-step mechanism tends to overpredict flame propagation velocities, with errors that are of the order of 20% for $\phi = 0.6$ and that become even larger for stoichiometric and rich flames. For lean flames with $\phi < 0.5$, however, the errors in v_l are very small, thereby justifying the adoption of the 7-step short mechanism as the starting point of the reduced-chemistry analysis for the conditions close to the flammability limit considered in the two following chapters. If

increased accuracy is required, then the additional recombination reactions H + H + M $\overset{9f}{\rightarrow}$ H_2 + M and H + OH + M $\overset{10f}{\rightarrow}$ H_2O + M should be considered also, especially in moderately lean flames with $\phi > 0.5$, addressed in chapter 4.

It should be noted that the simplified 7-step chemical-kinetic mechanism leads to a flame velocity that tends to zero as a kinetically determined lean flammability limit is approached. This flammability limit is however not observed in computations of planar adiabatic flames if the H_2O_2 chemistry is included, when a slow deflagration, with a propagation velocity on the order of a few mm/s at atmospheric conditions, is obtained for very lean mixtures beyond the kinetically determined lean flammability limit of the 7-step mechanism. In reality, such slow flames would readily extinguish in the presence of the slightest heat loss, so that their relevance for practical purposes is very limited, except at sufficiently high pressure, when the associated propagation velocity becomes significant, as discussed below in Section 2.5.

To investigate the accuracy with which the 7-step mechanism describes the radical pool, Figs. 1.3 and 1.4 show profiles of radical mol fractions X_i (i = H, OH, O and HO_2) across the flame for $\phi = 0.3$ and $\phi = 0.5$ respectively (additional computations from other values of the equivalence ratio are included in appendix E). The H_2 mol fraction is also shown in the upper plots (it is essentially the same in the lower plots) to enable comparisons of its magnitude with that of the radicals to be made. Also, the profile of H_2O_2 is included in the detailed-chemistry results to help clarify the following interpretations.

It can be seen from Figs. 1.3 and 1.4 that the resulting H-atom mol fraction compares reasonably well with that obtained from detailed-chemistry computations for both initial compositions. The comparison is more favorable for $\phi = 0.3$, whereas for $\phi = 0.5$ the 7-step description tends to overpredict X_H, mainly because of the neglect of the recombination reaction H + OH + M $\overset{10f}{\rightarrow}$ H_2O + M and, to a lesser extent, H + H + M $\overset{9f}{\rightarrow}$ H_2 + M.

On the other hand, the HO_2 mol fraction is noticeably different for the 7-step mechanism at the lowest equivalence ratio. The HO_2 concentration is relatively small for $\phi = 0.5$ but reaches values comparable to those of the other radicals for $\phi = 0.3$. The peak value of X_{HO_2} is located approximately at the position where H, O and OH vanish. The 7-step chemistry tends to overpredict X_{HO_2} both at the peak and also farther upstream. This discrepancy is explained by the fact that the 7-step description considers only the HO_2 consumption reactions $5f$–$7f$, which involve hydroperoxyl collisions with ei-

ther H or OH, but does not include the hydroperoxyl recombination reaction $HO_2 + HO_2 \rightarrow H_2O_2 + O_2$. This latter reaction becomes the dominant HO_2 consumption reaction in the absence of H and OH, and it is responsible for the appearance of significant amounts of H_2O_2, at the expense of a relatively rapid decay of HO_2, upstream from the location of H and OH depletion, as can be observed in the upper plot of Fig. 1.3. Consideration of the hydroperoxyl recombination reaction $HO_2 + HO_2 \rightarrow H_2O_2 + O_2$ is therefore needed in this upstream region for an accurate description of HO_2; the sum of HO_2 and H_2O_2 mole fraction calculated with the full mechanism approximates the HO_2 mole fraction of the 7-step mechanism fairly closely. Description of H_2O_2 production is, however, unnecessary for the computation of the overall combustion rate at pressures far enough below the third explosion limit, as seen below, and it will not be introduced here.

Figures 1.3 and 1.4 also reveal that the 7-step description for X_O and X_{OH}, which is reasonable for $\phi = 0.5$, is much less satisfactory for $\phi = 0.3$, where the 7-step mechanism gives too large a concentration of O atoms and too small a concentration of OH, which decays downstream much too fast. This disagreement can be remedied by including in the chemistry the fourth shuffle reaction $H_2O + O \overset{8}{\rightleftharpoons} OH + OH$. For sufficiently rich conditions (e.g., $\phi \gtrsim 0.4$ for $p = 1$ atm and $T_u = 300$ K) this reaction maintains partial equilibrium throughout the controlling reaction zone, as can be seen in the plots shown in appendix E, and need not be taken into account in the computation; consideration of the shuffle reactions 1-3 suffices to describe accurately X_O and X_{OH} in the presence of this partial equilibrium. For leaner flames, however, reaction 8 is no longer in partial equilibrium and needs to be included in the chemistry description for a correct computation of the OH and O content of the radical pool, a point that is investigated further in appendix C.

In summary, we have seen that the 7 elementary reactions shown in Table 1.1 suffice to describe lean deflagrations close to the lean flammability limit, although consideration of the additional shuffle reaction $H_2O + O \overset{8}{\rightleftharpoons} OH + OH$ improves descriptions of O and OH radical profiles. The resulting 7-step mechanism will be used below as starting point for the analytical developments of the two following chapters, which are devoted to near-limit lean flames, and the modifications associated with the 8-step mechanism are considered separately in appendix C. As the radical level increases for richer flames away from the flammability limit, the direct radical recombination reactions $H + H + M \overset{9f}{\rightarrow} H_2 + M$ and $H + OH + M \overset{10f}{\rightarrow} H_2O + M$ need to be

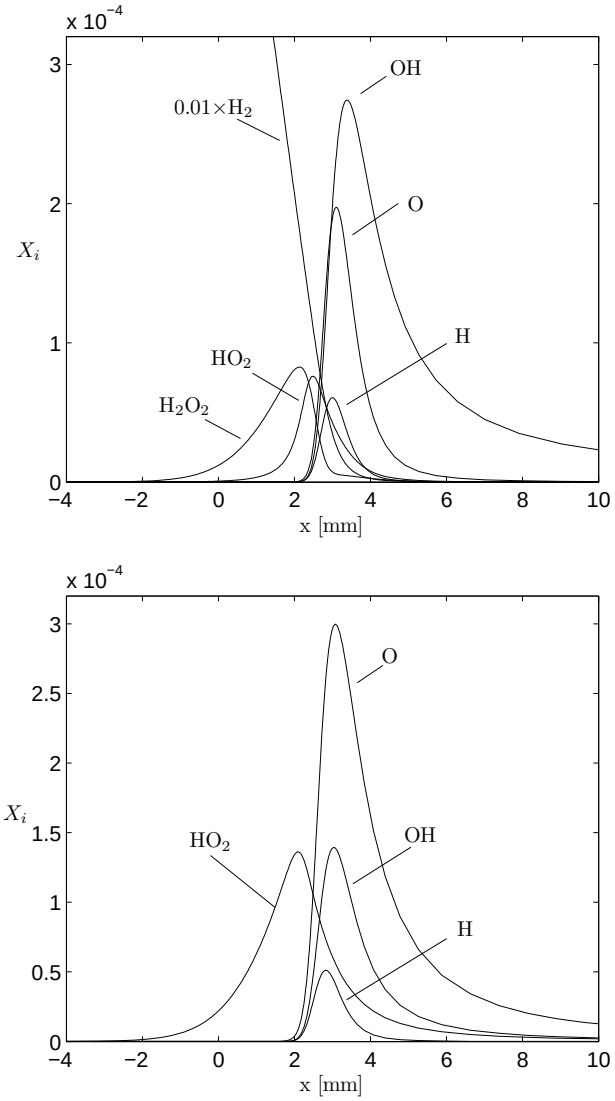

Figure 1.3: Profiles of the radical mol fractions in the flame as obtained from detailed kinetics (upper plot) and from the 7-step mechanism (lower plot) for $\phi = 0.3$, $p = 1$ atm and $T_u = 300K$.

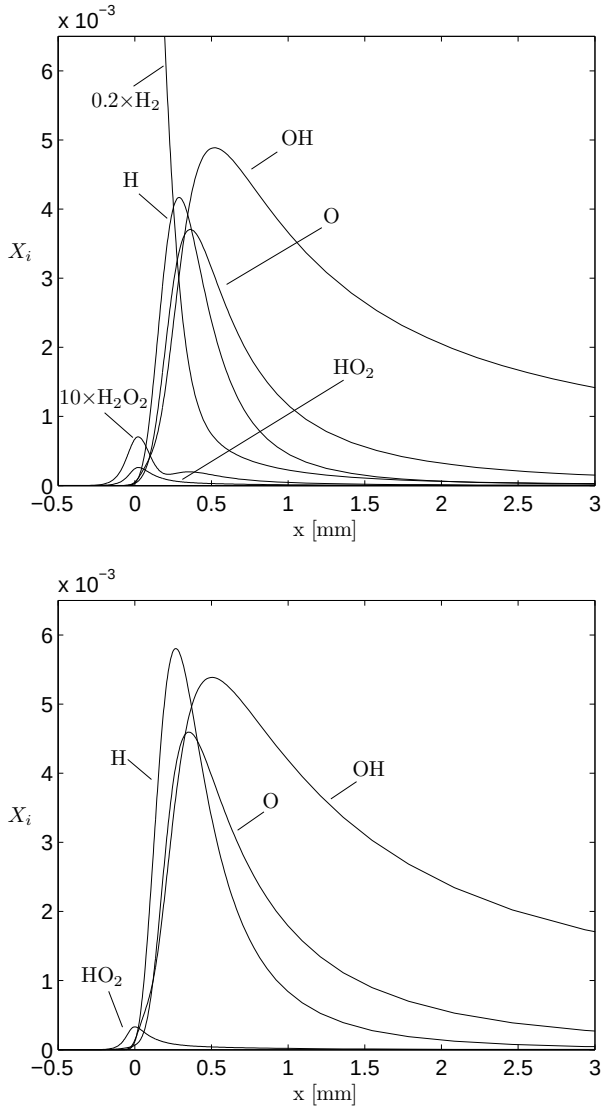

Figure 1.4: Profiles of the radical mol fractions in the flame as obtained from detailed kinetics (upper plot) and from the 7-step mechanism (lower plot) for $\phi = 0.5$, $p = 1$ atm and $T_u = 300K$.

included for improved accuracy, whereas the effect of reaction 8 becomes negligible. Consequently, the resulting 9-step description is to be used below in chapter 4 for the analysis of moderately lean and stoichiometric flames. To characterize the variation with temperature of the rates of these reactions $1-10$, it is of interest to evaluate their associated characteristic times, as done in Fig. 1.5, which can be used to assess their relative importance at different temperature conditions.

1.3 Outline of the dissertation

The present dissertation is organized as follows. Chapter 2 presents the derivation of the one-step mechanism for hydrogen oxidation, which is applicable near the lean flammability limit. The mechanism, used in computations of planar deflagrations, is seen to provide flammability limits and flame propagation velocities with great accuracy. Analysis of the structure of the thin reactive region, which includes a layer where the steady-state assumption fails, is given in chapter 3. Lean flames relatively far from the flammability limit are analyzed next in chapter 4 with use made of a two-step reduced mechanism in the limit of large activation temperature of the radical production step. Finally, conclusions and future prospects are given in chapter 5. The results presented here are collected in three separate publications [24–26].

The appendices provide detailed information on a number of issues. For instance, the complete 21 elementary reactions of the San Diego Mechanism and their corresponding reaction-rate parameters are given in appendix A and a detailed account of the pressure dependence of the reaction $H+O_2+M \overset{4f}{\rightarrow} HO_2+M$ is presented in appendix B. The modifications to the one-step chemistry that arise when considering the effect of the shuffle reaction $H_2O + O \overset{8}{\rightleftharpoons} OH + OH$ are given in appendix C. The asymptotic analysis of the layer of steady-state failure, presented in chapter 3, can be motivated with a simple, more academic, example, as shown in appendix D. Although only a limited number of computations of laminar flames obtained with the COSILAB code [15] are exhibited in the main text of the dissertation for selected conditions of composition, pressure and initial temperature, many more computations were performed in the course of the investigation. We consider that the associated information could be valuable for the interested reader, and have therefore decided to collect the results in two separate appendices E and F, including profiles of chemical species and temperature and of chemical rates of produc-

tion and consumption across the flame. Finally, values of the adiabatic flame temperature, used throughout the text in evaluating different quantities, are computed in appendix G for different conditions of pressure, temperature and composition.

References

[1] R. W. Shefer, Hydrogen enrichment for improved lean flame stability, Int. J. Hydrogen Energy 28 (2003) 1131–1141.

[2] F. A. Williams, Detailed and reduced chemistry for hydrogen autoignition, J. Loss Prevent. Process Indust. 21 (2008) 131–135.

[3] J. B. Bell, M. S. Day, I. G. Shepherd, M. Johnson, R. K. Cheng, J. F. Grcar, V. E. Beckner, M. J. Lijewski, Numerical simulation of a laboratory-scale turbulent v-flame, Proc. Natl. Acad. Sci. USA 102 (29) (2005) 10006–10011.

[4] G. Dixon-Lewis, Kinetic mechanism, structure and properties of premixed flames in hydrogen-oxygen-nitrogen mixtures, Phil. Trans. Roy. Soc. London 292 (1388) (1979) 45–99.

[5] G. Balakrishnan, M. D. Smooke, F. A. Williams, A numerical investigation of extinction and ignition limits in laminar nonpremixed counterflowing hydrogen-air streams for both elementary and reduced chemistry, Combust. Flame 102 (1995) 329–340.

[6] L. He, P. Clavin, Premixed hydrogen-oxygen flames. part I: Flame structure near the flammability limits, Combust. Flame 93 (1993) 391–407.

[7] F. Mauss, N. Peters, B. Rogg, F. A. Williams, Reduced kinetic mechanisms for premixed hydrogen flames, in: N. Peters, B. Rogg (Eds.), Reduced Kinetic Mechanisms for Applications in Combustion Systems, Springer-Verlag, 1993, pp. 29–43.

[8] K. Seshadri, N. Peters, F. A. Williams, Asymptotic analysis of stoichiometric and lean hydrogen-air flames, Combust. Flame 96 (1994) 407–427.

[9] F. A. Williams, Progress in knowledge of flamelet structure and extinction, Prog. Energy and Combust. Sci. 26 (2000) 657–682.

[10] http://maeweb.ucsd.edu/~combustion/cermech/ (2005).

[11] J. Warnatz, Concentration, pressure and temperature dependence of the flame velocity in Hydrogen-Oxygen-Nitrogen mixtures, Combust. Sci. Tech. 26 (1981) 203–213.

[12] M. O. Conaire, H. J. Curran, J. M. Simmie, W. J. Pitz, C. K. Westbrook, A comprehensive modelling study of hydrogen oxidation, Intl. J. Chem. Kinet. 36 (11) (2004) 603–622.

[13] http://www.me.berkeley.edu/gri-mech/ (Last updated 2000).

[14] P. Saxena, F. A. Williams, Testing a small detailed chemical-kinetic mechanism for the combustion of hydrogen and carbon monoxide, Combust. Flame 145 (2006) 316–323.

[15] Version 2.0.7, Rotexo-Softpredict-Cosilab Gmbh & Co. KG, http://www.SoftPredict.com (2007).

[16] D. R. Dowdy, D. B. Smith, S. C. Taylor, A. Williams, The use of expanding spherical flames to determine burning velocities and stretch effects in hydrogen/air mixtures, Proc. Combust. Inst. 23 (1990) 325–332.

[17] F. N. Egolfopoulos, C. K. Law, An experimental and computational study of the burning rates of ultra-lean to moderately rich $H_2/O_2/N_2$ laminar flames with pressure variations, Proc. Combust. Inst. 23 (1990) 333–340.

[18] O. C. Kwon, G. M. Faeth, Flame/stretch interactions of premixed hydrogen-fueled flames: Measurements and predictions, Combust. Flame 124 (2001) 590–610.

[19] H. Bongers, L. P. H. de Goey, The effectof simplified transport modeling on the burning velocity of laminar premixed flames, Combust. Sci. Tech. 175 (2003) 1915–1928.

[20] F. A. Williams, J. F. Grcar, A hypothetical burning-velocity formula for very lean hydrogen-air mixtures, Proc. Combust. Inst. 32 (2009) 1351–1357.

[21] R. G. Gilbert, K. Luther, J. Troe, Theory of thermal unimolecular reactions in the fall-off range. II. Weak collisions rate constants, Ber. Bursenges. Phys. Chem. 87 (1983) 169–177.

[22] J. Troe, Predictive possibilities of unimolecular rate theory, J. Phys. Chem. 83 (1) (1979) 114–126.

[23] J. Troe, Detailed modeling of the temperature and pressure dependence of the reaction H + O_2 (+M) $\rightarrow$ HO_2 (+M), Proc. Combust. Inst. 28 (2000) 1463–1469.

[24] D. Fernández-Galisteo, A. L. Sánchez, A. Liñán, F. A. Williams, One-step reduced kinetics for lean hydrogen-air deflagration, Combust. Flame 156 (2009) 985–996.

[25] D. Fernández-Galisteo, A. L. Sánchez, A. Liñán, F. A. Williams, The hydrogen-air burning rate near the lean flammability limit, Combust. Theory Modelling 13 (4) (2009) 741–761.

[26] D. Fernández-Galisteo, A. L. Sánchez, A. Liñán, F. A. Williams, Zel'dovich analysis of lean hydrogen-air flames. In preparation.

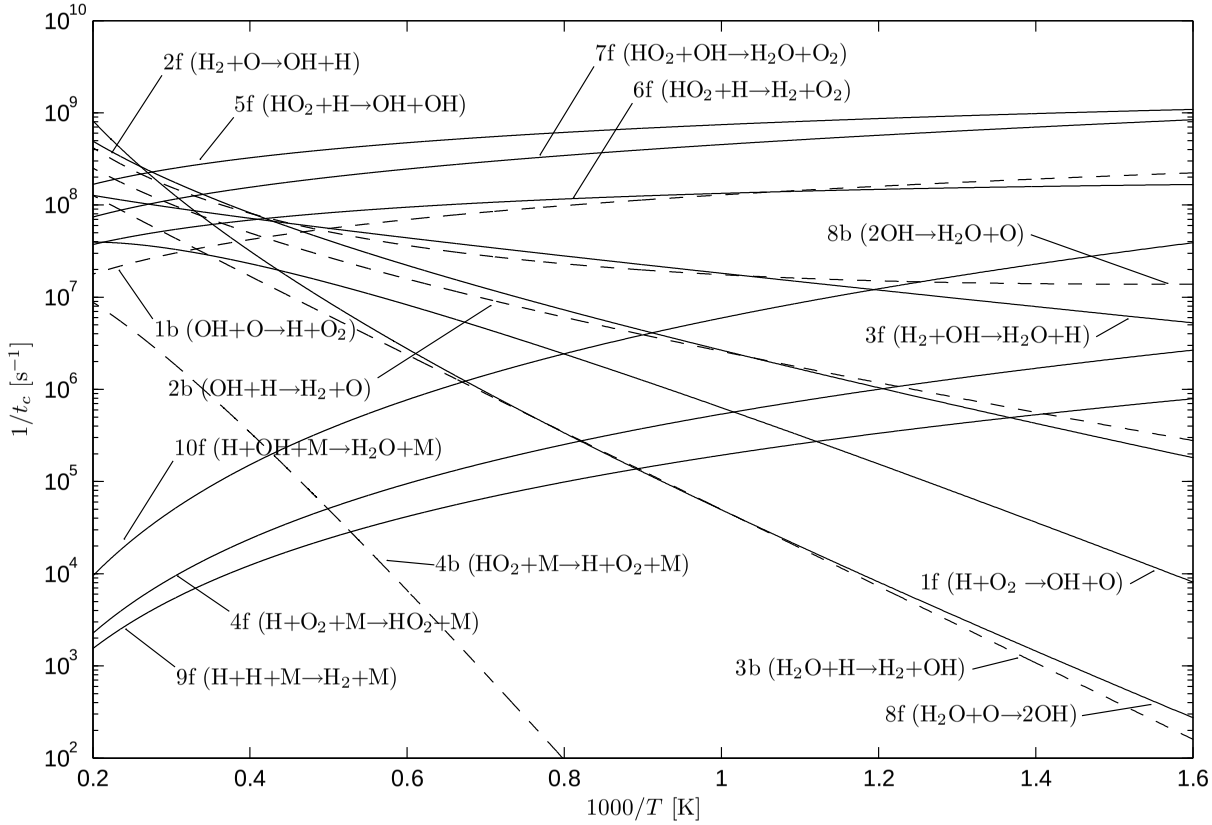

Figure 1.5: The inverse of the characteristic times of reactions $1-10$ at $p = 1$ atm as computed according to $t_{c_j}^{-1} = k_j C_{\mathrm{M}}$ for $j = 1-3$ and $j = 5f-8f$, and $t_{c_j}^{-1} = k C_{\mathrm{M}}^2$ for $j = 4f, 9f$, and $10f$.

CHAPTER

TWO

One-step reduced kinetics for lean hydrogen-air deflagration

2.1 Introduction

It has long been believed that a one-step systematically reduced mechanism would be too inaccurate for any realistic hydrogen-combustion application. However, it will be shown below that for hydrogen-air deflagrations over a range of equivalence ratios adjacent to the lean flammability limit the concentrations of all chemical intermediates are small enough for them to follow accurately a steady state approximation, while the main reactants obey the overall irreversible reaction $2H_2 + O_2 \rightarrow 2H_2O$, with a global hydrogen-oxidation non-Arrhenius rate determined by those of the elementary reactions of the starting detailed mechanism. This one-step reduced mechanism, which has been published recently [1], is seen to provide reasonable predictions of limits for lean deflagrations as well as good results for deflagration velocities for conditions near the lean flammability limit. For richer mixtures, radical concentrations in the reaction layer increase, and their associated steady-state approximations, especially that of H, become less accurate, leading to the failure of the one-step reduced kinetics, which away from the flammability limit must be replaced by the two-step or three-step descriptions previously derived [2, 3]. These limitations of the one-step mechanism are explored, and the simplifications of the chemistry that lead to the one-step approximation are evaluated. The one-step result is explicit and could readily be implemented in future codes for the calculation of lean hydrogen combustion in complex configurations.

The development below starts by considering the 7-step mechanism given in Table 1.1, which has been shown above to be an appropriate description for the chemistry near the lean flammability limit. The performance of this

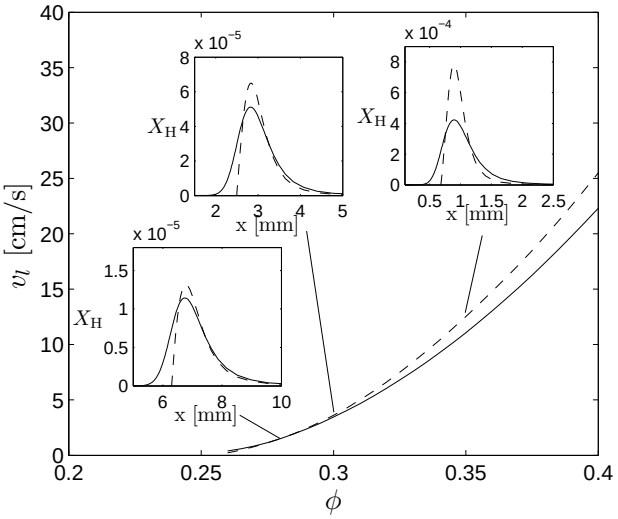

Figure 2.1: The variation with equivalence ratio of the H_2-air flame-propagation velocity v_l, as obtained from numerical computations with detailed chemistry (solid curve) and with the 7-step mechanism (dashed curve) for $p = 1$ atm and $T_u = 300$ K. The insets compare the H-atom mol-fraction profiles in the flame for the 7-step computations (solid curves) with those obtained by evaluating equation (2.27) for $\phi = (0.28, 0.3, 0.35)$ (dashed curves).

7-step mechanism in very fuel-lean conditions is tested further in Fig. 2.1, which shows a blowup of Fig. 1.2 with comparisons of the detailed and 7-step chemistry computations, along with H-atom profiles, to be discussed later. Clearly, the errors in v_l are reasonably small, thereby justifying the adoption of the 7-step short mechanism as the starting point of the reduced-chemistry analysis.

As discussed in the preceeding chapter, inclusion of the reaction HO_2 + $HO_2 \rightarrow H_2O_2 + O_2$, necessary for a correct description of the HO_2 profile upstream from the location of H and OH depletion, and of the reaction H_2O + O $\overset{8}{\rightleftharpoons}$ OH + OH, necessary to describe the profiles of O and OH for lean flames near the flammability conditions, does not modify appreciably the resulting H-atom profile, which is described with sufficient accuracy by the 7-step mechanism for near-limit flames. As seen below, it is the concentration of H that determines the burning rate for very lean conditions, and therefore the following analysis will use the 7-step mechanism as a starting point for the

reduced-chemistry development, the objective being the derivation of a one-step mechanism that correctly predicts flame propagation velocities. The augmented mechanism that follows from adding reaction 8, necessary to compute O and OH concentrations accurately, is analyzed separately in appendix C.

2.2 One-step reduced kinetics

Previous investigators of hydrogen-air combustion have simplified the chemistry by assuming that O, OH and HO_2 maintain steady states throughout the flame, so that H remains the only intermediate species not following a steady-state approximation [3]. The chemistry description is then simplified to a well-known two-step reduced mechanism composed of an overall branching reaction $3H_2 + O_2 \rightleftharpoons 2H + 2H_2O$, with a rate given mainly by that of the elementary reaction $H + O_2 \overset{1f}{\rightleftharpoons} OH + O$, and an overall recombination reaction $2H \rightarrow H_2$, with a rate given mainly by that of the elementary reaction $H + O_2 + M \overset{4f}{\rightarrow} HO_2 + M$. This simple mechanism, used in analytical developments [4] and also hereafter in chapter 4, was found to provide predictions of flame structure and propagation velocities in good agreement with those obtained with detailed chemistry [3]. If H is also put into steady state, then this mechanism becomes a one-step mechanism. Previous efforts to accomplish this have not produced satisfactory results, primarily because of further approximations that were introduced to make the one-step reaction-rate description tractable. For example, step $7f$ was omitted in certain steady-state formulas in [4]. Such "truncation" approximations are not made here; the present one-step kinetics can be viewed as being derivable from the two-step description by introducing the H-atom steady state while fully retaining all of the elementary steps of Table 1.1.

For the conditions of interest here, fuel-lean mixtures not too far from the flammability limit, the concentrations of all four radicals H, O, OH and HO_2 are so small that they can be assumed to be in steady state, although the accuracy of the approximation decreases for richer flames. To illustrate this, we have plotted in Fig. 2.2 the variation of the rates of chemical production, chemical consumption and transport of the four radicals as obtained from the detailed-chemistry computations for $\phi = 0.3$ and $\phi = 0.5$. Results of additional computations for a wide range of conditions can be found in appendix F. It can be seen in Fig. 2.2 that for $\phi = 0.3$ the radical concentrations, shown in Fig. 1.3, are so small that their resulting transport rates are negligible

compared with their chemical rates everywhere across the reaction zone for all four radicals. For $\phi = 0.5$, the concentrations of O, OH and H are much larger, as can be seen in Fig. 1.4, while that of HO_2 remains comparatively small. The corresponding transport rates of O, OH and HO_2 are still negligible, as can be seen in Fig. 2.2. Although H appears in concentrations that are comparable to those of O and OH, its diffusivity is about five times larger, leading to a transport rate that can be seen in Fig. 2.2 to be comparable to the H-atom chemical rates in the upstream part of the reaction zone, in agreement with previous results [3]. In view of Fig. 2.2, one can expect the steady-state approximation for all four intermediates to provide a very accurate description for $\phi = 0.3$ and less accurate results for $\phi = 0.5$. This situation is different from that encountered in autoignition, in which HO_2 is not in steady state, OH and O obey good steady states only under fuel-rich conditions, and the H steady state is accurate only for $\phi \lesssim 0.05$ [5].

To begin to incorporate the steady-state approximations in the chemistry description, the production rates associated with the 7-step mechanism are first written in general as

$$\dot{C}_{\mathrm{O}} = \omega_1 - \omega_2 \tag{2.1}$$

$$\dot{C}_{\mathrm{OH}} = \omega_1 + \omega_2 - \omega_3 + 2\omega_{5f} - \omega_{7f} \tag{2.2}$$

$$\dot{C}_{\mathrm{H}} = -\omega_1 + \omega_2 + \omega_3 - \omega_{4f} - \omega_{5f} - \omega_{6f} \tag{2.3}$$

$$\dot{C}_{\mathrm{HO_2}} = \omega_{4f} - \omega_{5f} - \omega_{6f} - \omega_{7f} \tag{2.4}$$

$$\dot{C}_{\mathrm{H_2}} = -\omega_2 - \omega_3 + \omega_{6f} \tag{2.5}$$

$$\dot{C}_{\mathrm{O_2}} = -\omega_1 - \omega_{4f} + \omega_{6f} + \omega_{7f} \tag{2.6}$$

$$\dot{C}_{\mathrm{H_2O}} = \omega_3 + \omega_{7f}, \tag{2.7}$$

where ω_j is the rate of reaction j and $\dot{C}_i$ is the production rate of species i (mols per unit time per unit volume), with C_i denoting below the concentration of species i. Use of linear combinations of the above expressions leads to

$$\dot{C}_{\mathrm{H_2}} + \{\dot{C}_{\mathrm{O}} + \frac{1}{2}\dot{C}_{\mathrm{OH}} + \frac{3}{2}\dot{C}_{\mathrm{H}} - \frac{1}{2}\dot{C}_{\mathrm{HO_2}}\} = -2\omega_{4f} \tag{2.8}$$

$$\dot{C}_{\mathrm{O_2}} + \{\dot{C}_{\mathrm{O}} + \frac{1}{2}\dot{C}_{\mathrm{OH}} + \frac{1}{2}\dot{C}_{\mathrm{H}} + \frac{1}{2}\dot{C}_{\mathrm{HO_2}}\} = -\omega_{4f} \tag{2.9}$$

$$\dot{C}_{\mathrm{H_2O}} - \{\dot{C}_{\mathrm{O}} + \dot{C}_{\mathrm{H}} - \dot{C}_{\mathrm{HO_2}}\} = 2\omega_{4f}, \tag{2.10}$$

as replacements for equations (2.5)–(2.7). At steady state, radicals can be anticipated to achieve concentrations that are much smaller than those of the reactants and H_2O, so that the terms in curly brackets can be discarded in (2.8)–

$\phi = 0.3$:

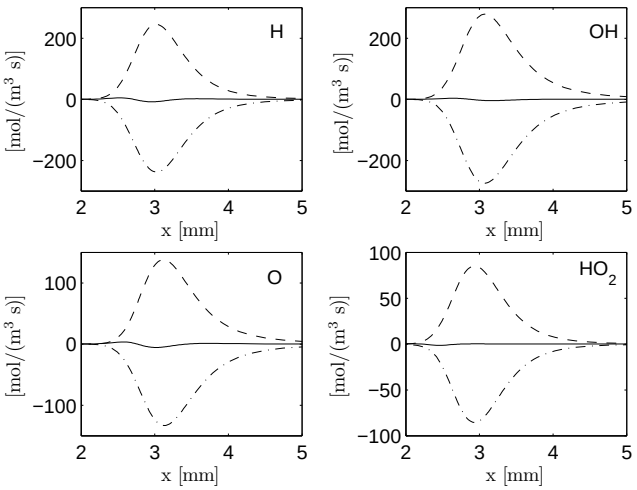

$\phi = 0.5$:

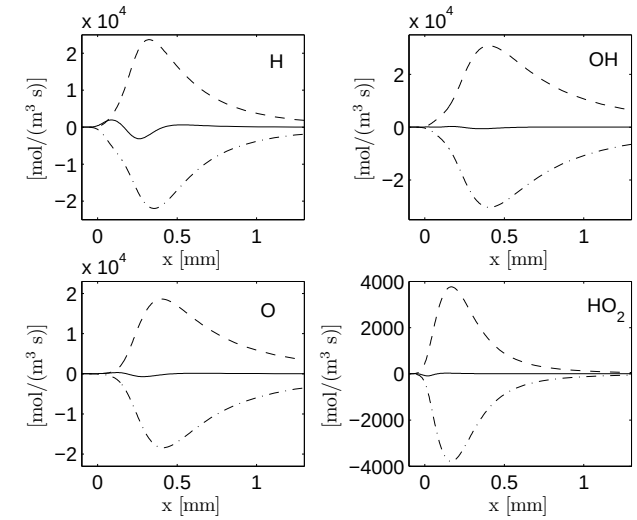

Figure 2.2: The rates of production (dashed curves), consumption (dot-dashed curves) and transport (solid curves) for H, OH, O and HO_2 across the flame as obtained with detailed chemistry for $p = 1$ atm and $T_u = 300$ K.

(2.10). The resulting expressions

$$-\frac{1}{2}\dot{C}_{H_2} = -\dot{C}_{O_2} = \frac{1}{2}\dot{C}_{H_2O} = \omega_{4f} = k_{4f}C_M C_{O_2} C_H, \tag{2.11}$$

indicate that, because of the steady-state approximations for the radicals, the 7-step short mechanism reduces to the global reaction

$$2H_2 + O_2 \rightarrow 2H_2O \tag{2.12}$$

with a rate equal to that of reaction $4f$. In view of the chaperon efficiencies listed in Table 1.1, $C_M = (1 + 15X_{H_2O} + 1.5X_{H_2})p/(R^oT)$, where X_i denotes the mole fraction of species i, and R^o is the universal gas constant.

2.3 Steady-state expressions for the radical concentrations

To determine the concentrations of the radicals, in particular that of H atoms, which is needed for the computation of ω_{4f}, it is necessary to use the algebraic steady-state equations,

$$\omega_1 - \omega_2 = 0 \tag{2.13}$$

$$\omega_1 + \omega_2 - \omega_3 + 2\omega_{5f} - \omega_{7f} = 0 \tag{2.14}$$

$$-\omega_1 + \omega_2 + \omega_3 - \omega_{4f} - \omega_{5f} - \omega_{6f} = 0 \tag{2.15}$$

$$\omega_{4f} - \omega_{5f} - \omega_{6f} - \omega_{7f} = 0, \tag{2.16}$$

obtained from (2.1)–(2.4), leading to exact explicit expressions for all four radicals in terms of the concentrations of O_2, H_2, H_2O and the temperature. The development starts by employing (2.13) and (2.16), respectively, to write

$$\frac{C_O}{C_H} = \frac{k_{1f}C_{O_2} + k_{2b}C_{OH}}{k_{1b}C_{OH} + k_{2f}C_{H_2}} \tag{2.17}$$

and

$$\frac{C_{HO_2}}{C_H} = \frac{k_{4f}C_M C_{O_2}}{(k_{5f} + k_{6f})C_H + k_{7f}C_{OH}}. \tag{2.18}$$

On the other hand, adding (2.13) and (2.15) and solving for C_{OH}/C_H provides

$$\frac{C_{OH}}{C_H} = \frac{Gk_{4f}C_M C_{O_2}}{k_{3f}C_{H_2}}, \tag{2.19}$$

where

$$G = \frac{1+\gamma_{3b}}{2} + \frac{f}{2}\left\{[1+2(3+\gamma_{3b})/f + (1+\gamma_{3b})^2/f^2]^{1/2} - 1\right\} \tag{2.20}$$

is a function of the rescaled fuel concentration

$$f = \frac{k_{5f}+k_{6f}}{k_{7f}} \frac{k_{3f}}{k_{4f}C_{\mathrm{M}}} \frac{C_{\mathrm{H_2}}}{C_{\mathrm{O_2}}}, \tag{2.21}$$

with

$$\gamma_{3b} = \frac{k_{3b}C_{\mathrm{H_2O}}}{k_{4f}C_{\mathrm{M}}C_{\mathrm{O_2}}} \tag{2.22}$$

representing the ratio of the rates of reactions $3b$ and $4f$. The function G is of order unity and approaches the limiting values $G = 1+\gamma_{3b}$ for $f \ll 1$ and $G = 2+\gamma_{3b}$ for $f \gg 1$.

Adding now (2.14), (2.15) and (2.16) and using (2.17), (2.18) and (2.19) yields an equation that can be solved for C_{OH} to give

$$C_{\mathrm{OH}} = \frac{1}{H}\frac{k_{2f}C_{\mathrm{H_2}}}{k_{1b}}\left(\frac{k_{1f}}{k_{4f}C_{\mathrm{M}}}\frac{f+G}{\alpha f+G} - 1\right) \tag{2.23}$$

where

$$H = \frac{1}{2} + \frac{1}{2}\left[1 + 4\gamma_{2b}f\frac{f+G}{\alpha f+G}\left(\frac{k_{1f}}{k_{4f}C_{\mathrm{M}}}\frac{f+G}{\alpha f+G} - 1\right)\right]^{1/2} \tag{2.24}$$

with

$$\gamma_{2b} = \frac{k_{7f}}{k_{5f}+k_{6f}}\frac{k_{2b}k_{2f}}{k_{1b}k_{3f}} \tag{2.25}$$

and

$$\alpha = \frac{k_{6f}}{k_{5f}+k_{6f}}. \tag{2.26}$$

Evaluation of these reaction-rate ratios indicates that $\gamma_{2b} \ll 1$ in the range of temperatures of interest (e.g., $\gamma_{2b} \simeq 1.5\times10^{-3}$ at $T = 1000$ K and $\gamma_{2b} \simeq 1.6\times10^{-2}$ at $T = 1400$ K), while α can be taken as $\alpha \simeq 1/6$ with sufficiently good accuracy. Substituting (2.23) into (2.19) gives

$$C_{\mathrm{H}} = \frac{1}{GH}\frac{k_{2f}k_{3f}C_{\mathrm{H_2}}^2}{k_{1b}k_{4f}C_{\mathrm{M}}C_{\mathrm{O_2}}}\left(\frac{k_{1f}}{k_{4f}C_{\mathrm{M}}}\frac{f+G}{\alpha f+G} - 1\right), \tag{2.27}$$

the desired expression for use in equation (2.11), while from (2.17) with use of (2.19) and (2.27) the O-atom concentration reduces to

$$C_O = \frac{\alpha f + G}{f + G} \frac{k_{3f} C_{H_2}}{G k_{1b}} \left(\frac{k_{1f}}{k_{4f} C_M} \frac{f + G}{\alpha f + G} - 1 \right). \tag{2.28}$$

It is of interest that, according to (2.23), (2.27) and (2.28), in the steady-state approximation adopted here the concentrations of OH, H and O, vanish as the temperature approaches the crossover value T_c, defined by the condition

$$k_{1f} = \frac{\alpha f + G}{f + G} k_{4f} C_M, \tag{2.29}$$

giving a value that depends on the composition through the functions f and G. The concentration of the hydroperoxyl radical, given from (2.18), (2.19) and (2.21) by

$$C_{HO_2} = \frac{k_{3f}}{(f + G) k_{7f}} C_{H_2}, \tag{2.30}$$

reaches a nonzero value at the crossover temperature and is positive also for $T < T_c$. At temperatures below T_c the steady-state approximation predicts $C_O = C_{OH} = C_H = 0$, so that the reaction rate in equation (2.11) is cut off at that temperature.

The explicit rate expression for the global reaction (2.12) can be further simplified by noting that, because of the small value of γ_{2b} at temperatures of practical interest, the departures of the factor H from unity in (2.24) are negligible at the very lean equivalence ratios and therefore one can use $H = 1$ in (2.27), thereby yielding a simpler one-step rate in (2.31). However, the formal one-step result without this approximation yields the one-step rate

$$\omega = \omega_{4f} = \frac{1}{GH} \left(\frac{k_{1f}}{k_{4f} C_M} \frac{f + G}{\alpha f + G} - 1 \right) \frac{k_{2f} k_{3f}}{k_{1b}} C_{H_2}^2 \tag{2.31}$$

if $k_{1f} > k_{4f} C_M (\alpha f + G)/(f + G)$ and $\omega = 0$ otherwise, with G and f evaluated from (2.20) and (2.21). Implications of (2.31) both with and without this additional factor H will be explored further on.

2.4 The lean flammability limit

In lean premixed flames, the chemical reaction takes place near the hot boundary in a thin layer where the temperature is above its crossover value defined by (2.29). Since use of this formula involves evaluating f, it is evident

from (2.21) that the H_2 concentration in the reaction zone plays a role. Because of the presence of the upstream convective-diffusive zone, in this layer the fuel concentration is small compared with its initial value and in the planar reaction zone takes on values of the order

$$C_{H_{2c}} \sim \frac{T_\infty - T_c}{T_\infty - T_u} L_{H_2} C_{H_{2u}}, \tag{2.32}$$

where T_∞ represents the burnt temperature (the adiabatic flame temperature), and the subscript u denotes conditions in the unburnt mixture. The hydrogen Lewis number L_{H_2} appears in the above expression due to differential diffusion effects in the preheat region [6].

According to the steady-state description (2.27), H atoms can exist only within this thin layer where $T_c < T < T_\infty$, with a small concentration that determines the rate of the overall H_2-oxidation reaction (2.12). Clearly, the flame can no longer exist if the temperature remains below crossover throughout, so that the flammability limit corresponds to conditions such that $T_\infty = T_c$, an equation that can be used in calculating the critical value of the equivalence ratio at the lean flammability limit, ϕ_l, of the planar flame. To determine the value of T_c at the flammability limit, $(T_c)_l$, it is necessary to observe from (2.32) that $C_{H_{2c}}$ vanishes at $T_\infty = T_c$, so that the factor $(\alpha f + G)/(f + G)$ in (2.29) must be taken as unity according to (2.20) and (2.21), that is, $f = 0$ and $G = 1 + \gamma_{3b}$. Equation (2.29) thus provides the simple expression $k_{1f} = k_{4f} C_M$ at the lean flammability limit.

To use this result for finding ϕ_l and $(T_c)_l$, it may be observed that the third-body efficiency factor, appearing in the equation for C_M given below (2.12), reduces to $(15 X_{H_2O} + 1)$ with $X_{H_2O} = 2\phi/(4.76 + \phi)$, the burnt gas value, giving a value of T_c that depends on the equivalence ratio. Representative results are shown in Fig. 2.3 for $p = 1$ atm and $p = 10$ atm. The figure also exhibits the adiabatic flame temperature T_∞ obtained from chemical equilibrium for the same values of the pressure. For $p = 1$ atm, the initial temperature in this figure is taken to be $T_u = 300$ K; for $p = 10$ atm the value $T_u = 580$ K is selected here because this value corresponds to a gas mixture preheated from atmospheric conditions through an isentropic compression, of interest in engine applications. The figure illustrates the slight increase of $(T_c)_l$ with ϕ, associated with the increase of X_{H_2O}, and the well-known stronger increase of T_∞ with ϕ. For a given pressure, the crossing point between the two curves in Fig. 2.3 determines the critical values of the equivalence ratio and crossover temperature at the lean flammability limit of the steady planar flame, yielding $\phi_l = 0.251$ and $(T_c)_l = 1064$ K for $T_u = 300$ K and $p = 1$ atm and $\phi_l = 0.279$

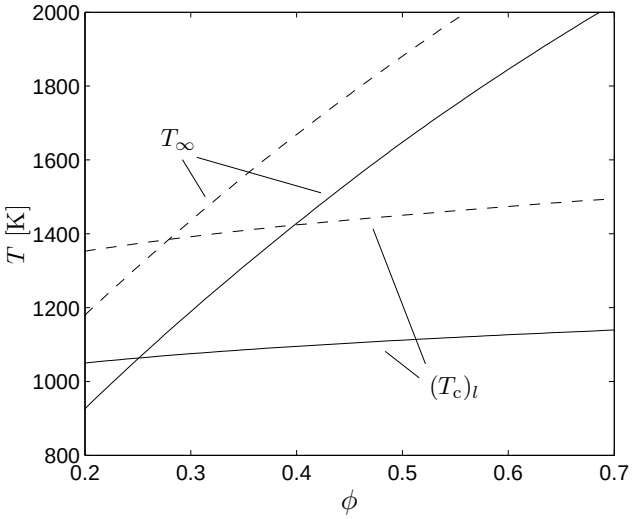

Figure 2.3: The variation with equivalence ratio of the H_2-air adiabatic flame temperature T_∞, as obtained from chemical equilibrium, and of the crossover temperature at the lean flammability limit $(T_c)_l$, as obtained for atmospheric pressure from $k_{1f} = k_{4f}C_M$, for $p = 1$ atm and $T_u = 300$ K (solid line) and for $p = 10$ atm and $T_u = 580$ K (dashed line).

and $(T_c)_l = 1380$ K for $T_u = 580$ K and $p = 10$ atm.

From the crossing points in Fig. 2.3, flammability limits were calculated as functions of pressure for four different initial temperatures. The results are shown by the solid curves in Fig. 2.4. Also shown (by dashed curves) in the figure are the calculated flame temperatures at the limit for the two extreme cases. The results illustrate the increase of ϕ_l and $(T_c)_l$ with p, arising from the associated increase in C_M, the three-body recombination becoming relatively faster than the two-body branching with increasing pressure; the strength of this dependence is seen to increase with p. In these calculations, falloff was included for k_{4f} as described previously, and T_∞ was obtained from a chemical-equilibrium routine [7]. For completeness, the calculated adiabatic temperatures T_∞, used along the dissertation, have been tabulated in appendix G for different conditions of the unburnt mixture. The temperatures obtained are within a few degrees of those found in the final downstream conditions predicted by COSILAB [8] with detailed chemistry and within 10 K to 20 K of those calculated for complete combustion to H_2O at these relatively

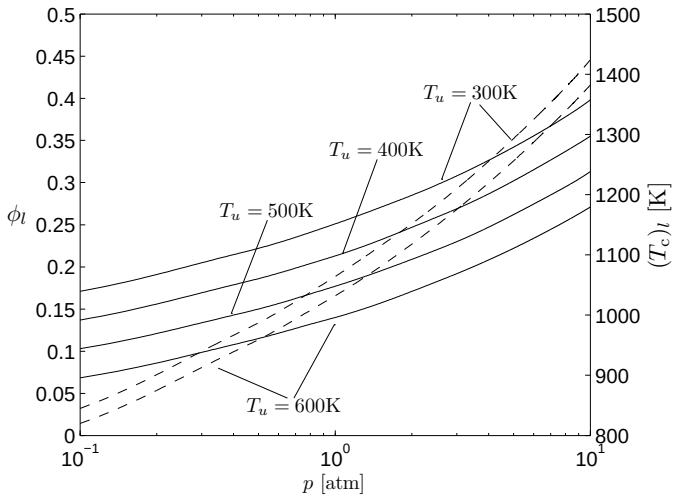

Figure 2.4: The calculated variation of the equivalence ratio ϕ_l (solid curves) and flame temperature $(T_c)_l$ (dashed curves) with pressure at the lean flammability limit for four different values of the initial temperature T_u.

low-temperature, near-limit conditions, the largest differences occurring at the largest values of ϕ in the figure. The results shown in Fig. 2.4 thus are accurate within a few percent, comparable to the accuracy of the plotting. They do, however, ignore influences of heat losses on flammability limits, which would tend to increase ϕ_l, and they exclude reactions that may occur below crossover (increasingly important with increasing pressure) and effects of nonplanar differential diffusion, both of which tend to decrease ϕ_l, the latter significantly.

2.5 The flame propagation velocity

The one-step kinetics in (2.31) was employed in computations of adiabatic flame propagation velocities for the conditions of pressure and initial temperature of Fig. 2.3, giving results that are compared in Fig. 2.5 with results for detailed and 7-step chemistry. The computations are based on the numerical integrations of the differential equations which were performed with the COSILAB code [8], with the one-step chemistry defined within an external subroutine that supplements the original code.

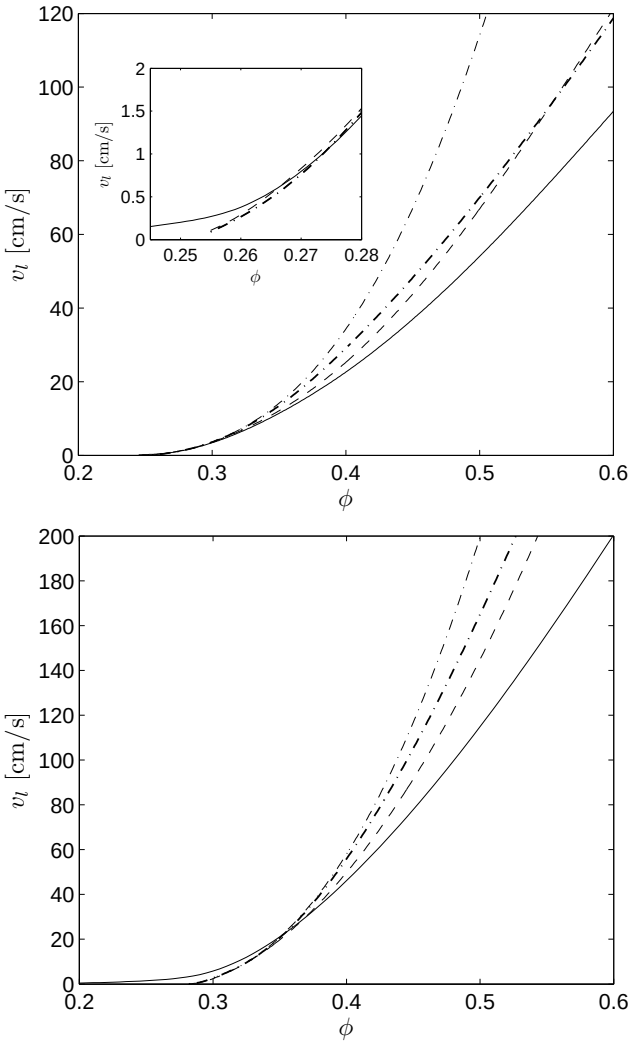

Figure 2.5: The variation with equivalence ratio of the propagation velocity of a premixed hydrogen-air flame for $p = 1$ atm and $T_u = 300K$ (upper plot) and for $p = 10$ atm $T_u = 580K$ (lower plot) as obtained from numerical integrations with detailed chemistry (solid curve), with the 7-step mechanism of Table 1.1 (dashed curve), with the one-step reduced mechanism for $H = 1$ (thin dot-dashed curve), and with the one-step reduced mechanism for variable H (thick dot-dashed curve). The inset in the upper figure shows a blowup near the flammability limit.

For atmospheric pressure, the agreement between the detailed and short mechanisms seen in Fig. 2.5 is excellent, with values of v_l that differ by less than 20% for $\phi_l < \phi < 0.6$. The steady-state description predicts accurately the lean flammability limit ($v_l = 0$ according to the approximations that lead to the one-step description), which also agrees well with the detailed-chemistry prediction. The burning velocity obtained from the steady-state approximations also agrees well with the short chemistry results. The agreement extends over values of the equivalence ratio far away from the lean flammability limit. As indicated by the plots in Fig. 2.2, for values of $\phi \gtrsim 0.45$ the agreement is however fortuitous, in that the steady-state assumption for H atoms is no longer valid. On the other hand, the simpler reaction-rate formula that arises by imposing $H = 1$ in (2.31) produces burning velocities that agree with the short-chemistry results only at very lean conditions, and tends to overpredict burning velocities as the mixture becomes richer.

From the bottom plot in Fig. 2.5 it is seen that at 10 atm the departures of the predictions of the one-step mechanism from those of the 7-step mechanism on which it is based are slightly greater than at 1 atm. In general, decreasing pressure improves the burning-velocity agreement of the one-step and 7-step mechanisms (and also improves the agreement of the 7-step mechanism with detailed chemistry), and at subatmospheric pressures the one-step mechanism is quite good for lean flames. The predictions of the one-step and 7-step mechanisms are in excellent agreement near the flammability limit, even with the simpler expression $H = 1$ in (2.31), and keeps the predictions very close even farther from the steady-state failure at all pressures investigated here. However, near the lean limit at 10 atm both the one-step and the 7-step mechanisms significantly underpredict the burning velocity of the detailed mechanism.

This last difference is due to the approach to the third explosion limit with detailed chemistry; the formation of H_2O_2 from HO_2 and its regeneration of active radicals is not entirely negligible at 10 atm. This is seen in the lower plot of Fig. 2.5 to have a potentially large effect on the lean flammability limit, if it is defined by $v_l \approx 0$. To that extent, the flammability limits predicted in the preceding section are inaccurate at high pressure. Since heat losses, however, typically extinguish flames readily if their burning velocities are below about 5 cm/s, the limits predicted in the preceding section may remain reasonable for planar flames up to 10 atm. In general, the detailed mechanism predicts positive burning velocities for all equivalence ratios, but at very low equivalence ratios these velocities are extremely small, although they increase significantly with increasing p at any given T_u. The 7-step mechanism is seen

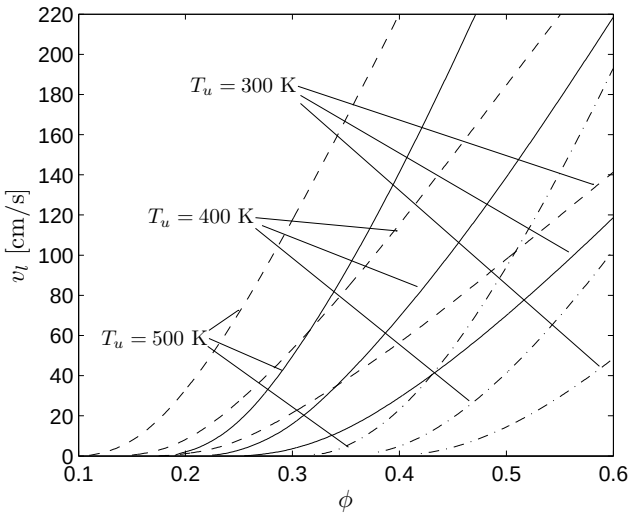

Figure 2.6: The variation with equivalence ratio of the propagation velocity of planar premixed hydrogen-air flames predicted by the one-step mechanism with $H = 1$ for $p = 0.1$ atm (dashed curves), $p = 1$ atm (solid curves) and $p = 10$ atm (dot-dashed curves) for three different initial temperatures.

to provide good burning-velocity agreement with the detailed mechanism at 10 atm with $T_u = 580$ K for $0.33 < \phi < 0.43$.

With these comparisons in mind, it is of interest to exhibit the burning-velocity predictions of the one-step mechanism for various pressures and initial temperatures, for $0.1 < \phi < 0.6$. Fig. 2.6 shows such predictions, demonstrating how v_l increases with T_u and varies much less strongly with p.

2.6 Arrhenius approximation

It is of interest to test how well the present results can be matched by one-step Arrhenius reaction-rate approximations. Such approximations have been investigated previously on the basis of experimental [9] and numerical [2] results. Although the burning velocities of Fig. 2.6 could be used for these tests, it is in a sense more fundamental to work with the rate expression of equation (2.31), employing the flame-structure solutions to construct an Arrhenius plot of the quantity multiplying $C_{\mathrm{H_2}}^2$ in order to obtain a second-order rate expression of the form $\omega = B \exp(-T_a/T) C_{\mathrm{H_2}}^2$. Fig. 2.7 shows such plots for four

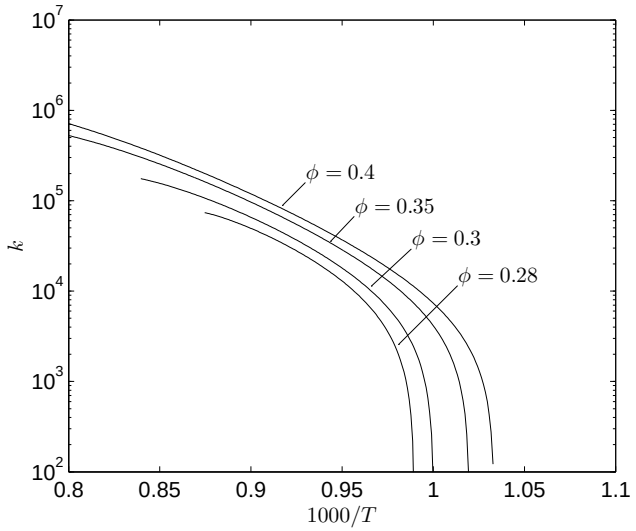

Figure 2.7: The variation with temperature of the factor $k = (k_{2f}k_{3f})/(Gk_{1b})\{k_{1f}(f + G)/[k_{4f}C_M(\alpha f + G)] - 1\}$ for four different equivalence ratios at $p = 1$ atm and $T_u = 300$ K.

different equivalence ratios at $p = 1$ atm and $T_u = 300$ K, with k denoting in the figure the quantity multiplying $C_{H_2}^2$ on the right-hand side of (2.31), where the near-limit assumption of $H = 1$ has been introduced, as discussed above. It is seen from this figure that, although such an approximation can be fit to the numerical results without excessive inaccuracy in an intermediate temperature range, the resulting activation temperatures vary appreciably, especially as crossover is approached. Away from crossover, the resulting values of the overall activation temperatures are of the order of $T_a \simeq 20000$ K, somewhat larger than the values reported earlier [2, 9], which correspond however to different conditions. In view of the plot, it is clear that a simple Arrhenius expression does not suffice to reproduce correctly the profile of the overall reaction rate near the lean flammability limit and that future efforts to derive a simplified reaction rate must account for the effect of the crossover temperature.

2.7 Limitations of the one-step chemistry

Further study of the limitations of the one-step chemistry is desirable. The explicit steady-state expression (2.27) is tested in Fig. 2.1, which includes comparisons of the H-atom profiles determined numerically on the basis of the 7-step mechanism with those determined from evaluating (2.27). In the evaluations, use has been made of the profiles of reactant and water-vapor mol fractions and of temperature obtained numerically with the 7-step mechanism.

It can be seen that the accuracy of the steady-state expression is best at very lean conditions, but it worsens as the mixture becomes richer, in agreement with the observations of Fig. 2.2. For the three conditions plotted in Fig. 2.1, it is evident that the steady-state assumption clearly fails at crossover, where the steady state predicts H atoms to disappear abruptly, thereby giving a profile with a discontinuous slope. Diffusive transport enters to remove this discontinuity, so that a smooth corner-layer profile replaces the abrupt change of the steady-state predictions when the 7-step mechanism is employed in the computations. In addition, it is seen in Fig. 2.1 that for all three conditions shown the steady-state approximation tends to overpredict the radical peak, giving values that exceed those obtained with detailed kinetics by roughly 50% for $\phi = 0.35$. The analysis of the corner layer, in which the steady-state approximations fail, will provide corrections to burning velocities predicted by the one-step mechanism, as shown in the following chapter.

The one-step chemistry fails, however, if $\phi - \phi_l$ becomes too large. In deriving the first equality in (2.11) from (2.8) we have assumed that in the reaction layer radicals exhibit concentrations that are much smaller than H_2 concentrations, a condition that can be seen to be clearly satisfied by the radicals plotted for $\phi = 0.3$ in Fig. 1.3 but not so clearly by those corresponding to $\phi = 0.5$ shown in Fig. 1.4. Radical concentrations, which are very small for flames near the flammability limit, become increasingly larger for increasing values of the equivalence ratio, causing the one-step description to break down. If H is considered to be the dominant radical in the radical pool, which can be seen to apply increasingly as the mixture becomes richer, the validity of the reduced kinetics is associated with the condition that $C_{\mathrm{H}} \ll C_{\mathrm{H}_2}$ in the reaction layer. To determine the characteristic value of C_{H} in the reaction zone, use may be made of (2.27), taking $H = 1$ for simplicity, with

$$\left(\frac{k_{1f}}{k_{4f} C_{\mathrm{M}}} \frac{f + G}{\alpha f + G} - 1 \right) \sim \frac{T_{a_{1f}}}{T_c} \frac{T_\infty - T_c}{T_c}, \tag{2.33}$$

implied by an expansion for T_∞ near T_c. The result is

$$C_{\mathrm{H}_c} = \frac{1}{G}\frac{k_{2f}k_{3f}C_{\mathrm{H}_2}^2}{k_{1b}k_{4f}C_{\mathrm{M}}C_{\mathrm{O}_2}}\frac{T_{a_{1f}}}{T_c}\frac{T_\infty - T_c}{T_c}. \tag{2.34}$$

Furthermore, in the first approximation one may employ (2.32) to estimate the amount of H_2 in the reaction layer and take $C_{\mathrm{O}_2} \sim C_{\mathrm{O}_{2u}}(1-\phi)$. With these simplifications, the condition that $C_{\mathrm{H}} \ll C_{\mathrm{H}_2}$ in the reaction layer reduces to

$$\left(\frac{2\phi\beta L_{\mathrm{H}_2}k_{2f}k_{3f}}{(1-\phi)Gk_{1b}k_{4f}C_{\mathrm{M}}}\right)\left(\frac{T_\infty - T_c}{T_\infty - T_u}\right)^2 \ll 1, \tag{2.35}$$

where $\beta = T_{a_{1f}}(T_\infty - T_u)/T_c^2$ is the relevant Zeldovich number.

The restriction given by (2.35) can be used to estimate the validity of the proposed one-step reduced kinetics for given conditions of pressure, composition and initial temperature. In the computation, the plots of Fig. 2.3 may be used to obtain T_∞ and $T_c = (T_c)_l$, and G may be taken equal to unity. Evaluating the left-hand side of (2.35) with the equilibrium mol fractions given by which remain constant in the reaction zone at leading order, to compute the third-body efficiency of reaction $4f$ and with the reaction-rate constants evaluated at T_c yields values of the left-hand side of (2.35) of 1.8×10^{-2} and 0.61 for $\phi = 0.3$ and $\phi = 0.5$, respectively. The approximate criterion (2.35) for the validity of the steady-state assumption thus clearly holds for $\phi = 0.3$ but is not so clearly satisfied for $\phi = 0.5$, a result that might be anticipated from Fig. 2.2 but that is not reflected explicitly in Fig. 2.5. For lean flames with $\phi \gtrsim 0.5$, a two-step description is needed [4]. Further comments on the conditions of validity of the H-atom steady-state assumption are to be offered in the following chapter.

References

[1] D. Fernández-Galisteo, A. L. Sánchez, A. Liñán, F. A. Williams, One-step reduced kinetics for lean hydrogen-air deflagration, Combust. Flame 156 (2009) 985–996.

[2] L. He, P. Clavin, Premixed hydrogen-oxygen flames. part I: Flame structure near the flammability limits, Combust. Flame 93 (1993) 391–407.

[3] F. Mauss, N. Peters, B. Rogg, F. A. Williams, Reduced kinetic mechanisms for premixed hydrogen flames, in: N. Peters, B. Rogg (Eds.), Reduced

Kinetic Mechanisms for Applications in Combustion Systems, Springer-Verlag, 1993, pp. 29–43.

[4] K. Seshadri, N. Peters, F. A. Williams, Asymptotic analysis of stoichiometric and lean hydrogen-air flames, Combust. Flame 96 (1994) 407–427.

[5] G. del Álamo, F. A. Williams, A. L. Sánchez, Hydrogen-oxygen induction times above crossover temperatures, Combust. Sci. Tech. 176 (2004) 1599–1626.

[6] A. Liñán, F. A. Williams, Fundamental Aspects of Combustion, Oxford University Press, 1993.

[7] W. C. Reynolds, The element potential method for chemical equilibrium analysis: Implementation in the interactive program stanjan [technical report], Tech. rep., Stanford University, Dept. of Mechanical Eng. (1986).

[8] Version 2.0.7, Rotexo-Softpredict-Cosilab Gmbh & Co. KG, http://www.SoftPredict.com (2007).

[9] T. Mitani, F. A. Williams, Studies of cellular flames in hydrogen-oxygen-nitrogen mixtures, Combust. Flame 39 (1980) 169–190.

CHAPTER

THREE

The hydrogen-air burning rate near the lean flammability limit

3.1 Introduction

Theoretical investigations of flame dynamics often take into account that the structure of planar steady deflagrations typically involves two layers, a frozen upstream preheat region and a much thinner diffusive-reactive layer with negligible effects of convection. In the presence of flame perturbations, unsteady effects, as well as curvature and strain effects, enter first to modify the thicker preheat region, while the reactive-diffusive layer behaves as planar in the first approximation and reacts to the external perturbations in a quasi-steady manner, giving a burning rate (fuel burnt per unit flame surface per unit time) that is mainly a function of the perturbed burnt temperature. This chapter is intended to facilitate perturbation analyses by providing a simplified description for the resulting burning rate for hydrogen-air flames near the lean flammability limit, to be used, for instance, in the investigation of diffusive-thermal instabilities leading to cellular structures in such flames and in the study of the dynamics of these flames under perturbations.

The present work, which has been published recently [1], builds on our previous chapter, which identified a detailed mechanism of seven elementary reactions, shown in Table 1.1, that describes accurately the propagation of atmospheric and sub-atmospheric lean hydrogen-air flames. The resulting chemistry description predicts, in particular, a kinetically controlled flammability limit at which the planar deflagration velocity vanishes, when the adiabatic flame temperature equals the crossover temperature T_c, the latter defined such that the rate of reaction H + O_2 $\overset{1f}{\rightarrow}$ OH+O equals that of reaction H + O_2 + M $\overset{4f}{\rightarrow}$ HO_2 + M.

It is found that for the temperature conditions typically encountered the

reaction constants are such that the concentrations of O, OH and HO_2 are much smaller than that of H_2 and consequently can be treated in the steady-state approximation at leading order. On the other hand, the ratio of the H and H_2 concentrations in the reaction layer will be found to be of the order of the ratio of the H_2 and O_2 concentrations there, and therefore is proportional to $(T_b - T_c)/(T_b - T_u)$, with T_u and T_b representing the initial temperature of the unburnt mixture and the burnt temperature, respectively. When, for lean flames close to the flammability limit, the burnt temperature T_b is close to the crossover value T_c, the resulting H-atom concentration is much smaller than the H_2 concentration in the reaction layer, thereby ensuring the applicability of the steady-state approximation at leading order also for H atoms. With all radicals maintaining chemical-kinetic steady states in the first approximation, the development leads to a one-step reduced mechanism in which the main species react according to the single overall reaction $2H_2 + O_2 \rightarrow 2H_2O$ with a non-Arrhenius global rate. The resulting steady-state expressions for H, O and OH predict radicals to exist only in a small intermediate temperature range that extends from crossover to the burnt temperature T_b. Radicals disappear abruptly at crossover where the resulting radical profiles exhibit an unrealistic discontinuous slope and the steady-state assumptions fail.

The analysis below will use the ratio, ε, of the characteristic values of the H-atom and H_2 concentrations in the reaction layer as a small asymptotic parameter for the description of the reaction zone in lean hydrogen-air deflagrations. For the temperatures typically encountered, this small parameter satisfies $\varepsilon \sim (T_b - T_c)/(T_b - T_u)$, and therefore is also proportional to the ratio of the reaction-layer thickness to the flame thickness. Small values of ε, associated with values of the burnt temperature T_b close to T_c, therefore also imply that convection can be neglected in the first approximation in the reaction zone. The analysis of the resulting diffusive-reactive layer, including the region where steady-state approximations hold for all radicals and the layer of steady-state failure, located around the crossover temperature, will provide, in particular, the burning rate as a function of the burnt temperature and the pressure, which will be tested by comparisons of predictions of propagation velocities of steady planar flames, employing the 7-step mechanism, in order to be able to evaluate better how accurate the results of the present development may be.

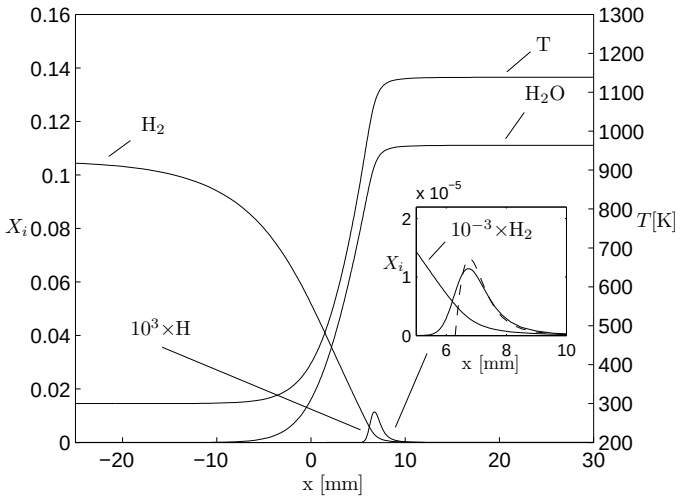

Figure 3.1: The temperature and mole fractions across a premixed hydrogen-air mixture for $p = 1$ atm, $T_u = 300$ K and $\phi = 0.28$ as calculated with the 7-step short mechanism; the inset compares the H-atom mole fraction computed numerically with that predicted by the steady-state expression (3.29).

3.2 Problem formulation

As shown in chapter 1, for hydrogen-air mixtures that are very fuel lean, the seven steps shown in Table 1.1 suffice to describe accurately flame propagation velocities. A sample computation of a steady planar deflagration obtained with the COSILAB code [2] with this 7-step mechanism is shown in Fig. 3.1 for pressure $p = 1$ atm, initial temperature $T_u = 300$ K and equivalence ratio $\phi = 0.28$. As can be seen, for these very lean conditions radicals only exist in a relatively thin reactive layer that is preceded by a chemically frozen preheat region. The main effect of curvature and unsteadiness, together with preferential diffusion effects, is to change the structure of the preheat region from that shown in the figure for a steady planar flame, modifying the burnt temperature and, therefore, the resulting burning rate.

We shall investigate below the structure of the thin reactive layer where radicals are present to determine the fuel mass burning rate as a function of the burnt temperature, giving results that may be used not only for computations of steady planar deflagration velocities but also in studies of flame dynamics

and stability. Because of its small thickness, convection can be neglected in the first approximation in this reactive layer, along with changes of density ρ and thermal diffusivity D_T from their downstream values at equilibrium. If n is defined as the coordinate normal to the reaction layer, then the resulting species conservation equations become

$$-\frac{D_T}{L_{H_2}}\frac{d^2C_{H_2}}{dn^2} = \dot{C}_{H_2} = -\omega_2 - \omega_3 + \omega_{6f} \tag{3.1}$$

$$-\frac{D_T}{L_{O_2}}\frac{d^2C_{O_2}}{dn^2} = \dot{C}_{O_2} = -\omega_1 - \omega_{4f} + \omega_{6f} + \omega_{7f} \tag{3.2}$$

$$-\frac{D_T}{L_{H_2O}}\frac{d^2C_{H_2O}}{dn^2} = \dot{C}_{H_2O} = \omega_3 + \omega_{7f} \tag{3.3}$$

$$-\frac{D_T}{L_O}\frac{d^2C_O}{dn^2} = \dot{C}_O = \omega_1 - \omega_2 \tag{3.4}$$

$$-\frac{D_T}{L_{OH}}\frac{d^2C_{OH}}{dn^2} = \dot{C}_{OH} = \omega_1 + \omega_2 - \omega_3 + 2\omega_{5f} - \omega_{7f} \tag{3.5}$$

$$-\frac{D_T}{L_H}\frac{d^2C_H}{dn^2} = \dot{C}_H = -\omega_1 + \omega_2 + \omega_3 - \omega_{4f} - \omega_{5f} - \omega_{6f} \tag{3.6}$$

$$-\frac{D_T}{L_{HO_2}}\frac{d^2C_{HO_2}}{dn^2} = \dot{C}_{HO_2} = \omega_{4f} - \omega_{5f} - \omega_{6f} - \omega_{7f} \tag{3.7}$$

where C_i and L_i are the concentration and Lewis number of species i, and $\dot{C}_i$ denotes its corresponding chemical production rate (moles per unit volume per unit time), to be computed from the rates ω_j of the elementary reactions shown in Table 1.1. At the same level of approximation, the energy conservation equation becomes

$$\rho c_p D_T \frac{d^2T}{dn^2} = \sum h_i^o \dot{C}_i, \tag{3.8}$$

where c_p is the specific heat at constant pressure, assumed to be constant, T is the temperature, and h_i^o is the enthalpy of formation per mol of species i at T_b. The above equations are to be integrated with boundary conditions corresponding to matching with the upstream chemically frozen preheat region as $n \to -\infty$

$$\frac{\dot{m}_{H_2}}{W_{H_2}D_T} = -\frac{1}{L_{H_2}}\frac{dC_{H_2}}{dn} = -\frac{2}{L_{O_2}}\frac{dC_{O_2}}{dn} = \frac{1}{L_{H_2O}}\frac{dC_{H_2O}}{dn} = -\frac{\rho c_p}{h^o_{H_2O}}\frac{dT}{dn} \tag{3.9}$$

and

$$C_{\mathrm{O}} = C_{\mathrm{OH}} = C_{\mathrm{H}} = C_{\mathrm{HO}_2} = 0, \tag{3.10}$$

where $\dot{m}_{\mathrm{H}_2}$ is the mass fuel burning rate and W_{H_2} is the molecular mass of H_2. The accompanying boundary conditions as $n \to +\infty$ correspond to the downstream state reached as the gradients of concentrations and temperature vanish

$$C_{\mathrm{H}_2} = C_{\mathrm{O}_2} - C_{\mathrm{O}_{2b}} = C_{\mathrm{H}_2\mathrm{O}} - C_{\mathrm{H}_2\mathrm{O}_b} = C_{\mathrm{O}} = C_{\mathrm{OH}} = C_{\mathrm{H}} = C_{\mathrm{HO}_2} = T - T_b = 0, \tag{3.11}$$

where the subscript b denotes conditions in the burnt gas.

Note that in a planar steady deflagration, the burnt conditions can be computed as the chemical equilibrium state for the fresh gas mixture upstream from the preheat region, so that in particular the burnt temperature T_b would be equal to the adiabatic flame temperature T_∞. In the presence of flame perturbations, however, unsteady effects, as well as curvature and strain effects, enter to modify the flame structure in the thick preheat region that precedes the reaction zone, causing the value of T_b to differ from the adiabatic flame temperature. In particular, lean hydrogen flames are known to be strongly prone to diffusive-thermal instabilities that induce departures from presumed steady, planar structures. In the resulting curved flames, because of differential diffusion effects the burnt temperature T_b is larger than the adiabatic flame temperature T_∞ in the convex parts of the flame, and smaller in the concave parts. When the departures are sufficiently small for T_b to remain above the crossover value everywhere, hydrogen is depleted behind the reaction sheet, which is followed by a postflame region in chemical equilibrium, of thickness comparable to or larger than that of the preheat region. Across this region transverse heat conduction causes the solution to evolve slowly from the burnt state with $T = T_b$ found immediately downstream from the reaction zone towards the final equilibrium state with $T = T_\infty$. When the flame perturbations are such that $T_\infty - T_b \ll T_\infty$ the gradients found in this postflame region are much smaller than those found in the reaction zone and can be therefore neglected in the first approximation when computing the burning rate, which can be determined with consideration of vanishing gradients downstream from the reaction zone, a condition employed above when writing the boundary conditions (3.11).

On the other hand, for conditions near the lean flammability limit, relatively small temperature excursions $T_\infty - T_b$ in curved flames may lead to

values of the burnt temperature below crossover in the concave parts of the flame, leading to local extinction of the chemical reaction and to the appearance of cellular flames, seen in recent numerical simulations [3]. These cellular flames, which could be investigated with the one-step chemistry recently derived [4], exist even for equivalence ratios well below the kinetically controlled flammability limit of planar flames. Because of their relatively large curvature, peak temperatures above crossover are found behind the reaction layer in each individual flame cell, whose hot products mix downstream with the cold reactant mixture that flows between cells, leading to a relatively cold postflame region where chemical reaction proceeds at a negligibly slow rate. These cellular flames fall outside the scope of the present analysis, which considers weakly perturbed flames with burned temperatures above crossover such that the downstream zone does not influence the preheat or reaction zones, its properties departing negligibly from those of the equilibrium state.

The solution of the above problem for given values of T_b, $C_{O_{2b}}$, $C_{H_2O_b}$ and pressure determines the fuel burning rate $\dot{m}_{H_2}$. To facilitate the development, it is convenient to combine linearly (3.1), (3.2) and (3.3) with (3.4)–(3.7) to obtain the alternative equations

$$D_T \frac{d^2}{dn^2}\left(\frac{C_{H_2}}{L_{H_2}} + \frac{C_O}{L_O} + \frac{1}{2}\frac{C_{OH}}{L_{OH}} + \frac{3}{2}\frac{C_H}{L_H} - \frac{1}{2}\frac{C_{HO_2}}{L_{HO_2}}\right) = 2\omega_{4f} \tag{3.12}$$

$$D_T \frac{d^2}{dn^2}\left(\frac{C_{O_2}}{L_{O_2}} + \frac{C_O}{L_O} + \frac{1}{2}\frac{C_{OH}}{L_{OH}} + \frac{1}{2}\frac{C_H}{L_H} + \frac{1}{2}\frac{C_{HO_2}}{L_{HO_2}}\right) = \omega_{4f} \tag{3.13}$$

$$D_T \frac{d^2}{dn^2}\left(\frac{C_{H_2O}}{L_{H_2O}} - \frac{C_O}{L_O} - \frac{C_H}{L_H} + \frac{C_{HO_2}}{L_{HO_2}}\right) = -2\omega_{4f}, \tag{3.14}$$

where

$$\omega_{4f} = k_{4f} C_M C_{O_2} C_H \tag{3.15}$$

is the rate of the three-body recombination reaction, with

$$C_M = p/(R^o T) + 15 C_{H_2O} + 1.5 C_{H_2} \tag{3.16}$$

representing the effective third-body concentration, which accounts for the non-unity third-body chaperon efficiencies of water vapor and molecular hydrogen. Integrating once (3.12) with the boundary conditions given above provides

$$\dot{m}_{H_2} = 2W_{H_2} \int_{-\infty}^{+\infty} k_{4f} C_M C_{O_2} C_H dn, \tag{3.17}$$

indicating that the burning rate is linearly proportional to the rate of the recombination reaction $4f$ integrated across the flame. An accurate description of the H-atom concentration is therefore needed to compute $\dot{m}_{H_2}$. We shall see below that such a description requires consideration of two different regions: a relatively thick layer where all radicals follow a steady-state approximation to leading order and a thinner upstream layer where the steady-state approximations for O, OH and H break down. Both regions will be analyzed separately below and their corresponding contributions to the burning rate will be determined.

3.3 Fuel burning rate based on analysis of the steady-state region

As seen in Fig. 3.1 for the radical H, taken as representative of the radical pool, near the lean flammability limit radicals appear in concentrations that are much smaller than those of H_2. Neglecting radical concentrations on the left-hand side of (3.12), (3.13) and (3.14) provides

$$\frac{D_T}{L_{O_2}}\frac{d^2C_{O_2}}{dn^2} = -\frac{D_T}{2L_{H_2O}}\frac{d^2C_{H_2O}}{dn^2} = \frac{D_T}{2L_{H_2}}\frac{d^2C_{H_2}}{dn^2} = \omega_{4f}, \tag{3.18}$$

indicating that, in the first approximation, the fuel burns as dictated by the irreversible overall reaction $2H_2 + O_2 \rightarrow 2H_2O$ with a rate equal to that of reaction $4f$. At the same level of approximation, the energy conservation equation becomes

$$\rho c_p D_T \frac{d^2T}{dn^2} = -2q\omega_{4f}, \tag{3.19}$$

and diffusive transport of radicals can be neglected in (3.4)–(3.7) to give

$$\omega_1 - \omega_2 = 0 \tag{3.20}$$

$$\omega_1 + \omega_2 - \omega_3 + 2\omega_{5f} - \omega_{7f} = 0 \tag{3.21}$$

$$-\omega_1 + \omega_2 + \omega_3 - \omega_{4f} - \omega_{5f} - \omega_{6f} = 0 \tag{3.22}$$

$$\omega_{4f} - \omega_{5f} - \omega_{6f} - \omega_{7f} = 0. \tag{3.23}$$

In (3.19), $q = -h^o_{H_2O}$ denotes the amount of heat released per mole of H_2 consumed. The new set of equations (3.18)–(3.23), including the steady-state approximations (3.20)–(3.23) for the radicals, apply at leading order provided the radicals concentrations are much smaller than C_{H_2}.

Using the boundary conditions as $n \to \infty$ in integrating the first two equations in (3.18) yields

$$C_{O_2} = C_{O_{2b}} + \frac{L_{O_2}}{2L_{H_2}} C_{H_2} \tag{3.24}$$

$$C_{H_2O} = C_{H_2O_b} - \frac{L_{H_2O}}{L_{H_2}} C_{H_2} \tag{3.25}$$

while a similar integration of $d^2(\rho c_p T + qC_{H_2}/L_{H_2})/dn^2 = 0$, obtained from a linear combination of the last equation in (3.18) and (3.19), gives

$$T_b - T = qC_{H_2}/(\rho c_p L_{H_2}). \tag{3.26}$$

Equations (3.24)–(3.26) can be used to relate the concentrations of oxygen and water vapor and the temperature to the local H_2 concentration. In the computations below, the values $L_{O_2} = 1.11$, $L_{H_2} = 0.3$, $L_{H_2O} = 0.83$ are employed for the different Lewis numbers, and the constant values of the density and specific heat are evaluated at equilibrium.

To proceed with the analysis, (3.20)–(3.23) must be solved to give expressions for the radical concentrations, as done before in chapter 2. If the reverse reaction $2b$ is neglected, an excellent approximation under these fuel-lean conditions (see, e.g., the evaluations below (2.26)), the resulting explicit expressions become

$$C_{O_{ss}} = \frac{\bar{\alpha} k_{3f} C_{H_2}}{G k_{1b}} \left(\frac{k_{1f}}{\bar{\alpha} k_{4f} C_M} - 1 \right) \tag{3.27}$$

$$C_{OH_{ss}} = \frac{k_{2f} C_{H_2}}{k_{1b}} \left(\frac{k_{1f}}{\bar{\alpha} k_{4f} C_M} - 1 \right) \tag{3.28}$$

$$C_{H_{ss}} = \frac{1}{G} \frac{k_{2f} k_{3f} C_{H_2}^2}{k_{1b} k_{4f} C_M C_{O_2}} \left(\frac{k_{1f}}{\bar{\alpha} k_{4f} C_M} - 1 \right) \tag{3.29}$$

$$C_{HO_{2ss}} = \frac{k_{3f}}{(f+G) k_{7f}} C_{H_2}, \tag{3.30}$$

where

$$f = \frac{k_{5f} + k_{6f}}{k_{7f}} \frac{k_{3f}}{k_{4f} C_M} \frac{C_{H_2}}{C_{O_2}}, \tag{3.31}$$

$$G = \frac{1+\gamma_{3b}}{2} + \frac{f}{2} \left\{ [1 + 2(3+\gamma_{3b})/f + (1+\gamma_{3b})^2/f^2]^{1/2} - 1 \right\} \tag{3.32}$$

and

$$\bar{\alpha} = \frac{k_{6f} f/(k_{5f} + k_{6f}) + G}{f + G}, \tag{3.33}$$

with

$$\gamma_{3b} = \frac{k_{3b} C_{H_2O}}{k_{4f} C_M C_{O_2}}. \tag{3.34}$$

Note that, to simplify the notation, a new factor $\bar{\alpha} = (\alpha f + G)/(f + G)$, not present in the derivation of the previous chapter, has been introduced here. Substituting the H-atom concentration (3.29) into the expression for ω_{4f} given in (3.15) provides an explicit non-Arrhenius expression for the overall rate of the global reaction $2H_2 + O_2 \rightarrow 2H_2O$.

It is of interest that, according to (3.27), (3.28) and (3.29), in the steady-state approximation adopted here the concentrations of O, OH and H vanish as the temperature approaches the crossover value T_c, as can be also clearly seen in the one-step results shown in appendix E. This crossover temperature T_c is defined by the condition given in 2.29, which is rewritten here for convenience

$$k_{1f} = \bar{\alpha} k_{4f} C_M, \tag{3.35}$$

giving a value that depends on the composition through the function $\bar{\alpha}$ and the effective third-body concentration C_M. At temperatures below T_c the steady-state approximation predicts $C_O = C_{OH} = C_H = 0$, while the concentration of the hydroperoxyl radical, given in (3.30), reaches a nonzero value at the crossover temperature and is positive also for $T < T_c$. In fact HO_2 continues to react for $T < T_c$ by steps not included in the 7-step mechanism; it is eventually consumed completely when $T = T_u$, but this chemistry exerts very small influences on burning rates, entirely negligible at the orders addressed here. Because of the linear dependence of ω_{4f} on the H-atom concentration, the overall oxidation reaction $2H_2 + O_2 \rightarrow 2H_2O$ is restricted to a high-temperature reaction layer adjacent to the flame hot boundary where the temperature lies in the range $T_c < T < T_b$. This layer is thin compared with the flame provided $T_b - T_c \ll T_b - T_u$, where the subscript u denotes unburnt conditions in the fresh mixture upstream from the deflagration. This requirement justifies the neglect of convective effects in the reaction layer.

Because of the relatively strong temperature sensitivity of the rate of the branching reaction $1f$, the cutoff factor $k_{1f}/(\bar{\alpha} k_{4f} C_M) - 1$ readily takes on values of order unity across the thin reaction layer for relatively small values of the temperature increment $T_b - T_c$ of order $\beta_{1f}^{-1} T_c \ll T_b - T_u$,where $\beta_{1f} = T_{a_{1f}}/T_c + n_{1f} - n_{4f} + 1 \sim 10$ is an appropriately defined dimensionless activation temperature that accounts for the different algebraic temper-

ature dependences present in $k_{1f}/(\bar{\alpha}k_{4f}C_M)$. Under these conditions, equation (3.29) indicates that

$$\frac{C_H}{C_{H_2}} \sim \frac{k_{2f}k_{3f}}{k_{1b}k_{1f}} \frac{k_{1f}}{k_{4f}C_M} \frac{C_{H_2}}{C_{O_2}}, \tag{3.36}$$

which can also be written in the form

$$\frac{C_H}{C_{H_2}} \sim \frac{k_{2f}k_{3f}}{k_{1b}k_{1f}} \frac{k_{1f}}{k_{4f}C_M} \frac{L_{H_2}C_{H_{2u}}}{C_{O_{2u}}} \frac{T_b - T_c}{T_b - T_u}, \tag{3.37}$$

where the value of the hydrogen-oxygen ratio C_{H_2}/C_{O_2} in the reaction zone has been evaluated approximately using (3.26) with $qC_{H_{2u}}/(\rho c_p) \simeq (T_b - T_u)$. Since the shuffle-reaction rate-constant factor $(k_{2f}k_{3f})/(k_{1b}k_{1f})$ is a quantity of order unity, e.g., $(k_{2f}k_{3f})/(k_{1b}k_{1f}) = 0.59$ at $T = 1000$ K, it is clear from (3.37) that the small value of $(T_b - T_c)/(T_b - T_u) \ll 1$ associated with the existence of a thin reaction layer is sufficient to guarantee the validity of the steady-state approximation for H atoms, which requires that $C_H/C_{H_2} \ll 1$ in the reaction zone. It is also of interest that, according to (3.27) and (3.28), for values of the cutoff factor $k_{1f}/(\bar{\alpha}k_{4f}C_M) - 1$ of order unity the O and OH concentrations satisfy $C_O/C_{H_2} \sim k_{3f}/k_{1b}$ and $C_{OH}/C_{H_2} \sim k_{2f}/k_{1b}$. The steady-state approximations for these two radicals are therefore directly related to the large value of k_{1b} relative to those of k_{3f} and k_{2f} (e.g., $k_{3f}/k_{1b} = 0.14$ and $k_{2f}/k_{1b} = 0.02$ at $T = 1000$ K), which causes the concentrations of O and OH to remain small compared to that of H_2. Similarly, with $f + G$ being typically of order unity, it follows from (3.30) that $C_{HO_2}/C_{H_2} \sim k_{3f}/k_{7f}$, again a very small quantity at the temperatures typically encountered in the reaction zone, e.g., $k_{3f}/k_{7f} = 0.04$ at $T = 1000$ K, thereby ensuring the accuracy of the HO_2 steady state.

Observation of (3.36) reveals that as the temperature difference $T_b - T_c$ increases, the ratio C_H/C_{H_2} also increases, partly because of the dependence on C_{H_2}/C_{O_2} and partly because of the exponential temperature dependence of $k_{1f}/(k_{4f}C_M)$, which would also enter through the cutoff factor appearing in (3.29), eventually leading to failure of the steady-state assumption for H atoms for sufficiently large values of $T_b - T_c$ such that $C_H \sim C_{H_2}$ in the reaction zone. Under these conditions, the one-step approximation must be replaced with a two-step description, as done in previous analyses of stoichiometric and moderately lean flames [5, 6]. It can be anticipated that, because of the temperature dependence of k_{1f}, the flame structure that replaces the steady-state regime analyzed here will show a relatively thin branching layer of radical production surrounded by thicker layers of radical recombination.

The analysis of this multi-layer structure, not further considered here, is to be addressed in the next chapter.

To obtain the burning rate associated with the steady-state description the last equation in (3.18) multiplied by $\mathrm{d}C_{\mathrm{H}_2}/\mathrm{d}n$ may be integrated once with the boundary conditions as $n \to \pm\infty$ to give

$$(\dot{m}_{\mathrm{H}_2})_{ss} = 2W_{\mathrm{H}_2}\left(\frac{D_T}{L_{\mathrm{H}_2}}\int_0^\infty \omega_{4f}\mathrm{d}C_{\mathrm{H}_2}\right)^{1/2}. \tag{3.38}$$

Because of the reaction-rate cutoff at the crossover point, this expression becomes

$$(\dot{m}_{\mathrm{H}_2})_{ss} = 2W_{\mathrm{H}_2}\left(\frac{D_T}{L_{\mathrm{H}_2}}\int_0^{C_{\mathrm{H}_{2c}}} \frac{k_{2f}k_{3f}C_{\mathrm{H}_2}^2}{Gk_{1b}}\left(\frac{k_{1f}}{\bar{\alpha}k_{4f}C_{\mathrm{M}}}-1\right)\mathrm{d}C_{\mathrm{H}_2}\right)^{1/2}, \tag{3.39}$$

when the steady-state expression (3.29) is used to evaluate C_{H}. In the integration, use must be made of (3.26) to compute the temperature (and therefore evaluate the reaction-rate constants) in terms of C_{H_2}. Similarly, the concentrations C_{O_2} and $C_{\mathrm{H}_2\mathrm{O}}$, which enter in the computation of G, $\bar{\alpha}$ and C_{M}, are to be evaluated from (3.24) and (3.25). The integration is extended until the H_2 concentration reaches its limiting value at crossover

$$C_{\mathrm{H}_{2c}} = \rho c_p L_{\mathrm{H}_2}(T_b - T_c)/q, \tag{3.40}$$

at which (3.35) is satisfied.

3.4 Sample leading-order results and useful simplifications

The burning rate given in (3.39) depends mainly on the burnt temperature T_b, which appears in (3.26), and on the pressure, which determines C_{M}, whereas the dependence on the burnt-gas composition through the values $C_{\mathrm{O}_{2b}}$ and $C_{\mathrm{H}_2\mathrm{O}_b}$ that enter in (3.24) and (3.25) is somewhat weaker, with the value of $C_{\mathrm{H}_2\mathrm{O}_b}$ affecting mainly the flammability limit, as discussed below. The variation of $(\dot{m}_{\mathrm{H}_2})_{ss}$ with the burnt temperature for $p = 0.1$ atm and $p = 1$ atm is shown in Fig. 3.2. In the computation, for each value of T_b, the accompanying values of $C_{\mathrm{O}_{2b}}$ and $C_{\mathrm{H}_2\mathrm{O}_b}$ are selected as the downstream equilibrium values of a planar deflagration with $T_u = 300$ K and equivalence ratio ϕ such that the associated adiabatic flame temperature equals T_b. In the evaluation, the

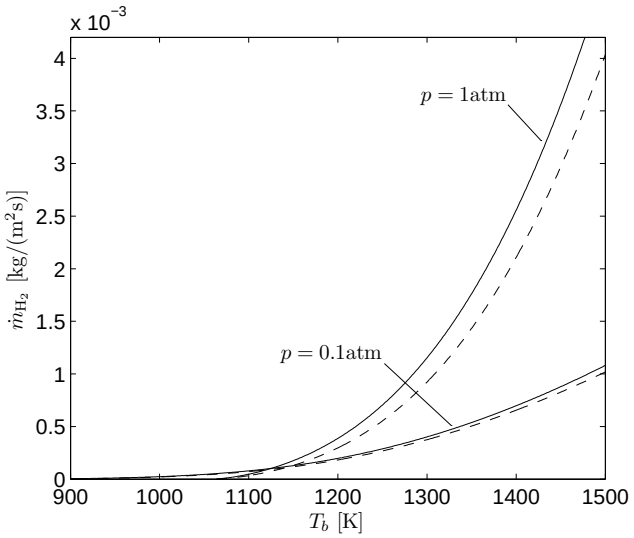

Figure 3.2: The variation with the burnt temperature T_b of the fuel burning rate $\dot{m}_{H_2}$ for $p = 0.1$ atm and $p = 1$ atm as obtained from the evaluating the steady-state expression (3.39) (dashed curves) and from adding to this result the correction (3.73) due to steady-state failure in the crossover layer (solid curves); in the computation, for each T_b the values of $C_{O_{2_b}}$ and $C_{H_2O_b}$ are taken as the equilibrium values for a hydrogen-air planar deflagration with $T_u = 300$ K.

approximate expression $\rho D_T = 2.58 \times 10^{-5}(T/298)^{0.7}$ kg/(m s) [7] is used, and the NASA polynomial fits are employed in the evaluation of c_p.

The expression given in (3.39) predicts a fuel burning rate $(\dot{m}_{H_2})_{ss}$ that is positive provided the burnt temperature is sufficiently high for the cutoff factor $k_{1f}/(\bar{\alpha}k_{4f}C_M) - 1$ to be positive across the reactive layer. Correspondingly, the steady-state approximation provides a prediction for the lean flammability limit, associated with conditions such that the burnt temperature equals the critical crossover value $T_b = (T_c)_l$ below which $k_{1f}/(\bar{\alpha}k_{4f}C_M) - 1 < 0$ everywhere across the flame. As implied by (3.40), the hydrogen concentration in the reaction layer is very small near the flammability limit, so that in the first approximation one may take $\bar{\alpha} = 1$ in (3.35) to compute the critical crossover value $(T_c)_l$, as done in the previous chapter.

The resulting value depends through C_M on the pressure and also on the water vapor concentration $C_{H_2O_b}$, as can be seen in (3.16). When the equilibrium composition is computed as that of a planar deflagration, differences in

$(T_c)_l$ appear for different values of T_u and of the initial composition. For instance, at $p = 1$ atm the resulting values are $(T_c)_l = (1072, 1064, 1054)$ K when $C_{H_2O_b} = (1.3, 1.15, 0.99)$ mol/m^3 is used in computing $k_{1f} = k_{4f}C_M$, as corresponds to a planar H_2-air deflagration with $T_u = (200, 300, 400)$ K, while $(T_c)_l = (1075, 1067, 1057)$ for the values $C_{H_2O_b} = (1.35, 1.2, 1.04)$ mol/m^3 corresponding to a planar H_2-O_2 deflagration, also with $T_u = (200, 300, 400)$ K. These variations of the flammability limit can be readily incorporated when representing the temperature variation of the burning rate by employing the temperature increment $T_b - (T_c)_l$. When this is done only relatively small differences in $(\dot{m}_{H_2})_{ss}$ are found between the results obtained with different values of $C_{O_{2b}}$ and $C_{H_2O_b}$, as may be seen in Fig. 3.3 for $p = 1$ atm and $p = 0.1$ atm.

Perturbations of (3.39) about the flammability conditions enable simplified expressions for $(\dot{m}_{H_2})_{ss}$ in terms of $T_b - (T_c)_l$ to be derived. For instance, using

$$\frac{k_{1f}}{\bar{\alpha}k_{4f}C_M} - 1 \simeq \beta_{1f}\frac{T - (T_c)_l}{(T_c)_l}, \tag{3.41}$$

where $\beta_{1f} = T_{a_{1f}}/(T_c)_l + n_{1f} - n_{4f} + 1$ is the value of the dimensionless activation temperature introduced above (3.36) evaluated at the crossover temperature, and neglecting variations of all other reaction-rate constants along with departures of $\bar{\alpha}$ from unity, it is found that (3.39) reduces to

$$(\dot{m}_{H_2})_{ss} = 2W_{H_2}\left[\frac{D_T}{12L_{H_2}}\frac{k_{2f}k_{3f}}{Gk_{1b}}\left(\frac{\rho c_p L_{H_2}}{q}\right)^3\frac{\beta_{1f}}{(T_c)_l}\right]^{1/2}(T_b - (T_c)_l)^2, \tag{3.42}$$

where $G = 1 + \gamma_{3b}$ as corresponds to $C_{H_2} = 0$. The factor in square brackets is to be evaluated at the flammability limit, yielding therefore a quadratic dependence of $(\dot{m}_{H_2})_{ss}$ on the temperature increment $T_b - (T_c)_l$. Since γ_{3b} is typically small at the flammability limit, the approximate value $G \simeq 1$ can be assumed for simplicity in the evaluations, as done for the corresponding curves that are shown in Fig. 3.3. As can be seen, the approximate solution (3.42) tends to underpredict the increase of $(\dot{m}_{H_2})_{ss}$ with $T_b - (T_c)_l$, although it becomes a reasonable approximation as the flammability limit is approached. Better agreement away from the limit is obtained when the exponential temperature variation of the different reaction-rate constants is retained by expressing (3.39) in terms of the dimensionless rescaled temperature increments

$$\theta = \beta_{1f}\frac{T - (T_c)_l}{(T_c)_l} \quad \text{and} \quad \theta_b = \beta_{1f}\frac{T_b - (T_c)_l}{(T_c)_l} \tag{3.43}$$

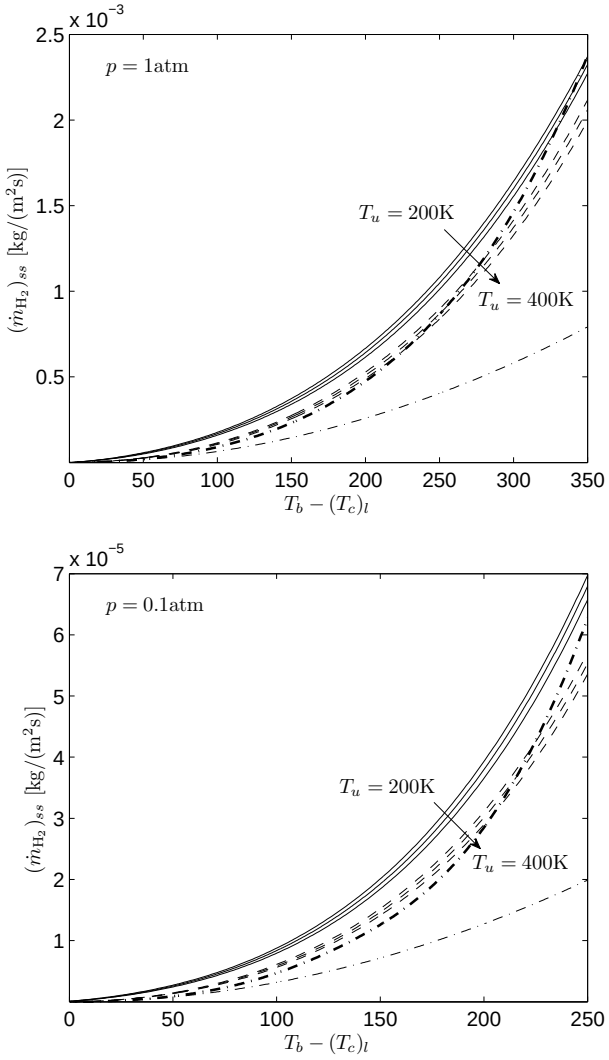

Figure 3.3: The variation with the temperature increment $T_b - (T_c)_l$ of the fuel burning rate $(\dot{m}_{\mathrm{H}_2})_{ss}$ of the steady-state region calculated from (3.39) for $p = 1$ atm (upper plot) and $p = 0.1$ atm (lower plot); in the computation, for each T_b the values of $C_{\mathrm{O}_{2b}}$ and $C_{\mathrm{H_2O}_b}$ are taken as the equilibrium values for a H_2-air (solid curves) and H_2-O_2 (dashed curves) planar deflagration with $T_u = (200, 300, 400)$ K. The dot-dashed lines correspond to results of evaluations of (3.42) (thin curve) and of (3.44) (thick curve) with the constant factor in square brackets evaluated with $G = 1$, $T = (T_c)_l$ and with the equilibrium composition at the flammability limit of a H_2-air deflagration with $T_u = 300$ K; they are essentially the same for H_2-air and H_2-O_2 systems.

with (3.26) used to relate the variations of C_{H_2} and temperature, yielding

$$(\dot{m}_{H_2})_{ss} = 2W_{H_2}\left[\frac{D_T}{L_{H_2}}\frac{k_{2f}k_{3f}}{Gk_{1b}}\left(\frac{\rho c_p L_{H_2}}{q}\right)^3\left(\frac{(T_c)_l}{\beta_{1f}}\right)^3\right]^{1/2}\times[J(\theta_b)]^{1/2}. \quad (3.44)$$

The integral

$$J(\theta_b) = \int_0^{\theta_b} e^{\beta\theta}(e^\theta - 1)(\theta_b - \theta)^2 \mathrm{d}\theta \quad (3.45)$$

can be integrated explicitly to give

$$\begin{aligned} J(\theta_b) &= 2e^{\beta\theta_b}\left(\frac{e^{\theta_b}}{(\beta+1)^3} - \frac{1}{\beta^3}\right) \\ &+ \frac{\theta_b^2}{\beta(\beta+1)} + \frac{2\theta_b(1+2\beta)}{\beta^2(\beta+1)^2} + \frac{2(3\beta^2+3\beta+1)}{\beta^3(\beta+1)^3} \end{aligned} \quad (3.46)$$

which takes on the limiting values $J = 2\exp[(\beta+1)\theta_b]/(\beta+1)^3$ for $\theta_b \gg 1$ and $J = \theta_b^4/12$ for $\theta_b \ll 1$, the latter limit indicating that (3.44) reduces naturally to (3.42) as the flammability limit is approached. Note that the temperature variation of the factor $k_{2f}k_{3f}/k_{1b}$ enters in (3.45) through the term $e^{\beta\theta}$, where $\beta = [(T_{a_{2f}} + T_{a_{3f}} - T_{a_{1b}})/(T_c)_l + n_{2f} + n_{3f} - n_{1b} - 2]/\beta_{1f}$. The expression (3.44) is seen to approximate reasonably well the burning rate (3.39), as can be seen in Fig. 3.3, which shows results for two different pressures.

The approximate burning-rate laws (3.42) and (3.44) can be useful for theoretical analysis of flame stability near the lean flammability limit. In particular, these expressions predict an effective activation energy that becomes singular according to

$$\frac{T_b}{(\dot{m}_{H_2})_{ss}}\frac{\mathrm{d}(\dot{m}_{H_2})_{ss}}{\mathrm{d}T_b} = \frac{2T_b}{T_b - (T_c)_l} \quad (3.47)$$

as the flammability limit is approached, i.e., as $T_b \to (T_c)_l$, thereby promoting flame instability.

Although the burning-rate results that have been discussed here provide reasonable accuracy for most purposes, there is interest in seeking better accuracy. Before considering other aspects of the reaction-layer structure that can significantly improve accuracies of burning-rate predictions, it is worth commenting further on the determination of the kinetically controlled flammability limit arising with the seven elementary reactions of Table 1.1. We have used above the equation $k_{1f} = k_{4f}C_M$ to determine the critical temperature

$(T_c)_l$, and assume that no flame may exist when the burnt temperature T_b lies below that temperature. For a hydrogen-air mixture with $p = 1$ atm and $T_u = 300$ K, this simple criterion gives $(T_c)_l = 1064$ K and $\phi_l = 0.251$. The numerical computations with the COSILAB code for the 7-step mechanism yield however a small but finite flame propagation velocity $v_l \simeq 2$ mm/s at these conditions, and they also predict flames to exist for equivalence ratios in the range $0.249 \lesssim \phi < 0.251$. This very small difference is associated with complexities that arise from the steady-state approximation very near the flammability limit and that increase in importance with decreasing pressure but still produce only small effects. The complexity is related to the variation of $\bar{\alpha}$ near the hot boundary under conditions close to the flammability limit.

Normally the cutoff factor $k_{1f}/(\bar{\alpha}k_{4f}C_M) - 1$ in (3.39) increases monotonically with temperature because of the increase of k_{1f}. For conditions near the flammability limit, however, very near the hot boundary it is found that the factor $\bar{\alpha}$ increases with temperature more rapidly, causing the cutoff factor to decrease with temperature. This occurs because of the decrease of f with decreasing C_{H_2}, according to (3.31), which is seen from (3.33) to produce an increase in $\bar{\alpha}$. Under conditions that are extremely close to the flammability limit this effect in fact causes the cutoff factor to reach zero again just upstream from the hot boundary, leading to fuel leakage according to the steady-state approximations that have been employed over an extremely small range of conditions near the flammability limit. This effect increases with decreasing pressure and with increasing dilution, as may be inferred from (3.31), and it does not occur for H_2-O_2 systems at the pressures for which results are shown below.

A more formal analysis, to be formulated in the following section as an asymptotic expansion in the small parameter ε of equation (3.52), shows that as the downstream boundary is approached and the cutoff factor as well as the properly scaled radical concentrations y_O, y_{OH} and y_H become of order ε, the steady-state approximation must be replaced by a diffusion-reaction balance. This will be evident from equation (3.64) in the following section. Although there is a consequent correction to the burning rate, this correction is of order ε and therefore is small compared with the correction to be derived in the following section. Even when the cutoff factor does not become small at the hot boundary, a diffusive-reactive character arises where y_O and y_{OH} decrease to order ε, but under conditions very near the limit, when this factor does become sufficiently small, there may well be fuel leakage that results in a downstream convective-reactive zone not described by the starting equations

of the present paper. Since these intricacies affect neither burning rates nor flammability limits significantly, they are not addressed here.

3.5 The crossover layer

The accuracy of the explicit steady-state expression (3.29) is demonstrated in the inset of Fig. 3.1, which includes the comparison of the H-atom profile determined numerically on the basis of the 7-step mechanism with that determined from evaluating (3.29). In the evaluation, use has been made of the profiles of reactant and water-vapor mol fractions and of temperature obtained numerically with the 7-step mechanism. It can be seen that the accuracy of the steady-state expression is excellent across the reaction layer, except at crossover, where the steady state predicts H atoms to disappear abruptly, thereby giving a profile with a discontinuous slope. Diffusive transport enters to remove this discontinuity, so that a smooth corner-layer profile replaces the abrupt change of the steady-state prediction when the 7-step mechanism is employed in the computations. Because of the direct proportionality of the burning rate and the H-atom content displayed in (3.17), the increased H-atom concentration in the layer of steady-state failure provides a nonnegligible additional contribution to the burning rate, which needs to be computed for increased accuracy.

Failure of the steady states for the radicals O, OH and H at a given upstream location is somewhat unexpected. To better clarify the problem it is of interest to write the radical conservation equations in dimensionless form, an effort that serves to identify the small parameter underlying the validity of the steady-state assumptions and the magnitude of the errors expected from the present analytical development. For that purpose, the fuel concentration is scaled with its crossover value $C_{\mathrm{H}_{2_c}}$ according to $y_{\mathrm{H}_2} = C_{\mathrm{H}_2}/C_{\mathrm{H}_{2_c}}$, whereas the radical concentrations $y_{\mathrm{O}} = C_{\mathrm{O}}/C_{\mathrm{O}_o}$, $y_{\mathrm{OH}} = C_{\mathrm{OH}}/C_{\mathrm{OH}_o}$ and $y_{\mathrm{H}} = C_{\mathrm{H}}/C_{\mathrm{H}_o}$ are scaled with their characteristic values implied by (3.27)–(3.29)

$$C_{\mathrm{O}_o} = \bar{\alpha}\frac{k_{3f}C_{\mathrm{H}_{2_c}}}{Gk_{1b}} \tag{3.48}$$

$$C_{\mathrm{OH}_o} = \frac{k_{2f}C_{\mathrm{H}_{2_c}}}{k_{1b}} \tag{3.49}$$

$$C_{\mathrm{H}_o} = \frac{1}{G}\frac{k_{2f}k_{3f}C^2_{\mathrm{H}_{2_c}}}{k_{1b}k_{4f}C_{\mathrm{M}}C_{\mathrm{O}_{2_c}}}, \tag{3.50}$$

where the different reaction-rate constants are evaluated at the crossover temperature, which is also used in evaluating the effective third-body concentration C_M and the functions f and G from (3.16), (3.31), and (3.32), respectively, with the oxygen and water vapor concentrations evaluated from (3.24) and (3.25) with the H_2 concentration reached at crossover, that is from (3.40).

The characteristic thickness of the reaction region

$$\delta = [D_T/(k_{4f} C_M C_{O_{2c}} \varepsilon)]^{1/2}, \tag{3.51}$$

arising from an order-of-magnitude analysis of the last equation in (3.18), is employed to scale the dimensionless coordinate $x = n/\delta$, with

$$\varepsilon = \frac{C_{H_o}}{C_{H_{2c}}} = \frac{1}{G} \frac{k_{2f} k_{3f} C_{H_{2c}}}{k_{1b} k_{4f} C_M C_{O_{2c}}} \tag{3.52}$$

representing the characteristic H-to-H_2 concentration ratio, the small parameter for our steady-state analysis. Introducing these variables reduces (3.4)–(3.6) to the dimensionless form

$$-\varepsilon \frac{\Lambda_O}{L_O} \frac{d^2 y_O}{dx^2} = \frac{k_{1f}}{k_{4f} C_M} y_H - \bar{\alpha}(y_{OH} y_O + y_{H_2} y_O) \tag{3.53}$$

$$\begin{aligned} -\varepsilon \frac{\Lambda_{OH}}{L_{OH}} \frac{d^2 y_{OH}}{dx^2} = {} & \frac{k_{1f}}{k_{4f} C_M} y_H - \bar{\alpha}(y_{OH} y_O - y_{H_2} y_O) \\ & - (2 + \gamma_{3b})(y_{H_2} y_{OH} - y_H) - 2\bar{\alpha} y_H \end{aligned} \tag{3.54}$$

$$\begin{aligned} -\varepsilon \frac{1}{L_H} \frac{d^2 y_H}{dx^2} = {} & -\frac{k_{1f}}{k_{4f} C_M} y_H + \bar{\alpha}(y_{OH} y_O + y_{H_2} y_O) \\ & + (2 + \gamma_{3b})(y_{H_2} y_{OH} - y_H), \end{aligned} \tag{3.55}$$

where we have neglected the reverse of reaction 2, along with the variation of C_{O_2} and C_{H_2O} from their crossover values $C_{O_{2c}}$ and $C_{H_2O_c}$ and the temperature dependence of the different reaction-rate constants, except that of reaction $1f$, whose sensitivity near crossover must be taken into account.

To achieve a more compact form, we have used the steady-state equation (3.7) to write $-\omega_{5f} - \omega_{6f} = -\omega_{4f} + \omega_{7f}$ in (3.6), and neglect the H_2 variation when writing ω_{5f} in (3.5). The constant radical-radical ratios $\Lambda_O = C_{O_o}/C_{H_o}$ and $\Lambda_{OH} = C_{OH_o}/C_{H_o}$ appear as factors of order unity. Since the hydroperoxyl steady-state approximation does not fail, one may use in the first approximation

$$C_{HO_2} = \frac{k_{3f}}{(f + G) k_{7f}} C_{H_{2c}} y_{H_2} \tag{3.56}$$

for the present purposes. The radical Lewis numbers $L_{\mathrm{H}} = 0.18$, $L_{\mathrm{O}} = 0.7$ and $L_{\mathrm{OH}} = 0.73$ are used below in the numerical evaluations.

Equations (3.53)–(3.55) are the dimensionless form of (3.4)–(3.6). Although they are simplified by evaluating at crossover the O_2 and H_2O concentrations as well as all of the reaction-rate constants but k_{1f}, they still retain the essential nonlinearities of the problem, associated with consumption of fuel and with the temperature variation of the chain-branching controlling reaction $1f$. One could in principle write similar conservation equations for y_{H_2} and T/T_c to provide the dimensionless formulation of the burning-rate problem, to be solved by appropriately matching expansions of the different variables in powers of the asymptotically small parameter ε, but these additional equations are unnecessary for computing the H-atom concentration near crossover and are therefore omitted here.

Observation of (3.53)–(3.55) reveals that radical diffusion is negligible at leading order when the H-to-H_2 characteristic ratio ε is small, and the steady-state expressions

$$y_{\mathrm{O}_{ss}} = y_{\mathrm{OH}_{ss}} = y_{\mathrm{H}_{ss}}/y_{\mathrm{H}_2} = \left(\frac{k_{1f}}{\bar{\alpha} k_{4f} C_{\mathrm{M}}} - 1 \right) y_{\mathrm{H}_2} \tag{3.57}$$

are recovered, as corresponds to the dimensionless form of (3.27)–(3.29) under the simplifying assumptions listed before Eq. (3.56). These expressions apply, with relative errors of order ε, for $x > 0$, with the arbitrary origin of x assumed to be at the crossover point, where $k_{1f} = \bar{\alpha} k_{4f} C_{\mathrm{M}}$, whereas $y_{\mathrm{O}} = y_{\mathrm{OH}} = y_{\mathrm{H}} = 0$ for $x < 0$. The steady-state approximations therefore hold provided $\varepsilon \ll 1$, so that evaluation of (3.52) serves to test the validity of the above development leading to (3.27)–(3.30). Note also that the steady-state description in the region $x \sim O(1)$ can be in principle improved by introducing expansions for the different dimensionless radical concentrations in ascending powers of ε. The analysis is not further pursued here because the associated relative corrections to the burning rate $(\dot{m}_{\mathrm{H}_2})_{ss}$ would be of order ε, smaller than the corrections, of order $\varepsilon^{2/3}$, arising from failure of the steady-state assumption at crossover, to be investigated below. The asymptotic procedure required to analyse the crossover layer was guided by the investigation of a much simpler model containing the main features of the crossover problem (3.53)–(3.55), as shown in appendix D.

Due to their discontinuous gradients, the steady-state radical profiles do not constitute an acceptable solution at $x = 0$, because they would be associated with infinite values of the diffusive rates appearing on the left-hand sides

of (3.53)–(3.55). In the solution that appears, radical diffusion becomes comparable to the chemical rates, yielding smooth profiles centered around $x = 0$ for the radicals, as seen for H in the 7-step computation shown in Fig. 3.1. Failure of the steady-state approximation occurs at distances $x \sim \varepsilon^{1/3}$, where $y_O \sim y_{OH} \sim y_H \sim 1 - y_{H_2} \sim \varepsilon^{1/3}$ and $k_{1f}/(\bar{\alpha} k_{4f} C_M) = 1 + Ax$, where

$$A = \frac{\mathrm{d}}{\mathrm{d}x}\left(\frac{k_{1f}}{\bar{\alpha} k_{4f} C_M}\right) = \delta \frac{T_{1f}}{T_c^2}\left(\frac{\mathrm{d}T}{\mathrm{d}n}\right)_c, \tag{3.58}$$

as implied by a Taylor expansion near $x = 0$ with account taken of the temperature sensitivity of k_{1f}. The resulting factor A is of order $T_{1f}(T_b - T_c)/T_c^2$. Note that the temperature gradient in (3.58) can be related to the burning rate of the steady-state region through (3.9), giving

$$\left(\frac{\mathrm{d}T}{\mathrm{d}n}\right)_c = \frac{q}{\rho c_p} \frac{(\dot{m}_{H_2})_{ss}}{W_{H_2} D_T}. \tag{3.59}$$

Introducing into (3.53)–(3.55) expansions for the radicals of the form $y_O = \varepsilon^{1/3}(\varphi_O^0 + \varepsilon^{1/3}\varphi_O^1 \cdots)$, $y_{OH} = \varepsilon^{1/3}(\varphi_{OH}^0 + \varepsilon^{1/3}\varphi_{OH}^1 \cdots)$, and $y_H = \varepsilon^{1/3}(\varphi_H^0 + \varepsilon^{1/3}\varphi_H^1 \cdots)$ yields at leading order the linear homogeneous problem

$$0 = \bar{\alpha}(\varphi_H^0 - \varphi_O^0) \tag{3.60}$$

$$0 = -\bar{\alpha}(\varphi_H^0 - \varphi_O^0) - (2 + \gamma_{3b})(\varphi_{OH}^0 - \varphi_H^0) \tag{3.61}$$

$$0 = -\bar{\alpha}(\varphi_H^0 - \varphi_O^0) + (2 + \gamma_{3b})(\varphi_{OH}^0 - \varphi_H^0). \tag{3.62}$$

This problem has a nontrivial solution with

$$\varphi_O^0 = \varphi_{OH}^0 = \varphi_H^0 \tag{3.63}$$

because the determinant of the coefficient matrix is zero, as can be seen by noticing that the sum 2 × (3.60) + (3.61) + (3.62) is identically zero. The solution can be found by writing the accompanying linear combination 2 × (3.53) + (3.54) + (3.55) of the radical conservation equations, leading to

$$-\frac{\varepsilon}{2\bar{\alpha}} \frac{\mathrm{d}^2}{\mathrm{d}x^2}\left(\frac{2\Lambda_O}{L_O} y_O + \frac{\Lambda_{OH}}{L_{OH}} y_{OH} + \frac{1}{L_H} y_H\right) = \left(\frac{k_{1f}}{\bar{\alpha} k_{4f} C_M} - 1\right) y_H - y_{OH} y_O. \tag{3.64}$$

From this result it is seen that near crossover the evolution of the radical pool depends on the balance between radical loss by diffusion (the terms on the left-hand side), radical production (the first term on the right-hand side), arising from departures from the crossover temperature, and radical consumption

through reaction $1b$ (the second term on the right-hand side). Introducing the expansions for y_i together with (3.63) provides the reduced problem

$$\frac{\mathrm{d}^2\varphi}{\mathrm{d}\xi^2} = \varphi(\varphi - \xi), \quad \varphi(-\infty) = \varphi(+\infty) - \xi = 0, \tag{3.65}$$

where the radical pool concentration

$$\varphi = \frac{\varphi_{\mathrm{H}}^0}{[BA^2/(2\bar{\alpha})]^{1/3}} \tag{3.66}$$

has been introduced, along with the rescaled coordinate

$$\xi = \frac{x}{[B\varepsilon/(2\bar{\alpha}A)]^{1/3}}, \tag{3.67}$$

where

$$B = \frac{2\Lambda_{\mathrm{O}}}{L_{\mathrm{O}}} + \frac{\Lambda_{\mathrm{OH}}}{L_{\mathrm{OH}}} + \frac{1}{L_{\mathrm{H}}}. \tag{3.68}$$

The problem defined by (3.65) was first encountered by Liñán in analyzing the inner structure of diffusion flames for large Damkohler numbers [8]. It is equivalent to a problem often attributed to Friedlander and Keller [9] whose solution in the combustion context was first published by Fendell [10]; see Williams [11]. The resulting solution is plotted for completeness in Fig. 3.4.

According to (3.17), the departures of the H-atom concentration from its steady-state value (3.29) result in corrections to the burning rate

$$\dot{m}_{\mathrm{H}_2} - (\dot{m}_{\mathrm{H}_2})_{ss} = 2W_{\mathrm{H}_2} \int_{-\infty}^{+\infty} k_{4f} C_{\mathrm{M}} C_{\mathrm{O}_2} (C_{\mathrm{H}} - C_{\mathrm{H}_{ss}}) \mathrm{d}n, \tag{3.69}$$

which can be alternatively written in the simplified form

$$\dot{m}_{\mathrm{H}_2} - (\dot{m}_{\mathrm{H}_2})_{ss} = 2W_{\mathrm{H}_2} C_{\mathrm{H}_o} \delta \int_{-\infty}^{+\infty} k_{4f} C_{\mathrm{M}} C_{\mathrm{O}_2} (y_{\mathrm{H}} - y_{\mathrm{H}_{ss}}) \mathrm{d}x. \tag{3.70}$$

Regarding this last equation it is clear that the errors of the steady-state approximation in the region $x \sim O(1)$, where $y_{\mathrm{H}} - y_{\mathrm{H}_{ss}} \sim \varepsilon$, produces small relative errors $(\dot{m}_{\mathrm{H}_2} - \dot{m}_{\mathrm{H}_{2_{ss}}})/\dot{m}_{\mathrm{H}_2} \sim \varepsilon$, whereas the departures $y_{\mathrm{H}} - y_{\mathrm{H}_{ss}} \sim \varepsilon^{1/3}$ seen in the crossover layer $x \sim \varepsilon^{1/3}$ gives a much larger contribution to the burning rate, of order $(\dot{m}_{\mathrm{H}_2} - \dot{m}_{\mathrm{H}_{2_{ss}}})/\dot{m}_{\mathrm{H}_2} \sim \varepsilon^{2/3}$. This last correction can be evaluated explicitly by introducing in (3.70) the inner variables φ and ξ to give

$$\dot{m}_{\mathrm{H}_2} - (\dot{m}_{\mathrm{H}_2})_{ss} = 2IW_{\mathrm{H}_2} (k_{4f} C_{\mathrm{M}} C_{\mathrm{O}_2})_c C_{\mathrm{H}_o} \delta \varepsilon^{2/3} \left(\frac{B}{2\bar{\alpha}} \right)_c^{2/3} A^{1/3}, \tag{3.71}$$

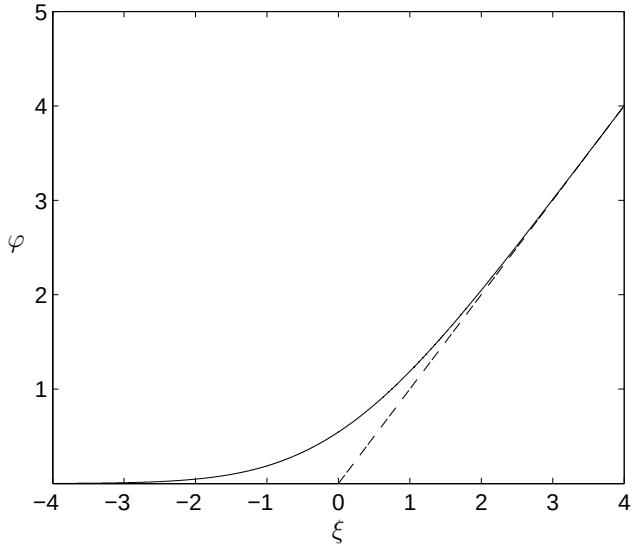

Figure 3.4: The rescaled radical concentration in the crossover layer as determined from numerical integration of (3.65); the dashed line represents the asymptote $\varphi = \xi$ corresponding to $\xi \to \infty$.

where the integral factor

$$I = \int_{-\infty}^{0} \varphi \mathrm{d}\xi + \int_{0}^{\infty} (\varphi - \xi)\mathrm{d}\xi = 0.95. \tag{3.72}$$

accounts for the increase in radical concentration from the steady-state prediction. Substitutions from (3.48)–(3.52), (3.58), (3.59) and (3.68) enable (3.71) to be written explicitly as

$$\begin{aligned} \dot{m}_{\mathrm{H}_2} - (\dot{m}_{\mathrm{H}_2})_{ss} &= 2I \left(\frac{k_{3f}}{Gk_{1b}}\right)_c [D_T W_{\mathrm{H}_2}^2 k_{2f} C_{\mathrm{H}_{2c}}^3 (\dot{m}_{\mathrm{H}_2})_{ss}]_c^{1/3} \left(\frac{qC_{\mathrm{H}_{2c}} T_{1f}}{\rho c_p T_c^2}\right)^{1/3} \\ &\times \left(\frac{1}{L_{\mathrm{O}}} + \frac{Gk_{2f}}{2\bar{\alpha}k_{3f}L_{\mathrm{OH}}} + \frac{k_{2f}C_{\mathrm{H}_{2c}}}{2\bar{\alpha}k_{4f}C_{\mathrm{M}}C_{\mathrm{O}_2}L_{\mathrm{H}}}\right)_c^{2/3}, \end{aligned} \tag{3.73}$$

where $\bar{\alpha}$ and G can be determined from (3.31)–(3.34).

The corrected burning rate, including the increase (3.73) due to the additional contribution of the crossover layer, is plotted in Fig. 3.2 for $p = 1$ atm and $p = 0.1$ atm. The extent of the resulting correction is tested in Fig. 3.5, which compares laminar flame propagation velocities obtained from 7-step chemistry with the burning-rate predictions $v_l = \dot{m}_{\mathrm{H}_2}/(W_{\mathrm{H}_2}C_{\mathrm{H}_{2u}})$. As can be

seen, incorporating the correction due to steady-state failure improves considerably the prediction of v_l near the flammability limit, its effect being quantitatively more significant at atmospheric conditions.

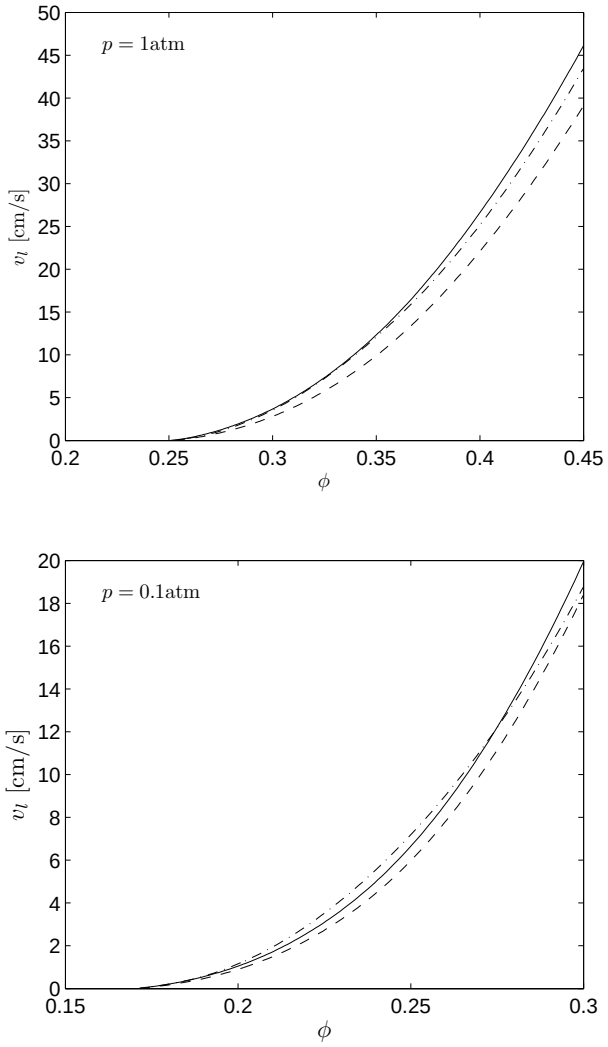

Figure 3.5: The variation with equivalence ratio of the planar propagation velocity of a premixed hydrogen-air flame for $p = 1$ atm (upper plot) and $p = 0.1$ atm (lower plot) as obtained for $T_u = 300$ K from the steady-state burning-rate prediction $v_l = (\dot{m}_{\mathrm{H}_2})_{ss}/(W_{\mathrm{H}_2} C_{\mathrm{H}_{2_u}})$ (dashed curves), from the burning-rate prediction including the contribution of the crossover layer $v_l = \dot{m}_{\mathrm{H}_2}/(W_{\mathrm{H}_2} C_{\mathrm{H}_{2_u}})$ (solid curves), and from numerical integrations with the 7-step short mechanism listed in Table 1.1 (dot-dashed curves).

References

[1] D. Fernández-Galisteo, A. L. Sánchez, A. Liñán, F. A. Williams, The hydrogen-air burning rate near the lean flammability limit, Combust. Theory Modelling 13 (4) (2009) 741–761.

[2] Version 2.0.7, Rotexo-Softpredict-Cosilab Gmbh & Co. KG, http://www.SoftPredict.com (2007).

[3] J. F. Grcar, A new type of steady and stable, laminar, premixed flame in ultra-lean, hydrogen-air combustion, Proc. Combust. Inst. 32 (2009) 1011–1018.

[4] D. Fernández-Galisteo, A. L. Sánchez, A. Liñán, F. A. Williams, One-step reduced kinetics for lean hydrogen-air deflagration, Combust. Flame 156 (2009) 985–996.

[5] F. Mauss, N. Peters, B. Rogg, F. A. Williams, Reduced kinetic mechanisms for premixed hydrogen flames, in: N. Peters, B. Rogg (Eds.), Reduced Kinetic Mechanisms for Applications in Combustion Systems, Springer-Verlag, 1993, pp. 29–43.

[6] K. Seshadri, N. Peters, F. A. Williams, Asymptotic analysis of stoichiometric and lean hydrogen-air flames, Combust. Flame 96 (1994) 407–427.

[7] M. D. Smooke, V. Giovangigli, Formulation of the premixed and nonpremixed test problems, in: M. D. Smooke (Ed.), Reduced Kinetic Mechanisms and Asymptotic Approximations for Methane-Air Flames, Vol. 384 of Lecture Notes in Physics, Springer-Verlag, 1991, pp. 1–28.

[8] A. Liñán, On the internal structure of laminar diffusion flames, OSR/EOAR TN 62-69, INTA (1961).

[9] S. K. Friedlander, K. H. Keller, The structure of the zone of diffusion controlled reaction, Chem. Eng. Sci. 18 (1963) 365–375.

[10] F. E. Fendell, Ignition and extinction in combustion of initially unmixed reactants, J. Fluid Mech. 21 (1965) 281–303.

[11] F. A. Williams, Theory of combustion in laminar flows, Ann. Rev. Fluid Mech. 3 (1971) 172–174.

CHAPTER

FOUR

Zel'dovich analysis of lean hydrogen-air flames

4.1 Introduction

As previously seen, for lean hydrogen-air premixed flames away from the flammability limit, the concentration of H atoms in the reaction layer becomes sufficiently large for the associated steady-state assumption to lose accuracy, as occurs for instance for $\phi > 0.45$ at atmospheric normal conditions. To describe the resulting flames, the one-step mechanism must be replaced with a two-step mechanism, as done before [1]. Unlike the previous work, which was based on rate-ratio arguments, we shall exploit in the following development the relatively large activation temperature of the branching step to provide a simplified flame description, as done by Zel'dovich [2] for the model two-step kinetics R + X $\rightarrow$ 2X and X + X + M $\rightarrow$ P + M, where the chemical species R, X, and P represent the reactant, intermediate and product, and M is a third body. The Zel'dovich model assumes that the heat is released only by the recombination reaction, whose reaction-rate constant is independent of the temperature, and that the branching reaction is energetically neutral and posseses a rate constant with an Arrhenius temperature dependence with large activation energy. As seen in the following section, all these features are also found in the two-step reduced chemistry that describes H_2-air flames, thereby enabling an analytical development parallel to that of Zel'dovich [2] to be performed.

As seen by Zel'dovich [2] and also by Joulin et al. [3] and others, branching occurs in a very thin layer located at a temperature slightly above the crossover temperature, defined as the temperature at which the rate of radical production through branching equals the rate of radical consumption through recombination, whereas radical recombination occurs in a distributed manner both upstream and downstream from this layer, in fairly large regions where

recombination, convection and diffusion all occur simultaneously. An analytic solution was found by Zel'dovich [2] for the flame propagation velocity when the rate of radical recombination was assumed to be linearly proportional to the radical concentration. Variants of the Zel'dovich model chemistry have been employed in numerous more recent combustion studies, among which one may cite the premixed-combustion investigations of Dold and coworkers [4, 5], who include consideration of the structure and stability of spherical flame balls.

4.2 Simplified two-step chemical kinetics

The computations shown above in Fig. 1.2 indicate that the seven elementary reactions of Table 1.1 suffice to describe flames for equivalence ratios near the lean flammabity limit and that addition of the two direct recombination reactions $H + H + M \overset{9f}{\rightarrow} H_2 + M$ and $H + OH + M \overset{10f}{\rightarrow} H_2O + M$ provides greater accuracy as the radical level increases for larger values of ϕ. Neglecting these two reactions, as done in previous theoretical investigations [1], leads to non-negligible overpredictions of flame velocities, on the order of 15 % for stoichiometric flames. In the following, the 9-step mechanism will be considered as a starting point for developing a two-step reduced-chemistry description.

The reaction-rate constants for these two additional reactions, not shown in Table 1.1, are, respectively, $k_{9f} = 1.30 \times 10^{18} T^{-1}$ $(\mathrm{mol/cm^3})^{-2}\mathrm{s}^{-1}$ and $k_{10f} = 4.00 \times 10^{22} T^{-2}$ $(\mathrm{mol/cm^3})^{-2}\mathrm{s}^{-1}$. Since the chaperon efficiencies for these two recombination steps (2.5 for H_2, 12.0 for H_2O, and 1.0 for all other species) are different from those of reaction $4f$, for the formulation of this chapter two different third-body concentrations are introduced

$$C_{M1} = p/(R^o T)(1 + 15X_{H_2O} + 1.5X_{H_2}) \tag{4.1}$$

and

$$C_{M2} = p/(R^o T)(1 + 11X_{H_2O} + 1.5X_{H_2}), \tag{4.2}$$

with p and R^o being the pressure and universal gas constant and X_i representing the mole fraction of species i.

4.2.1 The two-step mechanism

The simplification of the chemistry can be continued by introducing steady-state approximations for OH, O and HO_2, which leads to a two-step chemical-

kinetic reduced mechanism [6] described by the global branching step

$$3H_2 + O_2 \rightleftharpoons 2H_2O + 2H \qquad \text{(I)}$$

and the recombination step

$$2H \rightarrow H_2\,, \qquad \text{(II)}$$

with global rates

$$\begin{aligned} \omega_{\text{I}} &= \omega_1 + \omega_{5f} \\ \omega_{\text{II}} &= \omega_{4f} + \omega_{9f} + \omega_{10f} \end{aligned} \tag{4.3}$$

written in terms of those of the elementary steps.

It is interesting to emphasize the similarities and differences between this chemistry, derived from the short 9-step mechanism by introduction of steady-state assumptions for all intermediaries other than H, and that proposed by Zeldovich [2] fifty years ago. In particular, the heat released by the global branching reaction I, which is given in terms of the standard formation enthalpy of each species $h^0_{f,i}$ by $q_{\text{I}} = -2(h^0_{f,\text{H}_2\text{O}} + h^0_{f,\text{H}}) \simeq 48$ KJ/mol, is only a small fraction of that released by recombination $q_{\text{II}} = 2h^0_{f,\text{H}} \simeq 436$ KJ/mol. Hence, the assumption of thermally neutral chain branching, present in the Zel'dovich chemistry model, applies in a good approximation to the above reduced description I-II, although the exothermicity of the branching reaction will be initially retained in the analysis below for increased accuracy. Also of interest is that the assumptions present in Zel'dovich model concerning the temperature dependence of the reaction-rate constants, i.e., temperature-independent recombination and temperature-sensitive branching through a large activation energy, also apply approximately to the two-step chemistry I-II. Thus, the rate of radical recombination ω_{II} is equal to the sum of the elementary rates $\omega_{4f} + \omega_{9f} + \omega_{10f}$, whose reaction-rate constants have only a weak algebraic dependence on temperature. On the other hand, as seen in Table 1.1, the activation temperature $T_{a_{1f}} = 8590$ K of the main rate-controlling reaction ω_{1f} for step I is relatively large, also in agreement with Zel'dovich approach, whose activation-energy analysis assumes a large temperature sensitivity of the branching step. Contrary to the Zel'dovich model, however, which considers an irreversible branching reaction, reaction I in our starting reduced chemistry is reversible. The backward rate, however, is negligibly small sufficiently far upstream, and it does not become significant until the temperature and the radical concentrations achieve sufficiently large values. The existence of a reverse rate has implications concerning the structure of the thin layer where branching occurs, as seen below.

4.2.2 Overall rates

The computation of the rates of reactions $1b$, $5f$ and $10f$ requires knowledge of the concentrations C_i of the steady-state intermediaries OH, O and HO_2, which can be determined in terms of those of H_2, O_2, H_2O, H and the temperature T by solution of the corresponding steady-state equations $\omega_1 + \omega_2 - \omega_3 + 2\omega_{5f} - \omega_{7f} - \omega_{10f} = 0$, $\omega_1 - \omega_2 = 0$ and $\omega_{4f} - \omega_{5f} - \omega_{6f} - \omega_{7f} = 0$. The last two equations can be solved for C_O and C_{HO_2} to give

$$\gamma_O = \frac{C_O}{C_H} = \frac{k_{1f}C_{O_2} + k_{2b}\gamma_{OH}C_H}{k_{2f}C_{H_2} + k_{1b}\gamma_{OH}C_H} \tag{4.4}$$

and

$$C_{HO_2} = \frac{k_{4f}C_{M1}C_{O_2}}{k_{5f} + k_{6f} + k_{7f}\gamma_{OH}}. \tag{4.5}$$

in terms of $\gamma_{OH} = C_{OH}/C_H$. Equations (4.4) and (4.5) can be then substituted in the steady-state equation for OH,

$$\begin{aligned} k_{3f}C_{H_2}\gamma_{OH} - k_{3b}C_{H_2O} - 2k_{5f}C_{HO_2} = 2(k_{1f}C_{O_2} - k_{1b}\gamma_O\gamma_{OH}C_H) \\ - k_{7f}C_{HO_2}\gamma_{OH} - k_{10f}\gamma_{OH}C_H\,, \end{aligned} \tag{4.6}$$

giving a cubic equation for γ_{OH} that can be solved numerically, thereby closing the definition of the overall rates

$$\begin{aligned} \omega_I &= k_{1f}C_{O_2}C_H\left(1 - \tfrac{k_{1b}\gamma_O\gamma_{OH}C_H}{k_{1f}C_{O_2}}\right) + (1-\tilde{\alpha})k_{4f}C_{M1}C_{O_2}C_H \\ \omega_{II} &= k_{4f}C_{M1}C_{O_2}C_H + k_{9f}C_{M2}C_H^2 + k_{10f}C_{M2}\gamma_{OH}C_H^2. \end{aligned} \tag{4.7}$$

The factor

$$\tilde{\alpha} = \frac{k_{6f} + k_{7f}\gamma_{OH}}{k_{5f} + k_{6f} + k_{7f}\gamma_{OH}}, \tag{4.8}$$

representing the fraction of hydroperoxyl molecules consumed through the chain-terminating path, is analogous to the factor $\bar{\alpha}$ defined in (3.33) for the one-step kinetics. Note, in particular, that (4.8) reduces to (3.33) by use of the steady-state expression (2.19), which becomes applicable when the H atoms are also in steady state, as occurs when approaching the lean flammability limit.

The performance of the two-step mechanism is tested in Fig. 4.1 by comparison with results obtained with the 9-step mechanism. As can be seen, the steady-state approximation for O, OH and HO_2 leads to small overpredictions of flame propagation velocities v_l on the order of 10%.

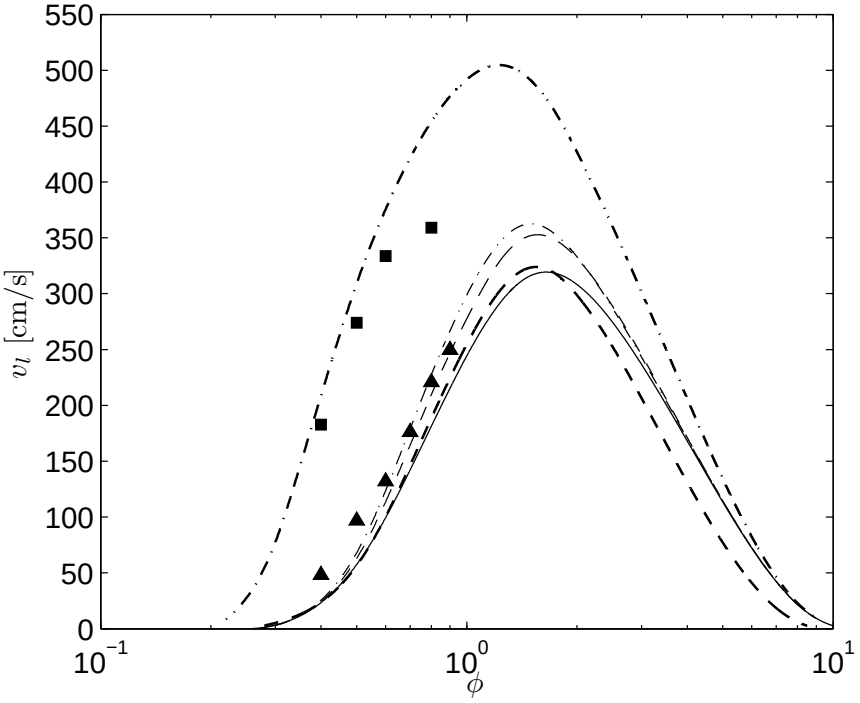

Figure 4.1: The lines represent the variation with equivalence ratio of the propagation velocity of premixed hydrogen-air flames for $T_u = 300K$ and $p = 1$ bar as obtained from numerical integrations with thermal diffusion excluded with the 9-step mechanism (solid line) and with the corresponding two-step reduced descriptions with different steady-state expressions for the intermediates O and OH (thin dashed line: equations (4.4) and (4.6); thick dashed line: equations (4.4) and (4.6) and $\tilde{\alpha} = 0.4$; thin dot-dashed line: equations (4.4) and (4.9); thick dot-dashed line: partial-equilibrium equations (4.10)). The symbols are results of the Zel'dovich analysis, with the triangles representing the results obtained from integrations of the outer problem with $T_B = T_B^*$ and with the squares denoting the solution of the outer problem coupled with that of the branching layer, according to the iterative procedure discussed in section 4.6.

As explained in [6], a simpler alternative description, with a similar degree of accuracy, follows from retaining only the largest terms in the steady-state equation for OH, which are those on the left-hand side of (4.6). The simplified equation $\omega_3 - 2\omega_{5f} = 0$ can then be solved explicitely to give

$$\gamma_{\rm OH} = \frac{C_{\rm OH}}{C_{\rm H}} = \frac{k_{3b}C_{\rm H_2O} + 2[k_{5f}/(k_{5f}+k_{6f})]k_{4f}C_{\rm M1}C_{\rm O_2}}{k_{3f}C_{\rm H_2}}. \tag{4.9}$$

Results obtained with this truncated expression for $\gamma_{\rm OH}$ are also included in Fig. 4.1. As can be seen, use of (4.9) does not modify appreciably the accuracy of the two-step description.

The reverse rates of reactions 1-3 are negligibly small sufficiently far upstream, but become significant downstream as the temperature and the radical concentrations reach sufficiently large values. In fact, on the hot side of the flame these three reactions are so fast that they achieve partial equilibrium, a condition that gives three equations that relate the concentrations of the different chemical species. Although these equations do not apply upstream, they can be used in principle to simplify the description. For instance, the partial-equilibrium equations for reactions 2 and 3 can be used to write

$$\gamma_{\rm O} = \frac{C_{\rm O}}{C_{\rm H}} = \frac{C_{\rm H_2O}C_{\rm H}}{K_2K_3C_{\rm H_2}^2}, \quad \text{and} \quad \gamma_{\rm OH} = \frac{C_{\rm OH}}{C_{\rm H}} = \frac{C_{\rm H_2O}}{K_3C_{\rm H_2}} \tag{4.10}$$

as replacements for the steady-state expressions given in (4.4) and (4.9), where $K_j = k_{j_f}/k_{j_B}$ represents the equilibrium constant of the elementary step j. Note that this approximation corresponds to neglecting simultaneously production of OH through reaction $5f$ in (4.9) and production and consumption of O through reaction 1 in (4.4). Although the resulting simplified expressions (4.10) are used below for the discussion of the flame structure and also in analysing the branching layer, they lead to relatively large overpredictions of flame velocities when applied everywhere across the flame to determine the O and OH concentrations of the two-step mechanism, a result that can be seen in the computations of Fig. 4.1.

The value of $\tilde{\alpha}$ varies across the flame, as dictated by the relative OH-to-H content of the mixture. Evaluations of (4.8) using results of detailed-chemistry computations reveal that the parameter $\tilde{\alpha}$, although tends to decrease for increasing equivalence ratios, takes for moderately lean flames a value in the range $0.3 \lesssim \tilde{\alpha} \lesssim 0.5$ in the intermediate region where radical concentrations peak. This finding motivates the use of the constant value for $\tilde{\alpha} = 0.4$ in computing the branching rate $\omega_{\rm I}$ in (4.7), a considerable simplification that

provides accurate results for lean flames, as can be seen in the comparisons shown in Fig. 4.1.The results for $\tilde{\alpha} = 0.4$ are obtained with the O and OH concentrations evaluated from the implicit equations (4.4) and (4.6). A similar approach was employed in previous analytical works [1]. As expected, as the concentration of OH becomes smaller than that of H for richer flames, so that $\gamma_{\mathrm{OH}} \to 0$ and $\tilde{\alpha} \to k_{6f}/(k_{5f} + k_{6f}) \simeq 1/6$, the accuracy of the approximation $\tilde{\alpha} = 0.4$ deteriorates.

4.3 Formulation

4.3.1 Governing equations

The conservation equations for a steady, adiabatic, planar, premixed laminar flame with the two-step kinetics having the reaction rates described in (4.7) provide the starting point for the analysis. Integration of the continuity equation gives $\rho v = \rho_u v_l$, with ρ and v denoting density and velocity, the subscript u representing unburnt conditions, and v_l being the flame propagation velocity. The problem then reduces to that of integrating [7]

$$\rho_u v_l \frac{\mathrm{d}Y_i}{\mathrm{d}x} - \frac{\mathrm{d}}{\mathrm{d}x}\left(\frac{\lambda}{c_p L_i}\frac{\mathrm{d}Y_i}{\mathrm{d}x}\right) = \dot{m}_i \tag{4.11}$$

for the species $i = \mathrm{H_2}, \mathrm{O_2}, \mathrm{H_2O}$, and H, with local mass production rates $\dot{m}_{\mathrm{H_2}} = W_{\mathrm{H_2}}(-3\omega_{\mathrm{I}} + \omega_{\mathrm{II}})$, $\dot{m}_{\mathrm{O_2}} = -W_{\mathrm{O_2}}\omega_{\mathrm{I}}$, $\dot{m}_{\mathrm{H_2O}} = 2W_{\mathrm{H_2O}}\omega_{\mathrm{I}}$, and $\dot{m}_{\mathrm{H}} = W_{\mathrm{H}}(2\omega_{\mathrm{I}} - 2\omega_{\mathrm{II}})$, and the energy conservation equation

$$\rho_u v_l c_p \frac{\mathrm{d}T}{\mathrm{d}x} - \frac{\mathrm{d}}{\mathrm{d}x}\left(\lambda\frac{\mathrm{d}T}{\mathrm{d}x}\right) = q_{\mathrm{I}}\omega_{\mathrm{I}} + q_{\mathrm{II}}\omega_{\mathrm{II}}. \tag{4.12}$$

In this formulation Y_i, W_i, λ and c_p denote the mass fraction and molecular weight of species i, and the thermal conductivity and specific heat at constant pressure of the gas mixture. Upstream boundary conditions for Eqs. (4.11) and (4.12) are $T = T_u$, $Y_{\mathrm{O_2}} = Y_{\mathrm{O_2}u}$, $Y_{\mathrm{H_2}} = Y_{\mathrm{H_2}u}$, $Y_{\mathrm{H_2O}} = Y_{\mathrm{H}} = 0$, whereas the equilibrium conditions $\mathrm{d}T/\mathrm{d}x = \mathrm{d}Y_i/\mathrm{d}x = 0$ apply downstream. As in [1], binary diffusion approximations are used in writing (4.11) with the Lewis numbers $L_i = \lambda/(\rho c_p D_i)$ assumed to be constant and equal to $L_{\mathrm{H_2}} = 0.30$, $L_{\mathrm{O_2}} = 1.11$, $L_{\mathrm{H_2O}} = 0.83$ and $L_{\mathrm{H}} = 0.18$, where D_i is the binary diffusion coefficient of species i with respect to nitrogen. In addition, in the energy conservation equation, terms involving the derivatives of c_p or sums over products of individual specific heats with diffusion fluxes are neglected for simplicity,

and the approximate expression $(\lambda/c_p) = 2.58 \times 10^{-5}(T/298)^{0.7}$ kg/(m s) proposed in [7] will be used when evaluating the temperature variation of the transport properties, as done in the two previous chapters.

4.3.2 Flame structure

The activation temperature of the controlling elementary step $1f$ is sufficiently large for the limit of large activation energy to be a reasonable approach in addressing the solution of the above problem. For the discussion that follows, it is of interest to write the H-atom production rate $\dot{C}_{\rm H} = 2(\omega_{\rm I} - \omega_{\rm II})$ without the direct recombination terms $9f$ and $10f$ and with the simplified expressions (4.10) for the concentrations of O and OH to give

$$\dot{C}_{\rm H} = 2\left(k_{1f}\left[1 - \frac{C_{\rm H_2O}^2 C_{\rm H}^2}{K C_{\rm H_2}^3 C_{\rm O_2}}\right] - \tilde{\alpha} k_{4f} C_{\rm M1}\right) C_{\rm O_2} C_{\rm H}, \tag{4.13}$$

where the equilibrium constant

$$K = K_1 K_2 K_3^2 \tag{4.14}$$

is related to those of the shuffle reactions 1-3. Evaluation of the expression for K indicates that this quantity takes fairly large values at temperatures of interest for H_2-air lean deflagrations, giving for instance $K \simeq 400$ at $T \simeq 1100$ K and $K \simeq 100$ at $T \simeq 1500$ K.

To anticipate the flame structure that arises in the limit of large activation temperature of the rate-controlling reaction $1f$, it is of interest to introduce the crossover temperature, T_c, associated with the second explosion limit of H_2-O_2 mixtures, defined as the temperature at which the net rate of H-atom production vanishes. If the contribution of ω_{1b} to the consumption of H atoms is neglected in (4.13), then the resulting equation $\dot{C}_{\rm H} = 0$ leads to

$$k_{1f_c} = \tilde{\alpha} k_{4f_c} C_{\rm M1_c}\,, \tag{4.15}$$

for evaluating the crossover temperature, where the subscript c denotes quantities evaluated at T_c. The resulting value of T_c depends on the pressure and on the mixture composition through the effective third-body concentration $C_{\rm M1_c}$ given in (4.1). Note that, for sufficiently lean flames, $\tilde{\alpha} = \bar{\alpha}$, and (4.15) reduces to (2.29), the corresponding definition of T_c determined from the one-step kinetics.

Because of the large temperature sensitivity of k_{1f}, at temperatures below crossover, branching becomes negligibly slow and can be correspondingly neglected in (4.13). Branching becomes significant as the temperature increases

to reach near-crossover values such that $T_c - T \sim (T_{a_{1f}}/T_c)^{-1}T_c$, for which $k_{1f} \sim \tilde{\alpha}k_{4f_c}C_{\mathrm{M1}_c}$. Correspondingly, as the temperature increases from T_c, the value of k_{1f} becomes large compared with $\tilde{\alpha}k_{4f}C_{\mathrm{M1}}$, causing the rapid consumption of H_2. Initially, the reverse of the branching rate is negligible, i.e., the factor $(C^2_{H_2O}C^2_H)/(KC^3_{H_2}C_{O_2})$ can be neglected in (4.13), but as the fuel concentration decreases, it becomes faster and must be taken into account to describe branching in the region where the fuel concentration achieves small values of the order $C_{H_2} \sim K^{-1/3}C^{2/3}_{H_2O}C^{2/3}_H/C^{1/3}_{O_2}$. Eventually, the exponential increase of k_{1f} for temperatures sufficiently above T_c causes the factor in square brackets in (4.13) to vanish, yiending the partial-equilibrium condition

$$KC^3_{H_2}C_{O_2} = C^2_{H_2O}C^2_H. \tag{4.16}$$

Since $K \gg 1$, the associated fuel-concentration equilibrium value

$$C_{H_2} = K^{-1/3}C^{2/3}_{H_2O}C^{2/3}_H/C^{1/3}_{O_2} \tag{4.17}$$

is very small, keeping the concentration of H_2 at a negligible level for temperatures sufficiently above crossover, the overall effect being that the branching reaction I rapidly eliminates the H_2 resulting from the recombination step II according to $\omega_{\mathrm{I}} = \frac{1}{3}\omega_{\mathrm{II}}$, placing the molecule H_2 into a steady state, as explained below.

Therefore, the large temperature sensitivity of k_{1f} combined with the condition $K \gg 1$ leads to a flame structure that corresponds at leading order to that first envisioned by Zel'dovich [2]: radical branching occurs in a very thin layer where H_2 is depleted, whereas radical recombination occurs in a distributed manner both upstream and downstream from this layer, in regions of thickness comparable to that of the flame, where recombination, convection and diffusion all occur simultaneously. The branching layer is located slightly downstream from the crossover point, at a location where the temperature reaches a branching temperature $T_B > T_c$ such that the rates of chemical branching and diffusional loss are comparable. The presumed flame structure is indicated in Fig. 4.2 using as sample profiles of temperature, H and H_2 those computed with detailed chemistry for $\phi = 0.6$, $T_u = 300K$ and $p = 1$ atm. Clearly, this flame structure must be modified near the lean flammability limit as the adiabatic flame temperature approaches the crossover value, when both branching and recombination occur in a relatively thin layer located at the hot side of the flame, which is preceded by a chemically frozen preheat region, the limiting case considered in the two previous chapters.

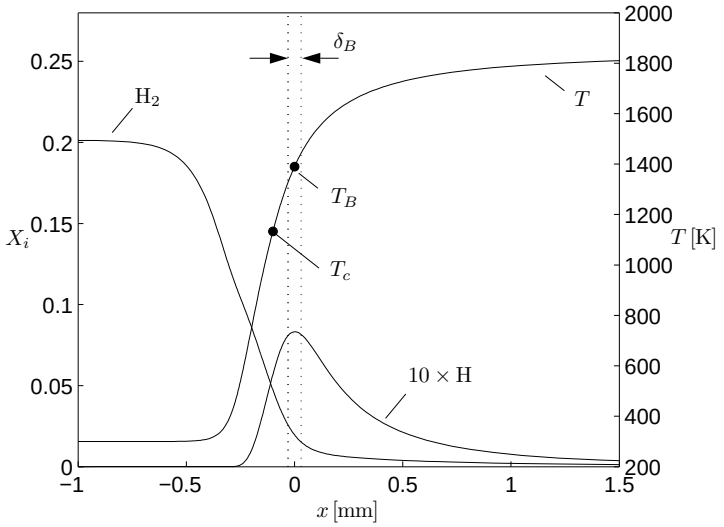

Figure 4.2: The temperature and mole fractions of H and H_2 across a hydrogen-air flame as computed with detailed chemistry for $\phi = 0.6$, $T_u = 300K$ and $p = 1$ bar. The plot shows schematically the location of the branching layer and the values of the crossover and branching temperatures.

4.3.3 Characteristic scales

The characteristic values of the flame propagation velocity V_l and flame thickness δ_l as well as an estimate for the temperature increment $T_B - T_c$ follow from a straightforward order-of-magnitude analysis of the first quadrature of the H-atom conservation equation

$$\rho_u v_l Y_{\mathrm{H}} - \frac{1}{L_{\mathrm{H}}}\rho D_T \frac{\mathrm{d}Y_{\mathrm{H}}}{\mathrm{d}x} = 2\int_{-\infty}^{x} k_{1f} C_{\mathrm{O}_2} \rho Y_{\mathrm{H}} \mathrm{d}x - 2\tilde{\alpha}\int_{-\infty}^{x} k_{4f} C_{\mathrm{M}} C_{\mathrm{O}_2} \rho Y_{\mathrm{H}} \mathrm{d}x, \tag{4.18}$$

$$\rho_u V_l \qquad \frac{\rho_c D_{T_c}}{\delta_l} \qquad k_{1f_B}\frac{\rho_c Y_{\mathrm{O}_{2u}}}{W_{\mathrm{O}_2}}\rho_c \delta_B \qquad \tilde{\alpha} k_{4f_c} C_{\mathrm{M}_c}\frac{\rho_c Y_{\mathrm{O}_{2u}}}{W_{\mathrm{O}_2}}\rho_c \delta_l$$

which is written with ω_{1b}, ω_{9f} and ω_{10f} neglected for simplicity and with the expressions $C_i = \rho Y_i / W_i$ and $D_T = \lambda/(\rho c_p)$ for the concentration and thermal diffusivity. The estimates given below each of the four terms are obtained by anticipating that radical recombination, convection and diffusion occur all across the flame, while radical branching is confined in a thin layer of thickness $\delta_B \ll \delta_l$ where the temperature is close to T_B. The different quantities

are estimated with their values at the crossover temperature, except for the temperature-sensitive reaction-rate constant of the branching reaction, k_{1f_B}, which is evaluated at the branching temperature. The condition that the diffusion, convection and recombination rates be comparable across the flame yields

$$\delta_l = (\lambda/c_p)_c/(\rho_u V_l) \tag{4.19}$$

and

$$V_l = (\rho_c/\rho_u)[(\lambda/c_p)_c\,\tilde{\alpha}\,k_{4f_c}C_{\mathrm{M}1_c}Y_{\mathrm{O}_2u}/W_{\mathrm{O}_2}]^{1/2} \tag{4.20}$$

for the characteristic values of the flame thickness and flame propagation velocity, respectively. On the other hand, to estimate the thickness δ_B of the branching layer we begin by linearizing the exponent of the branching constant according to $k_{1f} = k_{1f_B}\exp[T_{a_{1f}}(T-T_B)/T_B^2]$, which reveals that branching is confined to a thin layer where the temperature differs from the branching value by a small relative amount $(T-T_B)/T_B \sim (T_{a_{1f}}/T_B)^{-1}$. Since the total temperature increase across the flame is $T_\infty - T_u$, we can write $(T-T_B)/(T_\infty - T_u) \sim \delta_B/\delta_l$ and, therefore,

$$\delta_B/\delta_l = \left(\frac{T_{a_{1f}}}{T_B}\frac{(T_\infty - T_u)}{T_B}\right)^{-1} \tag{4.21}$$

The condition that the radicals produced in the thin branching layer recombine across the flame provides

$$k_{1f_B} = \tilde{\alpha}\,k_{4f_c}C_{\mathrm{M}1_c}\frac{T_{a_{1f}}}{T_B}\frac{(T_\infty - T_u)}{T_B}, \tag{4.22}$$

indicating that the branching temperature exceeds the crossover temperature by a relative amount

$$\frac{T_B - T_c}{T_c} \sim \frac{\ln(T_{a_{1f}}/T_B)}{(T_{a_{1f}}/T_B)}. \tag{4.23}$$

Although this difference is asymptotically small in the limit $T_{a_{1f}}/T_B \to \infty$ considered here, for the values of $T_{a_{1f}}/T_B \sim 8$ typically encountered, the difference is non-negligible, and needs to be taken into account in the computation, as shown below.

4.3.4 Dimensionless formulation

To write the problem in dimensionless form, we use the characteristic scales given in (4.19) and (4.20) to define the spatial coordinate

$$\eta = (\rho_u V_l) \int_{x_o}^{x} (c_p/\lambda)\mathrm{d}x \tag{4.24}$$

and the dimensionless flame propagation velocity $\vartheta = v_l/V_l$, with x_o denoting the arbitrary coordinate origin, to be selected below as the branching-layer location. The normalized species mass fractions $y_{\mathrm{H}_2} = Y_{\mathrm{H}_2}/Y_{\mathrm{H}_2 u}$, $y_{\mathrm{O}_2} = Y_{\mathrm{O}_2}/Y_{\mathrm{O}_2 u}$ and $y_{\mathrm{H}_2\mathrm{O}} = (W_{\mathrm{H}_2}/W_{\mathrm{H}_2\mathrm{O}})Y_{\mathrm{H}_2\mathrm{O}}/Y_{\mathrm{H}_2 u}$ are referred to the reactant upstream values while the H-atom mass fraction is normalized according to $y_{\mathrm{H}} = (W_{\mathrm{H}_2}/W_{\mathrm{H}})Y_{\mathrm{H}}/Y_{\mathrm{H}_2 u}$ and the temperature is expressed through the dimensionless variable $\theta = T/T_c$, different from the integration variable used in (3.45) for the function J. With these scalings, the nondimensional species and energy conservation equations become

$$\vartheta y'_{\mathrm{H}_2\mathrm{O}} - \frac{1}{L_{\mathrm{H}_2\mathrm{O}}} y''_{\mathrm{H}_2\mathrm{O}} = 2w_{\mathrm{I}} \tag{4.25}$$

$$\vartheta y'_{\mathrm{H}} - \frac{1}{L_{\mathrm{H}}} y''_{\mathrm{H}} = 2(w_{\mathrm{I}} - w_{\mathrm{II}}) \tag{4.26}$$

$$\vartheta y'_{\mathrm{H}_2} - \frac{1}{L_{\mathrm{H}_2}} y''_{\mathrm{H}_2} = -3w_{\mathrm{I}} + w_{\mathrm{II}} \tag{4.27}$$

$$\vartheta y'_{\mathrm{O}_2} - \frac{1}{L_{\mathrm{O}_2}} y''_{\mathrm{O}_2} = -2\phi w_{\mathrm{I}} \tag{4.28}$$

$$\vartheta\theta' - \theta'' = 2(\bar{q}_{\mathrm{I}} w_{\mathrm{I}} + \bar{q}_{\mathrm{II}} w_{\mathrm{II}}), \tag{4.29}$$

where the prime $'$ denotes differentiation with respect to η, $\phi = 8Y_{\mathrm{H}_2 u}/Y_{\mathrm{O}_2 u}$ is the equivalence ratio and

$$\bar{q}_{\mathrm{I}} = \frac{q_{\mathrm{I}} Y_{\mathrm{H}_2 u}}{2W_{\mathrm{H}_2} c_p T_c} \tag{4.30}$$

$$\bar{q}_{\mathrm{II}} = \frac{q_{\mathrm{II}} Y_{\mathrm{H}_2 u}}{2W_{\mathrm{H}_2} c_p T_c} \tag{4.31}$$

are the dimensionless reaction heats corresponding to branching and recombination, respectively. In the formulation,

$$w_{\mathrm{I}} = \theta^s \exp\left[\frac{T_{a_{1f}}}{T_c}\frac{\theta-1}{\theta}\right] y_{\mathrm{O}_2} y_{\mathrm{H}} \left[1 - \frac{2\phi}{K}\frac{y^2_{\mathrm{H}_2\mathrm{O}} y^2_{\mathrm{H}}}{y^3_{\mathrm{H}_2} y_{\mathrm{O}_2}}\right] + \frac{1-\tilde{\alpha}}{\tilde{\alpha}}\theta^r y_{\mathrm{O}_2} y_{\mathrm{H}} \tag{4.32}$$

and

$$w_{\mathrm{II}} = \frac{1}{\tilde{\alpha}}\theta^r y_{\mathrm{O}_2} y_{\mathrm{H}} + \Lambda_{9f}\theta^t y^2_{\mathrm{H}} + \Lambda_{10f}\theta^z \gamma_{\mathrm{OH}} y^2_{\mathrm{H}} \tag{4.33}$$

are the nondimensional branching and recombination rates. The weak algebraic dependence on temperature of the reaction-rate constants and concentrations has been taken into account through the exponents $r = n_{4f} + \sigma - 3 = -3.7$, $s = n_{1f} + \sigma - 2 = -2$, $t = n_{9f} + \sigma - 3$ and $z = n_{10f} + \sigma - 3$. The final equilibrium values $X_{H_2} = 0$ and $X_{H_2O} = X_{H_2O_\infty} = 2\phi/(4.76 + \phi)$ are used in evaluating the chaperon efficiencies of (4.1) and (4.2). The relative magnitude of the reaction rates of the direct recombination reactions are measured through the reaction-rate ratios

$$\Lambda_{9f} = \frac{1}{\tilde{\alpha}} \frac{k_{9f}}{k_{4f}} \frac{1 + 11 X_{H_2O_\infty}}{1 + 15 X_{H_2O_\infty}} \tag{4.34}$$

$$\Lambda_{10f} = \frac{2\phi}{\tilde{\alpha}} \frac{k_{10f}}{k_{4f}} \frac{1 + 11 X_{H_2O_\infty}}{1 + 15 X_{H_2O_\infty}}. \tag{4.35}$$

As previously explained, although the factor $\tilde{\alpha}$ varies considerably across the flame, in moderately lean flames consideration of a constant value $\tilde{\alpha} = 0.4$ suffices for computational purposes. For simplicity, the reverse of the branching rate has been evaluated with the concentrations of O and OH corresponding to partial equilibrium of the shuffle reactions 2 and 3, given in (4.10), which are only strictly applicable on the downstream side of the flame, where the temperature is sufficiently larger than T_c.

The above equations must be integrated with boundary conditions

$$y_{H_2} - 1 = y_{O_2} - 1 = y_{H_2O} = y_H = \theta - \theta_u = 0 \tag{4.36}$$

as $\eta \to -\infty$ and

$$y'_{H_2} = y'_{O_2} = y'_{H_2O} = y'_H = \theta' = 0 \tag{4.37}$$

as $\eta \to \infty$. In the solution below, we shall replace (4.25) with

$$y_{H_2O} = (1 - y_{O_2})/\phi, \tag{4.38}$$

which follows from integrating a chemistry-free linear combination of (4.25) and (4.28) with equal diffusivities assumed for molecular oxygen and water vapor.

For the chemistry description considered, the equilibrium conditions imply that

$$\begin{cases} y_{H_2} = y_H = 0, \; y_{O_2} = y_{O_{2\infty}} = 1 - \phi, \\ y_{H_2O} = 1, \; \theta = \theta_\infty = \theta_u + \bar{q}_I + \bar{q}_{II} \end{cases} \tag{4.39}$$

as $\eta \to \infty$. This last equation is used in the computations below to select the mean value of the specific heat $c_p = (q_{\rm I} + q_{\rm II})Y_{\rm H_2 u}/[2W_{\rm H_2}(T_\infty - T_u)]$, where T_∞ is the adiabatic flame temperature. The value of T_∞ can be obtained from chemical equilibrium [8] for given conditions of pressure, initial temperature T_u and equivalence ratio, giving for instance the results shown in Fig. 4.3 for $p = 1$ atm and $T_u = 300$ K. The value of T_c, also shown in the figure, can be determined from (4.15) with $\tilde{\alpha} = 0.4$ and with the equilibrium composition employed to evaluate the chaperon efficiencies of (4.1).

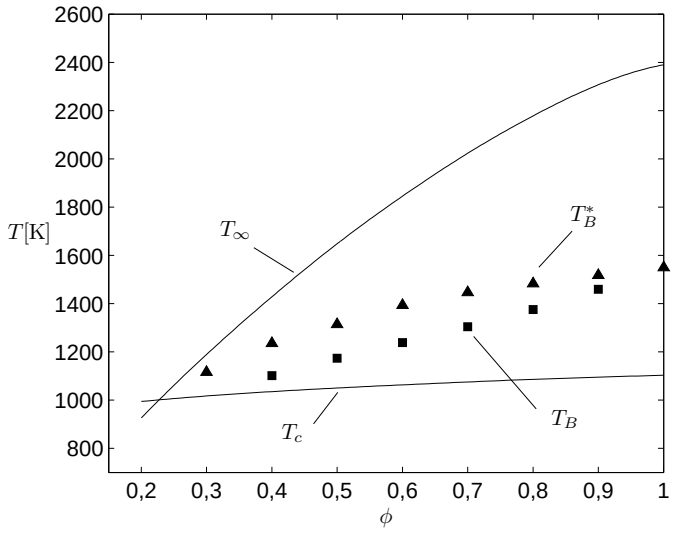

Figure 4.3: The variation with equivalence ratio of the adiabatic flame temperature T_∞ as obtained from equilibrium calculations with STANJAN [8] for $p = 1$ atm and $T_u = 300$ K and of the crossover temperature T_c as computed from (4.15) with $\tilde{\alpha} = 0.4$ and with the final equilibrium values $X_{\rm H_2} = 0$ and $X_{\rm H_2O} = X_{\rm H_2O_\infty} = 2\phi/(4.76 + \phi)$ used in evaluating the chaperon efficiencies of (4.1). The triangles represent the value of the temperature T_B^* at the location where the radical mass fraction reaches its peak value as obtained from detailed-chemistry computations, whereas the squares are the branching temperatures T_B determined from the iterative solution of the Zel'dovich problem, as stated in section 4.6.

4.4 The radical-recombination regions

An asymptotic solution of (4.26)–(4.38) is sought in the limit of large activation energy of the branching rate $T_{a_{1f}}/T_B \gg 1$. In this limit, branching is seen to occur at a thin layer located where $\theta = \theta_B$. To determine ϑ we need to integrate the conservation equations both upstream and downstream from this branching layer, subject to the boundary conditions at $\eta \to \pm\infty$ given in (4.36) and (4.37), and appropriate jump conditions at $\eta = 0$, which is selected as the branching-layer location.

Because of the large value of the activation temperature $T_{a_{1f}} \gg T_c$, for $\eta < 0$ reaction 1 is frozen, and the branching rate reduces to $w_{\rm I} = (1-\tilde{\alpha})\theta^r y_{\rm O_2} y_{\rm H}/\tilde{\alpha}$. Introducing this simplified branching rate into (4.26)–(4.29) gives

$$\vartheta y'_{\rm H} - \frac{1}{L_{\rm H}} y''_{\rm H} = -2(\theta^r y_{\rm O_2} y_{\rm H} + \Lambda_{9f}\theta^t y_{\rm H}^2 + \Lambda_{10f}\theta^z \gamma_{\rm OH} y_{\rm H}^2) \tag{4.40}$$

$$\vartheta y'_{\rm H_2} - \frac{1}{L_{\rm H_2}} y''_{\rm H_2} = -\frac{2-3\tilde{\alpha}}{\tilde{\alpha}}\theta^r y_{\rm O_2} y_{\rm H} + \Lambda_{9f}\theta^t y_{\rm H}^2 + \Lambda_{10f}\theta^z \gamma_{\rm OH} y_{\rm H}^2 \tag{4.41}$$

$$\vartheta y'_{\rm O_2} - \frac{1}{L_{\rm O_2}} y''_{\rm O_2} = -2\phi\frac{1-\tilde{\alpha}}{\tilde{\alpha}}\theta^r y_{\rm O_2} y_{\rm H} \tag{4.42}$$

$$\begin{aligned}\vartheta\theta' - \theta'' = {} & \frac{2}{\tilde{\alpha}}[(1-\tilde{\alpha})\bar{q}_{\rm I} + \bar{q}_{\rm II}]\theta^r y_{\rm O_2} y_{\rm H} \\ & + 2\bar{q}_{\rm II}(\Lambda_{9f}\theta^t y_{\rm H}^2 + \Lambda_{10f}\theta^z \gamma_{\rm OH} y_{\rm H}^2).\end{aligned} \tag{4.43}$$

The OH content of the mixture in this upstream region is sufficiently small for the effect of reaction $10f$ to be negligible, so that the factor $\gamma_{\rm OH}$ can be set equal to zero in (4.40), (4.41) and (4.43), thereby avoiding problems associated with the denominator in (4.9) becoming zero at the branching layer.

For $\eta > 0$, on the other hand, the exponential factor in (4.32) becomes asymptotically large, causing reaction I to achieve partial equilibrium according to

$$y_{\rm H_2} = \left[\frac{2\phi}{K}\right]^{1/3} (y_{\rm H_2O}^2 y_{\rm H}^2 / y_{\rm O_2})^{1/3}, \tag{4.44}$$

which is the dimensionless form of (4.17). For typical values of $K \sim 400$ and $T_{a_{1f}}/T_B \sim 8$ the relative scaling

$$\left(\frac{2\phi}{K}\right)^{1/3} \sim (T_{a_{1f}}/T_B)^{-1} \ll 1 \tag{4.45}$$

applies, so that in this downstream region rapid branching consumes the H_2 produced by radical recombination, causing H_2 to follow a steady state approximation with $y_{\rm H_2} \sim K^{-1/3} \sim (T_{a_{1f}}/T_B)^{-1} \ll 1$. Therefore, at leading

order in the asymptotic description for large values of $T_{a_{1f}}/T_B$, for $\eta > 0$ one finds $y_{H_2} = 0$. The steady state approximation for H_2 can be introduced by combining linearly (4.26)–(4.29) to eliminate the singular rate w_I according to

$$\vartheta y'_H - \frac{1}{L_H} y''_H + \frac{2}{3}\left\{\vartheta y'_{H_2} - \frac{1}{L_{H_2}} y''_{H_2}\right\} = -(4/3) w_{II} \tag{4.46}$$

$$\vartheta y'_{O_2} - \frac{1}{L_{O_2}} y''_{O_2} - \frac{2}{3}\phi\left\{\vartheta y'_{H_2} - \frac{1}{L_{H_2}} y''_{H_2}\right\} = -(2\phi/3) w_{II}\,, \tag{4.47}$$

$$\vartheta\theta' - \theta'' + \frac{2}{3}\bar{q}_I\left\{\vartheta y'_{H_2} - \frac{1}{L_{H_2}} y''_{H_2}\right\} = 2(\bar{q}_I/3 + \bar{q}_{II}) w_{II}\,. \tag{4.48}$$

Eliminating then the vanishing H_2 mass fraction on the left-hand side of the above equations leads to

$$\vartheta y'_H - \frac{1}{L_H} y''_H = -\frac{4}{3}\left(\frac{\theta^r}{\tilde{\alpha}} y_{O_2} y_H + \Lambda_{9f}\theta^t y_H^2 + \Lambda_{10f}\theta^z \gamma_{OH} y_H^2\right) \tag{4.49}$$

$$\vartheta y'_{O_2} - \frac{1}{L_{O_2}} y''_{O_2} = -\frac{2\phi}{3}\left(\frac{\theta^r}{\tilde{\alpha}} y_{O_2} y_H + \Lambda_{9f}\theta^t y_H^2 + \Lambda_{10f}\theta^z \gamma_{OH} y_H^2\right), \tag{4.50}$$

$$\vartheta\theta' - \theta'' = 2\left(\frac{\bar{q}_I}{3} + \bar{q}_{II}\right) \times \left(\frac{\theta^r}{\tilde{\alpha}} y_{O_2} y_H + \Lambda_{9f}\theta^t y_H^2 + \Lambda_{10f}\theta^z \gamma_{OH} y_H^2\right). \tag{4.51}$$

In this downstream region, all three shuffle reactions are in partial equilibrium, and the function γ_{OH} can be correspondingly evaluated from

$$\gamma_{OH} = \left(\frac{K_1 K_2}{K_3}\frac{y_{H_2O} y_{O_2}}{y_H^2}\right)^{1/3}. \tag{4.52}$$

Note that, because of the rapid H_2 consumption, the branching rate is distributed with a rate determined by the H_2 steady-state condition $w_I = \frac{1}{3} w_{II}$, giving an overall recombination reaction

$$\frac{4}{3}H + \frac{1}{3}O_2 \rightarrow \frac{2}{3}H_2O \tag{4.53}$$

with a rate equal to w_{II}.

The problem can be solved by integrating (4.40)–(4.43) for $\eta < 0$ with boundary conditions (4.36) and (4.49)–(4.51) for $\eta > 0$ with boundary con-

ditions (4.37), and using the additional matching conditions at $\eta = 0$

$$y_{\mathrm{H}_2} = \theta - \theta_B = 0 \tag{4.54}$$

$$\frac{1}{L_{\mathrm{H}}} y'_{\mathrm{H}_-} + \frac{2}{3}\frac{1}{L_{\mathrm{H}_2}} y'_{\mathrm{H}_2-} = \frac{1}{L_{\mathrm{H}}} y'_{\mathrm{H}_+} \tag{4.55}$$

$$\frac{1}{L_{\mathrm{O}_2}} y'_{\mathrm{O}_2-} - \frac{2}{3}\phi\frac{1}{L_{\mathrm{H}_2}} y'_{\mathrm{H}_2-} = \frac{1}{L_{\mathrm{O}_2}} y'_{\mathrm{O}_2+} \tag{4.56}$$

$$\theta'_- + \frac{2}{3}\frac{\bar{q}_{\mathrm{I}}}{L_{\mathrm{H}_2}} y'_{\mathrm{H}_2-} = \theta'_+ \tag{4.57}$$

where the last three equations, involving the gradients of temperature and reactants at $\eta = 0+$ and $\eta = 0-$, are obtained by integrating (4.46)–(4.48) across the branching sheet.

For a given value of the branching temperature $\theta_B = T_B/T_c$ the integration of the above problem determines the flame propagation velocity ϑ as an eigenvalue. Because of numerical stiffness, shooting methods were found to be inadequate for the above problem, which was finally integrated with a second-order finite-difference method. Besides the value of ϑ, the integration of the outer problem provides the profiles of species and temperature, including the values of the mass fractions at the branching sheet y_{H_B}, $y_{\mathrm{O}_{2B}}$ and $y_{\mathrm{H_2O}_B} = (1 - y_{\mathrm{O}_{2B}})/\phi$ and the corresponding upstream and downstream gradients y'_{H_2-}, y'_{H_-}, y'_{H_+}, y'_{O_2-}, y'_{O_2+}, θ'_-, and θ'_+. As seen in the following section, determination of θ_B requires analysis of the inner structure of the branching layer, whose solution depends on that of the outer problem through the values of y'_{H_2-}, θ'_+, y_{H_B}, $y_{\mathrm{H_2O}_B}$ and $y_{\mathrm{O}_{2B}}$, so that the outer and inner problems are coupled and need to be simultaneously solved in an iterative manner, thereby complicating the computation of ϑ.

A first estimate for θ_B to start the iterative procedure may be obtained for instance by application of the order-of-magnitude estimate (4.23) or, more simply, from observations of detailed-chemistry computations, which provide an estimate for the branching temperature as the value of the temperature T_B^* at the location where the H-atom concentration peaks. For a premixed flame with $p = 1$ atm and $T_u = 300$ K, the variation of this value with equivalence ratio is represented by the triangles in Fig. 4.3. For instance, for $\phi = 0.8$, the value obtained is $T_B^* = 1482$ K, yielding $\theta_B = 1.42$ as an estimate for the dimensionless branching temperature. Using this value in integrating the problem, determines the value $\vartheta = 1.358$ for the flame velocity, which can be employed to compute $v_l = 220.94$ cm/s.

The integration provides also the accompanying species and temperature

profiles shown in Fig. 4.4. This sample computation reveals in particular that, because of the relatively small value of $\bar{q}_{\mathrm{I}}$, the jump in the temperature gradient at the branching layer is relatively small. It can also be observed how the effect of convection causes the recombination region upstream from the branching layer to be much thinner than that located downstream.

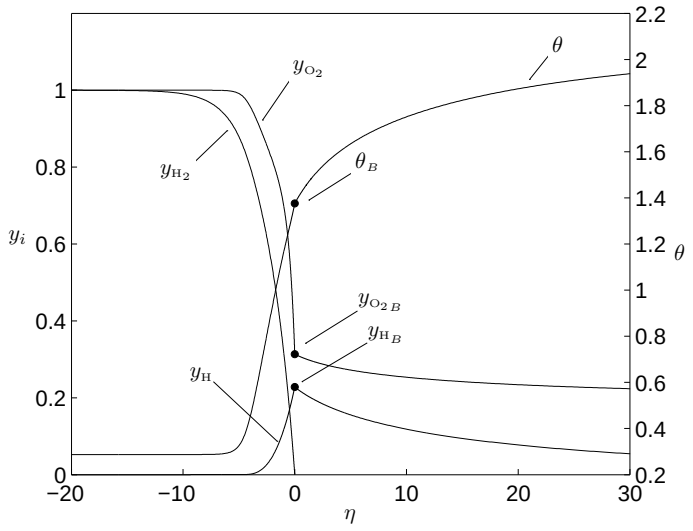

Figure 4.4: Species and temperature profiles obtained by integration of the outer problem for $\phi = 0.8$ with the value $\theta_B = 1.42$ assumed for the branching temperature.

4.5 The branching layer

4.5.1 Preliminary considerations and scalings

To close the problem, the value of the branching temperature $\theta_B = T_B/T_c$ at which radicals are produced needs to be computed from the analysis of the inner structure of the branching layer, of characteristic relative thickness $(T_{a_{1f}}/T_B)^{-1}$, within which the rates of branching and diffusion balance in the first approximation. Correspondingly, the profiles determined from the computation of the outer recombination regions, with their corresponding jumps in gradients, are rounded off within this layer, where we find small values of

$\theta - \theta_B \sim y_{O_2} - y_{O_{2B}} \sim y_H - y_{H_B} \sim y_{H_2} \sim y_{H_2O} - y_{H_2O_B} \sim (T_{a_{1f}}/T_B)^{-1}$. Since the branching temperature is larger than the crossover value, as indicated by the order-of-magnitude analysis leading to (4.23), the branching rate reduces to $\omega_I = \omega_1$. In writing the branching-diffusion conservation equations

$$-\theta'' = \frac{2}{3}\frac{\bar{q}_I}{L_{H_2}} y''_{H_2} = 2\bar{q}_I y_{O_{2B}} y_{H_B} \exp[\beta_B(T_B - T_c)/T_c] \times \exp[\beta_B(\theta - \theta_B)][1 - (y_{H_{2B}}/y_{H_2})^3], \tag{4.58}$$

the branching rate can be evaluated with constant species concentrations $y_{O_2} = y_{O_{2B}}$ and $y_H = y_{H_B}$ and with the temperature dependence of the reaction-rate constant linearized in the Frank-Kamenetskii way with account taken of the preexponential algebraic factor θ^s, so that

$$\beta_B = T_{a_{1f}}/T_B + s \tag{4.59}$$

is a modified dimensionless activation temperature. The resulting profiles of H_2 and temperature must match with the upstream profiles $y_{H_2} = y'_{H_{2-}}\eta$ and $\theta - \theta_B = \theta'_-\eta$, whereas downstream $\theta' \to \theta'_+$ and $y_{H_2} \to y_{H_{2B}}$, where

$$y_{H_{2B}} = \left[\frac{2\phi}{K_B}\frac{y^2_{H_2O_B} y^2_{H_B}}{y_{O_{2B}}}\right]^{1/3}, \tag{4.60}$$

with K_B denoting the value of K evaluated at the branching temperature T_B, is the small steady-state value of y_{H_2} reached immediately downstream from the branching layer, of order β_B^{-1} in the distinguished limit (4.45) considered here. Integrating once the first equation in (4.58) and matching with the outer gradients yields

$$\frac{2}{3}\frac{\bar{q}_I}{L_{H_2}} y'_{H_2} + \theta' = \theta'_+ = \frac{2}{3}\frac{\bar{q}_I}{L_{H_2}} y'_{H_{2-}} + \theta'_-, \tag{4.61}$$

while a second quadrature provides

$$\frac{2}{3}\frac{\bar{q}_I}{L_{H_2}} y_{H_2} + \theta - \theta_B = \theta'_+\eta \tag{4.62}$$

after matching with the upstream outer profiles. The above equations suggests the set of rescaled variables

$$\Theta = \beta_B(\theta - \theta_B), \quad \xi = \beta_B\theta'_+\eta \quad \text{and} \quad \varphi = \frac{2}{3}\frac{\bar{q}_I}{L_{H_2}}\beta_B y_{H_2} \tag{4.63}$$

for the analysis of the branching layer. Using the relationship

$$\varphi + \Theta = \xi, \tag{4.64}$$

as follows from (4.62), reduces the second equation in (4.58) to

$$\varphi_{\xi\xi} = \Lambda e^{\xi-\varphi}\left[1-\left(\frac{\varphi_B}{\varphi}\right)^3\right], \begin{cases} \xi \to -\infty: & \varphi - \dot{\varphi}_- \xi \to 0 \\ \xi \to \infty: & \varphi - \varphi_B \to 0 \end{cases} \tag{4.65}$$

where the subscript ξ denotes differentiation with respect to this variable, and

$$\Lambda = 2\bar{q}_{\rm I} y_{{\rm O}_2 B} y_{{\rm H}_B} \beta_B^{-1} (\theta'_+)^{-2} \exp[\beta_B (T_B - T_c)/T_c] \tag{4.66}$$

$$\varphi_B = \frac{2}{3}\frac{\bar{q}_{\rm I}}{L_{{\rm H}_2}} \beta_B y_{{\rm H}_2 B} \tag{4.67}$$

$$\dot{\varphi}_- = \frac{2}{3}\frac{\bar{q}_{\rm I}}{L_{{\rm H}_2}} \frac{y'_{{\rm H}_2 -}}{\theta'_+} \tag{4.68}$$

are, respectively, the reduced values of the reaction rate, hydrogen downstream concentration and hydrogen upstream diffusive rate.

4.5.2 The limit of thermally neutral branching

For given values of φ_B and $\dot{\varphi}_-$ the problem defined by (4.65) has solution for a single value of Λ which is therefore determined as an eigenvalue. The solution may be simplified by neglecting in (4.62) the heat release associated with the branching reaction, to give the linear temperature profile $\Theta = \xi$. Introducing the modified variable $\Psi = \varphi/\varphi_B$ and the parameters

$$A = -\frac{\dot{\varphi}_-}{\varphi_B} = -\frac{y'_{{\rm H}_2 -}}{\beta_B y_{{\rm H}_2 B} \theta'_+} \tag{4.69}$$

and

$$\Delta = \frac{\Lambda}{\varphi_B} = \frac{3 L_{{\rm H}_2} y_{{\rm O}_2 B} y_{{\rm H}_B}}{\beta_B^2 y_{{\rm H}_2 B} (\theta'_+)^2} \exp\left[\frac{\beta_B (T_B - T_c)}{T_c}\right] \tag{4.70}$$

reduces the problem to that of integrating

$$\Psi_{\xi\xi} = \Delta e^{\xi}\left(1 - \Psi^{-3}\right), \begin{cases} \xi \to -\infty: & \Psi + A\xi \to 0 \\ \xi \to +\infty: & \Psi - 1 \to 0. \end{cases} \tag{4.71}$$

The variation of Δ with A, obtained by numerical integration of (4.71), is shown in Fig. 4.5. The solution admits simplifications in the asymptotic limits $A \gg 1$ and $A \ll 1$.

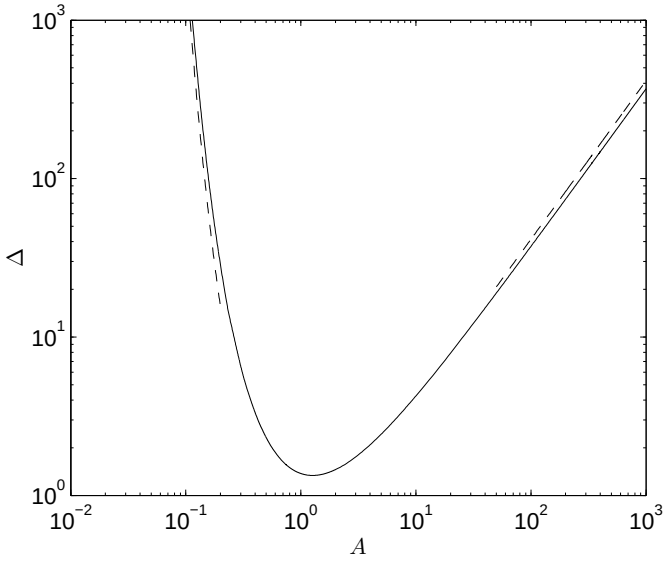

Figure 4.5: The variation of the modified reaction rate Δ with the modified hydrogen upstream diffusive rate A in the inner branching layer as obtained from numerical integration of (4.71). Dashed curves represent the asymptotics limits $A \ll 1$ and $A \gg 1$ from (4.72) and (4.77), respectively.

Small burning rate

For $A \ll 1$, the transition from the frozen solution $\Psi = -A\xi$ to the partial equilibrium solution $\Psi = 1$ takes place in an upstream layer located around $\xi = -A^{-1}$ where $\Psi - 1 \ll 1$. The problem can be rewritten in terms of the translated coordinate $\zeta = \xi + A^{-1}$ and rescaled H_2 concentration $\bar{\Psi} = (\Psi - 1)/A$ to give $\bar{\Psi}_{\zeta\zeta} = 3\Delta e^{-1/A} e^{\zeta} \bar{\Psi}$, which can be integrated with the boundary condition $\bar{\Psi} \to 0$ as $\zeta \to +\infty$ to yield $\bar{\Psi} = C K_0[(12\Delta e^{-1/A})^{1/2} e^{\zeta/2}]$, where K_0 is the modified Bessel function of zeroth order and C is a constant to be determined from the boundary condition as $\zeta \to -\infty$. Using now the boundary condition $\bar{\Psi} + \zeta \to 0$ as $\zeta \to -\infty$ together with the leading-order expansion $K_0 = \ln[(12\Delta e^{-1/A})^{1/2} e^{\zeta/2}] + \gamma_E$ finally provides

$$\Delta = \frac{1}{3} \exp\left(\frac{1}{A} - 2\gamma_E\right) \tag{4.72}$$

as the asymptotic form of Δ for $A \ll 1$, where $\gamma_E = 0.577$ is the Euler constant.

Large burning rate

For $A \gg 1$, on the other hand, the reverse branching rate is only significant in a thin layer of characteristic thickness A^{-1} located around the origin, where the small temperature variation can be neglected when writing the branching rate, thereby reducing the equation (4.71) to $\Psi_{\chi\chi} = (\Delta/A^2)(1-\Psi^{-3})$ when the rescaled coordinate $\chi = A\xi$ is introduced. Integrating twice with the boundary condition $\Psi(+\infty) = 1$ gives

$$\int_{\Psi_o}^{\Psi} \frac{\mathrm{d}\Psi}{(\Psi + \Psi^{-2}/2 - 3/2)^{1/2}} = -(2\Delta/A^2)^{1/2}\chi \tag{4.73}$$

in terms of the unknwon value $\Psi_o = \Psi(0)$. This implicit expression describes the evolution of Ψ from the equilibrium value $\Psi = 1$ as $\chi \to \infty$ to the asymptotic behavior

$$\Psi = B_o^2 - 2B_o \left(\frac{\Delta}{2A^2}\right)^{1/2} \chi + \left(\frac{\Delta}{2A^2}\right) \chi^2 \tag{4.74}$$

for $\chi \to -\infty$, where $B_o = \Psi_o^{1/2} - C_o$ and

$$2C_o = \int_{\Psi_o}^{\infty} \left(\frac{1}{(\Psi + \Psi^{-2}/2 - 3/2)^{1/2}} - \frac{1}{\Psi^{1/2}} \right) \mathrm{d}\Psi. \tag{4.75}$$

For $-\chi \sim O(1)$, on the other hand, the reverse of the branching rate is negligible, giving a reduced conservation equation $\Psi_{\xi\xi} = \Delta e^{\xi}$ that can be integrated with the boundary condition $\Psi + A\xi \to 0$ as $\xi \to -\infty$ to give $\Psi = \Delta e^{\xi} - A\xi$. The expansion for this last expression for $\xi \to 0$ written in terms of the inner variable χ yields

$$\Psi = \Delta - \frac{\Delta - A}{A}\chi + \left(\frac{\Delta}{2A^2}\right)\chi^2. \tag{4.76}$$

Matching with the inner solution then requires that the coefficients in (4.74) and (4.76) be identical, a condition that provides that $B_o = \Delta^{1/2}$ and

$$\Delta = (\sqrt{2} - 1)A, \tag{4.77}$$

the latter being the desired asymptotic form of Δ for $A \gg 1$. The predictions (4.72) and (4.77) are plotted in Fig. 4.5 along with the numerical results.

4.6 Predictions of flame propagation velocities

The computation of the eigenvalue ϑ is obtained iteratively by solving the outer problem coupled with the solution for the branching layer. The value of

T_B^* shown in Fig. 4.3, determined from detailed-chemistry computations as the temperature at the location of maximum H concentration, is used to construct an estimate for $\theta_B = T_B^*/T_c$ in the first integration of the outer problem. Besides the eigenvalue ϑ, the solution provides the values of $y'_{\mathrm{H}_{2-}}$, θ'_+, y_{H_B}, $y_{\mathrm{H_2O}_B}$ and $y_{\mathrm{O}_{2B}}$, which can be used to evaluate A from (4.69) with use made of (4.60) for the computation of the equilibrium value $y_{\mathrm{H}_{2B}}$. Introducing the resulting A in Fig. 4.5 gives the value of Δ, which can be substituted into (4.70). Solving then the resulting equation for T_B with $\beta_B = T_{a_{1f}}/T_B + s$ and with the values of $y_{\mathrm{O}_{2B}}$, y_{H_B}, $y_{\mathrm{H}_{2B}}$, and θ'_+ corresponding to the previous outer solution provides a new estimate for $\theta_B = T_B/T_c$, to be employed in solving again the outer problem. The iteration procedure is stopped once convergence to a value of T_B is achieved.

Predictions of burning velocities v_l obtained for $p = 1$ atm and $T_u = 300$ K are represented as symbols in Fig. 4.1. The plot includes the values of v_l predicted after the first integration, that is, those obtained from the solution of the outer problem when the branching temperature is taken to be equal to T_B^*, as well as the values determined after convergence is achieved, with the accompanying values of the converged branching temperatures T_B shown for completeness in Fig. 4.3.

The results indicate that, when the correct value of θ_B is used to integrate the outer problem by selecting $\theta_B = T_B^*/T_c$ from the detailed-chemistry computations, the resulting v_l found from the solution of the outer regions agrees well with the results of numerical integrations with the COSILAB code. The solution of the outer layer coupled with the branching layer gives however temperatures that are about 150 K below T_B^*, as seen in Fig. 4.3, which in turn produces severe overpredictions in v_l.

Improved accuracy therefore seems to require a more detailed description of the branching layer, leading to a more accurate prediction for T_B. In that respect, it is noteworthy the agreement between the results of the Zel'dovich analysis and those found in reduced-chemistry computations when the partial equilibrium of reactions 2 and 3 are used to determine the concentrations of O and OH. Since this same approximation is used above in the analysis of the branching layer, it can be concluded that future improvements of the Zel'dovich analysis should replace (4.10) with a more accurate steady-state description for these two radicals when formulating the inner branching problem. Efforts in that direction have not yet provided satisfactory results, and more research is necessary.

References

[1] K. Seshadri, N. Peters, F. A. Williams, Asymptotic analysis of stoichiometric and lean hydrogen-air flames, Combust. Flame 96 (1994) 407–427.

[2] Y. B. Zel'dovich, Chain reactions in hot flames - an approximate theory for flame velocity, Kinetika i Kataliz 2 (3) (1961) 308–318, english translation: International Chemical Engineering 2 (1962) 227-235.

[3] G. Joulin, A. Liñán, G. S. S. Ludford, N. Peters, C. Schmidt-Lainé, Flames with chain-branching/chain-breaking kinetics, SIAM J. Appl. Math. 45 (3) (1985) 420–434.

[4] J. W. Dold, R. W. Thatcher, A. Omon-Arancibia, J. Redman, From one-step to chain-branching premixed flame asymptotics, Proc. Combust. Inst. 29 (2002) 1519–1526.

[5] J. W. Dold, R. O. Weber, R. W. Thatcher, A. A. Shah, Flame balls with thermally sensitive intermediate kinetics, Combust. Theory Modelling 7 (2003) 175–203.

[6] F. Mauss, N. Peters, B. Rogg, F. A. Williams, Reduced kinetic mechanisms for premixed hydrogen flames, in: N. Peters, B. Rogg (Eds.), Reduced Kinetic Mechanisms for Applications in Combustion Systems, Springer-Verlag, 1993, pp. 29–43.

[7] M. D. Smooke, V. Giovangigli, Formulation of the premixed and nonpremixed test problems, in: M. D. Smooke (Ed.), Reduced Kinetic Mechanisms and Asymptotic Approximations for Methane-Air Flames, Vol. 384 of Lecture Notes in Physics, Springer-Verlag, 1991, pp. 1–28.

[8] W. C. Reynolds, The element potential method for chemical equilibrium analysis: Implementation in the interactive program stanjan [technical report], Tech. rep., Stanford University, Dept. of Mechanical Eng. (1986).

CHAPTER

FIVE

Conclusions and Future Prospects

5.1 Conclusions

This dissertation has used numerical and asymptotic techniques to investigate the structure and burning rate of lean hydrogen deflagrations for equivalence ratios spanning from the lean flammability limit ($\phi \simeq 0.258$ at normal conditions of pressure and temperature) to stoichiometric conditions. The underlying chemistry was addressed first. While a short mechanism of seven elementary steps succeeds in predicting burning rates and H-atom profiles near the lean flammability limit, short-chemistry descriptions of nine and eight elementary steps (with rate expressions in formats that do conform to existing codes) were identified and demonstrated to succeed in achieving additional objectives, such as improving predictions of concentration profiles of radicals other than the H atom or extending accurate burning-velocity predictions through stoichiometry to include all fuel-rich systems as well. These short mechanisms could facilitate computations having broader objectives and abilities to handle mechanisms larger than just a few steps.

Chapter 2 derives systematically an explicit one-step reaction-rate expression for the H_2 oxidation reaction

$$2H_2 + O_2 \rightarrow 2H_2O$$

that provides reasonable accuracy for calculating the lean flammability limit and laminar burning velocities of hydrogen-air systems from the lean limit to equivalence ratios that depend on the pressure and on the initial temperature, but that always are fuel-lean. The explicit reaction-rate formula does not conform to CHEMKIN or COSILAB formulas, for example, and so requires additional programming to be used with those codes, but it is especially well suited for use in future time-dependent, multidimensional codes for addressing hydrogen-air laminar or turbulent (DNS) flame propagation in complex

geometries, where descriptions employing detailed chemistry would be too large to be handled by existing or near-future computers.

The one-step mechanism is based on the demonstrated applicability of chemical-kinetic steady-state approximations for all reaction intermediaries, including the H atom, which is not in steady state in previously derived reduced-chemistry descriptions such as the two-step mechanism that earlier investigations have found to be useful for many purposes. The one-step mechanism applies for final flame temperatures between the crossover temperature (at which the rate of the H + O_2 $\rightarrow$ OH + O branching step equals the rate of the H + O_2 + M $\rightarrow$ HO_2 + M three-body step that leads to recombination) and a higher temperature at which the radical concentrations are too large for an H-atom steady state to be sufficiently accurate. This range of applicability decrease with increasing pressure and vanishes at sufficiently high pressures, approaching the third explosion limit at which H_2O_2 becomes an important intermediate radical generator, above about 10 atm for representative normal initial environmental temperatures. At 1 atm and an initial temperature of 300 K, for example, the one-step mechanism yields the burning velocity with an error less than 20% all the way from the lean limit of the planar flame, at an equivalence ratio of about 0.25, to an equivalence ratio well above the 0.60 shown in Fig. 2.5. This accuracy at equivalence ratios above 0.4, however, is fortuitous since the H-atom steady-state approximation begins to fail badly there. Overprediction in the peak of the H-atom together with corrections in the corner layer increase the burning velocity and therefore the failure of the steady-state must decrease velocity predictions to those values that fortuitously are in agreement with the short mechanism. If an approximation ($H = 1$) of a small relative rate of the backward step 2, H + OH $\rightarrow$ H_2 + O, that is, in (2.24) and (2.25) $\gamma_{2b} \rightarrow 0$ is imposed, the prediction of the burning velocity fails at equivalence ratio above 0.35 just slightly before the failure of the steady-state assumption. The one-step mechanism can be applied for the description of near-limit fuel-lean flames under wide range of conditions of pressure and initial temperature, including, for instance, subatmospheric pressures and cryogenic H_2-O_2 deflagrations, of interest in cryogenic rocket engines [1].

Near the lean flammability limit hydrogen-air and hydrogen-oxygen flames exhibit an extended preheat zone followed by a thin reaction zone, the structure of which is analyzed in chapter 3 as an asymptotic expansion in a small parameter ε representing the order of magnitude of the ratio of the H-atom concentration to the H_2 concentration in that zone. The analysis demonstrated

that throughout most of the reaction zone the reaction intermediates closely maintain chemical-kinetic steady states, resulting in the one-step approximation for the combustion chemistry derived in chapter 2. The resulting non-Arrhenius rate formula was employed to derive an expression for the burning rate in terms of an integral that can be evaluated numerically, and the lean flammability limit was obtained as the condition that this burning rate is zero, a kinetically controlled limit associated with the burnt-gas temperature becoming equal to a crossover temperature at which the branching and termination rates become equal. Simplified explicit formulas for the burning rate also were derived which produce values of burning rates that agree reasonably well with burning rates calculated by evaluating the integral numerically or by employing detailed chemistry. It was found, in particular, that similar to earlier results [2], as the lean flammability limit is approached, the burning rate becomes proportional to the square of the difference between the adiabatic flame temperature and the crossover temperature, leading to an effective overall activation temperature of four times the square of the flame temperature divided by this temperature difference, thus approaching infinity at the lean limit.

The steady-state approximation was found to fail in a region where the temperature is near the crossover temperature, having thickness of order $\varepsilon^{1/3}$ times the total reaction-zone thickness. The approximation also fails near the hot boundary. In these failure regions a one-step approximation to the chemistry no longer exists. Burning-rate corrections associated with failure near the hot boundary are of order ε and turn out to be negligible. However, those associated with failure near crossover, of order $\varepsilon^{2/3}$, are more significant. Analysis of the layer near crossover revealed its character to be that of a corner layer, the structure of which can be expressed in terms of a universal solution previously obtained for diffusion flames at large Damköhler numbers. Use of this solution provides an explicit correction to the burning rate that improves agreement with results obtained from numerical integrations with detailed chemistry, especially near normal atmospheric pressure. Above atmospheric pressure, HO_2 increasingly contributes to the burning rate, so that the chemistry on which the present analysis is based becomes increasingly inaccurate.

Chapter 4 explores the structure of lean flames away from the flammability limit, where the H-atom concentration appears in appreciable amounts, thereby invalidating its steady-state assumption, which was used in deriving the one-step reduced mechanism of chapter 2. The analysis of this regime therefore requires consideration of a two-step mechanism, including a branch-

ing step

$$3H_2 + O_2 \rightleftharpoons 2H_2O + 2H \qquad \text{(I)}$$

and a recombination step

$$2H \rightarrow H_2, \qquad \text{(II)}$$

with global rates that are computed in terms of the elementary reactions. Different expressions were tested for the steady-state descriptions of the intermediates O and OH, including those following from introducing partial-equilibrium assumptions for the shuffle reactions 2 and 3, which are not very accurate on the upstream side of the flame but are useful in deriving simplified analytical results. The analysis reveals that the high sensitivity of the branching rate to small changes in temperature causes branching to occur only in a thin layer located at a temperature slightly above the crossover value, whereas recombination occurs in a distributed manner both upstream and downstream of this branching layer, in regions of thickness comparable to that of the flame. The solution in the outer convective-diffusive-reactive regions requires integration of two separate sets of differential equations for species and temperature, which need to be matched at the branching layer, where the gradients exhibit jumps as dictated by the stoichiometry of the branching reaction. The solution is coupled to that of the branching layer, which determines the branching temperature. Preliminary integrations provide results in reasonable agreement with integrations of the starting flame problem with detailed chemistry and transport descriptions.

5.2 Future prospects

Hydrogen is a clean energy carrier that can be produced from any primary energy source, including renewable sources. It is bound to become key in the solution of the energy supply problem for the present century, enabling clean efficient production of power and heat. Fuel cells are envisioned as a central component in many applications, providing an efficient conversion tool to produce electricity from the chemical oxidation of hydrogen. Also, direct combustion in internal combustion engines and gas turbines is currently considered of technological interest. Besides these technological applications for power generation, combustion is viewed as a fundamental issue in the development of the hydrogen economy, with safety concerns associated with acci-

dental explosion events entering when considering options for hydrogen storage. A better understanding of the hydrogen combustion processes is therefore necessary both to improve designs of hydrogen combustion devices and to develop safety regulations and counter-measures for explosion protection. Lean deflagrations, in particular, are of interest for gas-turbine applications and also for safety reasons, so that there exists clear interest in extending the work presented here.

Further improvement of the chemical-kinetic descriptions developed here would be worthwhile. For example, the manner in which steady-state accuracy is lost at higher equivalence ratios also merits further investigations. Preliminary study indicates that the transition from the one-step regime, treated in chapters 2 and 3 to the two-step regime of chapter 4 is not simple, and the associated chemical-kinetic complexities need further study, not only for improving understanding but also for deriving more accurate burning-rate and species-profile results, as well as chemical-kinetic descriptions, that can be used in future investigations of hydrogen-air deflagration structure, propagation and dynamics.

Future research could extend the present analysis to higher pressures, addressing more complex chemistry involving H_2O_2. The results that have been obtained here can, however, be employed directly to study deflagration problems of interest at normal atmospheric pressure, or at somewhat reduced pressures. Improvements of the chemical-kinetic mechanisms presented here to enable computations of other combustion phenomena such as diffusion flames, detonations and autoignition could be particularly useful for computational purposes.

Consideration of other fuels containing hydrogen in appreciable proportions, such as that obtained from coal and biomass gasification, are likely to play a predominant role in any foreseeable energy supply system, in particular in connection with IGCC (integrated gasification combined cycle) applications, therefore justifying also additional interest in combustion of hydrogen in the presence of non-negligible amounts of CO, CO2 and water vapor. Specific work is required to develop short-chemistry and reduced-chemistry descriptions for such mixtures.

Besides being useful in computational studies, including DNS and LES applications, the one-step mechanism can facilitate future analytical work. Investigations of the stability of planar flames and of the structure of nonplanar flames near the lean limit can make good use of the one-step results. It is well known that lean hydrogen flames exhibit strong diffusive-thermal instabilities

[3], and nonplanar models for deflagration structures under such conditions have been investigated [4]. Burning-rate and flammability-limit descriptions are needed for analyzing the stability and dynamics of the deflagrations that occur in these lean mixtures. Analyses in the past have generally been based on one-step activation-energy asymptotics, an approach that is merely phenomenological and is not based directly on the underlying chemistry that actually is occurring. The present results now enable these analyses to be revised and tied to the real chemistry. The future studies must take into account effects of curvature and strain. The forms of the results developed here can be readily employed in such studies, enabling the future investigations to focus on the transport and flow aspects of the problem, with the chemistry restricted to the interiors of surfaces whose properties have been obtained here. The present results can be employed directly in this future work, whether it is analytical or computational, so long as gradients downstream from the reaction zones investigated here are not steep enough to affect their structures.

For instance, effects of strain could be addressed by consideration of premixed flames in a counterflow configuration in which a fresh mixture flows against a nonreacting stream or a stream of combustion products. For weak values of the strain rate smaller than the reciprocal of the residence time across the flame, the flame lies on the fresh side outside the mixing layer, so that the structure of the reaction layer becomes independent of the product-side temperature. In obtaining the solution, the reaction zone could be treated as a discontinuity, with vanishing downstream gradients and with upstream gradients towards the fresh side given in (3.9) in terms of the burning rate. In this case, the burning-rate computations presented above could be employed directly to close the problem. Note that for these weakly strained flames, differential diffusion of hydrogen enters in the preheat region, resulting in a value of the burnt temperature above the adiabatic flame temperature of the fresh mixture. As a result, stretched flames may be anticipated to exist for equivalence ratios below the kinetically controlled lean flammability limit of freely propagating planar flames. As the strain rate increases, the reaction zone moves into the mixing layer; in nonadiabatic configurations with reduced product-side temperatures, downstream heat loss from the reaction zone may then become important, reducing the burnt temperature, which may approach the crossover value, thereby leading to strain-induced extinction.

Effects of curvature should also be considered. In particular, the investigation of flame balls near extinction conditions could employ the one-step results presented here, enabling the development of realistic analytical de-

scriptions aimed at clariying the interplay of radiation and thermal diffusion with the underlying chemistry.

Future investigations of the type outlined above for stretched flames, as well as investigations of curved flames, can therefore benefit from the present results. The associated research efforts would be relevant to safety issues associated with increased utilization of hydrogen as well as to the operation and performance of devices that employ the combustion of hydrogen.

References

[1] L. He, P. Clavin, Premixed hydrogen-oxygen flames. part I: Flame structure near the flammability limits, Combust. Flame 93 (1993) 391–407.

[2] K. Seshadri, N. Peters, F. A. Williams, Asymptotic analysis of stoichiometric and lean hydrogen-air flames, Combust. Flame 96 (1994) 407–427.

[3] H. F. Coward, F. Brinsley, The dilution limits of inflammability of gaseous mixtures, Ann. Rev. Fluid Mech. 105 (1914) 1859–1866.

[4] F. A. Williams, J. F. Grcar, A hypothetical burning-velocity formula for very lean hydrogen-air mixtures, Proc. Combust. Inst. 32 (2009) 1351–1357.

APPENDIX

A

The San Diego 21-step Mechanism

Table A.1: Rate coeffients in Arrhenius form $k = AT^n \exp(-E/R^oT)$ as given in [1]. (**NOTE** that the numbering herein corresponds to that in [2]).

N°.	Reaction		A[a]	n	E[a]
1.	$H + O_2 \rightleftharpoons OH + O$		3.52×10^{16}	-0.7	71.42
2.	$H_2 + O \rightleftharpoons OH + H$		5.06×10^{4}	2.67	26.32
3.	$H_2 + OH \rightleftharpoons H_2O + H$		1.17×10^{9}	1.3	15.21
4.	$H_2O + O \rightleftharpoons 2OH$		7.06×10^{0}	3.84	53.47
5.	$2H + M \rightleftharpoons H_2 + M$[b]		1.30×10^{18}	-1.0	0.0
6.	$H + OH + M \rightleftharpoons H_2O + M$[b]		4.00×10^{22}	-2.0	0.0
7.	$2O + M \rightleftharpoons O_2 + M$[b]		6.17×10^{15}	-0.5	0.0
8.	$H + O + M \rightleftharpoons OH + M$[b]		4.71×10^{18}	-1.0	0.0
9.	$O + OH + M \rightleftharpoons HO_2 + M$[b]		8.30×10^{14}	0.0	0.0
10.	$H + O_2 + M \rightleftharpoons HO_2 + M$[c]	k_0	5.75×10^{19}	-1.4	0.0
		k_∞	4.65×10^{12}	0.44	0.0
11.	$HO_2 + H \rightleftharpoons 2OH$		7.08×10^{13}	0.0	1.23
12.	$HO_2 + H \rightleftharpoons H_2 + O_2$		1.66×10^{13}	0.0	3.44
13.	$HO_2 + H \rightleftharpoons H_2O + O$		3.10×10^{13}	0.0	7.20
14.	$HO_2 + O \rightleftharpoons OH + O_2$		2.00×10^{13}	0.0	0.0
15.	$HO_2 + OH \rightleftharpoons H_2O + O_2$		2.89×10^{13}	0.0	-2.08
16.	$2OH + M \rightleftharpoons H_2O_2 + M$[d]	k_0	2.30×10^{18}	-0.9	-7.12
		k_∞	7.40×10^{13}	-0.37	0.0
17.	$2HO_2 \rightleftharpoons H_2O_2 + O_2$		3.02×10^{12}	0.0	5.8
18.	$H_2O_2 + H \rightleftharpoons HO_2 + H_2$		4.79×10^{13}	0.0	33.3
19.	$H_2O_2 + H \rightleftharpoons H_2O + OH$		1.00×10^{13}	0.0	15.0
20.	$H_2O_2 + OH \rightleftharpoons H_2O + HO_2$		7.08×10^{12}	0.0	6.0
21.	$H_2O_2 + O \rightleftharpoons HO_2 + OH$		9.63×10^{6}	2.0	16.7

[a] Units are mol, s, cm^3, kJ, and K.

[b] Chaperon efficiencies are 2.5 for H_2, 12.0 for H_2O, and 1.0 for all other species.

[c] Chaperon efficiencies are 2.5 for H_2, 16.0 for H_2O, and 1.0 for all other species; Troe falloff with $F_c = 0.5$ [3]

[d] Chaperon efficiencies are 2.5 for H_2, 6.0 for H_2O, and 1.0 for all other species; $F_c = 0.265 \exp(-T/94\text{K}) + 0.735 \exp(-T/1756\text{K}) + \exp(-5182\text{K}/T)$

References

[1] P. Saxena, F. A. Williams, Testing a small detailed chemical-kinetic mechanism for the combustion of hydrogen and carbon monoxide, Combust. Flame 145 (2006) 316–323.

[2] http://maeweb.ucsd.edu/~combustion/cermech/ (2005).

[3] R. G. Gilbert, K. Luther, J. Troe, Theory of thermal unimolecular reactions in the fall-off range. II. Weak collisions rate constants, Ber. Bursenges. Phys. Chem. 87 (1983) 169–177.

APPENDIX

B

The pressure dependence of reaction $H + O_2 + M \rightarrow HO_2 + M$

Theoretical predictions of the lean flammability limit for planar deflagrations make use of the crossover temperature defined as the temperature at which the rates of the main branching and recombination reactions are equal. Reaction H + O_2 (+ M) $\overset{4f}{\rightarrow}$ HO_2 (+ M) involves the collision of three different molecules and, therefore, has a reaction-rate constant that depends on the pressure according to the Lindemann form

$$k = F\frac{k_0 C_M}{1 + k_0 C_M / k_\infty},$$

where the broadening factor F, which takes a unity value in the original Lindemann development, can be used to control de transition from the low pressure limit $k_0 C_M / k_\infty \ll 1$ (i.e., $k = k_0 C_M$) to the high pressure limit $k_0 C_M / k_\infty \gg 1$ (i.e., $k = k_\infty$). Different expressions for F have been proposed in the literature for the broadening factor, including that used in most commercial codes [1]

$$F = F_c^{\left\{1+\left[(\log\frac{k_0 C_M}{k_\infty}+c)/(n-d(\log\frac{k_0 C_M}{k_\infty}+c))\right]^2\right\}^{-1}},$$

where $n = 0.75 - 1.27\log F_c$, $c = -0.4 - 0.67\log F_c$, $d = 0.14$, and the central factor F_c is 0.5 for reaction $4f$. The function log defines the decimal logaritm. This last expression is employed in particular in all computations included in this dissertation. An alternative, more compact, form [2] is given by

$$F = F_c^{\left\{1+\left[n^{-1}(\log\frac{k_0 C_M}{k_\infty})\right]^2\right\}^{-1}},$$

where $n^{-1} \approx 0.8$, in good agreement with recent developments [3].

The above expressions, whose temperature variation is exhibited in Fig B.1, have been used in Fig B.2 in evaluating for two different temperatures the

variation of the constant k with pressure. As can be seen, departures of the broadening factor from unity significantly affect the transition between the two limiting values $k = k_0 C_M$ and $k = k_\infty$. In connection with our work, the computations reveal, in particular, that, although at the pressures considered here ($p < 10$ atm) reaction $4f$ is in the low pressure limit, in that $k_0 C_M / k_\infty \ll 1$, for an accurate computation of the crossover temperature the resulting reaction-rate constant must include the broadening factor according to $k = F k_0 C_M$, since $F - 1 \sim O\{[\log(k_0 C_M / k_\infty)]^{-2}\}$ is not entirely negligible at these pressures for the typical temperatures found in the reaction layer.

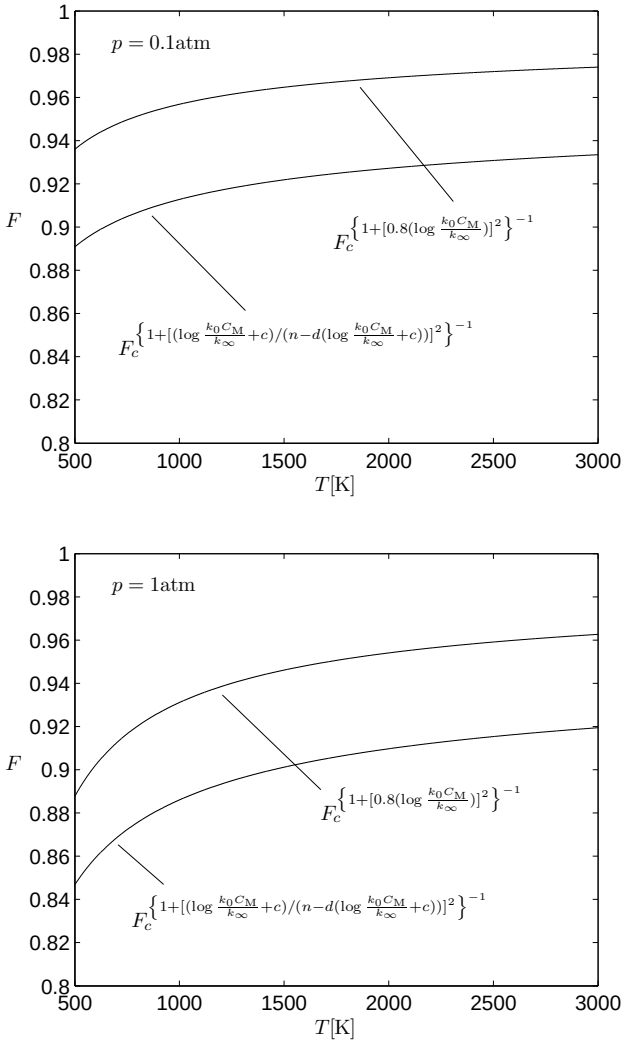

Figure B.1: The variation of the broadening factor F with the temperature for the recombination reaction H + O_2 (+ M) → HO_2 (+ M) at $p = 0.1$ atm (upper plot) and $p = 1$ atm (lower plot) evaluated from expressions given in [1] and [2].

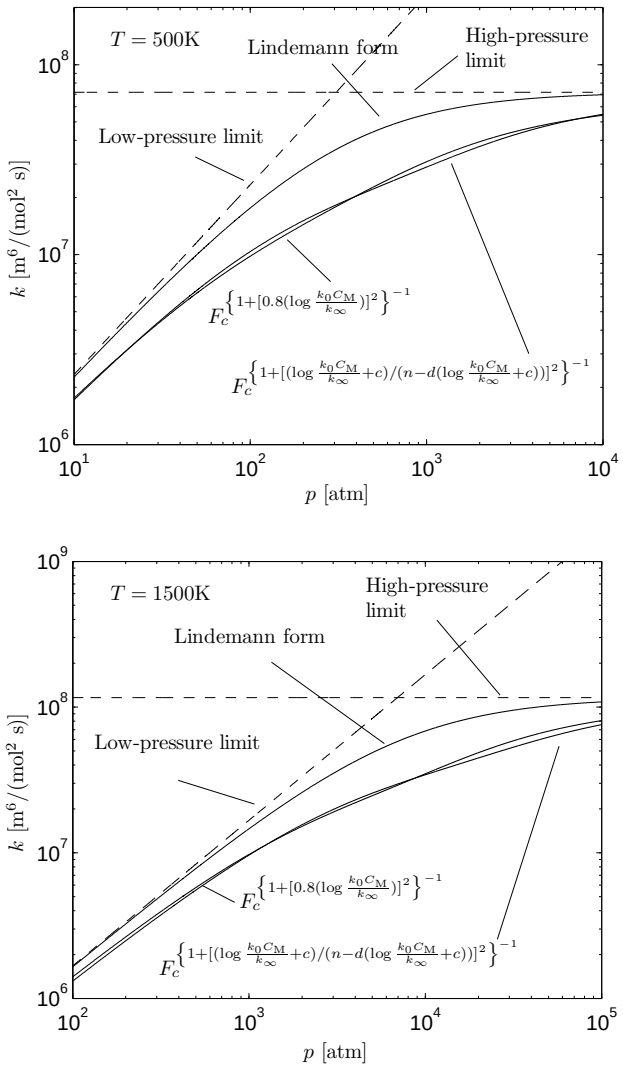

Figure B.2: The variation with pressure of the reaction-rate constant k for the recombination reaction H + O_2 (+ M) → HO_2 (+ M) at $T = 500$ K (upper plot) and $T = 1500$ K (lower plot) evaluated from expressions given in [1] and [2] for the boardening factor F.

References

[1] R. G. Gilbert, K. Luther, J. Troe, Theory of thermal unimolecular reactions in the fall-off range. II. Weak collisions rate constants, Ber. Bursenges. Phys. Chem. 87 (1983) 169–177.

[2] J. Troe, Predictive possibilities of unimolecular rate theory, J. Phys. Chem. 83 (1) (1979) 114–126.

[3] J. Troe, Detailed modeling of the temperature and pressure dependence of the reaction H + O_2 (+M) $\rightarrow$ HO_2 (+M), Proc. Combust. Inst. 28 (2000) 1463–1469.

APPENDIX

C

The steady-state expressions for the 8-step mechanism

As indicated in chapter 2, the description of the radicals O and OH given by the 7-step mechanism loses accuracy in flames close to the lean flammability limit. To correct this deficiency, it is necessary to include the shuffle reaction

$$H_2O + O \overset{8}{\rightleftharpoons} OH + OH \tag{C.1}$$

in the short mechanism of Table 1.1. When this is done, the resulting profiles of O and OH agree well with those calculated on the basis of the detailed chemistry, as can be seen in Fig. C.1 and also for diferent equivalence ratios in figures E.5, E.11, E.18, E.25, and E.33 of appendix E. In particular, the agreement of the O and OH profiles is much better than that seen in Fig. 1.3 for the 7-step mechanism; the agreement of the H profile in Fig. C.1 is so good that the solid and dashed curves cannot be distinguished. As mentioned before, the addition of reaction 8 does not affect significantly the H-atom profile, which remains practically unperturbed from that obtained with the 7-step mechanism, so that reaction 8 can be discarded for simplicity in computing the global rate of the one-step reduced kinetics, as is done in the main text. If, however, there is interest in the O and OH profiles under these conditions, then the further considerations given in this appendix become useful.

Inclusion of reaction 8 in the mechanism modifies the steady-state expressions for the radicals. The starting equations take the form

$$0 = \omega_1 - \omega_2 - \omega_8, \tag{C.2}$$

$$0 = \omega_1 + \omega_2 - \omega_3 + 2\omega_{5f} - \omega_{7f} + 2\omega_8, \tag{C.3}$$

$$0 = -\omega_1 + \omega_2 + \omega_3 - \omega_{4f} - \omega_{5f} - \omega_{6f}, \tag{C.4}$$

and

$$0 = \omega_{4f} - \omega_{5f} - \omega_{6f} - \omega_{7f}. \tag{C.5}$$

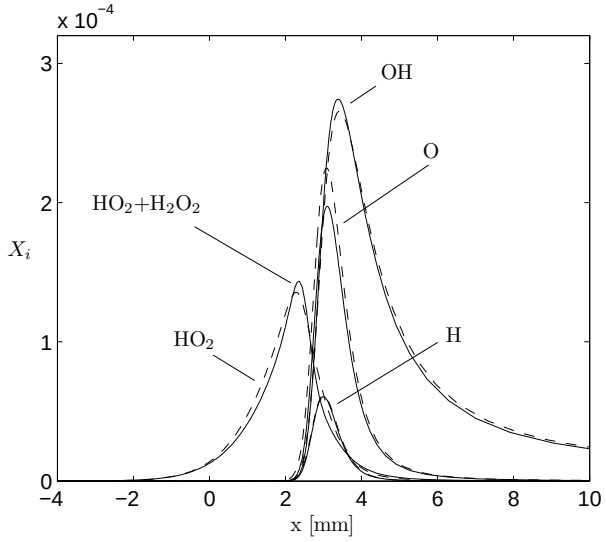

Figure C.1: Profiles of radical mole fractions in the flame, as obtained from detailed kinetics (solid curves) and from the 8-step mechanism (dashed curves) for $\phi = 0.3$, $p = 1$ atm and $T_u = 300$ K; the sum of the HO_2 and H_2O_2 mole fractions is shown for the detailed chemistry because H_2O_2 formation is absent in the short mechanism.

Appropriate manipulation then leads to the exact expressions

$$C_{\mathrm{O}} = \frac{\alpha f + \tilde{G}}{f + \tilde{G}} \frac{k_{3f} C_{\mathrm{H}_2}}{\tilde{G} k_{1b}} \left(\frac{k_{1f}}{k_{4f} C_{\mathrm{M}}} \frac{f + \tilde{G}}{\alpha f + \tilde{G}} - 1 \right), \tag{C.6}$$

$$C_{\mathrm{OH}} = \frac{1}{\tilde{H}} \frac{(k_{2f} C_{\mathrm{H}_2} + k_{8f} C_{\mathrm{H_2O}})}{k_{1b}} \left(\frac{k_{1f}}{k_{4f} C_{\mathrm{M}}} \frac{f + \tilde{G}}{\alpha f + \tilde{G}} - 1 \right) \tag{C.7}$$

$$C_{\mathrm{H}} = \frac{1}{\tilde{G}\tilde{H}} \frac{(k_{2f} C_{\mathrm{H}_2} + k_{8f} C_{\mathrm{H_2O}}) k_{3f} C_{\mathrm{H}_2}}{k_{1b} k_{4f} C_{\mathrm{M}} C_{\mathrm{O}_2}} \left(\frac{k_{1f}}{k_{4f} C_{\mathrm{M}}} \frac{f + \tilde{G}}{\alpha f + \tilde{G}} - 1 \right), \tag{C.8}$$

$$C_{\mathrm{HO}_2} = \frac{k_{3f}}{(f + \tilde{G}) k_{7f}} C_{\mathrm{H}_2}, \tag{C.9}$$

where the functions $\tilde{G}$ and $\tilde{H}$ are determined from the solution of the coupled equations

$$\tilde{H} = \frac{1}{2} + \frac{1}{2} \left[1 + 4 \left(\frac{\gamma_{2b} f}{1 - \gamma_{8f}} + \frac{\gamma_{8b} \tilde{G}}{f} \right) \frac{f + \tilde{G}}{\alpha f + \tilde{G}} \left(\frac{k_{1f}}{k_{4f} C_{\mathrm{M}}} \frac{f + \tilde{G}}{\alpha f + \tilde{G}} - 1 \right) \right]^{1/2} \tag{C.10}$$

and

$$\tilde{G} - \gamma_{3b} - \frac{\alpha f + \tilde{G}}{f + \tilde{G}} \gamma_{8f} \tilde{H} + \frac{\gamma_{8b} \tilde{G}}{f \tilde{H}} \left(\frac{k_{1f}}{k_{4f} C_{\mathrm{M}}} \frac{f + \tilde{G}}{\alpha f + \tilde{G}} - 1 \right) - \frac{2f + \tilde{G}}{f + \tilde{G}} = 0, \quad \text{(C.11)}$$

with

$$\gamma_{8f} = \frac{k_{8f} C_{\mathrm{H_2O}}}{k_{8f} C_{\mathrm{H_2O}} + k_{2f} C_{\mathrm{H_2}}} \quad \text{(C.12)}$$

and

$$\gamma_{8b} = \frac{k_{5f} + k_{6f}}{k_{7f}} \frac{k_{8b} (k_{8f} C_{\mathrm{H_2O}} + k_{2f} C_{\mathrm{H_2}})}{k_{1b} k_{4f} C_{\mathrm{M}} C_{\mathrm{O_2}}}. \quad \text{(C.13)}$$

It is easy to see that when $k_{8f} = k_{8b} = 0$ the solution reduces to $\tilde{H} = H$ and $\tilde{G} = G$, and the steady-state expressions of the 7-step mechanism given in (2.23), (2.27), (2.28) and (2.30) are recovered. By comparing the solid and dashed curves in Fig. C.2, where the temperature and concentrations of the main species are obtained from the 8-step mechanism, it is seen that the steady-state approximation is reasonably good for all four radicals under these conditions. Note that the O, OH and H concentrations given by (C.6)–(C.8) vanish at a crossover temperature defined by the equation

$$k_{1f} = \frac{\alpha f + \tilde{G}}{f + \tilde{G}} k_{4f} C_{\mathrm{M}}, \quad \text{(C.14)}$$

which differs from the expression (2.29) of the 7-step approximation, although their limiting forms at very lean conditions $k_{1f} = k_{4f} C_{\mathrm{M}}$ are identical, indicating that inclusion of reaction 8 does not modify the lean flammability results given in Fig. 2.4.

A disadvantage of Eqs. (C.6)–(C.9) is the necessity of solving complex algebraic equations numerically. Explicit expressions can be derived in the limit $C_{\mathrm{H_2}} \ll 1$ of small hydrogen concentrations, when the radicals concentrations achieve small values $C_{\mathrm{O}} \propto C_{\mathrm{H_2}}$, $C_{\mathrm{OH}} \propto C_{\mathrm{H_2}}^{1/2}$, $C_{\mathrm{H}} \propto C_{\mathrm{H_2}}^{3/2}$, and $C_{\mathrm{HO_2}} \propto C_{\mathrm{H_2}}$. Under those conditions, reaction 8 becomes faster than the others, and can be assumed to be in partial equilibrium, while reactions 2, $5f$ and $6f$ become negligibly slow, and can be correspondingly discarded in the steady-state equations (C.2)–(C.5). The problem reduces to that of solving the partial-equilibrium equation $\omega_8 = 0$, together with the ω_8-free linear combination of (C.2) and (C.3), $3\omega_1 - \omega_3 - \omega_{7f} = 0$, and with the simplified forms, $-\omega_1 +$

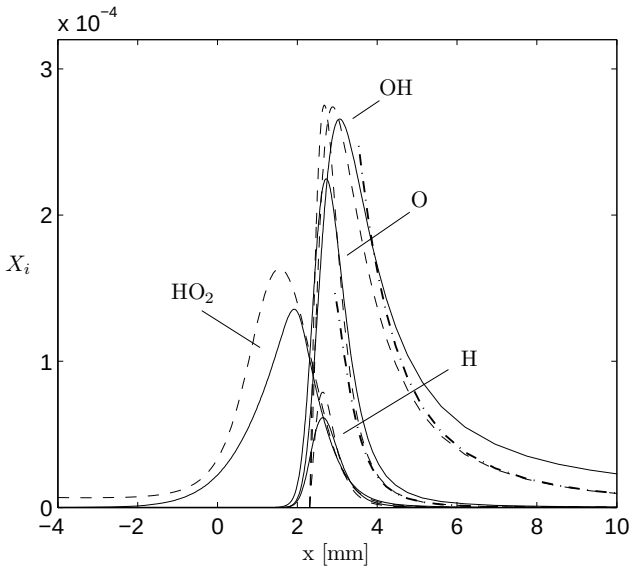

Figure C.2: Profiles of radical mole fractions in the flame as obtained with the 8-step mechanism (the 7-step mechanism augmented with the shuffle reaction 8) (solid curves), from numerical evaluations of the steady-state expressions (C.6)–(C.9) (dashed curves) and from use of the formulas (C.15) and (C.16) (dot-dashed curves), for $\phi = 0.3$, $p = 1$ atm and $T_u = 300$ K.

$\omega_3 - \omega_{4f} = 0$ and $\omega_{4f} - \omega_{7f} = 0$, of (C.4) and (C.5). The solution provides

$$C_{\mathrm{O}} = \frac{k_{3f} C_{\mathrm{H_2}}}{(2+\gamma_{3b}) k_{1b}} \left(\frac{k_{1f}}{k_{4f} C_{\mathrm{M}}} - 1 \right), \tag{C.15}$$

$$C_{\mathrm{OH}} = \left[\frac{k_{3f} k_{8f}}{k_{1b} k_{8b} (2+\gamma_{3b})} \left(\frac{k_{1f}}{k_{4f} C_{\mathrm{M}}} - 1 \right) \right]^{1/2} C_{\mathrm{H_2O}}^{1/2} C_{\mathrm{H_2}}^{1/2}, \tag{C.16}$$

$$C_{\mathrm{H}} = \left[\frac{k_{3f}^3 k_{8f}}{k_{1b} k_{8b} (2+\gamma_{3b})^3} \left(\frac{k_{1f}}{k_{4f} C_{\mathrm{M}}} - 1 \right) \right]^{1/2} \frac{C_{\mathrm{H_2O}}^{1/2} C_{\mathrm{H_2}}^{3/2}}{k_{4f} C_{\mathrm{M}} C_{\mathrm{O_2}}}, \tag{C.17}$$

and

$$C_{\mathrm{HO_2}} = \frac{k_{3f} C_{\mathrm{H_2}}}{k_{7f} (2+\gamma_{3b})}. \tag{C.18}$$

These simplified expressions become accurate for very small values of $C_{\mathrm{H_2}}$, as occurs for instance downstream from the reaction zone, where (C.15) and (C.16)

are seen to describe accurately the slow decay of the O and OH radicals, as shown by the dot-dashed curves in Fig. C.2.

Clearly, the above equations can be also obtained as the limiting forms of (C.6)–(C.9) for $C_{H_2} \ll 1$, when $\gamma_{8f} - 1 \ll 1$, $f \ll 1$, and, according to (C.10) and (C.11), $\tilde{G} = 2 + \gamma_{3b}$ and $\tilde{H} = \{\gamma_{8b}[k_{1f}/(k_{4f}C_M) - 1]\tilde{G}/f\}^{1/2}$. The need for the 8-step description of OH is apparent from Eq. (C.16), which becomes singular if reaction 8 is deleted from the mechanism. The intricacy of the algebra is illustrated by the observations that (C.15), which differs from (2.28), does not involve any rate parameters of reaction 8, even though that reaction and its rate parameters had to be included in its derivation, and that in all four denominators, the factor $2 + \gamma_{3b}$ differs from $1 + \gamma_{3b}$, the corresponding small-f limit of G in the 7-step mechanism.

Burning-velocity results can be derived from the 8-step mechanism that are quite similar to those obtained from the 7-step mechanism. In particular, agreements much like those seen in Fig. 2.5 are obtained. The analog of the approximation $H = 1$ for the 7-step mechanism is the formula for $\tilde{H}$ given in the preceding paragraph for the 8-step mechanism, and it leads to roughly comparable agreements. Since for near-lean flames the one-step approximation with $H = 1$ derived from the 7-step mechanism yields good results that are simpler than those of the 8-step mechanism, it qualifies as a better theory for the overall reaction rate.

APPENDIX

D

A model problem for the crossover layer

The analysis of (3.53) – (3.55) is not straightforward. In identifiying the associated scales and the required asymptotic procedure it is useful to consider the solution of the following model problem, in the limit $\varepsilon \to 0$

$$\varepsilon \frac{\mathrm{d}^2 Y}{\mathrm{d}X^2} = -Y(1+2X) + 2YZ + Z \tag{D.1}$$

$$\varepsilon \frac{\mathrm{d}^2 Z}{\mathrm{d}X^2} = Y - Z\,, \tag{D.2}$$

with boundary conditions

$$X \to -\infty \,:\, Y = Z = 0 \tag{D.3}$$

$$X \to +\infty \,:\, Y = Z = X\,, \tag{D.4}$$

which embodies the nonlinearities present in the original crossover problem. For $\varepsilon = 0$ two solutions are found

$$Y = Z = 0 \tag{D.5}$$

and

$$Y = Z = X\,. \tag{D.6}$$

In view of the boundary conditions it is clear that the first solution applies for $X \to -\infty$, whereas the second solution applies for $X \to +\infty$. The piecewise continuos solution $Y = Z = 0$ for $X < 0$ and $Y = Z = X$ for $X > 0$ satisfies the boundary conditions and the conservation equations everywhere, except at $X = 0$, where the second derivative on the left-hand side of (D.1) and (D.2) would become infinite, invalidating the solution. In determining the scales of the transition corner layer, where the diffusion terms are important, it is useful

to consider the equation resulting from adding (D.1) and (D.2), a combination that eliminates the leading linear terms on the right-hand side to yield

$$\varepsilon \frac{\mathrm{d}^2}{\mathrm{d}X^2}(Y+Z) = -2YX + 2YZ\,. \tag{D.7}$$

Anticipating that $Y \sim Z \sim X$, as follows from matching with the downstream solution (D.4), the result $Y \sim Z \sim X \sim \varepsilon^{1/3}$ then follows from imposing that diffusive transport be important in (D.7).

In terms of rescaled variables $y = \varepsilon^{-1/3}Y$ and $z = \varepsilon^{-1/3}Z$, and the rescaled coordinate $x = \varepsilon^{-1/3}X$, the problem reduces to that of integrating

$$\varepsilon^{1/3}\frac{\mathrm{d}^2 y}{\mathrm{d}x^2} = -y + z + (2yz - 2yx)\varepsilon^{1/3} \tag{D.8}$$

$$\varepsilon^{1/3}\frac{\mathrm{d}^2 z}{\mathrm{d}x^2} = y - z\,, \tag{D.9}$$

with boundary conditions $y = z = 0$ as $x \to -\infty$ and $y = z = x$ as $x \to +\infty$. Introducing the expansions $y = y_0 + \varepsilon^{1/3}y_1 + \ldots$ and $z = z_0 + \varepsilon^{1/3}z_1 + \ldots$ yields at leading order

$$y_0 = z_0\,, \tag{D.10}$$

while the solution at the following order comes from

$$\frac{\mathrm{d}^2 y_0}{\mathrm{d}x^2} = -y_1 + z_1 + 2y_0 z_0 - 2y_0 x \tag{D.11}$$

$$\frac{\mathrm{d}^2 z_0}{\mathrm{d}x^2} = y_1 - z_1\,. \tag{D.12}$$

To find the leading-order term in the expansion we consider the equation resulting from adding the last two equations, as suggested by the linear combination (D.7), to give

$$\frac{\mathrm{d}^2}{\mathrm{d}x^2}(y_0 + z_0) = 2y_0(z_0 - x) \tag{D.13}$$

which, after using (D.10), finally becomes

$$\frac{\mathrm{d}^2 y_0}{\mathrm{d}x^2} = y_0(y_0 - x)\,, \tag{D.14}$$

with boundary conditions $y_0(-\infty) = 0$ and $y_0(+\infty) = x$. This problem is identical to Liñán's seminal problem (3.65), obtained for the crossover layer in the main text.

APPENDIX

E

Species, temperature and reaction-rate profiles

The figures in this appendix show profiles of mol fractions X_i ($i = H_2$, O_2, H_2O, H, OH, O, HO_2, and H_2O_2), temperature T and rates of elementary reactions across H_2-air flames as computed with the COSILAB code [1] for different chemistry and transport descriptions, including 21-step detailed chemistry with and without thermal diffusion, 7-step short chemistry in chapter 2, 8-step short chemistry developed in appendix C, 9-step short chemistry included in chapter 4 and the one-step reduced mechanism of chapter 2 together with the two-step reduced mechanism based on the truncated expresion for γ_{OH} (4.9) in chapter 4. **NOTE** that the numbering of the rates j in the figures below corresponds to the original form in [2] and therefore differs from that in Table 1.1.

References

[1] Version 2.0.7, Rotexo-Softpredict-Cosilab Gmbh & Co. KG, http://www.SoftPredict.com (2007).

[2] http://maeweb.ucsd.edu/~combustion/cermech/ (2005).

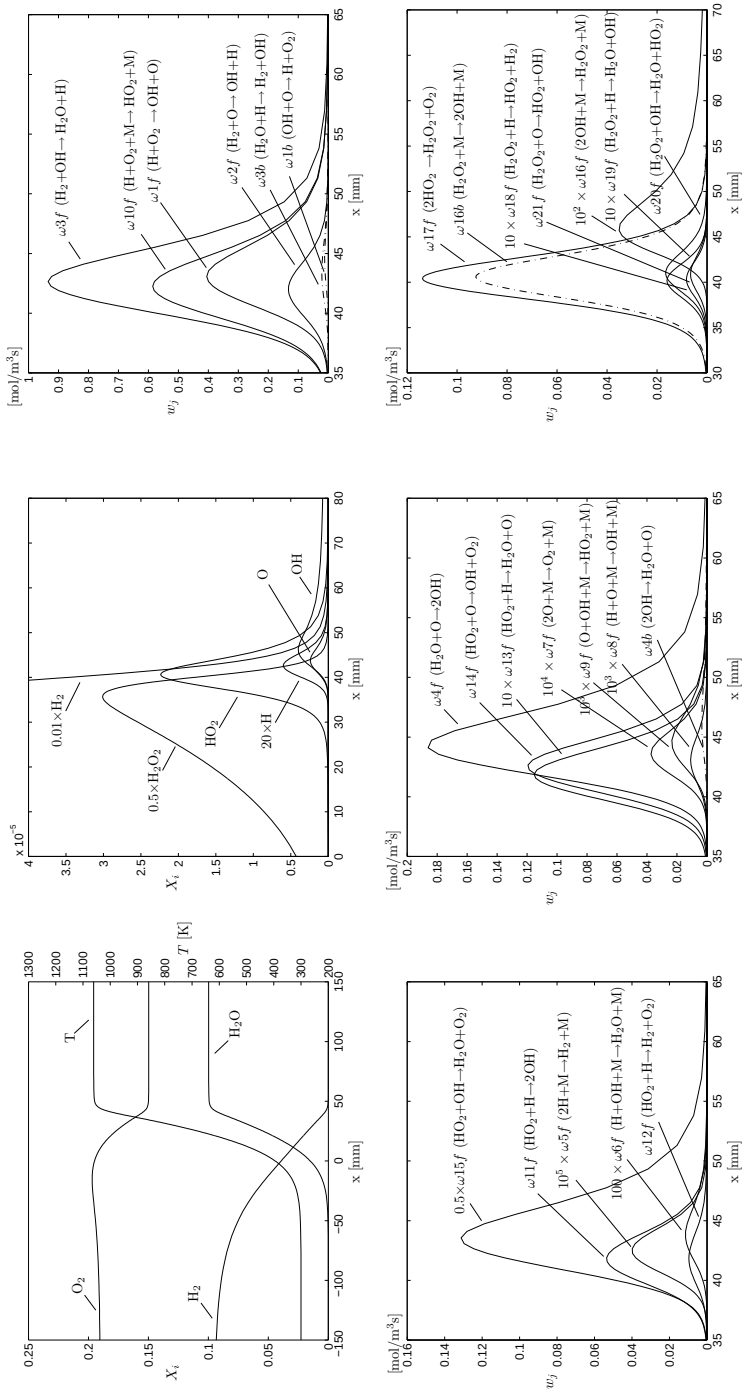

Figure E.1: Equivalence ratio $\phi = 0.25$, detailed mechanism (Table A.1) at $p = 1$ atm and $T_u = 300$ K.

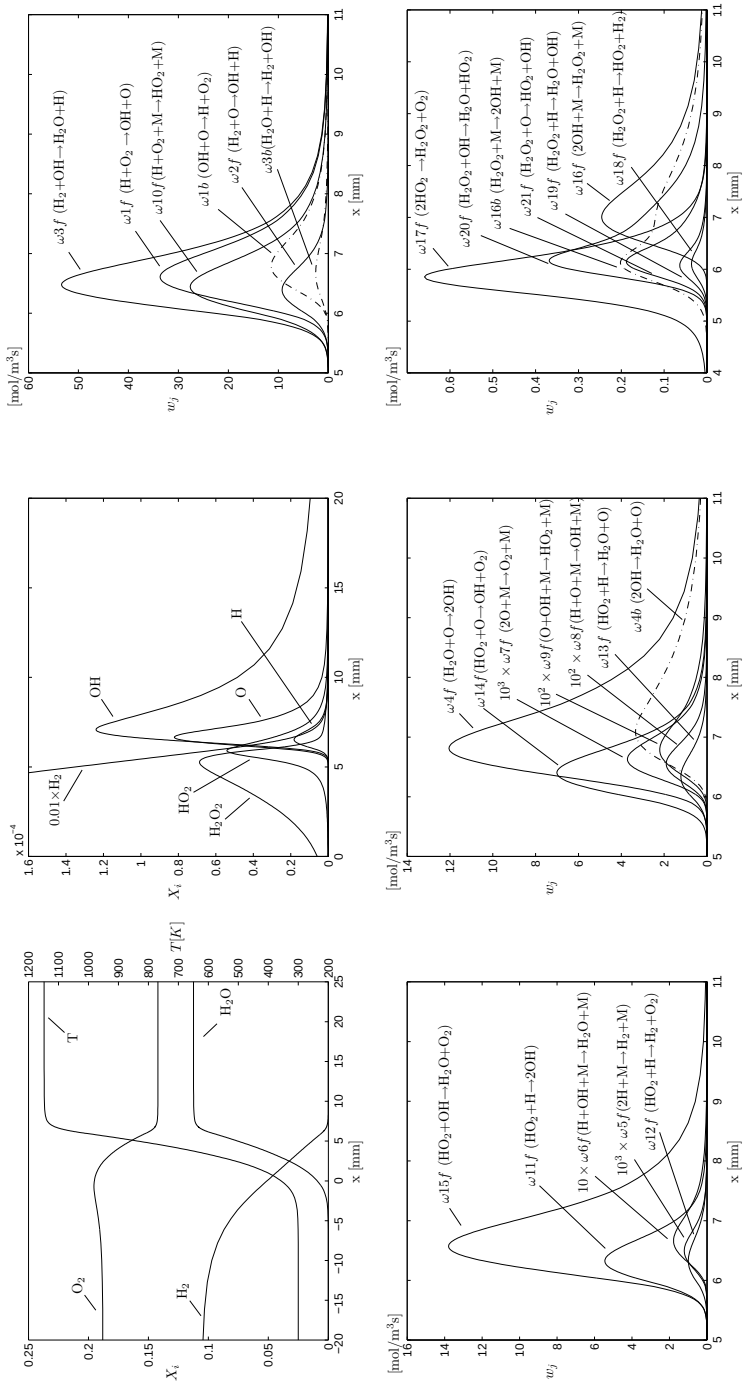

Figure E.2: Equivalence ratio $\phi = 0.28$, detailed mechanism (Table A.1) at $p = 1$ atm and $T_u = 300$ K.

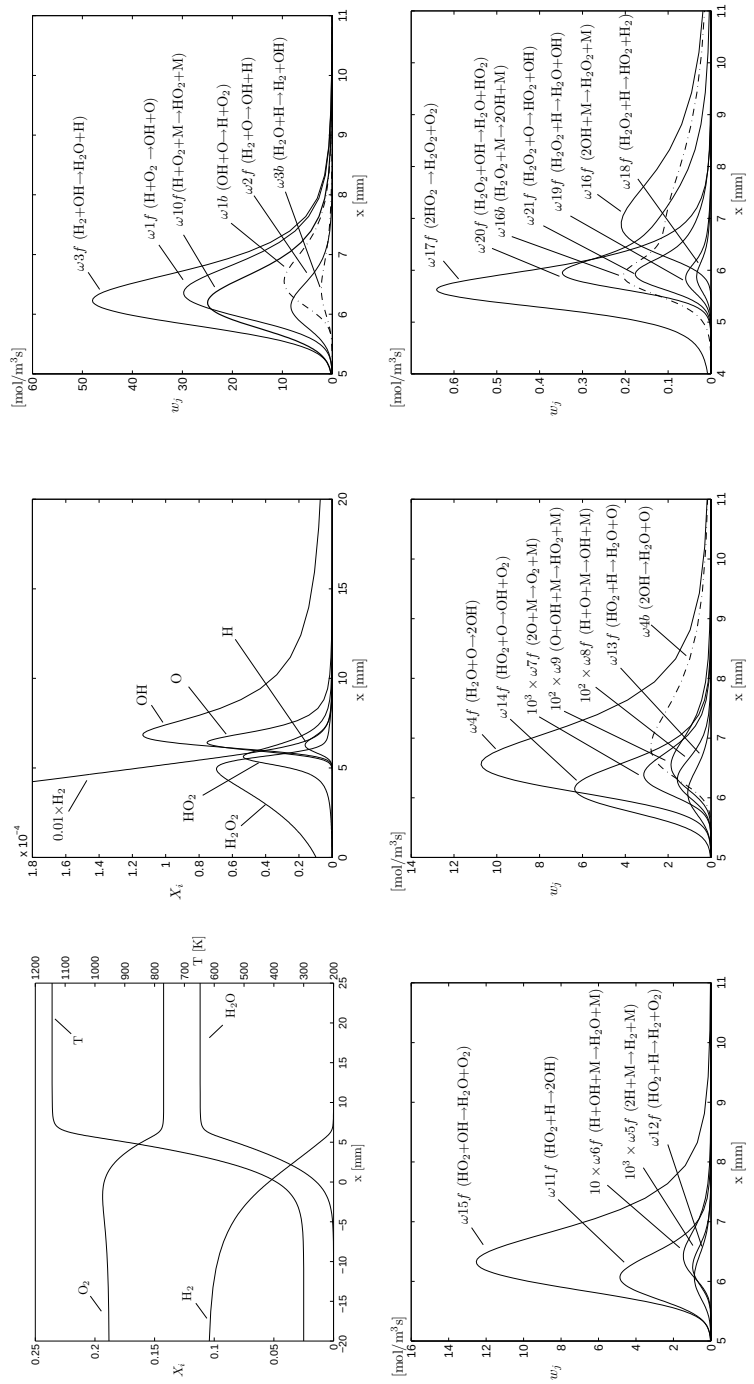

Figure E.3: Equivalence ratio $\phi = 0.28$, detailed mechanism (Table A.1) with thermal diffusion excluded at $p = 1$ atm and $T_u = 300$ K.

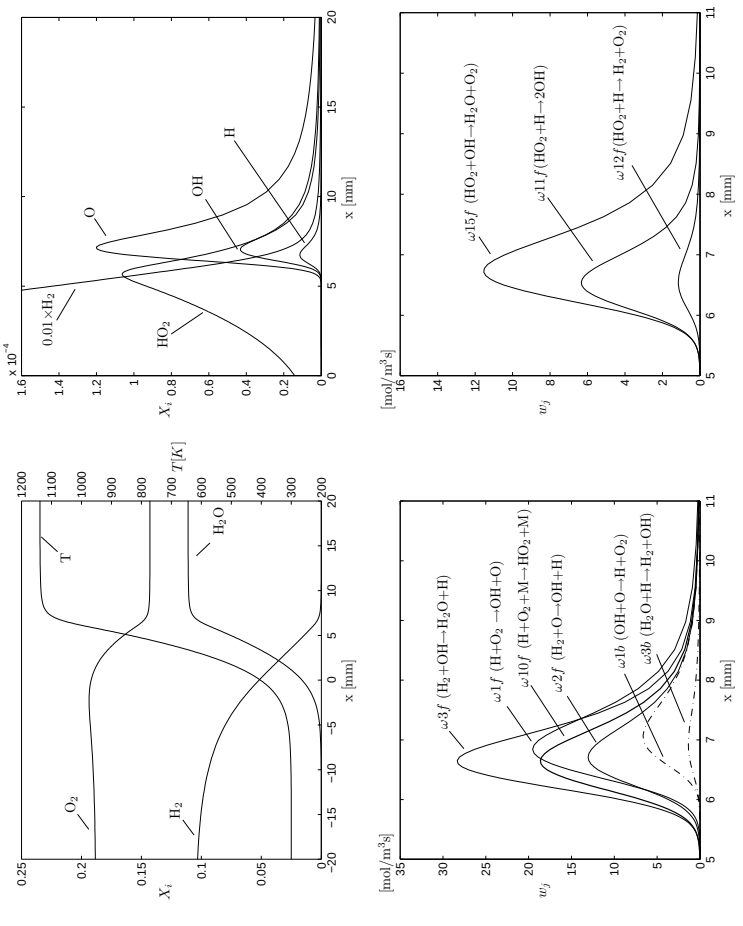

Figure E.4: Equivalence ratio $\phi = 0.28$, 7-step reduced mechanism at $p = 1$ atm and $T_u = 300$ K.

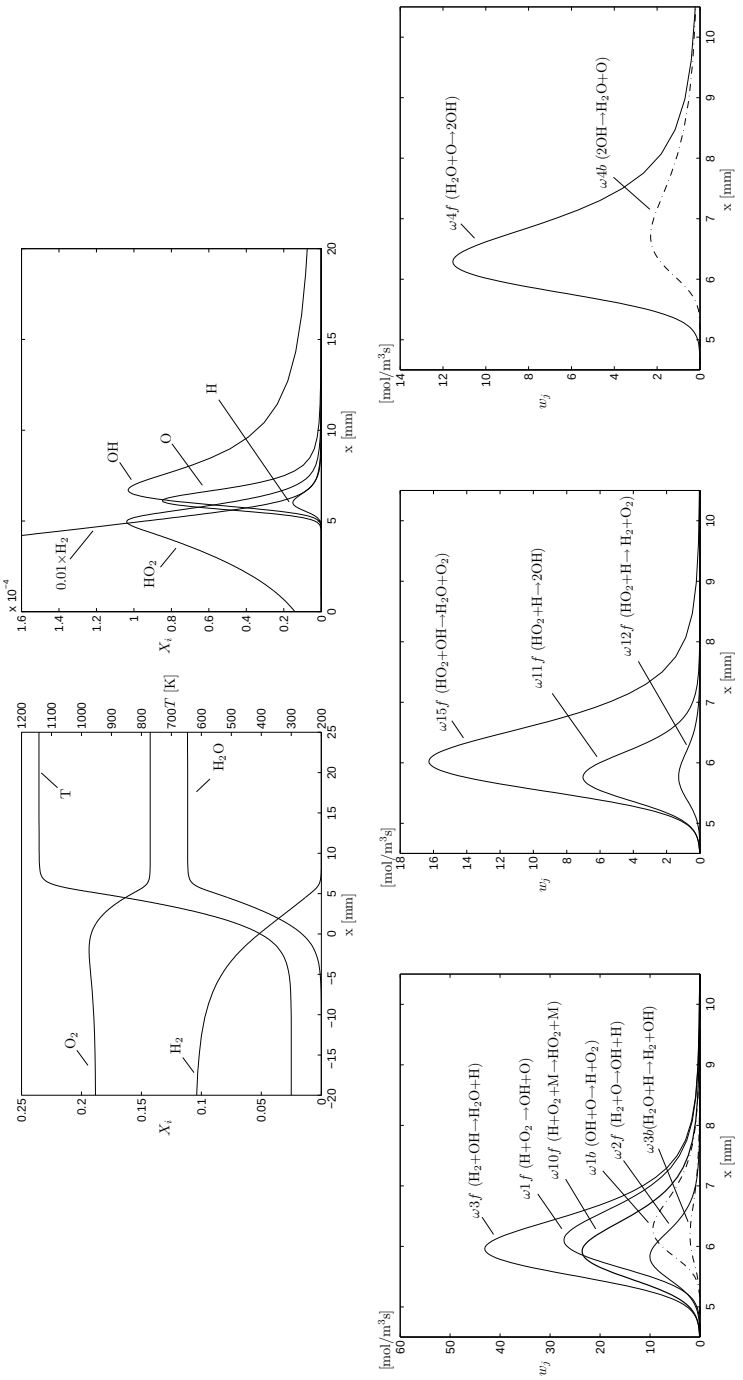

Figure E.5: Equivalence ratio $\phi = 0.28$, 8-step reduced mechanism (appendix C) at $p = 1$ atm and $T_u = 300$ K.

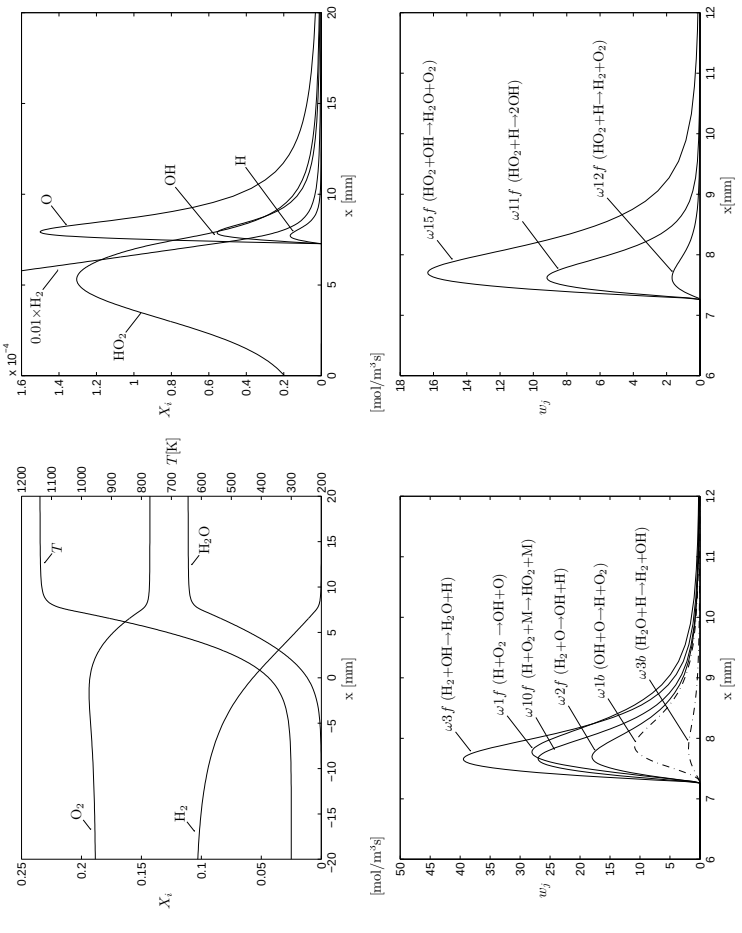

Figure E.6: Equivalence ratio $\phi = 0.28$, one-step reduced mechanism at $p = 1$ atm and $T_u = 300$ K.

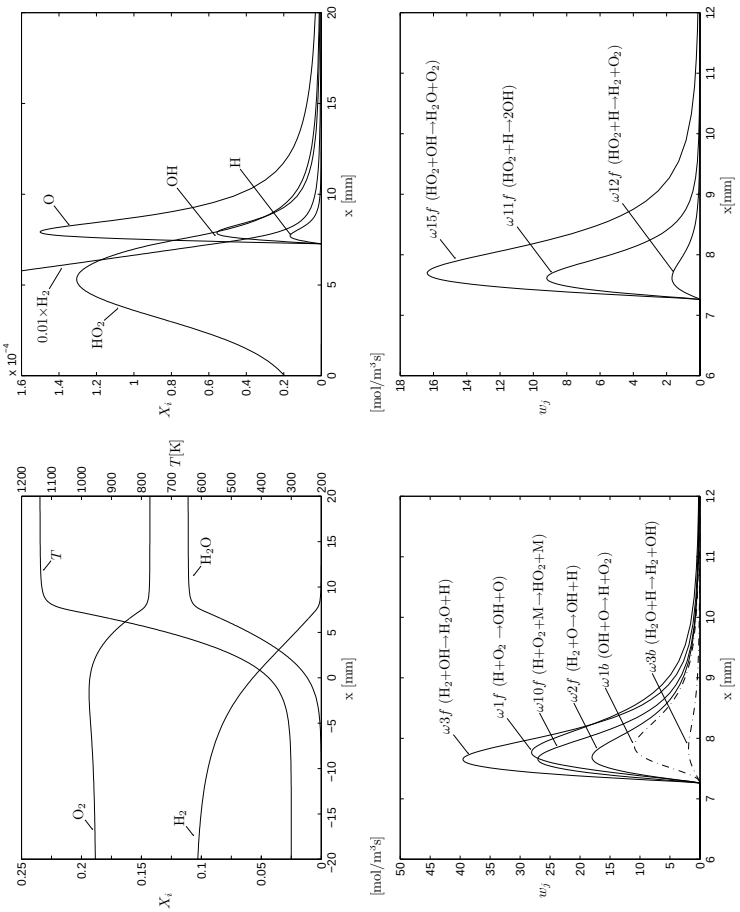

Figure E.7: Equivalence ratio $\phi = 0.28$, one-step reduced mechanism excluding reaction $2b$ ($H = 1$) at $p = 1$ atm and $T_u = 300$ K.

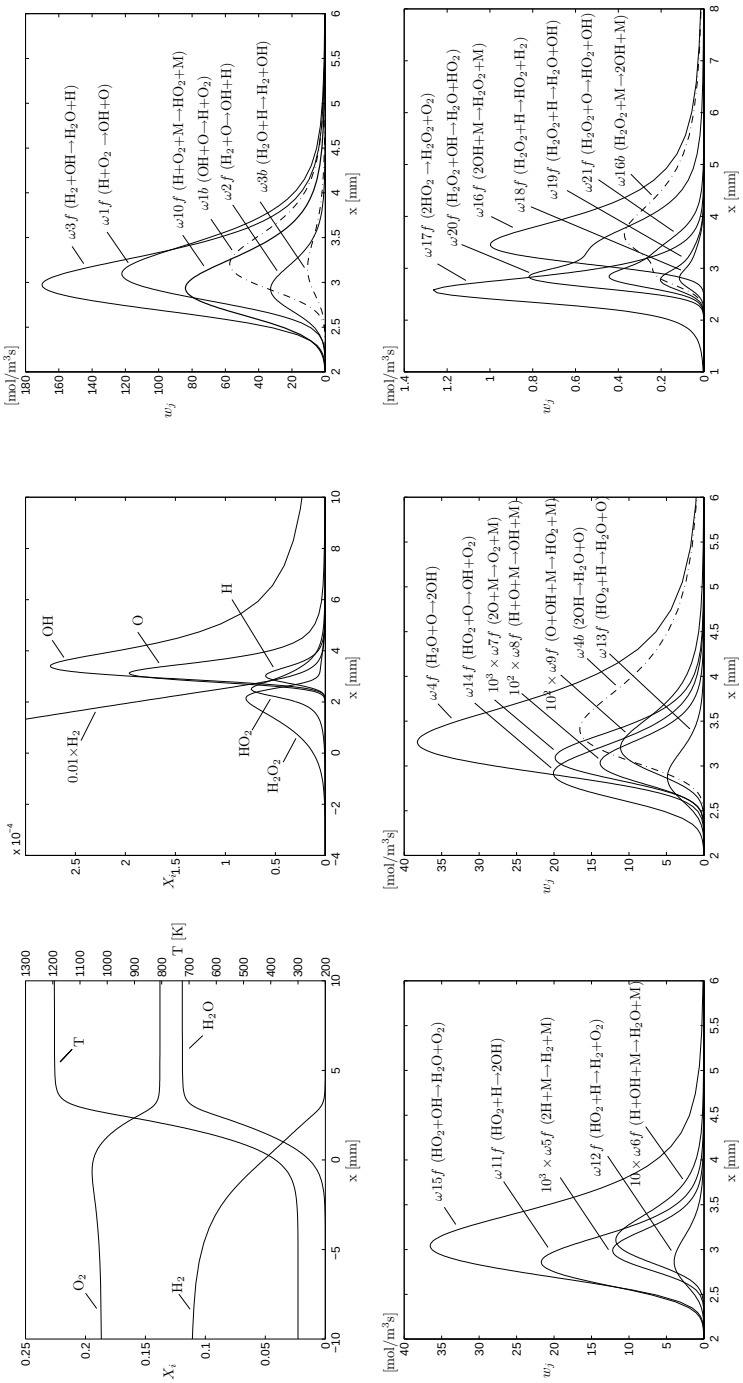

Figure E.8: Equivalence ratio $\phi = 0.3$, detailed mechanism (Table A.1) at $p = 1$ atm and $T_u = 300$ K.

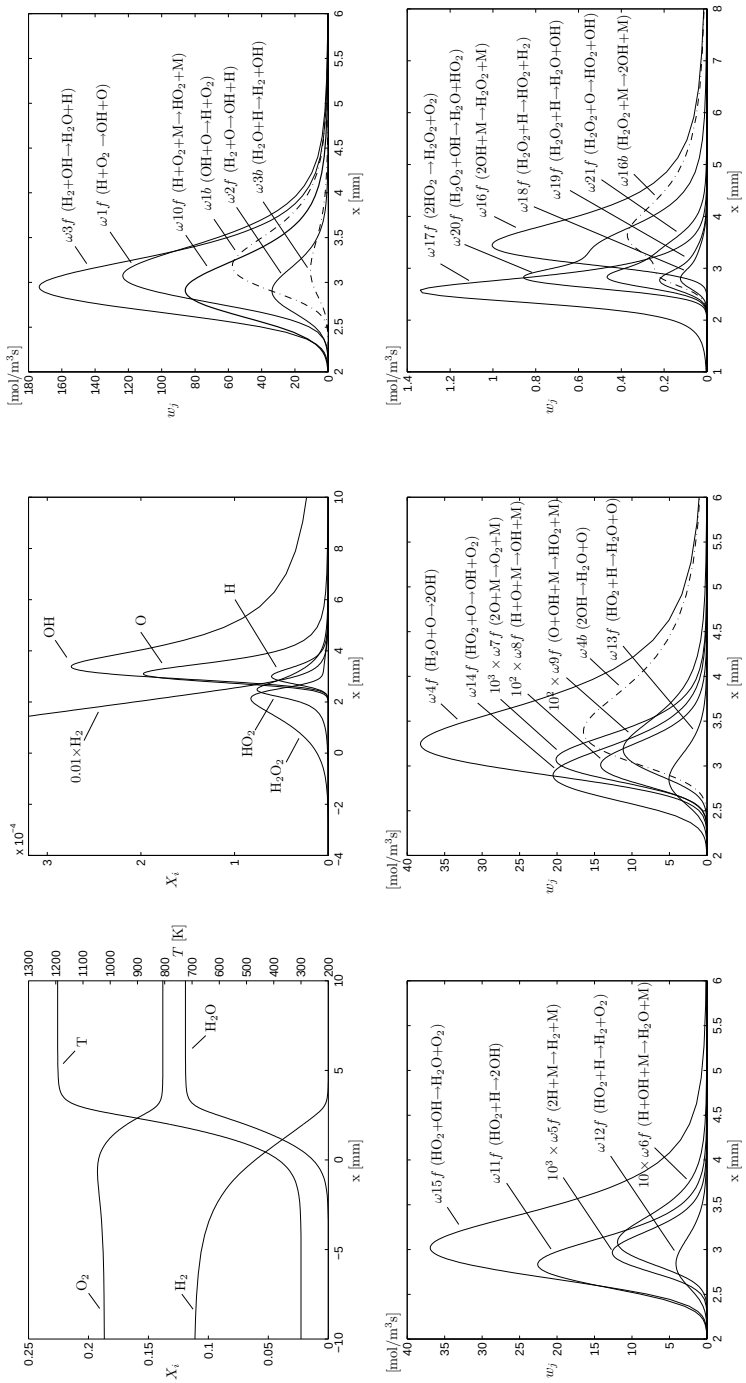

Figure E.9: Equivalence ratio $\phi = 0.3$, detailed mechanism (Table A.1) with thermal diffusion excluded at $p = 1$ atm and $T_u = 300$ K.

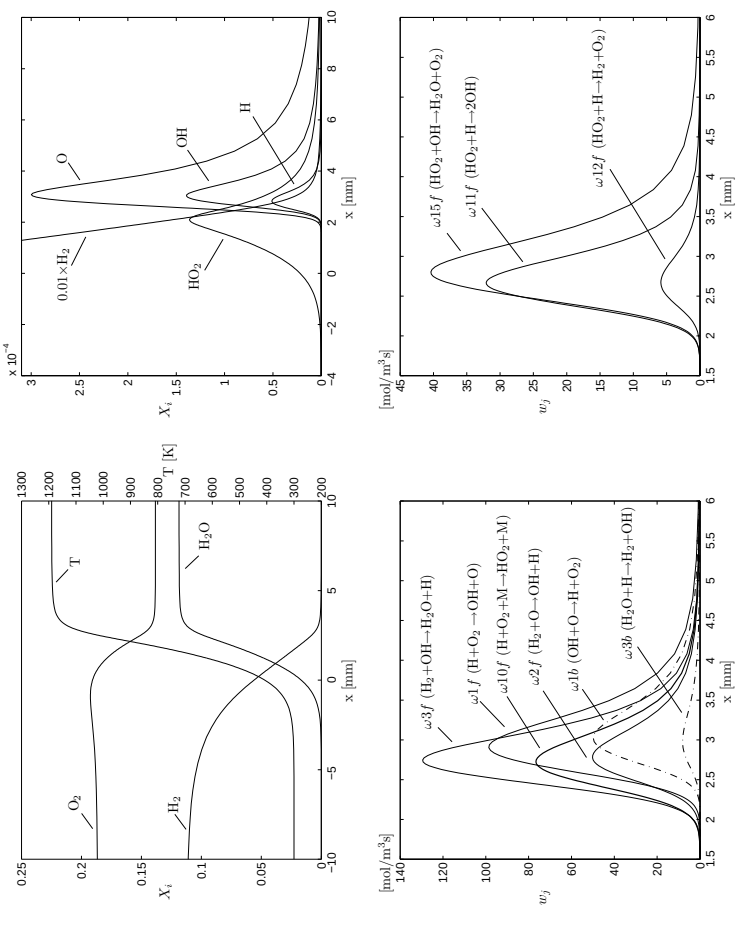

Figure E.10: Equivalence ratio $\phi = 0.3$, 7-step reduced mechanism at $p = 1$ atm and $T_u = 300$ K.

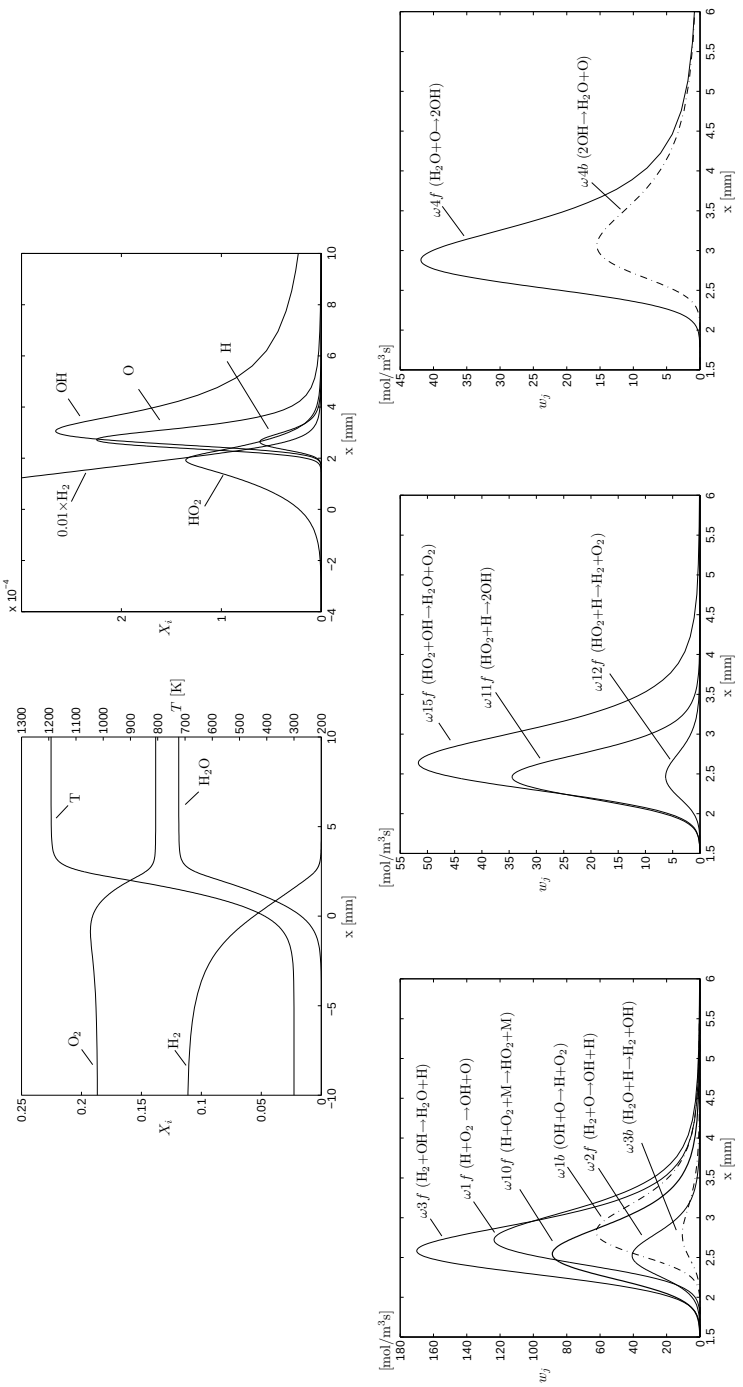

Figure E.11: Equivalence ratio $\phi = 0.3$, 8-step reduced mechanism (appendix C) at $p = 1$ atm and $T_u = 300$ K.

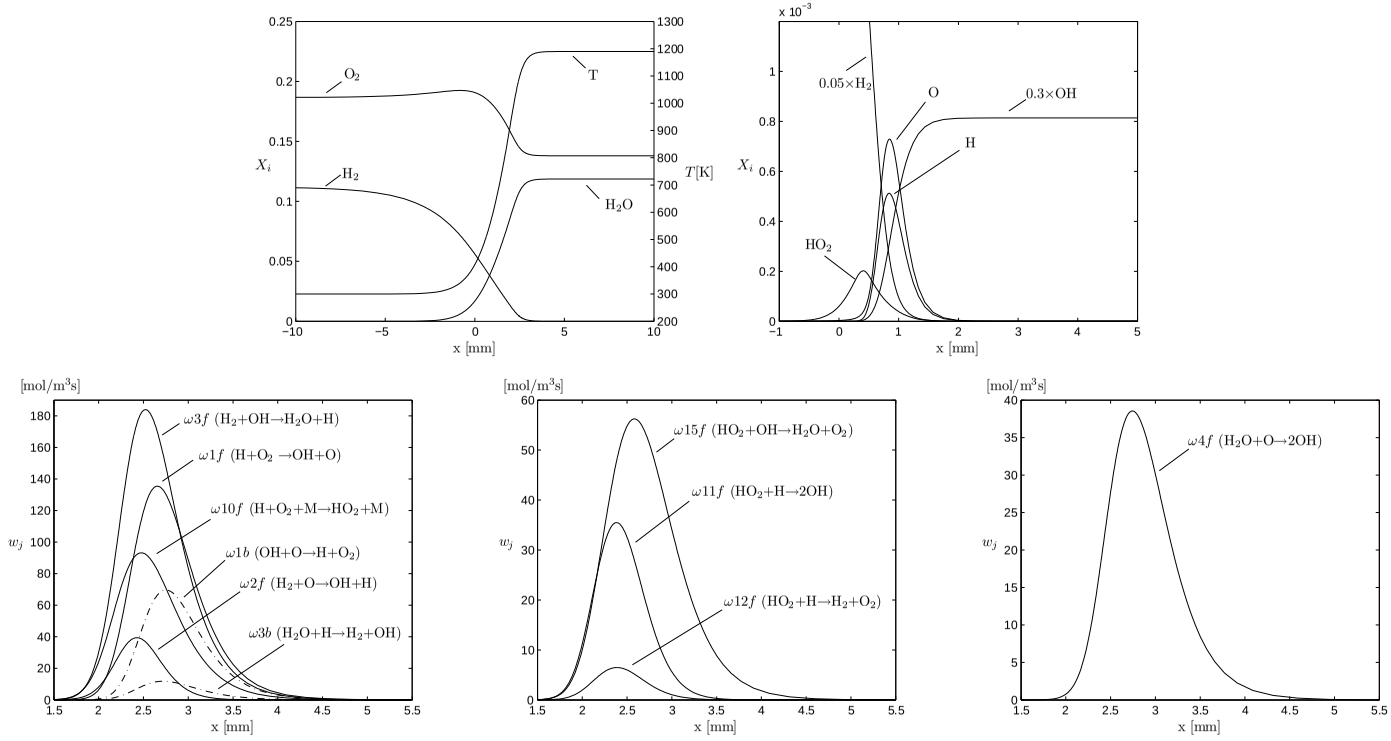

Figure E.12: Equivalence ratio $\phi = 0.3$, 7-step mechanism plus the forward shuffle reaction $H_2O + O \rightarrow OH + OH$ at $p = 1$ atm and $T_u = 300$ K.

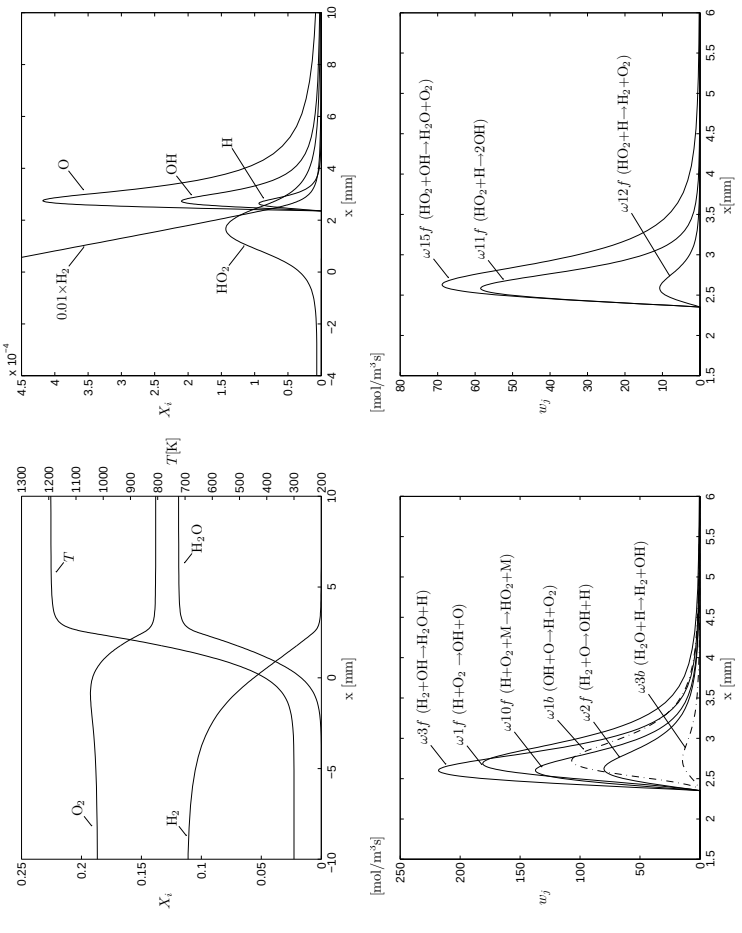

Figure E.13: Equivalence ratio $\phi = 0.3$, one-step reduced mechanism at $p = 1$ atm and $T_u = 300$ K.

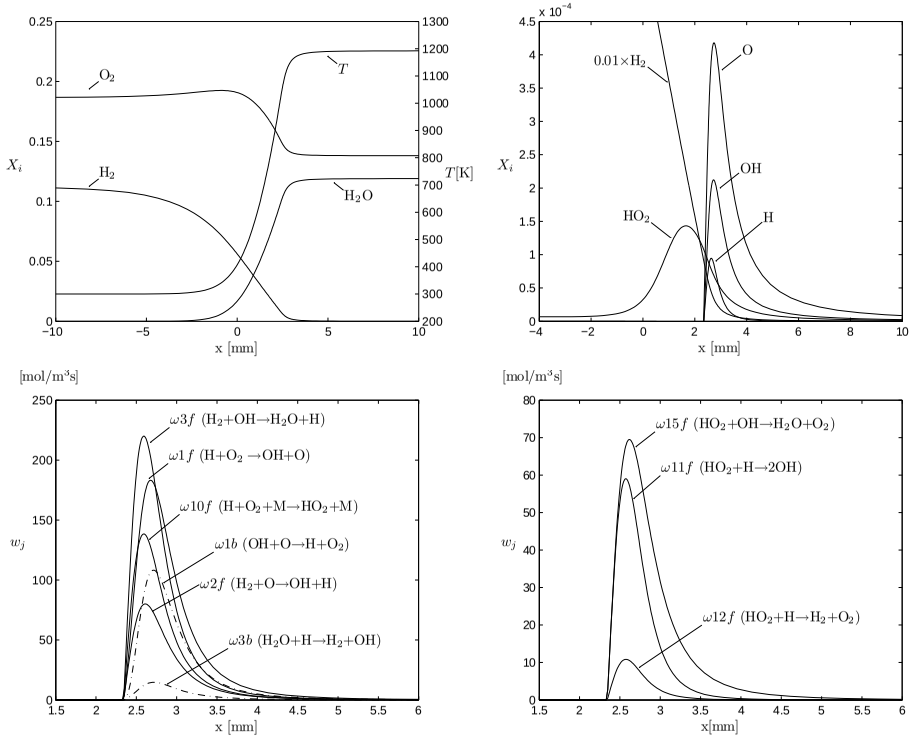

Figure E.14: Equivalence ratio $\phi = 0.3$, one-step reduced mechanism excluding reaction $2b$ ($H = 1$) at $p = 1$ atm and $T_u = 300$ K.

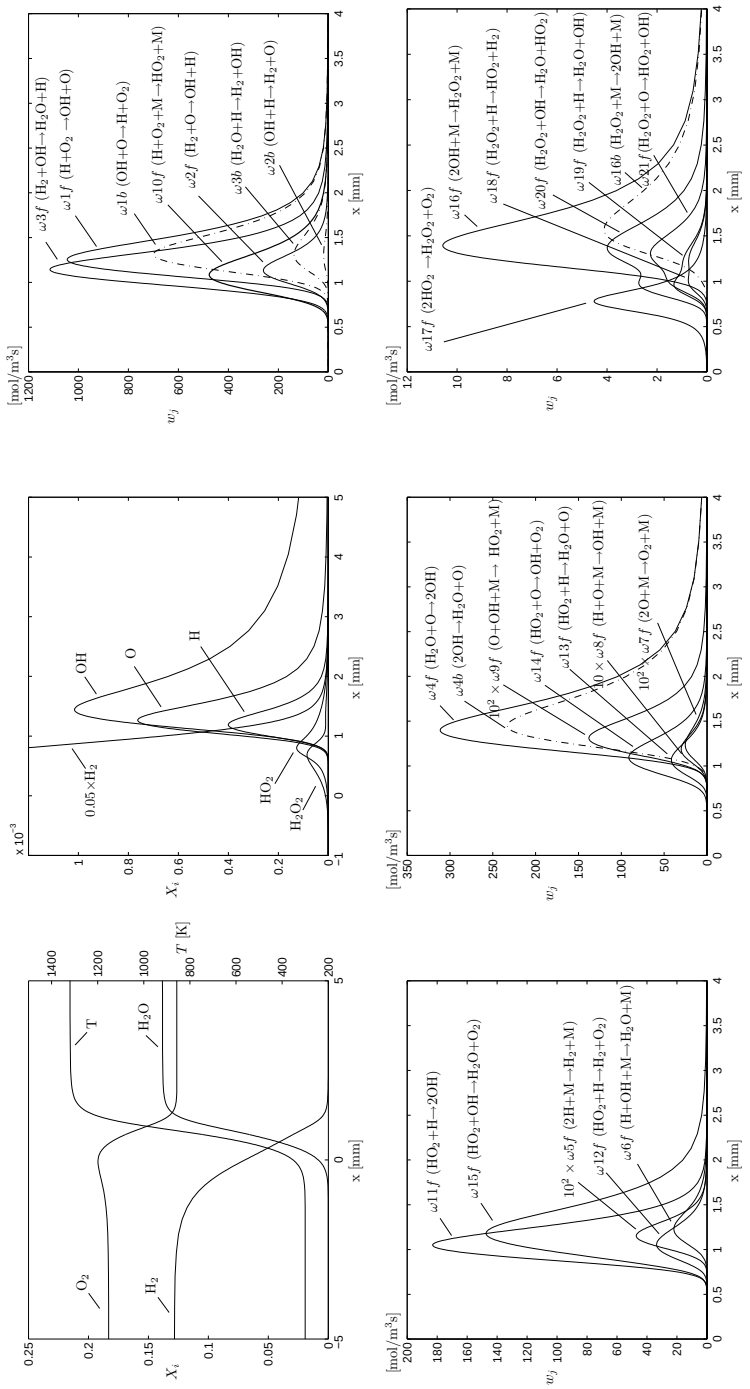

Figure E.15: Equivalence ratio $\phi = 0.35$, detailed mechanism (Table A.1) at $p = 1$ atm and $T_u = 300$ K.

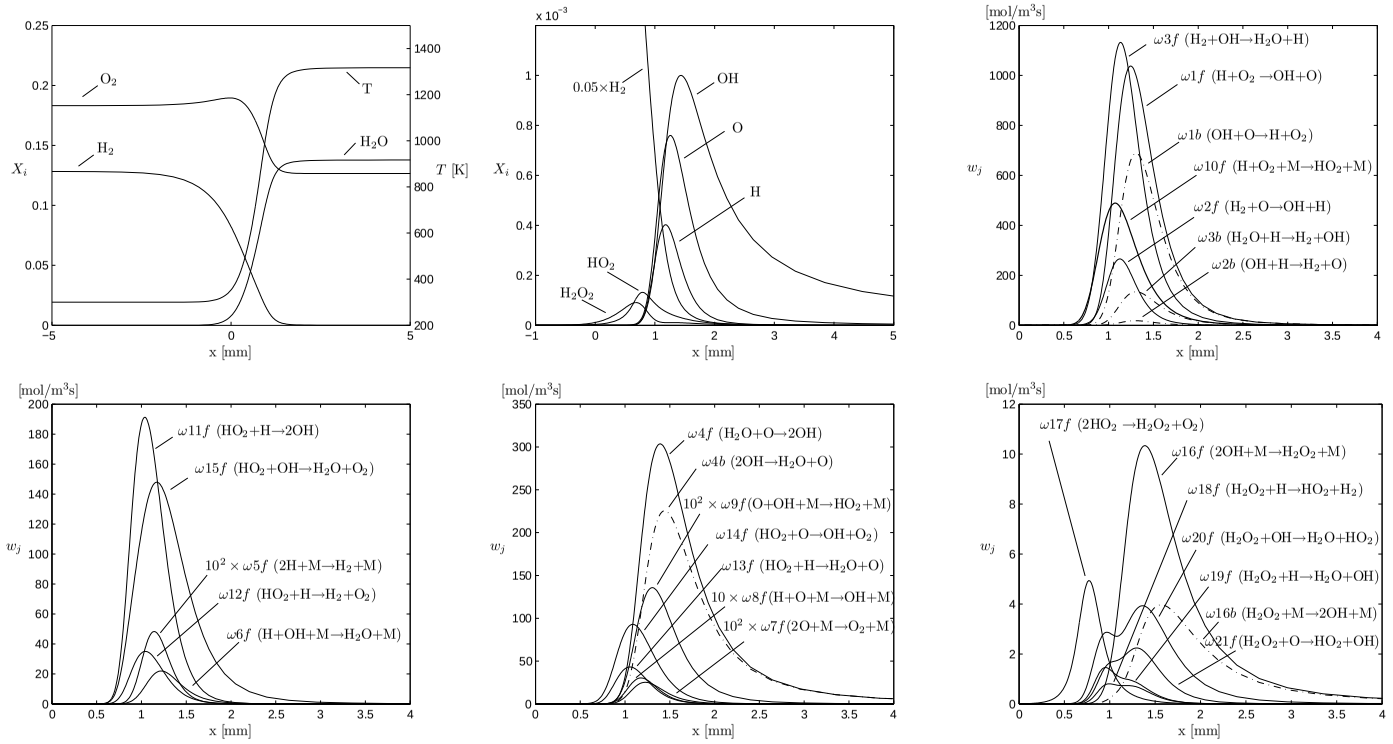

Figure E.16: Equivalence ratio $\phi = 0.35$, detailed mechanism (Table A.1) with thermal diffusion excluded at $p = 1$ atm and $T_u = 300$ K.

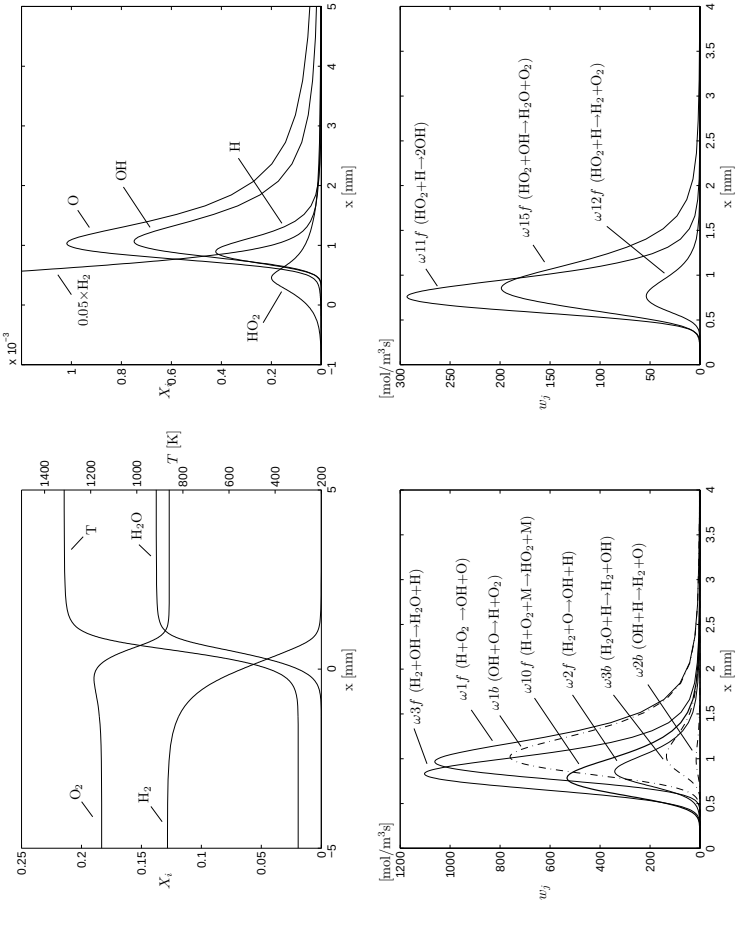

Figure E.17: Equivalence ratio $\phi = 0.35$, 7-step reduced mechanism at $p = 1$ atm and $T_u = 300$ K.

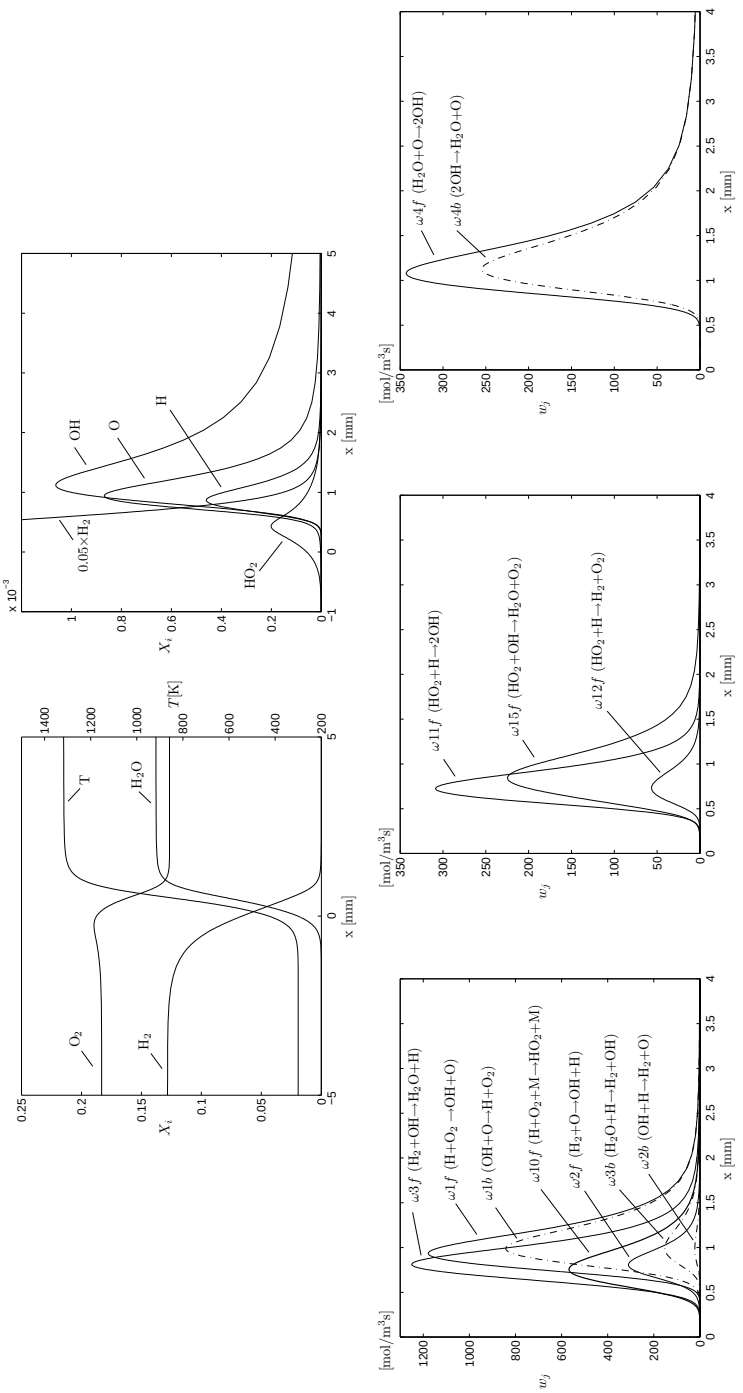

Figure E.18: Equivalence ratio $\phi = 0.35$, 8-step reduced mechanism (appendix C) at $p = 1$ atm and $T_u = 300$ K.

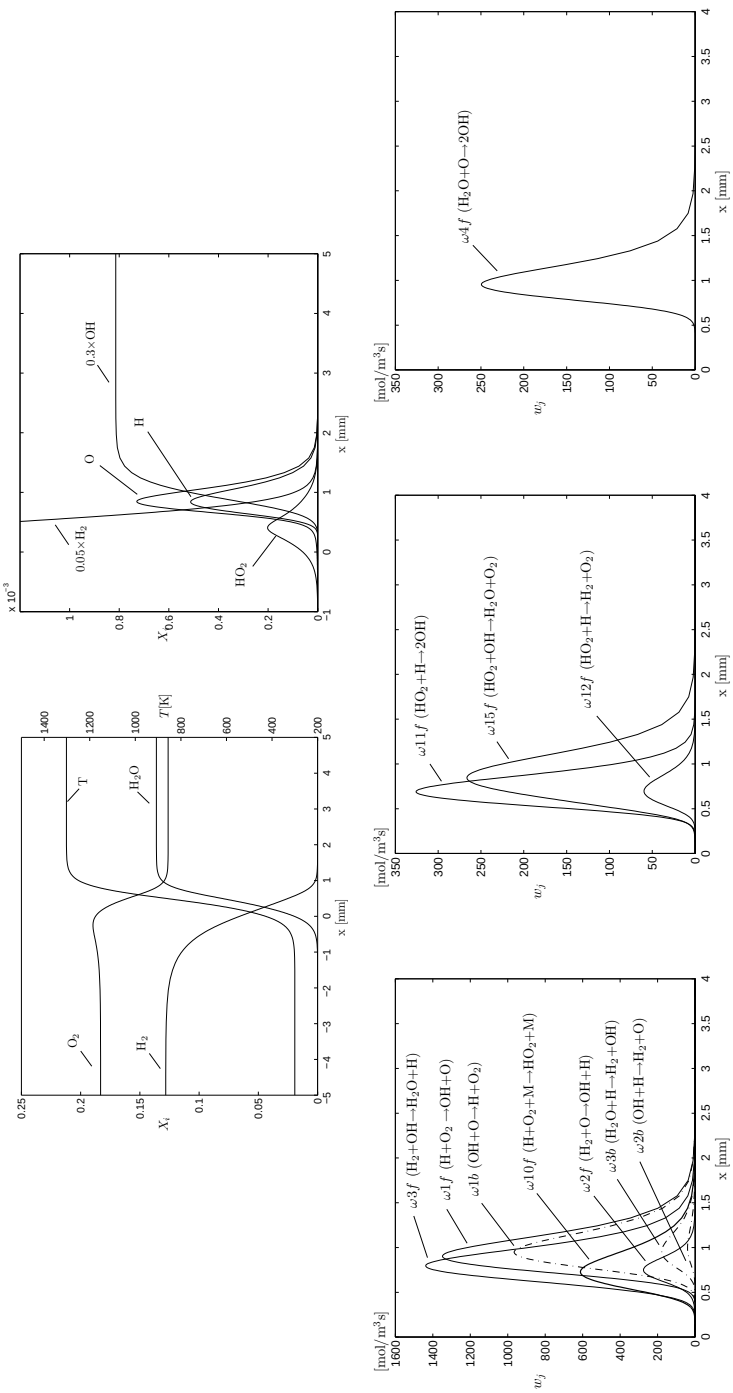

Figure E.19: Equivalence ratio $\phi = 0.35$, 7-step mechanism plus the forward shuffle reaction $H_2O + O \rightarrow OH + OH$ at $p = 1$ atm and $T_u = 300$ K.

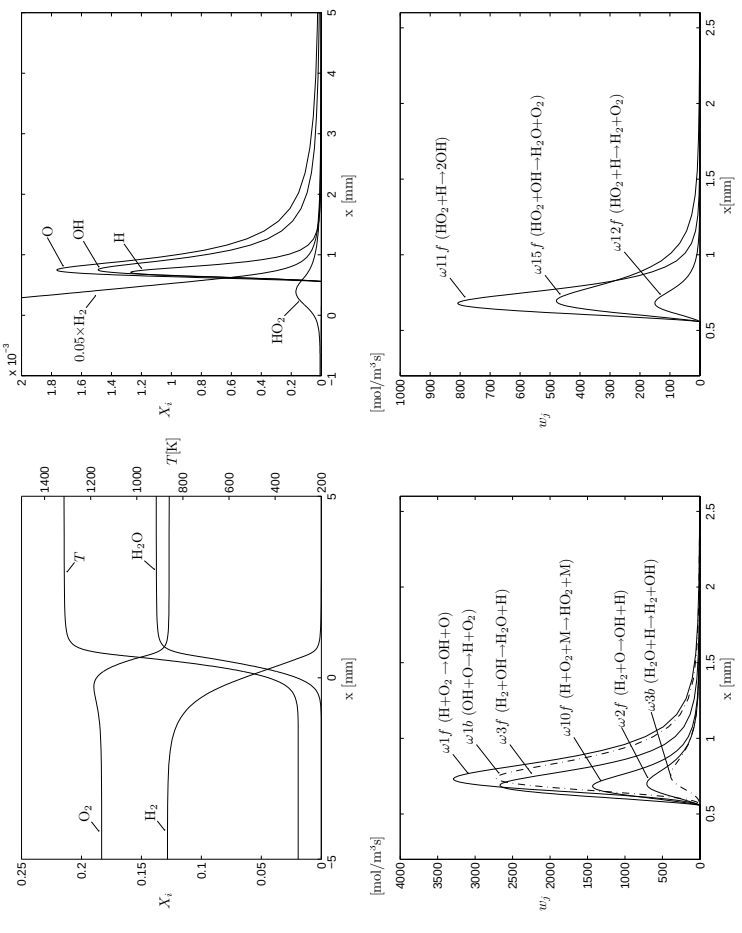

Figure E.20: Equivalence ratio $\phi = 0.35$, one-step reduced mechanism at $p = 1$ atm and $T_u = 300$ K.

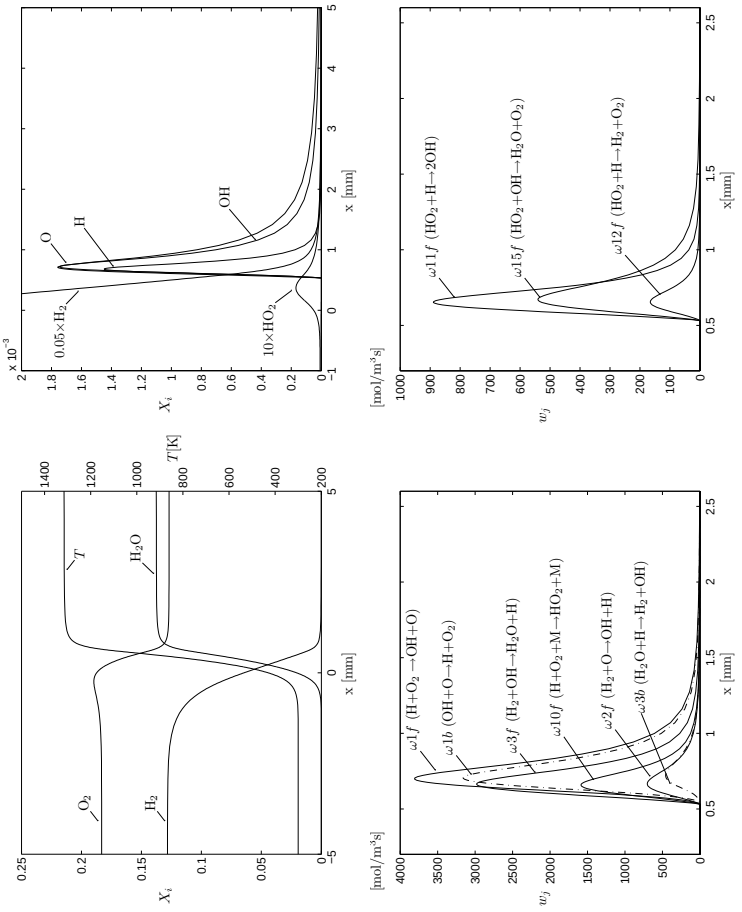

Figure E.21: Equivalence ratio $\phi = 0.35$, one-step reduced mechanism excluding reaction 2*b* ($H = 1$) at $p = 1$ atm and $T_u = 300$ K.

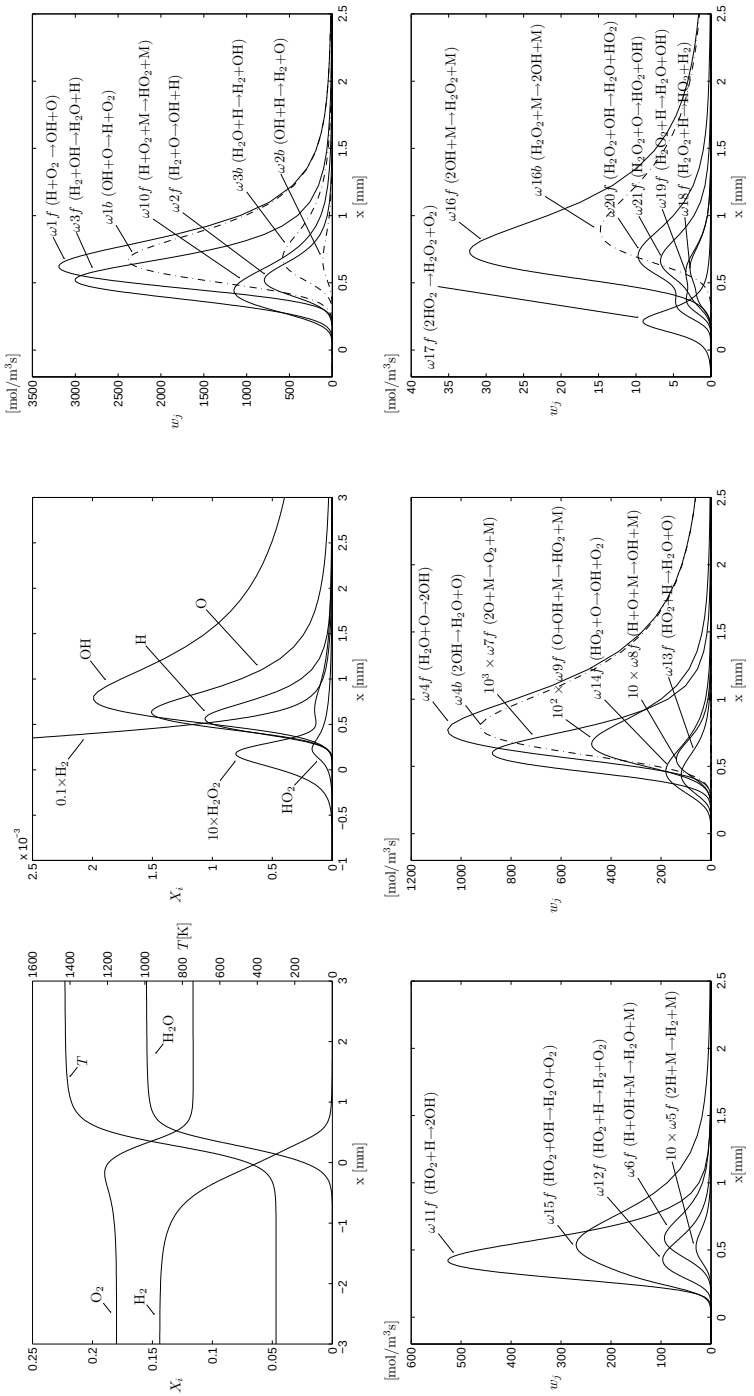

Figure E.22: Equivalence ratio $\phi = 0.4$, detailed mechanism (Table A.1) at $p = 1$ atm and $T_u = 300$ K.

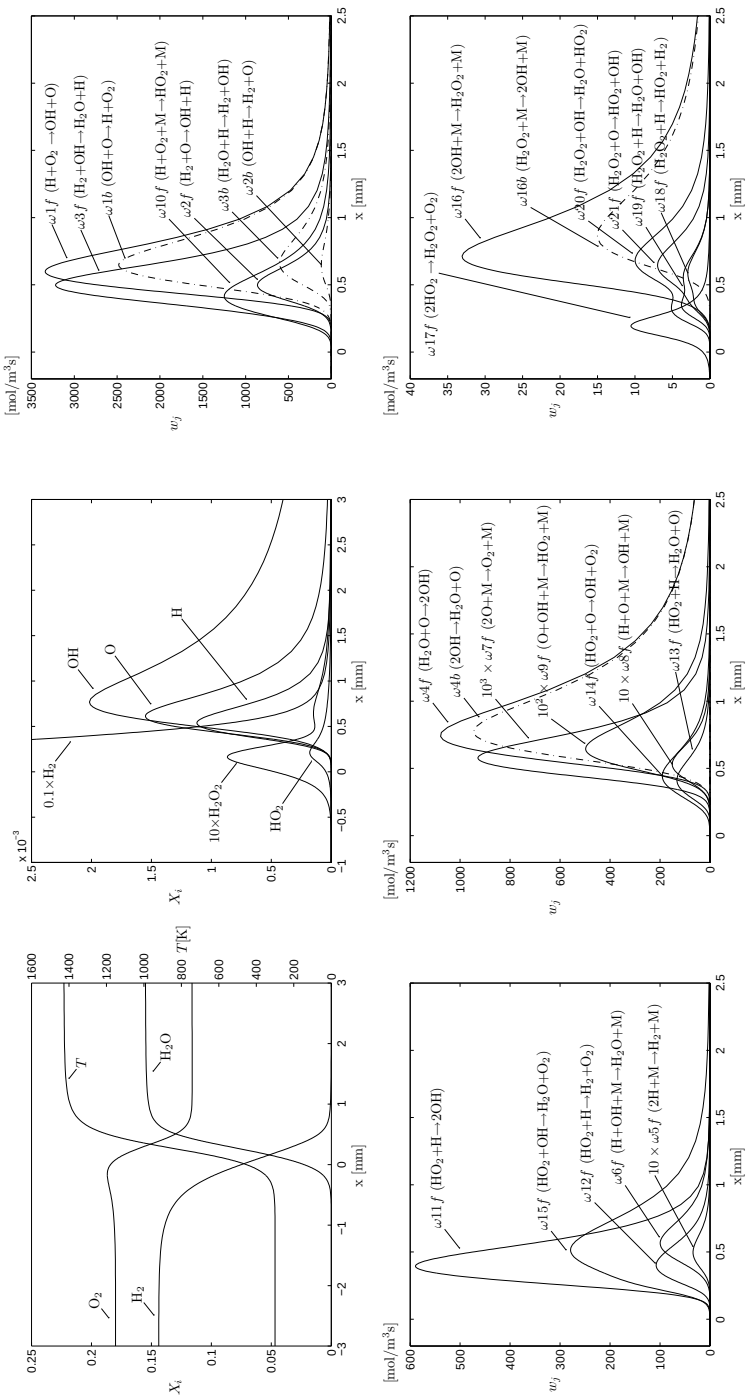

Figure E.23: Equivalence ratio $\phi = 0.4$, detailed mechanism (Table A.1) with thermal diffusion excluded at $p = 1$ atm and $T_u = 300$ K.

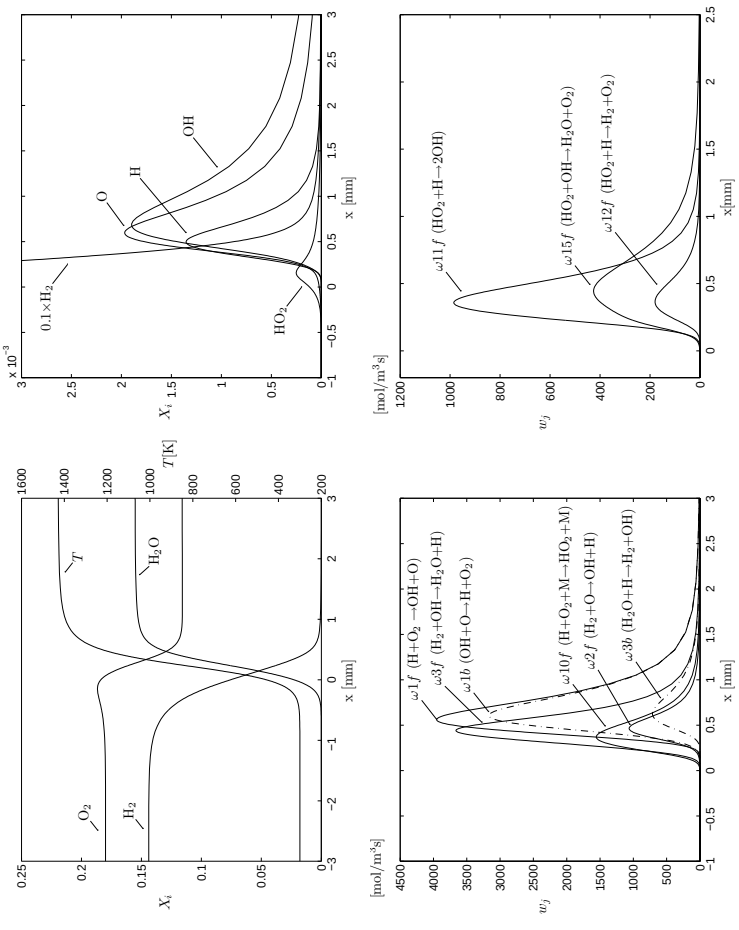

Figure E.24: Equivalence ratio $\phi = 0.4$, 7-step reduced mechanism at $p = 1$ atm and $T_u = 300$ K.

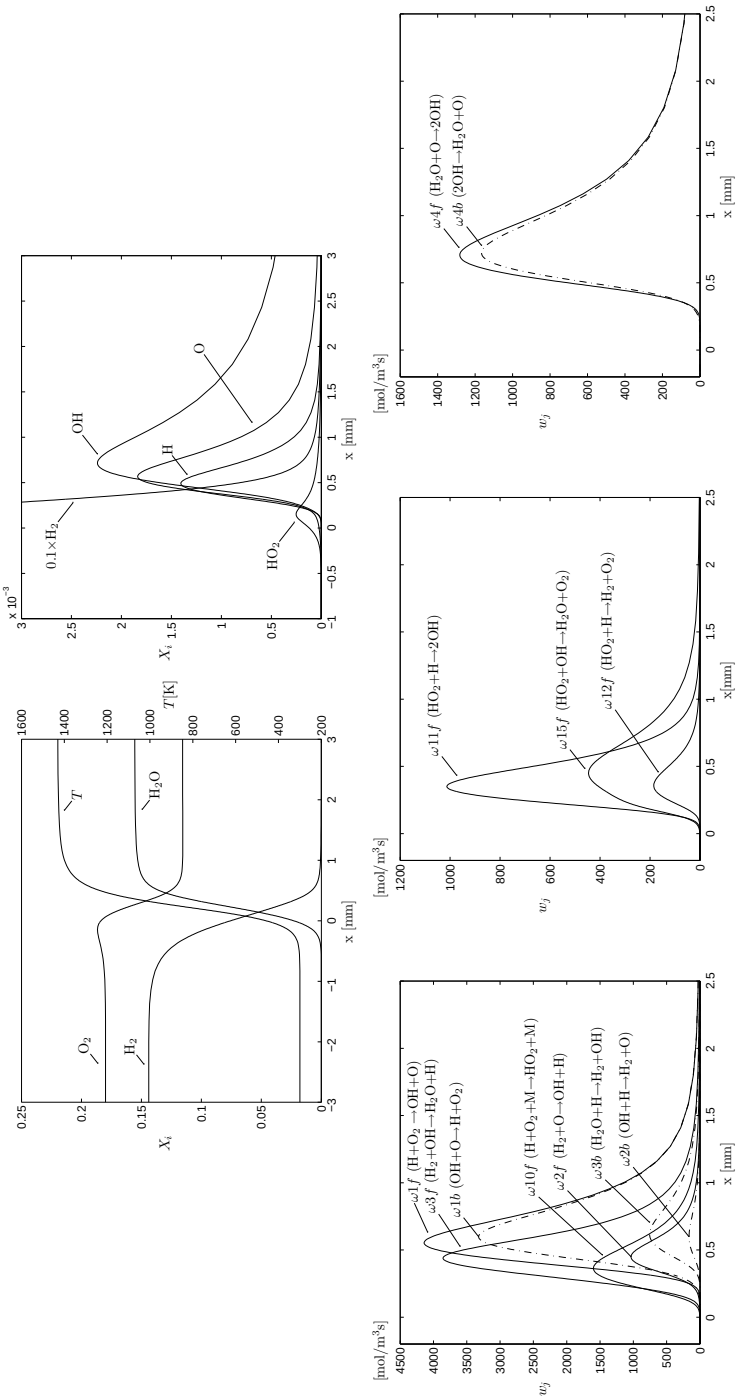

Figure E.25: Equivalence ratio $\phi = 0.4$, 8-step reduced mechanism (appendix C) at $p = 1$ atm and $T_u = 300$ K.

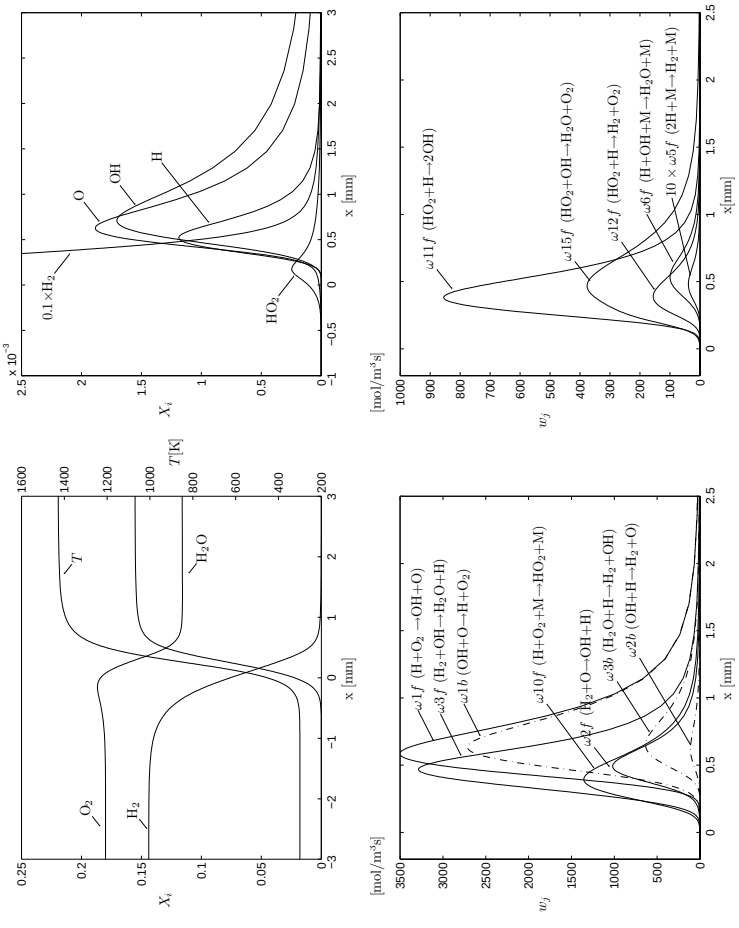

Figure E.26: Equivalence ratio $\phi = 0.4$, 9-step reduced mechanism at $p = 1$ atm and $T_u = 300$ K.

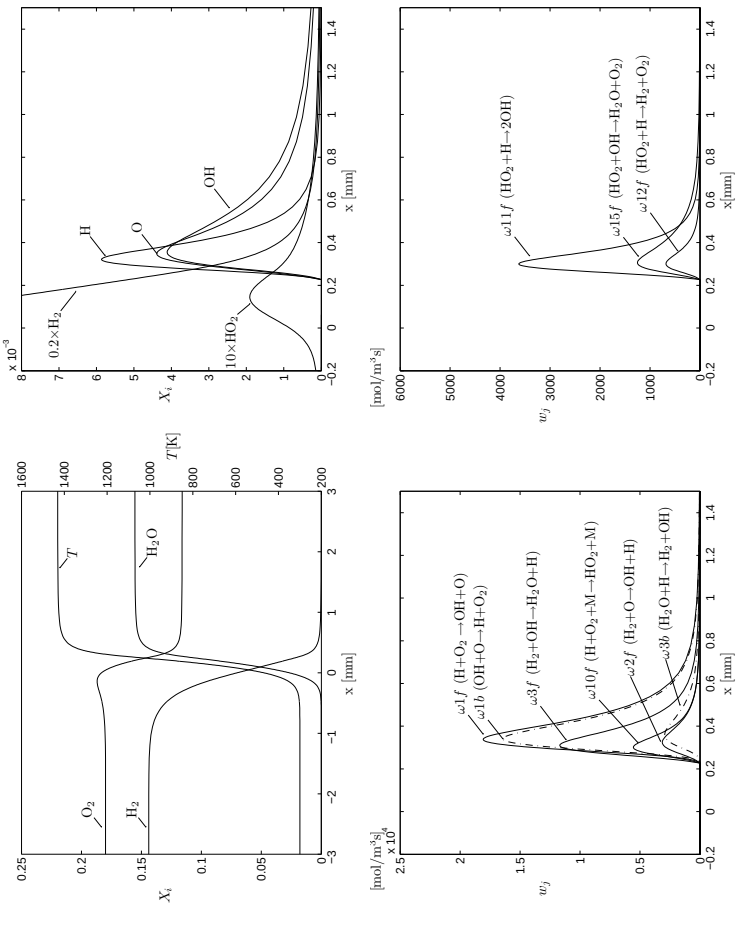

Figure E.27: Equivalence ratio $\phi = 0.4$, one-step reduced mechanism at $p = 1$ atm and $T_u = 300$ K.

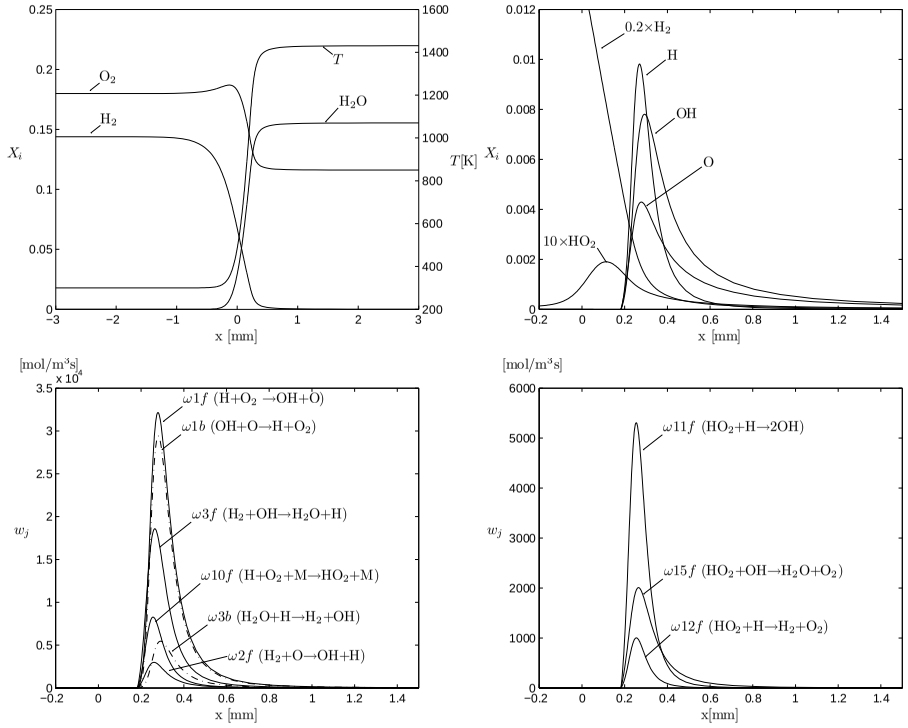

Figure E.28: Equivalence ratio $\phi = 0.4$, one-step reduced mechanism excluding reaction $2b$ ($H = 1$) at $p = 1$ atm and $T_u = 300$ K.

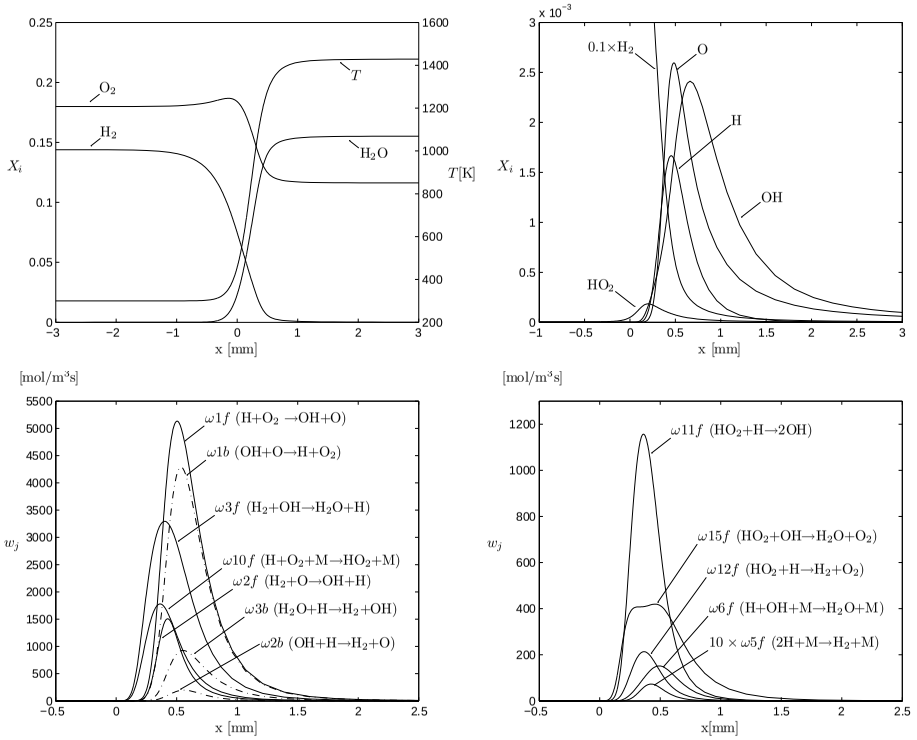

Figure E.29: Equivalence ratio $\phi = 0.4$, two-step reduced mechanism (4.3) based on truncated expresion for γ_{OH} (4.9) at $p = 1$ atm and $T_u = 300$ K.

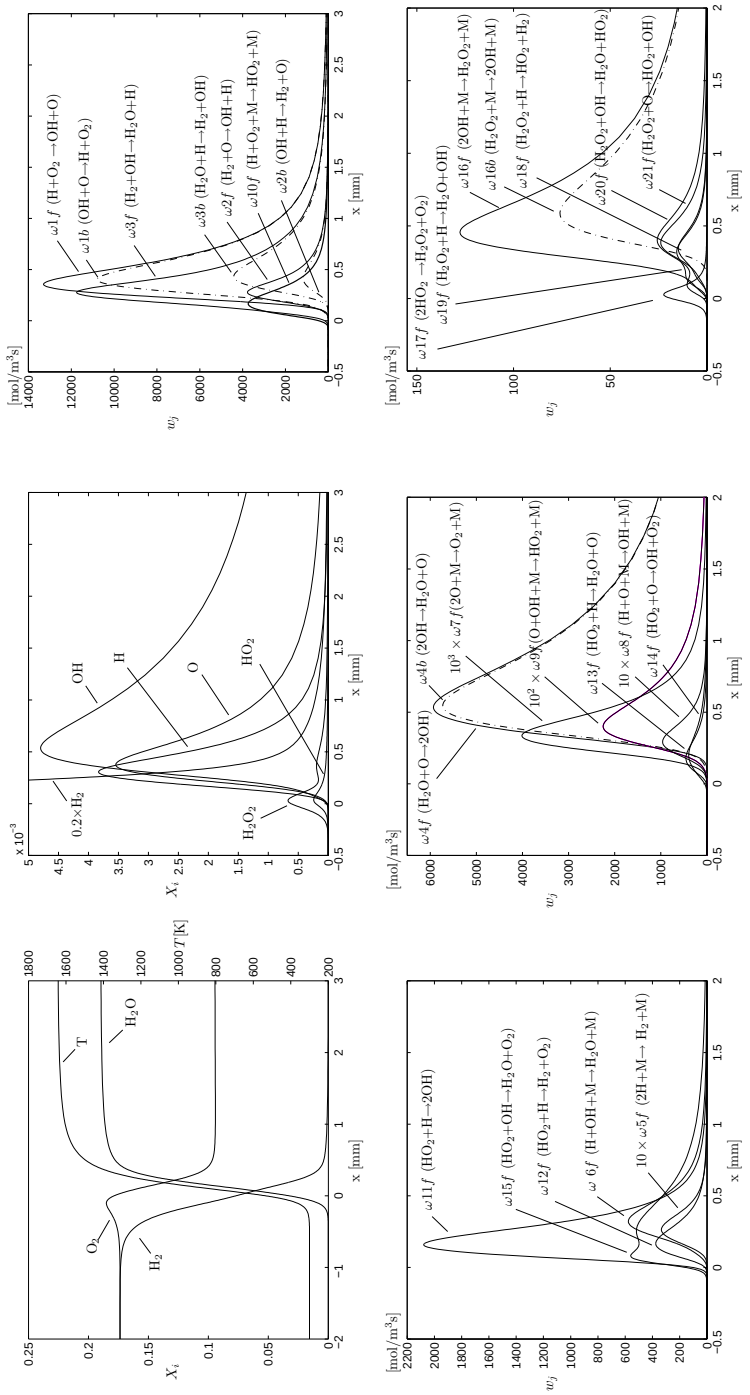

Figure E.30: Equivalence ratio $\phi = 0.5$, detailed mechanism (Table A.1) at $p = 1$ atm and $T_u = 300$ K.

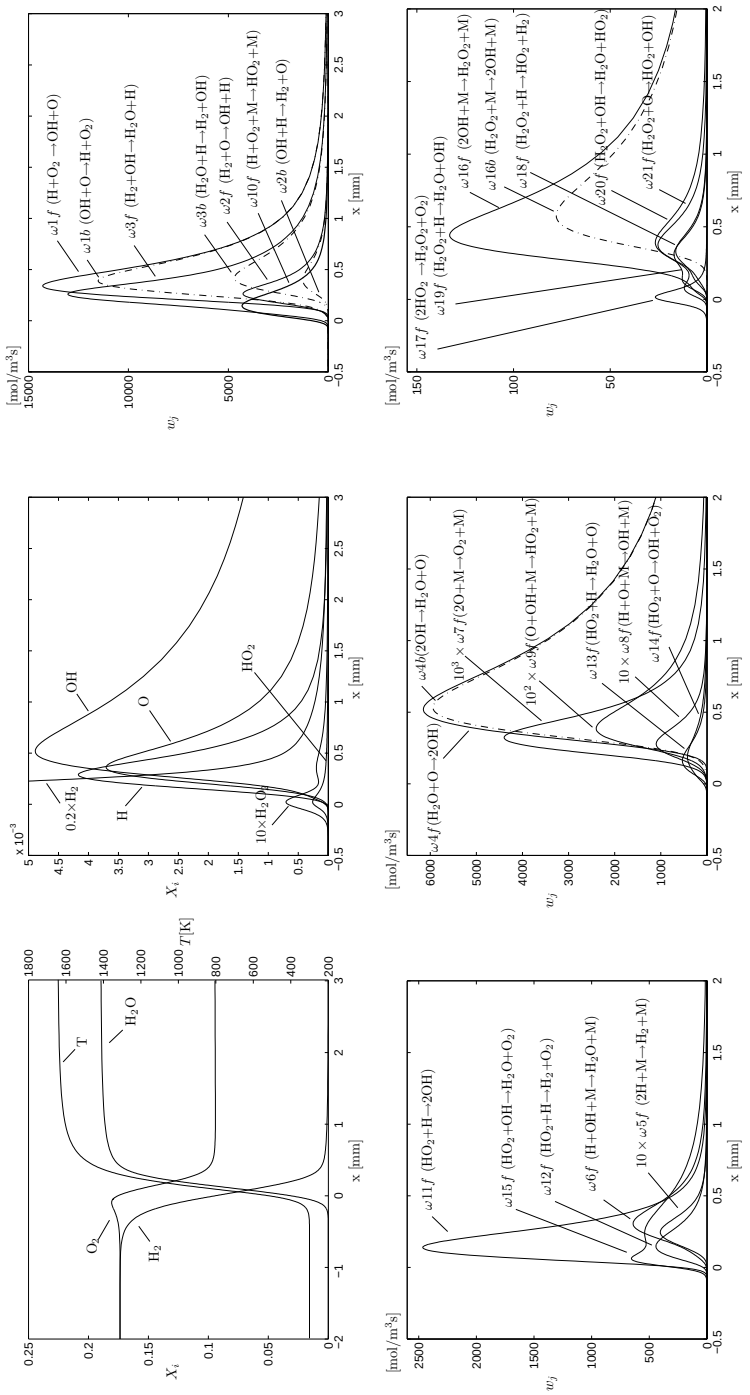

Figure E.31: Equivalence ratio $\phi = 0.5$, detailed mechanism (Table A.1) with thermal diffusion excluded at $p = 1$ atm and $T_u = 300$ K.

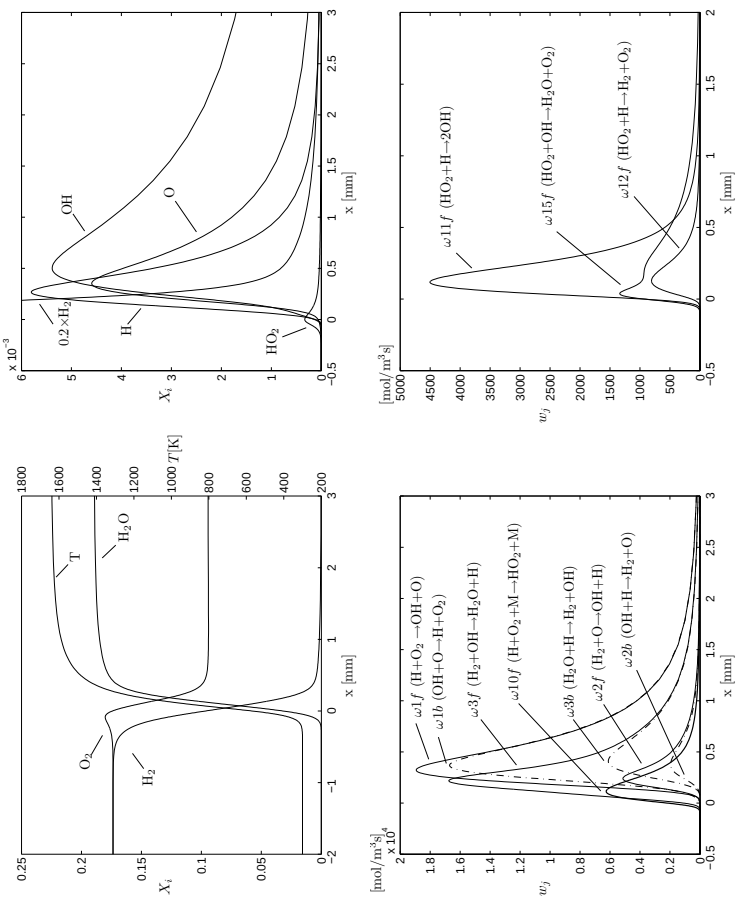

Figure E.32: Equivalence ratio $\phi = 0.5$, 7-step reduced mechanism at $p = 1$ atm and $T_u = 300$ K.

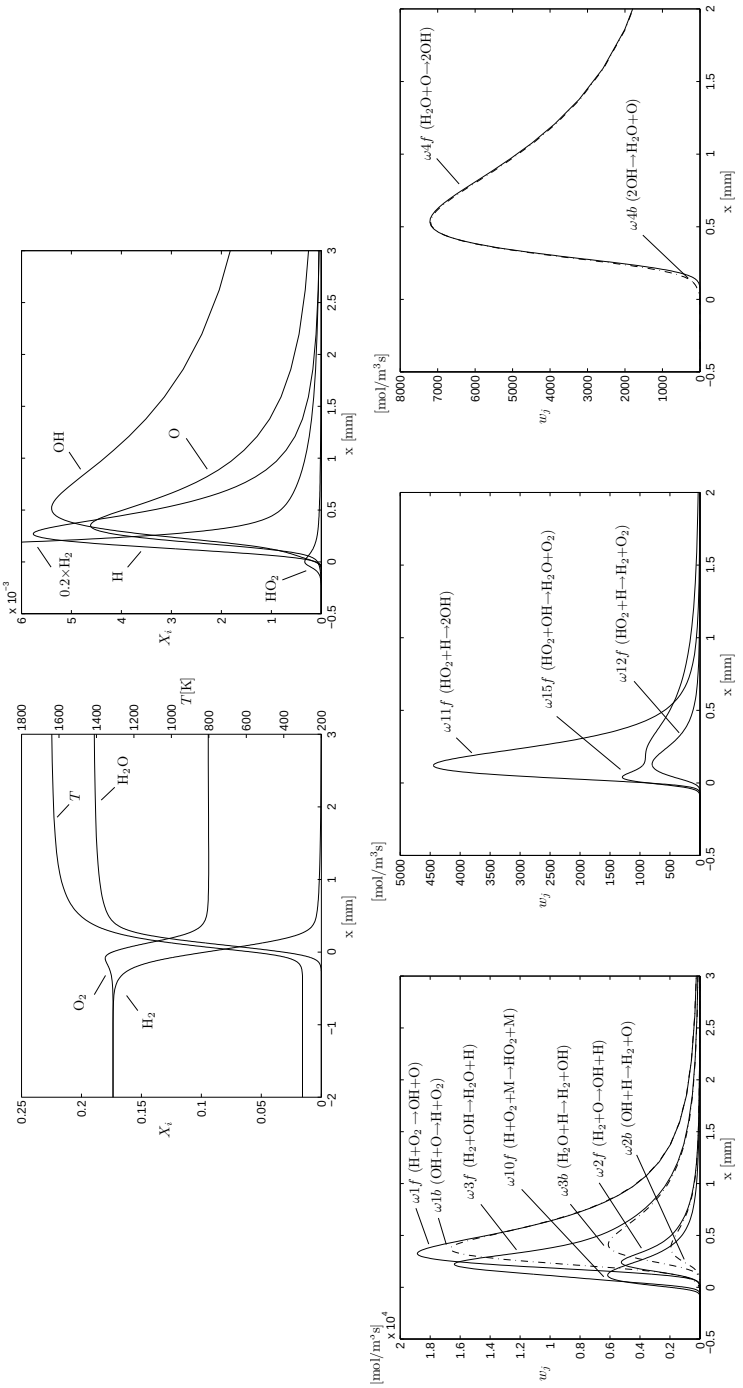

Figure E.33: Equivalence ratio $\phi = 0.5$, 8-step reduced mechanism (appendix C) at $p = 1$ atm and $T_u = 300$ K.

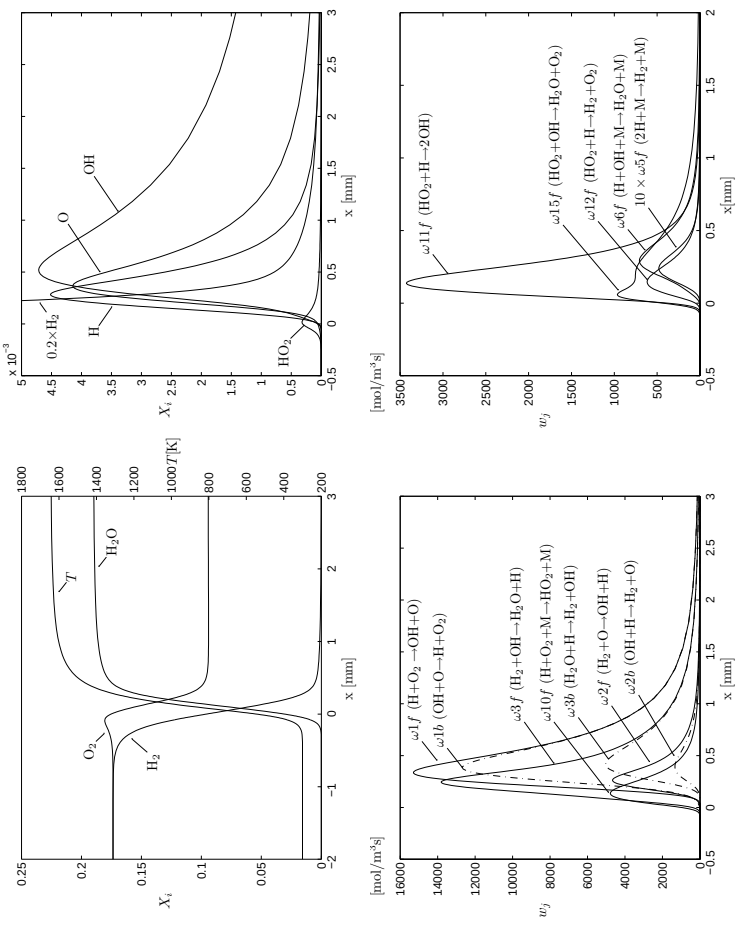

Figure E.34: Equivalence ratio $\phi = 0.5$, 9-step reduced mechanism at $p = 1$ atm and $T_u = 300$ K.

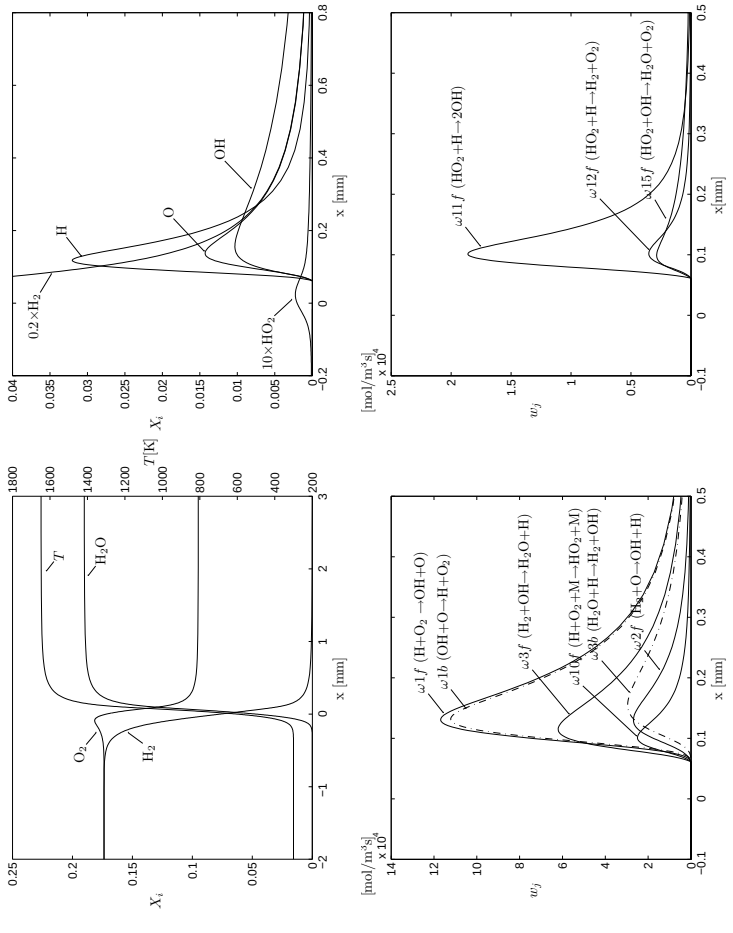

Figure E.35: Equivalence ratio $\phi = 0.5$, one-step reduced mechanism at $p = 1$ atm and $T_u = 300$ K.

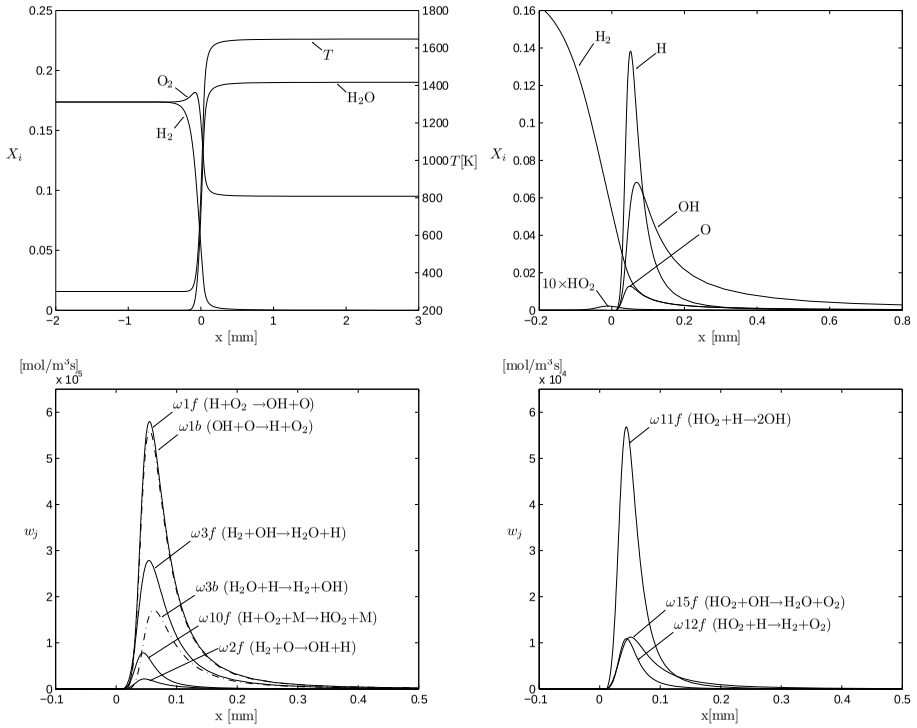

Figure E.36: Equivalence ratio $\phi = 0.5$, one-step reduced mechanism excluding reaction $2b$ ($H = 1$) at $p = 1$ atm and $T_u = 300$ K.

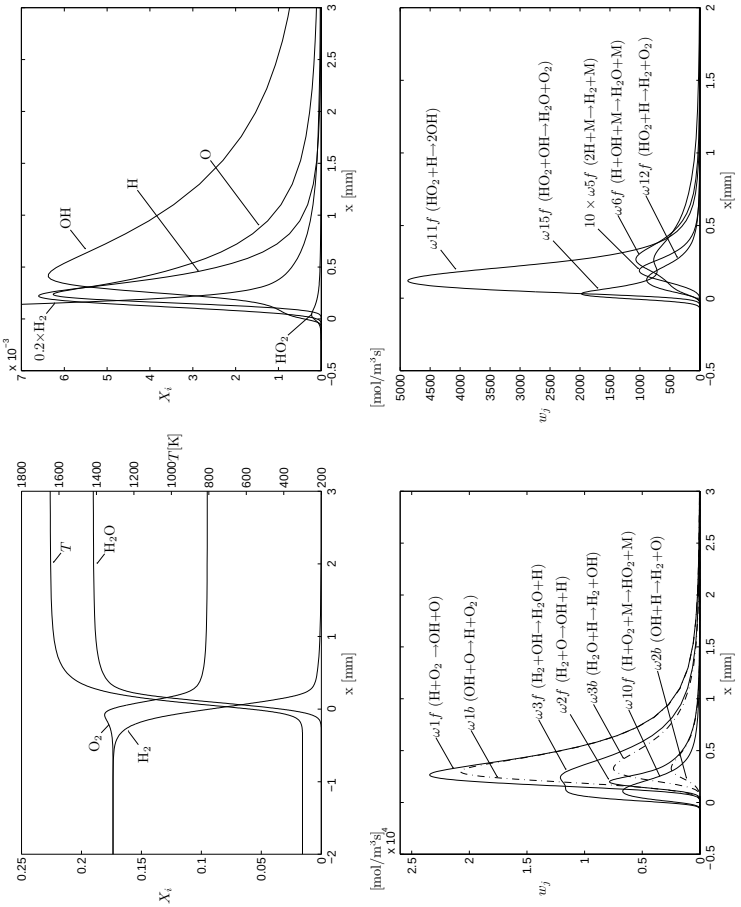

Figure E.37: Equivalence ratio $\phi = 0.5$, two-step reduced mechanism (4.3) based on truncated expresion for γ_{OH} (4.9) at $p = 1$ atm and $T_u = 300$ K.

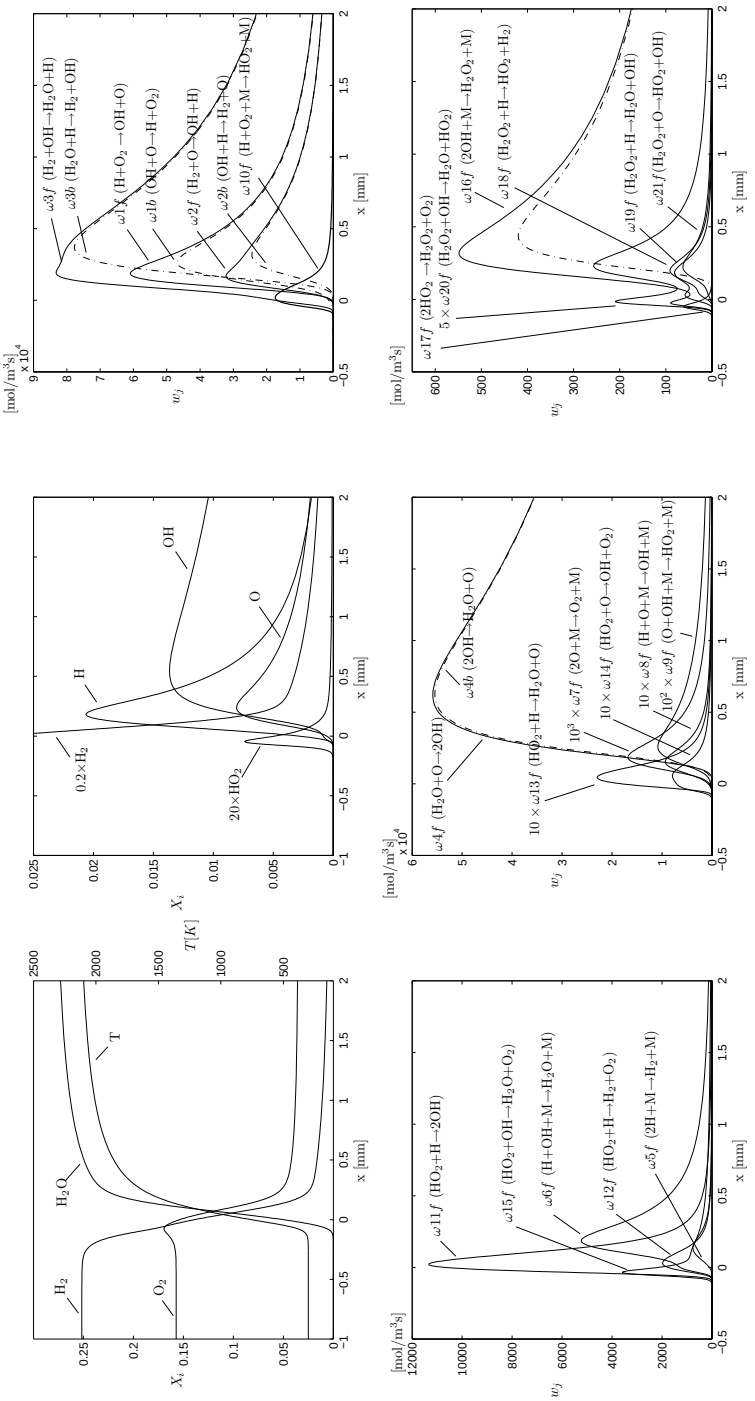

Figure E.38: Equivalence ratio $\phi = 0.8$, detailed mechanism (Table A.1) at $p = 1$ atm and $T_u = 300$ K.

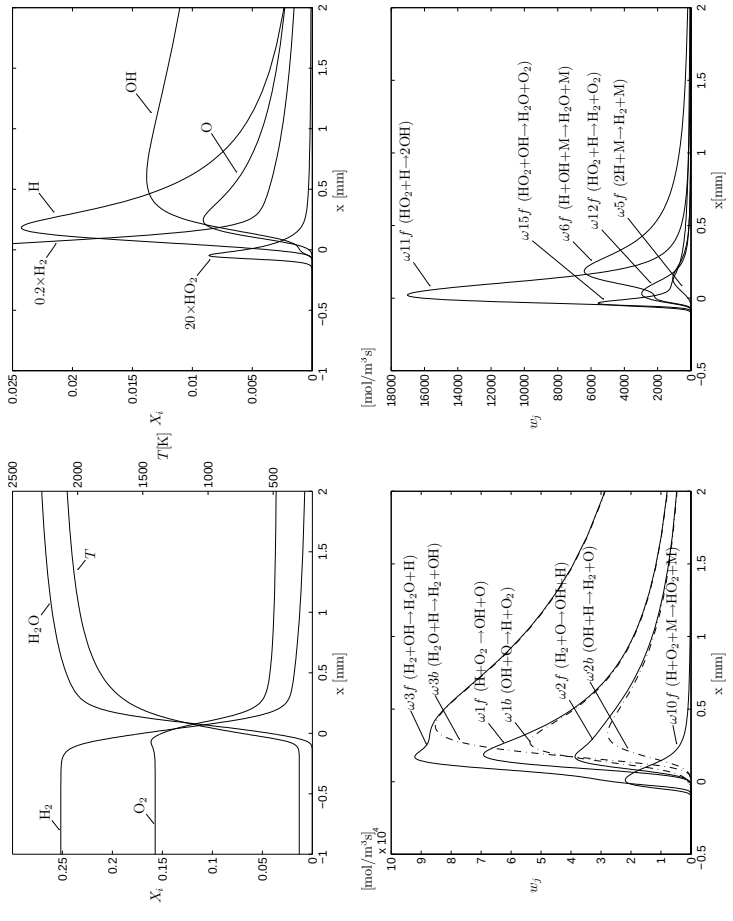

Figure E.39: Equivalence ratio $\phi = 0.8$, 9-step reduced mechanism at $p = 1$ atm and $T_u = 300$ K.

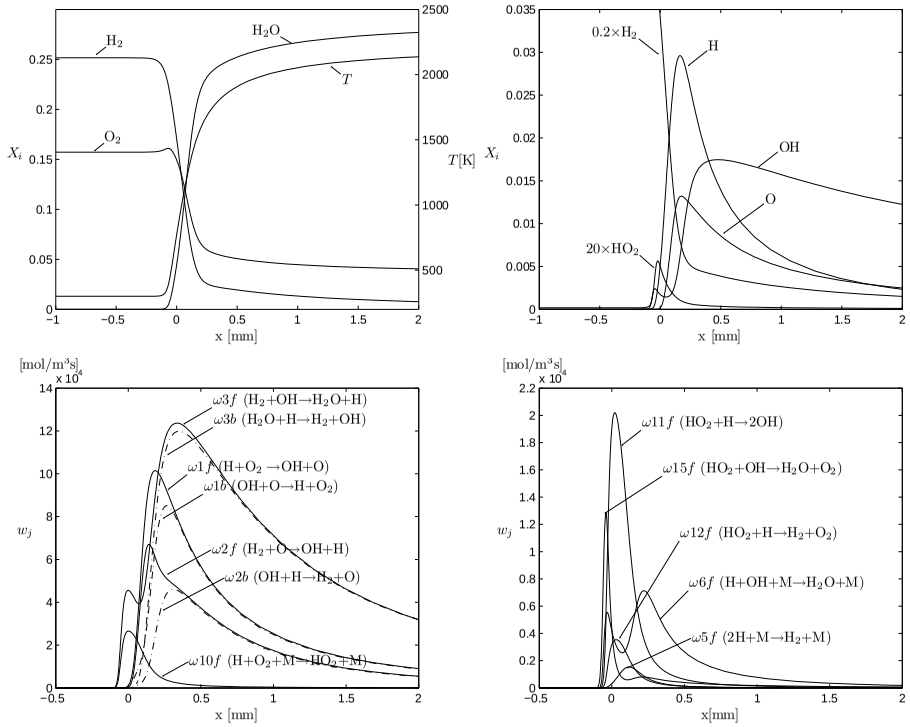

Figure E.40: Equivalence ratio $\phi = 0.8$, two-step reduced mechanism (4.3) based on truncated expresion for γ_{OH} (4.9) at $p = 1$ atm and $T_u = 300$ K.

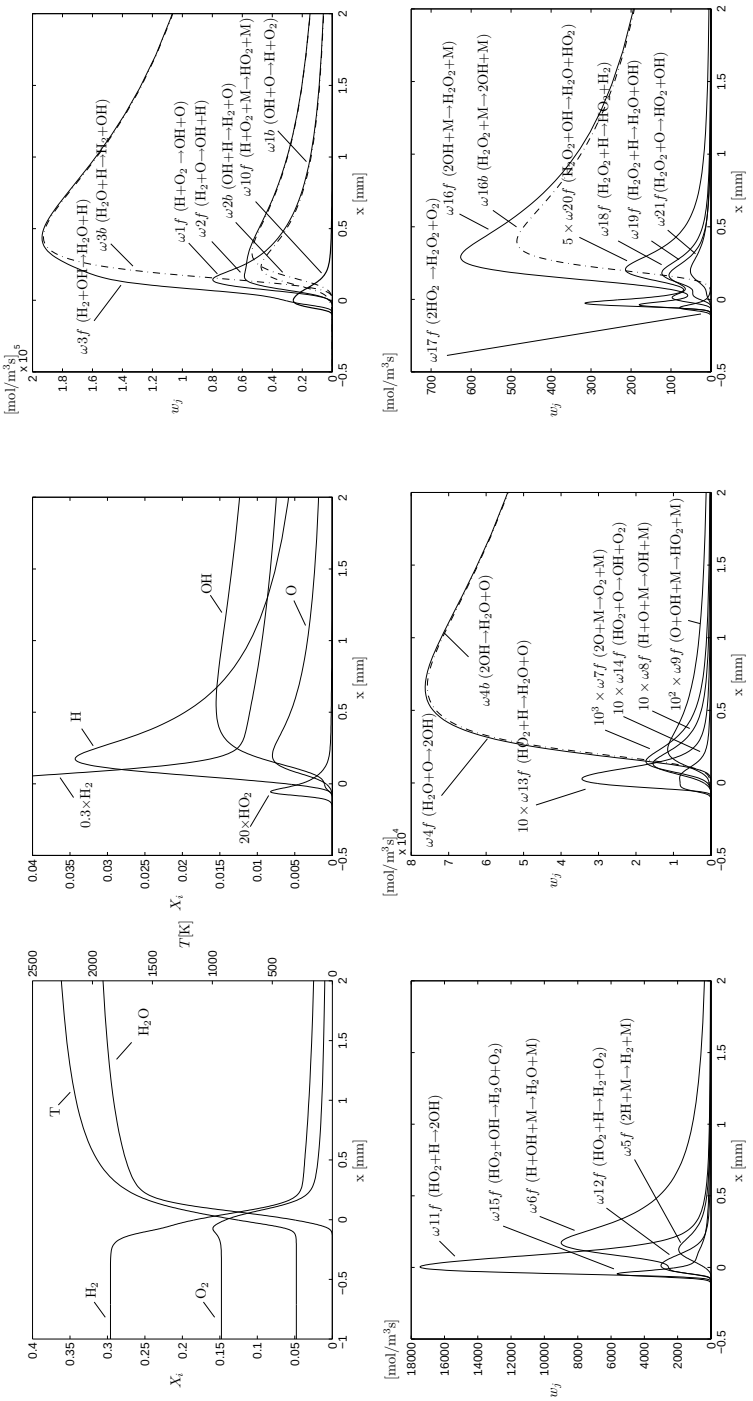

Figure E.41: Equivalence ratio $\phi = 1$, detailed mechanism (Table A.1) at $p = 1$ atm and $T_u = 300$ K.

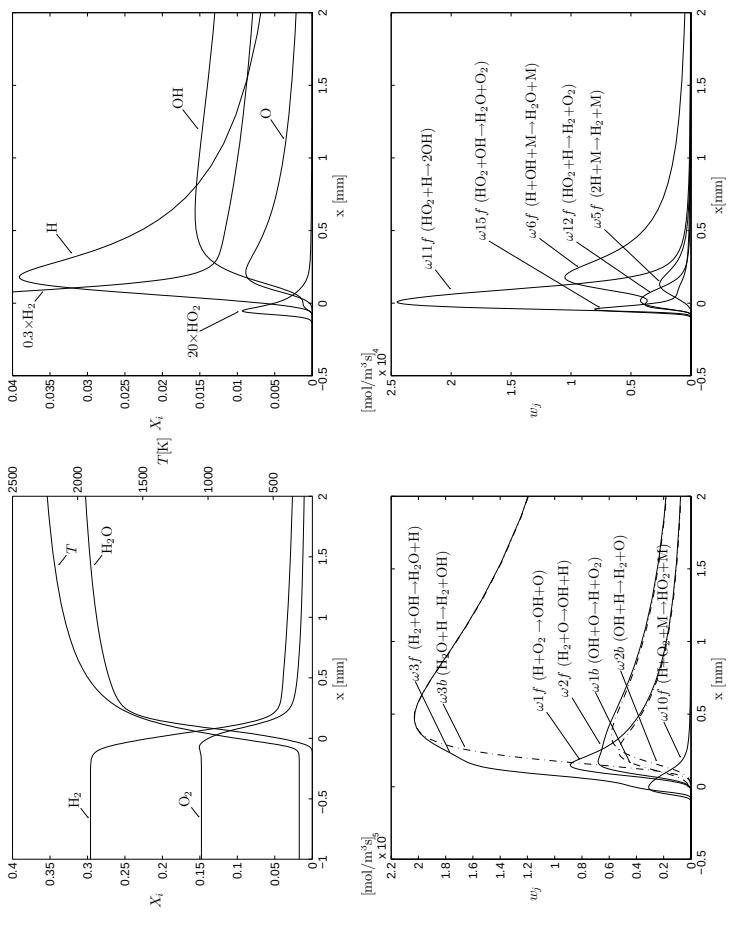

Figure E.42: Equivalence ratio $\phi = 1$, 9-step reduced mechanism at $p = 1$ atm and $T_u = 300$ K.

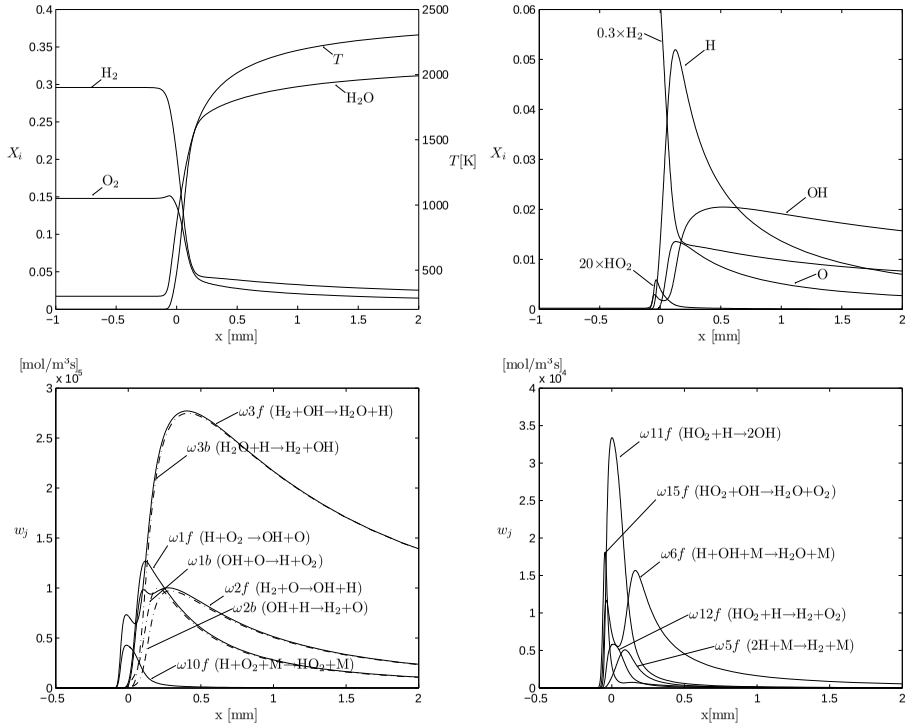

Figure E.43: Equivalence ratio $\phi = 1$, two-step reduced mechanism (4.3) based on truncated expresion for γ_{OH} (4.9) at $p = 1$ atm and $T_u = 300$ K.

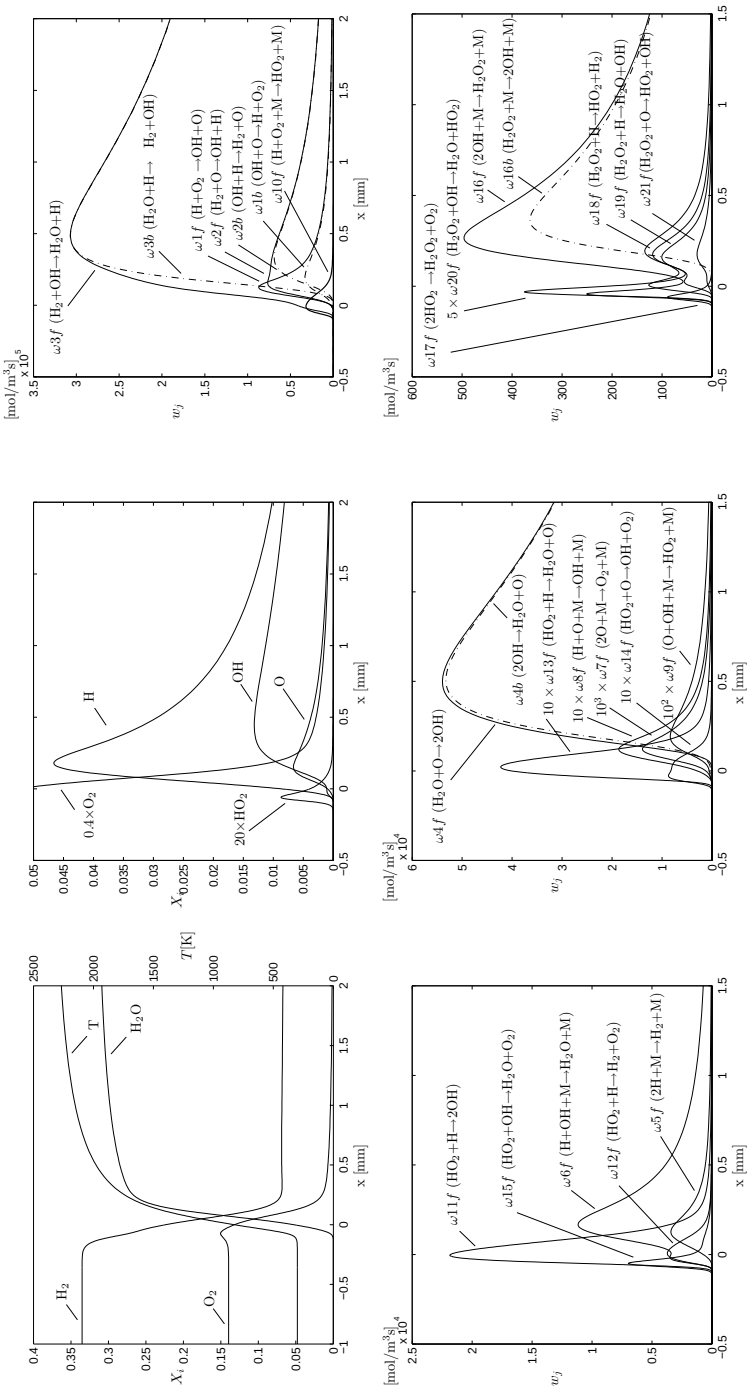

Figure E.44: Equivalence ratio $\phi = 1.2$, detailed mechanism (Table A.1) at $p = 1$ atm and $T_u = 300$ K.

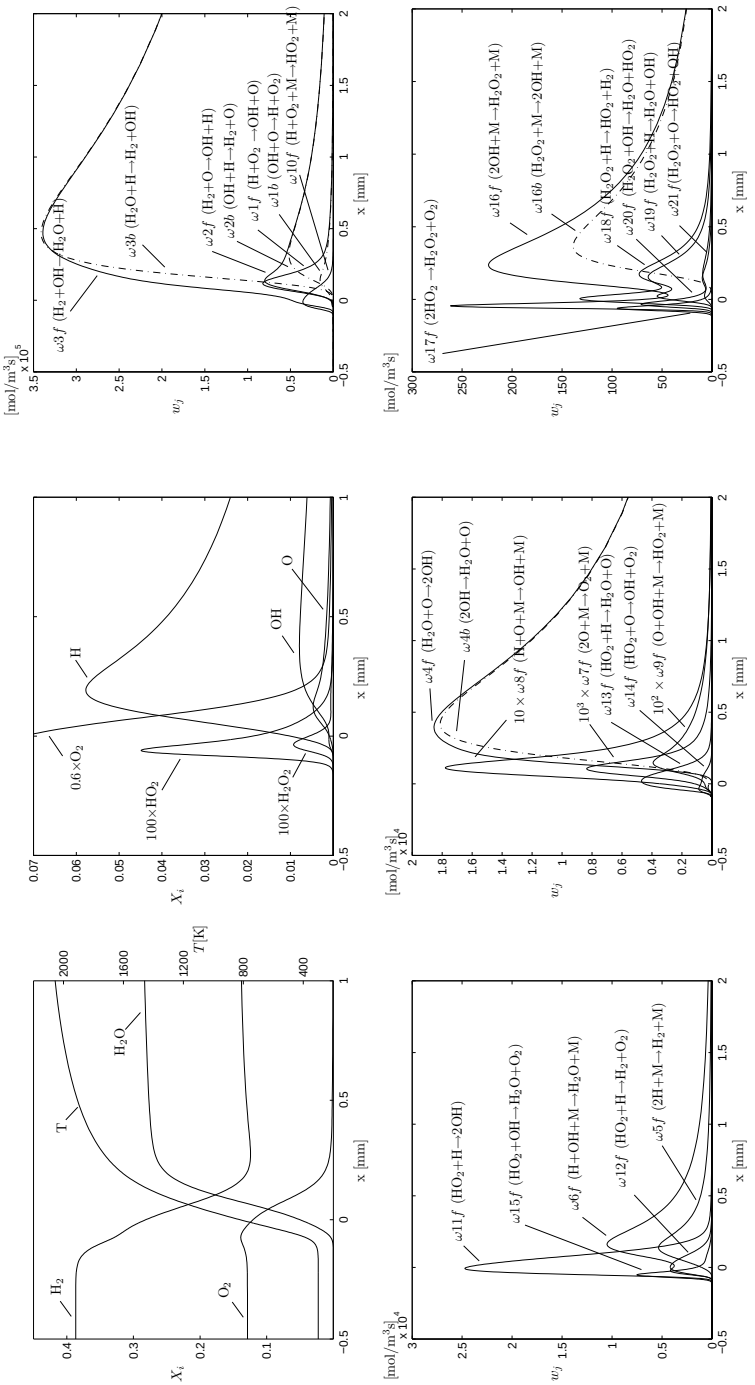

Figure E.45: Equivalence ratio $\phi = 1.5$, detailed mechanism (Table A.1) at $p = 1$ atm and $T_u = 300$ K.

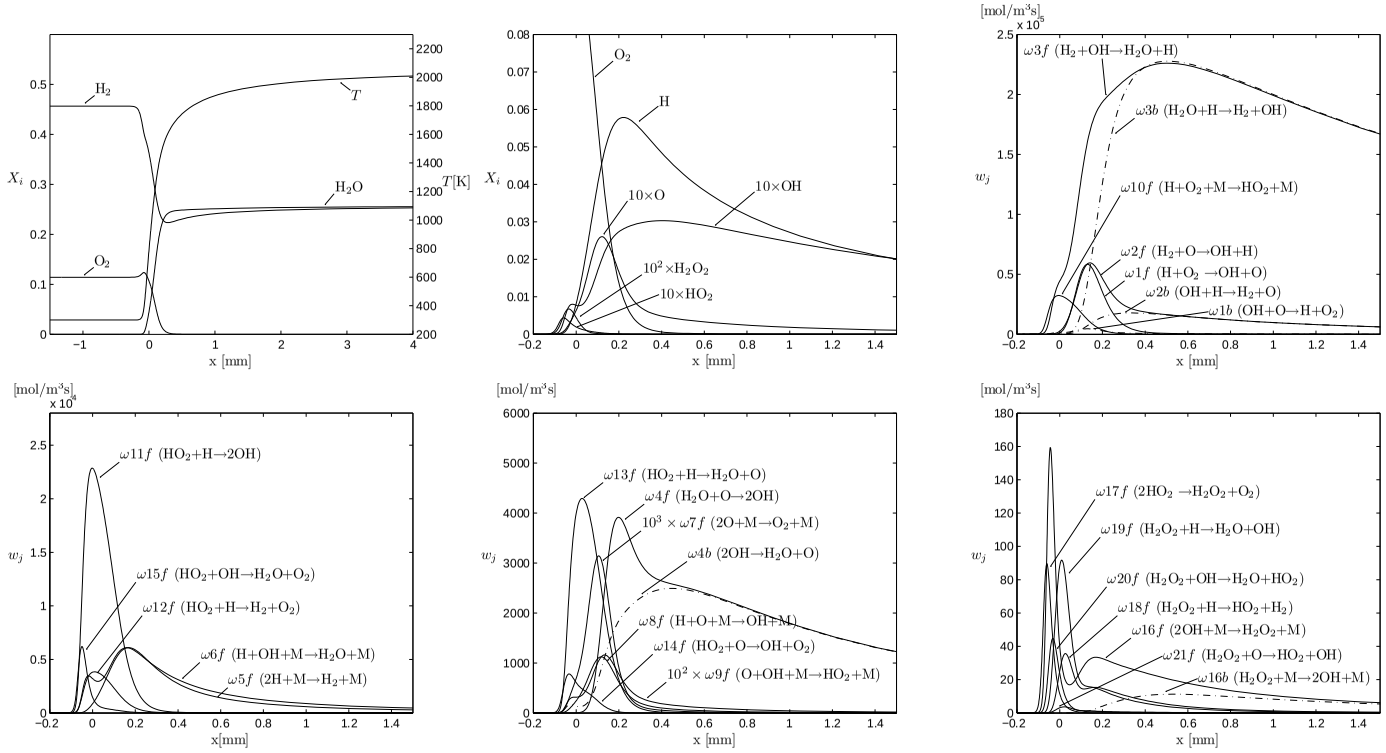

Figure E.46: Equivalence ratio $\phi = 2$, detailed mechanism (Table A.1) at $p = 1$ atm and $T_u = 300$ K.

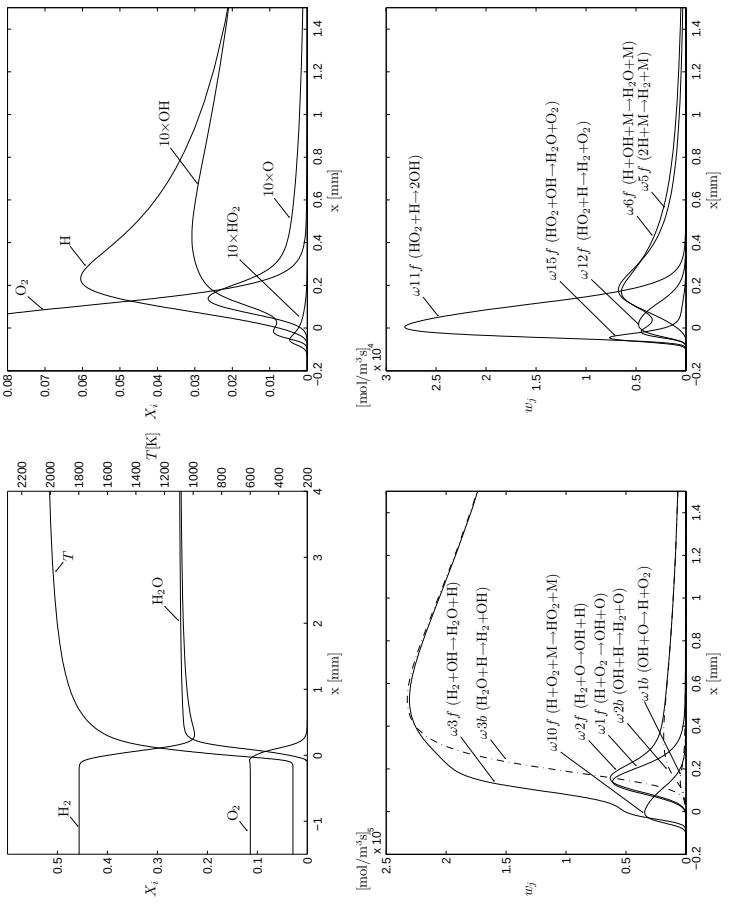

Figure E.47: Equivalence ratio $\phi = 2$, 9-step reduced mechanism at $p = 1$ atm and $T_u = 300$ K.

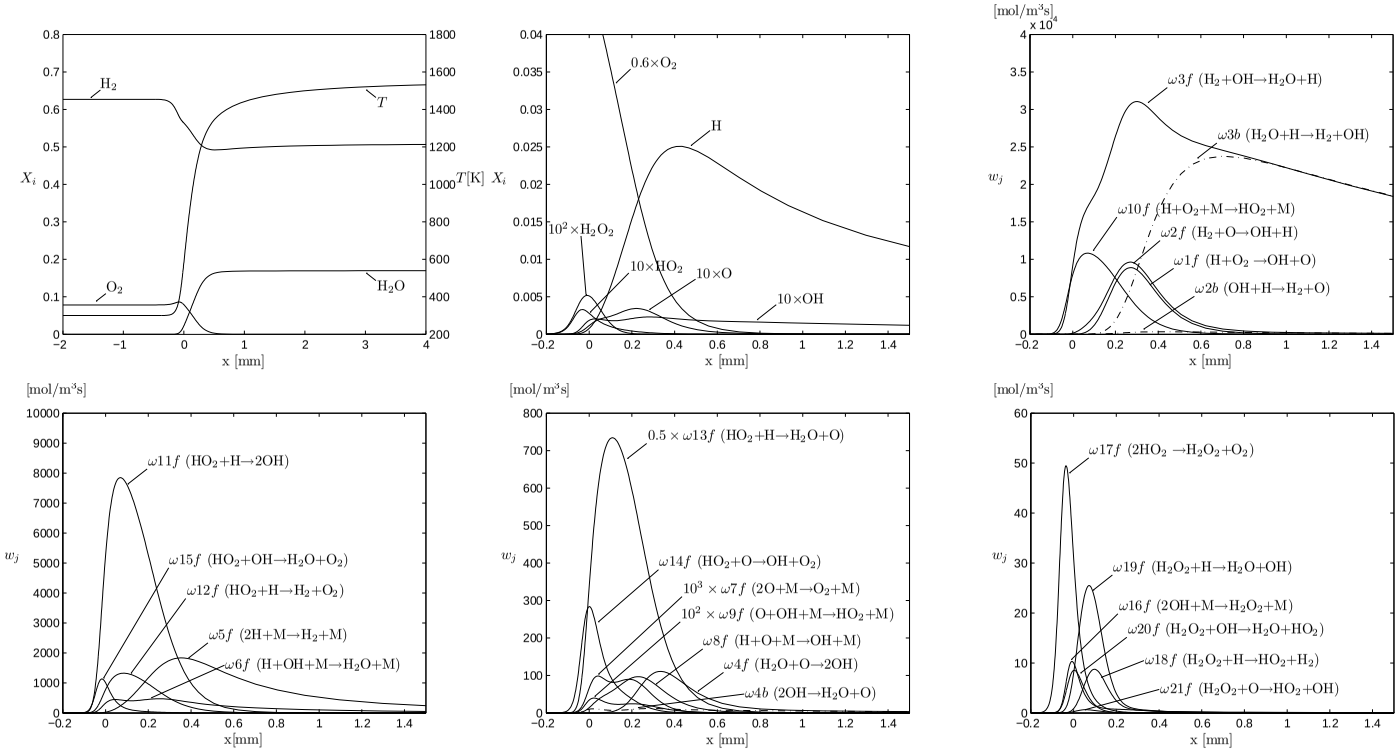

Figure E.48: Equivalence ratio $\phi = 4$, detailed mechanism (Table A.1) at $p = 1$ atm and $T_u = 300$ K.

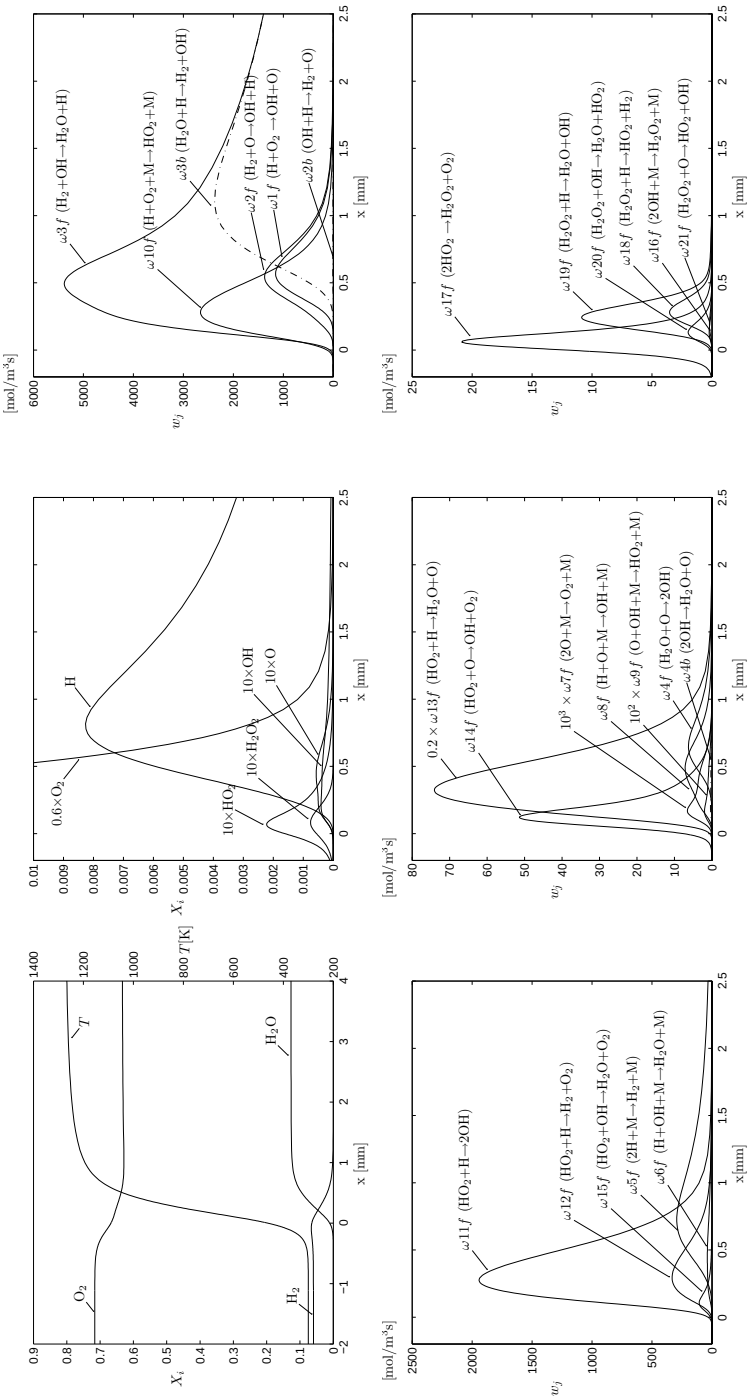

Figure E.49: Equivalence ratio $\phi = 6$, detailed mechanism (Table A.1) at $p = 1$ atm and $T_u = 300$ K.

APPENDIX

F

Balance of production, consumption and transport

Calculations of the rates of chemical production, chemical consumption and transport for relevant chemical species across the flame are shown in the figures below at different equivalence ratios. The results are obtained with the detailed chemistry description of Table A.1 for H_2-air mixtures and some specific H_2-O_2 mixtures.

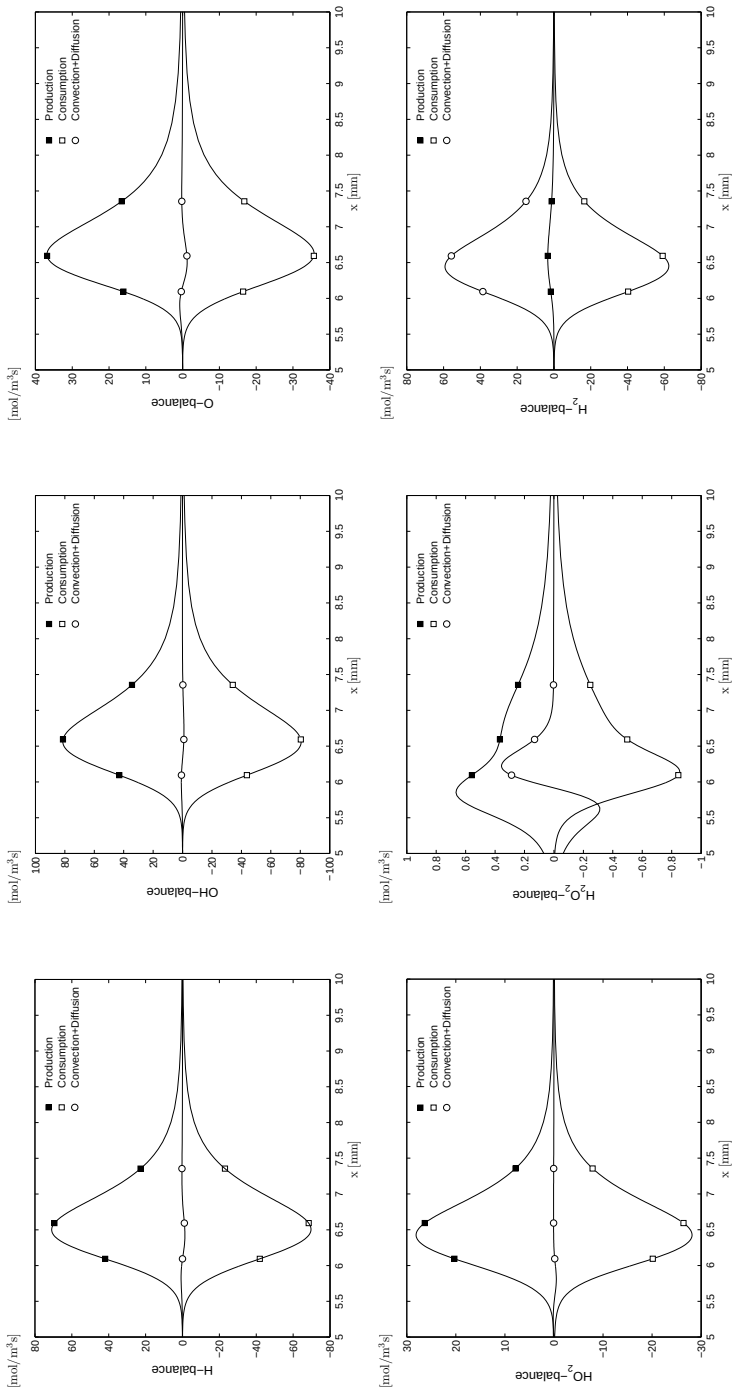

Figure F.1: Equivalence ratio $\phi = 0.28$ at $p = 1$ atm and $T_u = 300$ K.

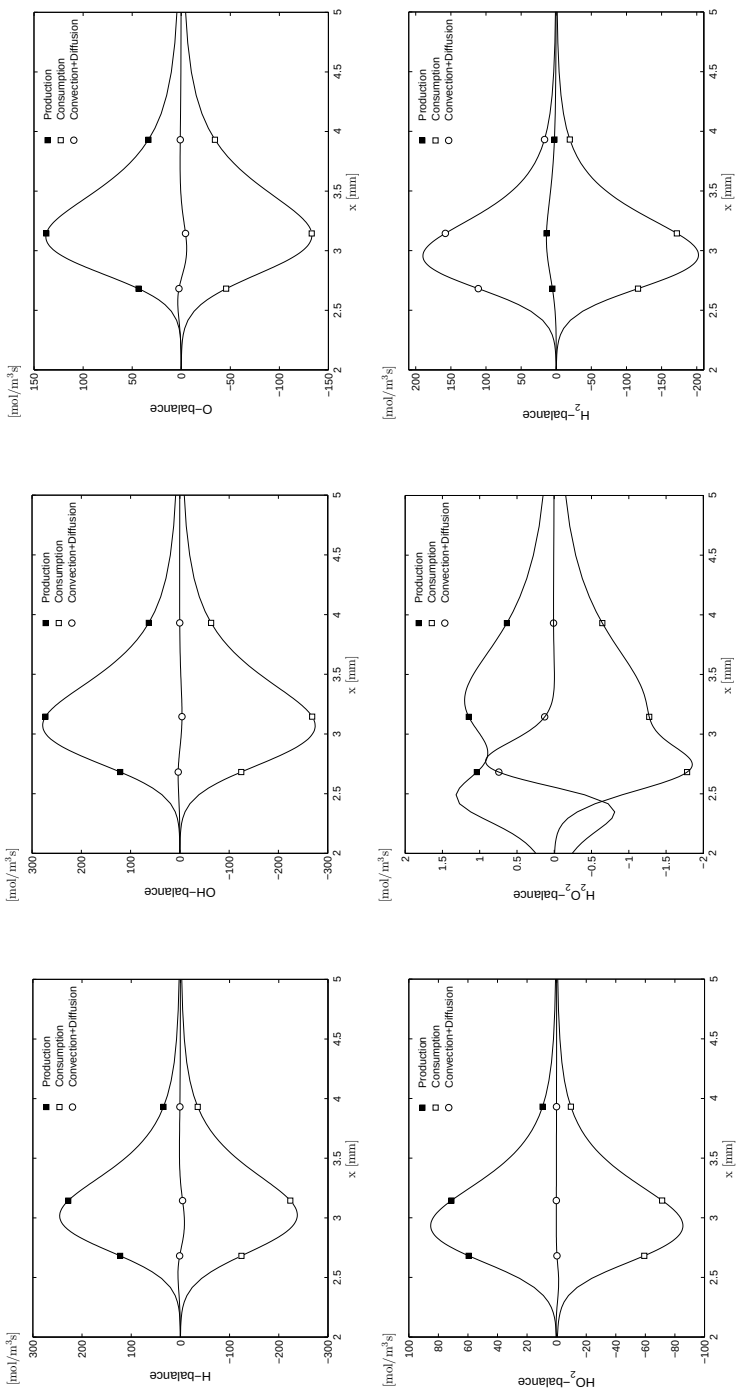

Figure E.2: Equivalence ratio $\phi = 0.3$ at $p = 1$ atm and $T_u = 300$ K.

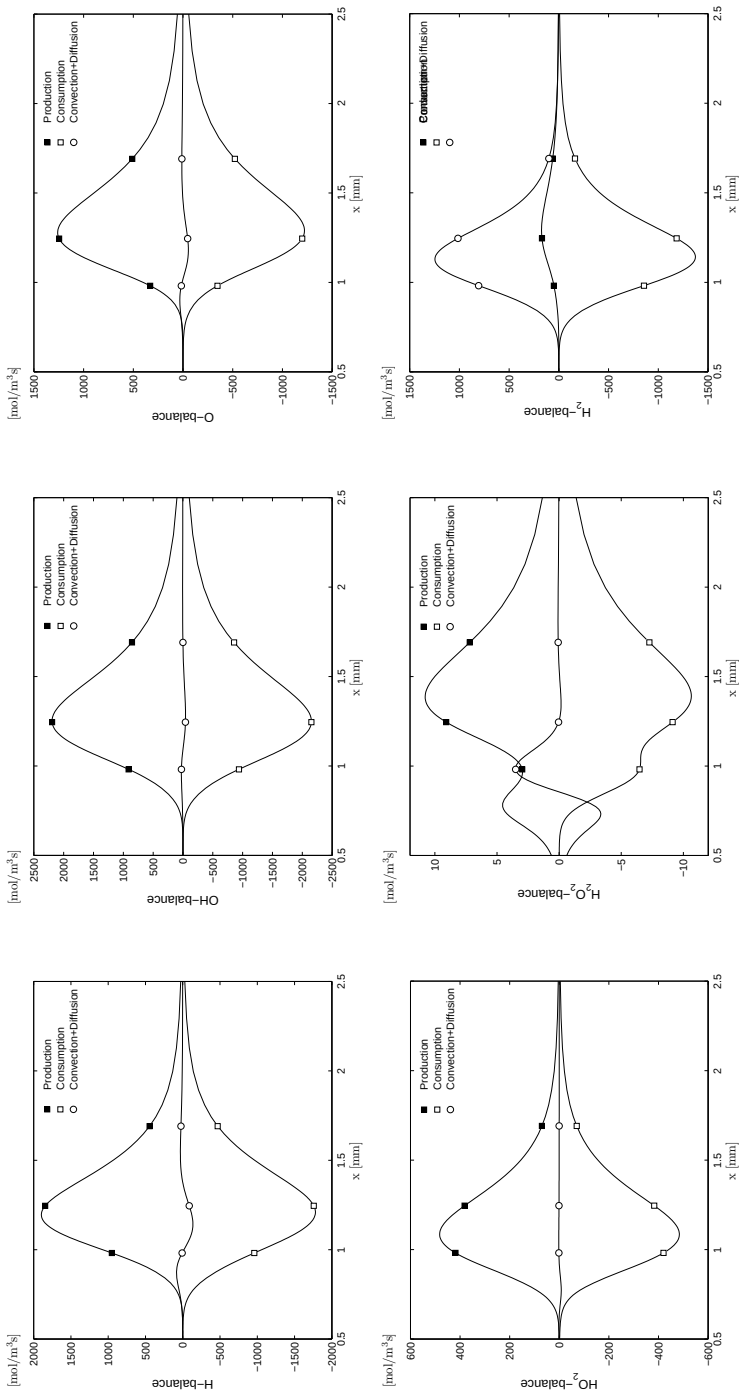

Figure F.3: Equivalence ratio $\phi = 0.35$ at $p = 1$ atm and $T_u = 300$ K.

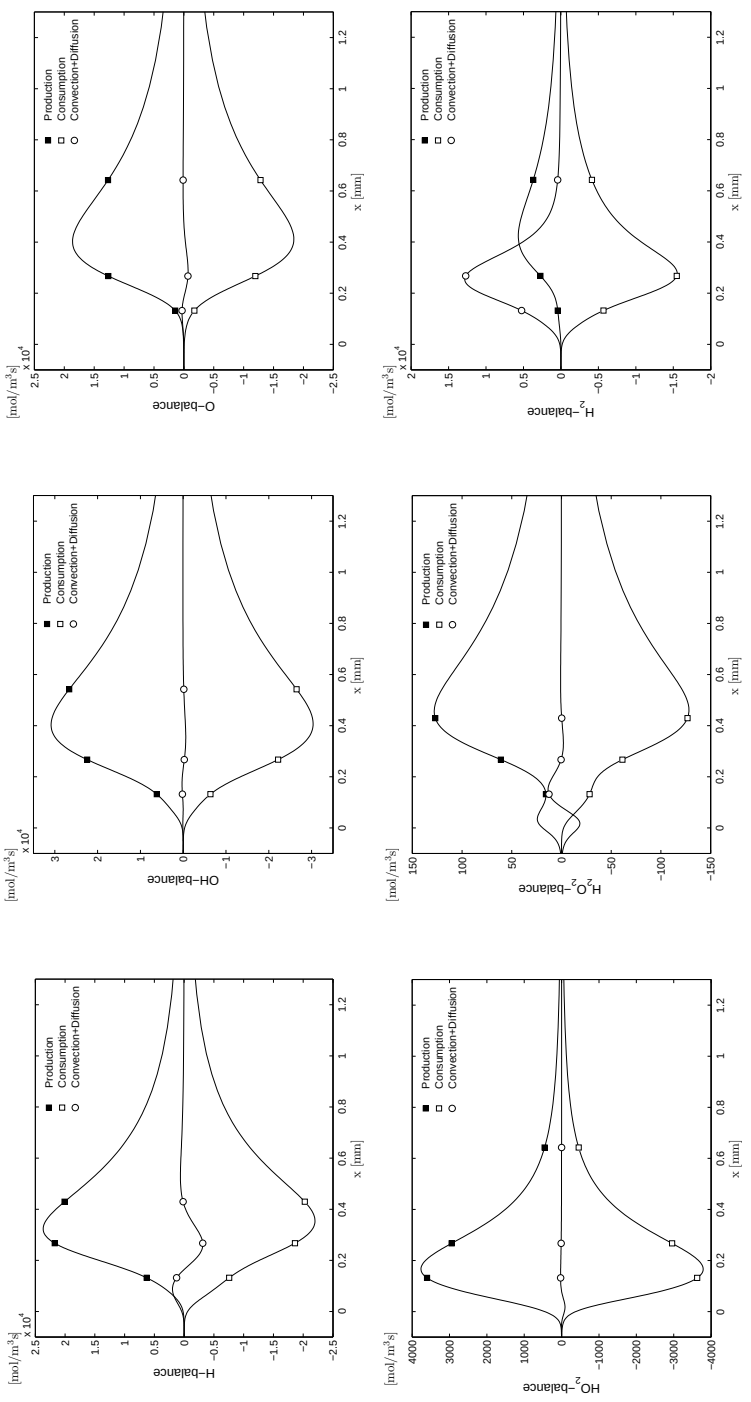

Figure F.4: Equivalence ratio $\phi = 0.5$ at $p = 1$ atm and $T_u = 300$ K.

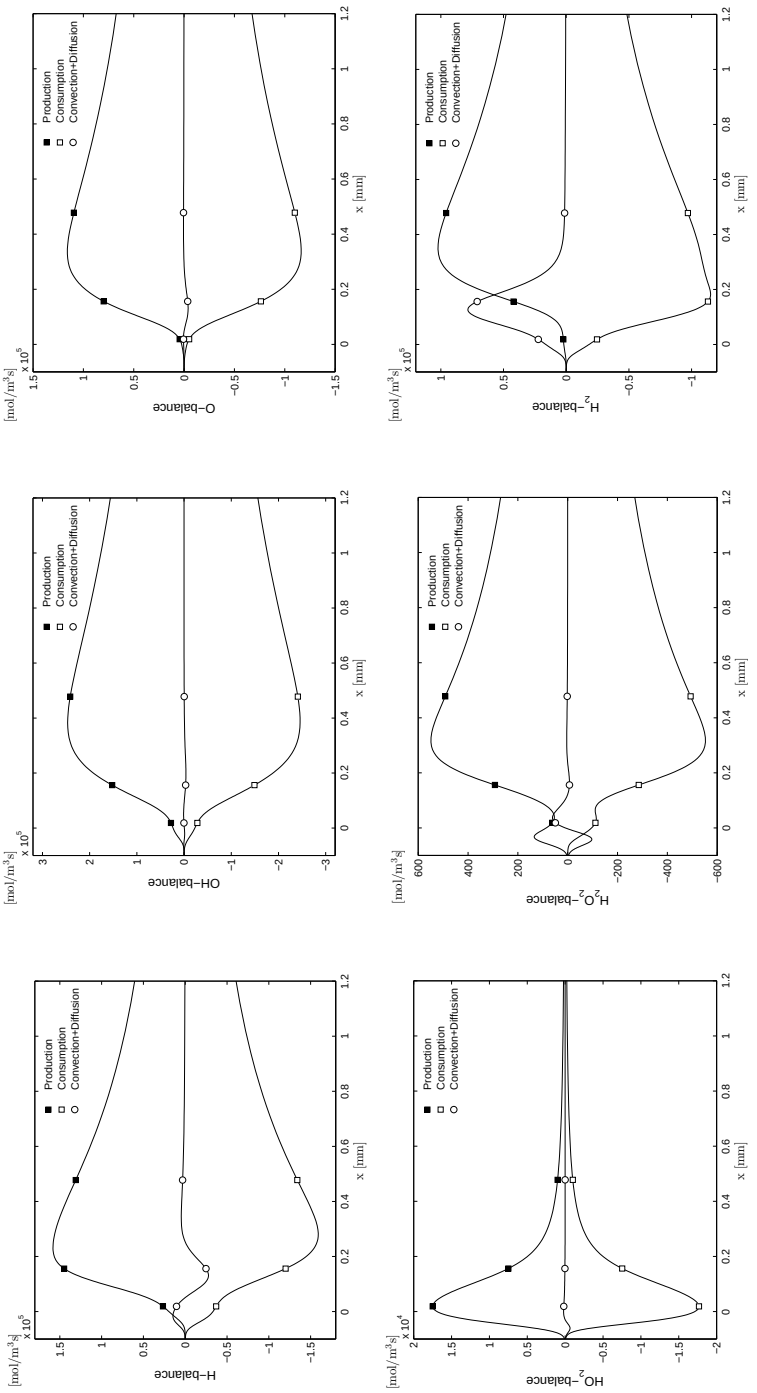

Figure E.5: Equivalence ratio $\phi = 0.8$ at $p = 1$ atm and $T_u = 300$ K.

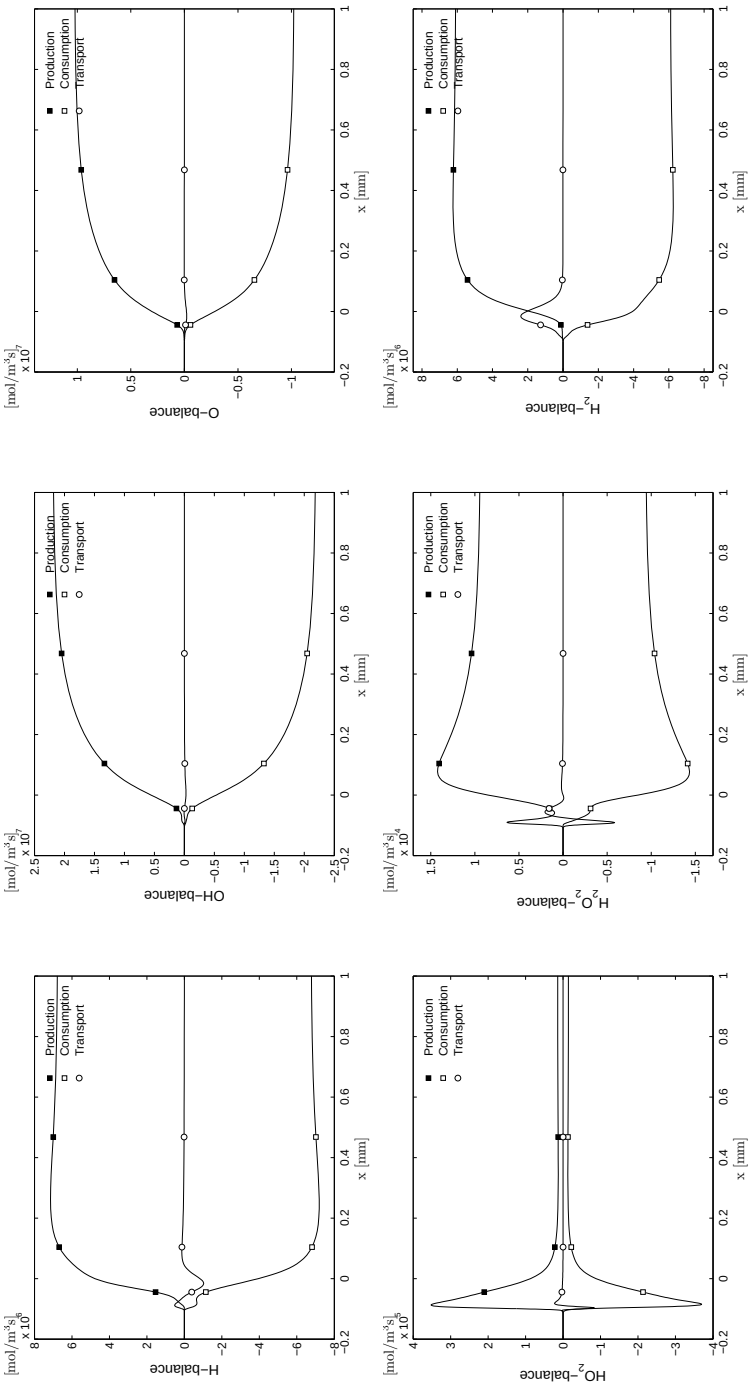

Figure F.6: Equivalence ratio $\phi = 0.8$ at $p = 1$ atm and $T_u = 100$ K for a H_2-O_2 mixture.

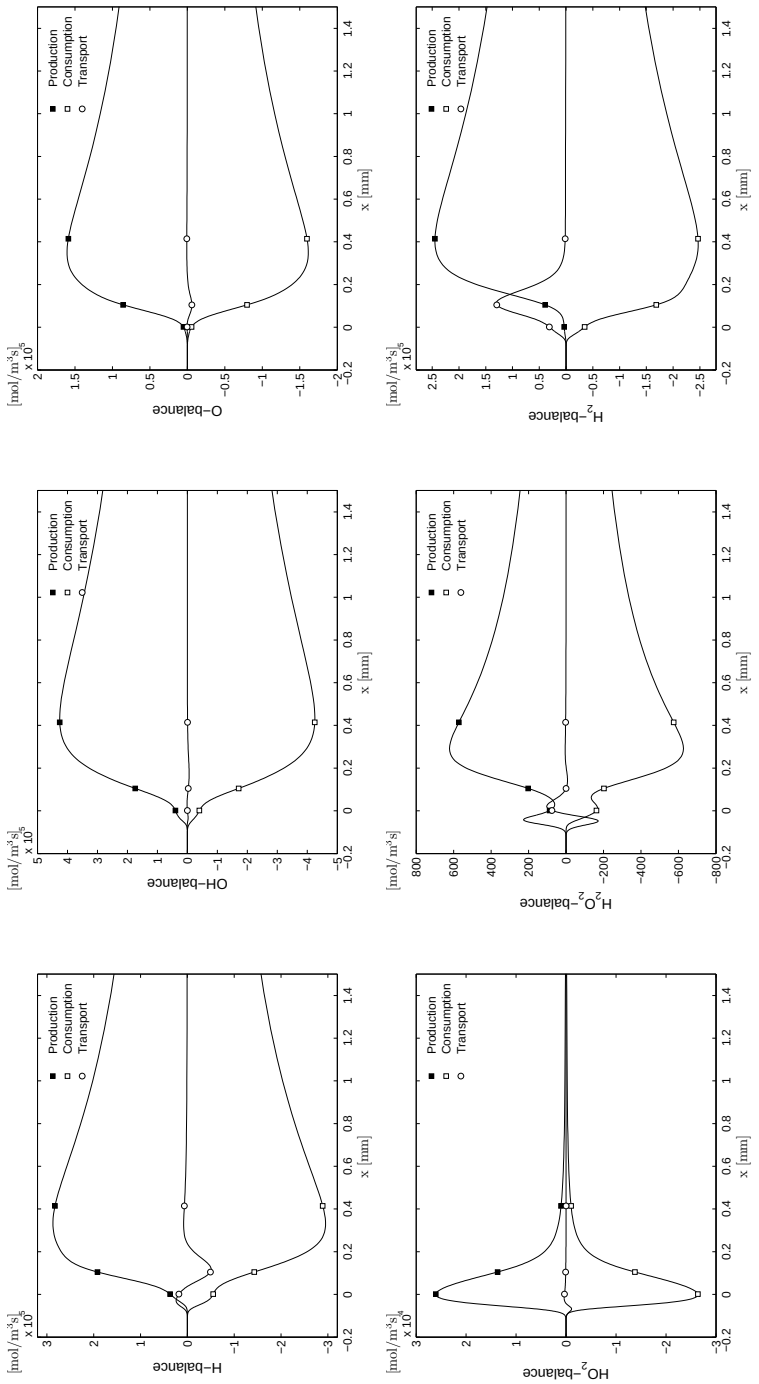

Figure F.7: Equivalence ratio $\phi = 1$ at $p = 1$ atm and $T_u = 300$ K.

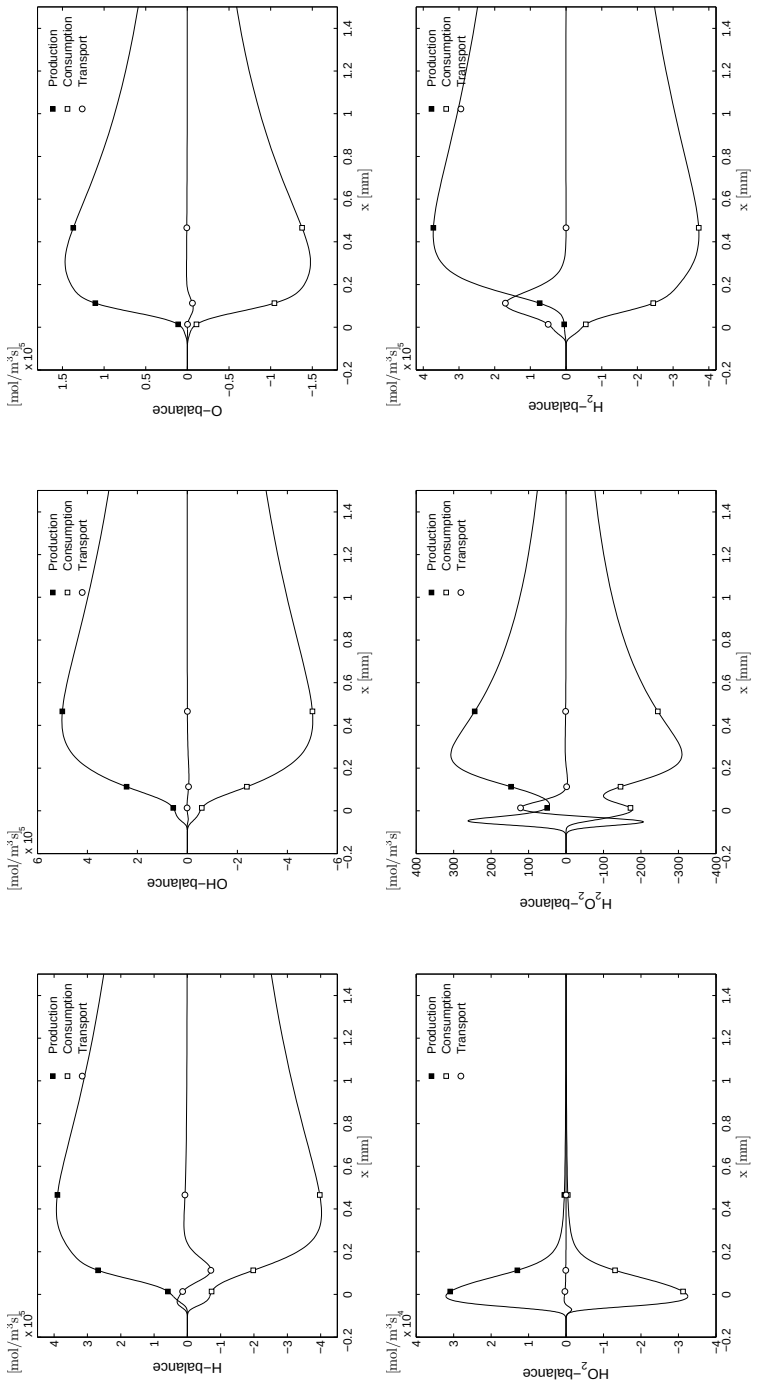

Figure E8: Equivalence ratio $\phi = 1.2$ at $p = 1$ atm and $T_u = 300$ K.

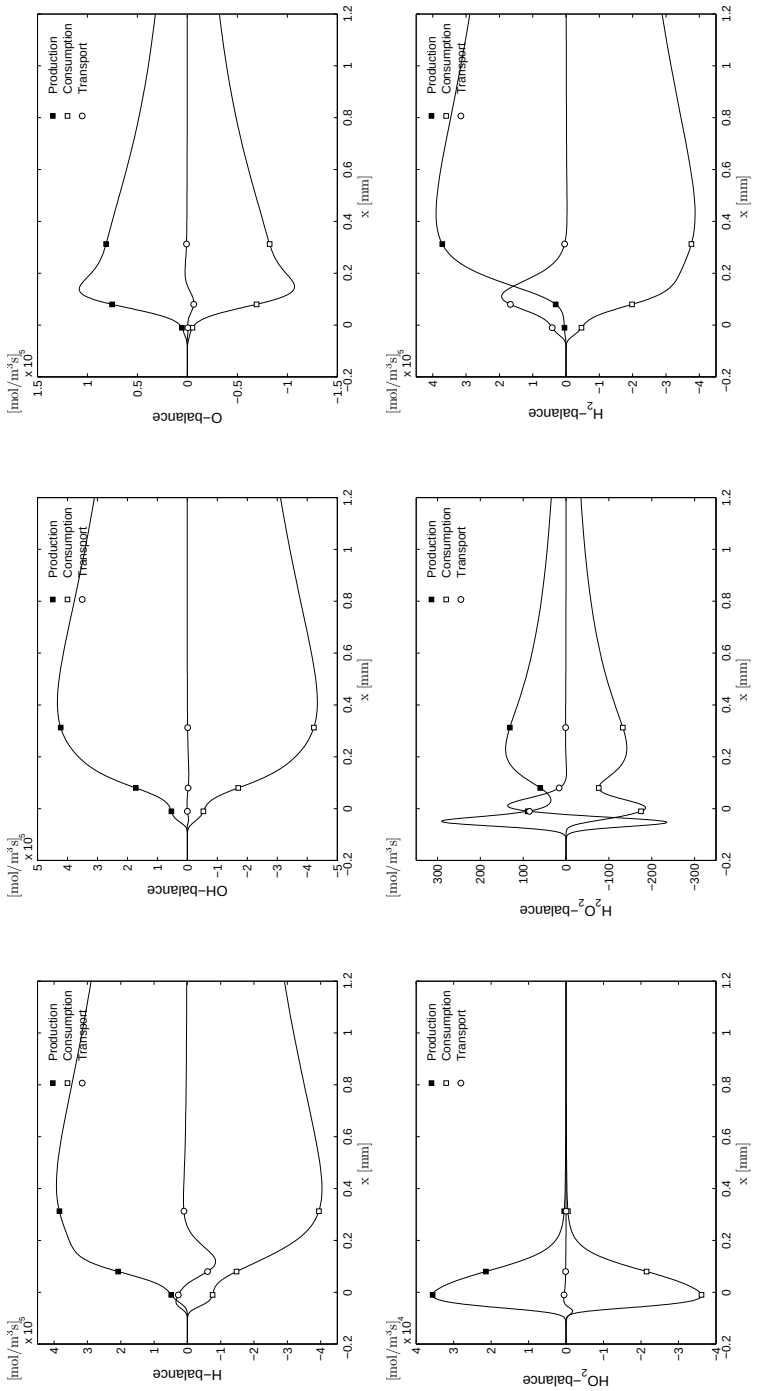

Figure E9: Equivalence ratio $\phi = 1.5$ at $p = 1$ atm and $T_u = 300$ K.

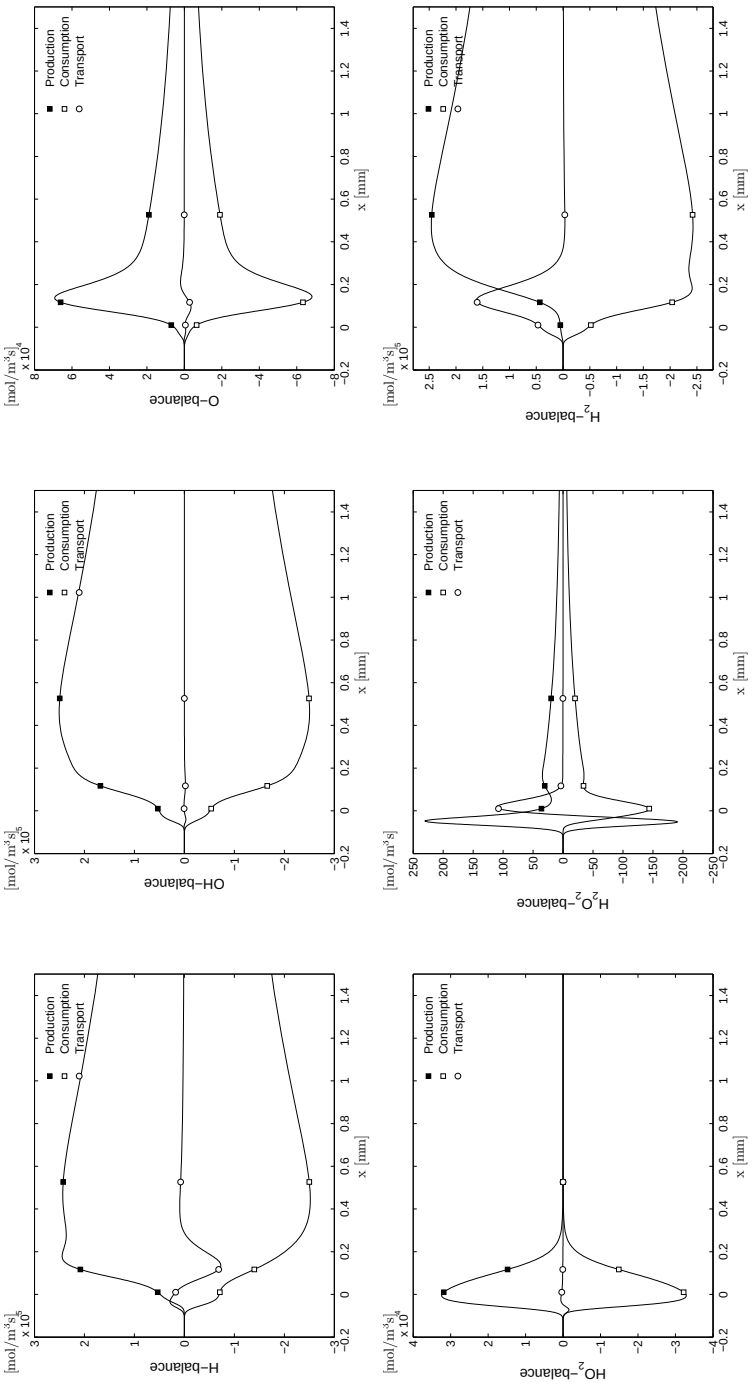

Figure F.10: Equivalence ratio $\phi = 2$ at $p = 1$ atm and $T_u = 300$ K.

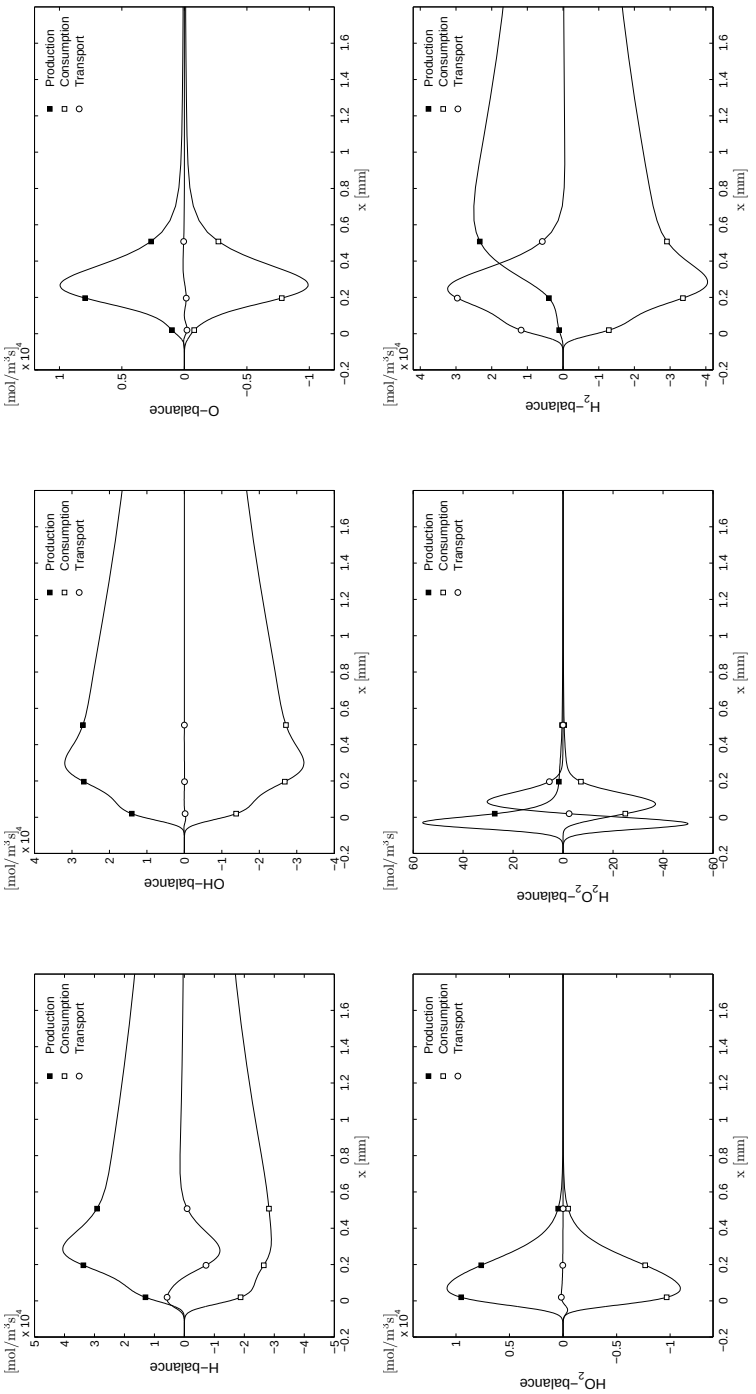

Figure F.11: Equivalence ratio $\phi = 4$ at $p = 1$ atm and $T_u = 300$ K.

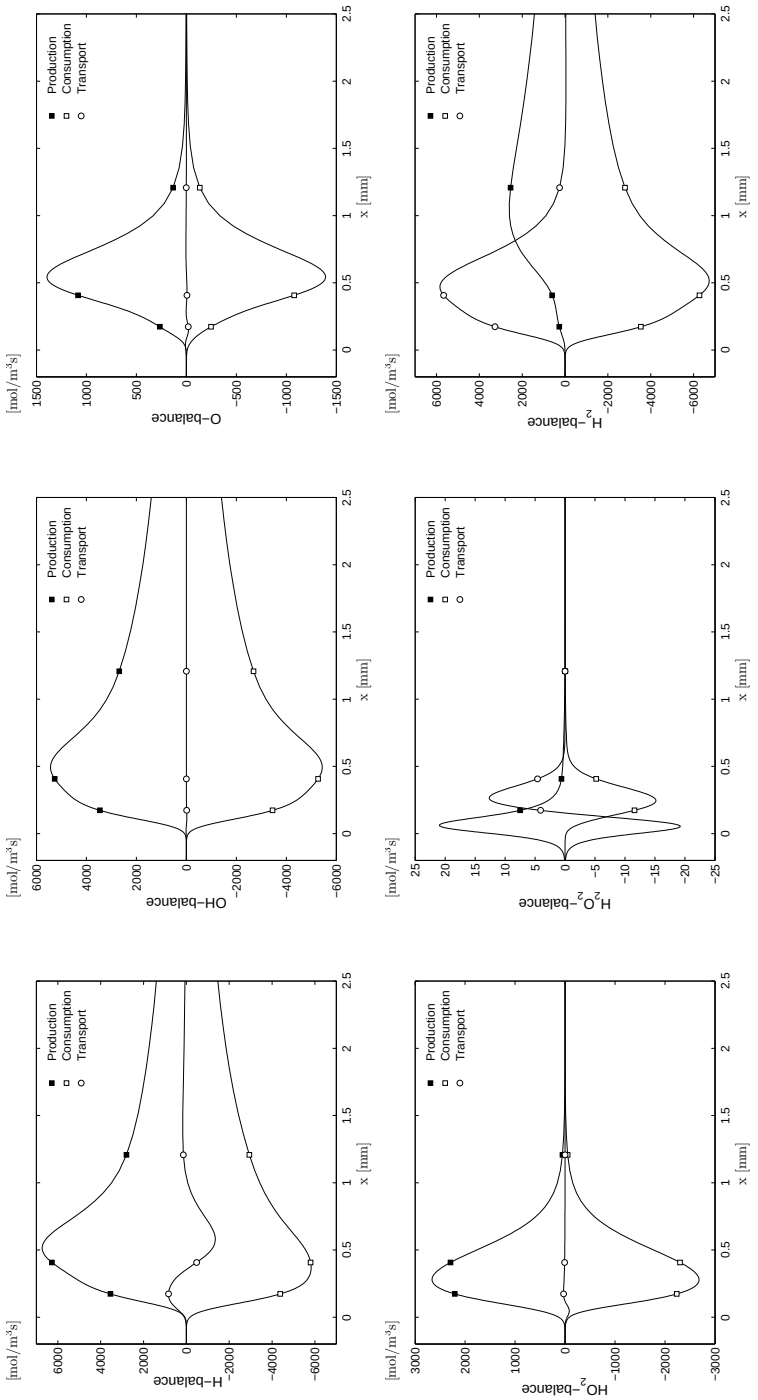

Figure F.12: Equivalence ratio $\phi = 6$ at $p = 1$ atm and $T_u = 300$ K.

APPENDIX

G

Adiabatic temperatures for H_2-air and H_2-O_2 mixtures

Calculations of the adiabatic flame temperatures T_∞ for H_2-air and H_2-O_2 mixtures are shown in the tables below as a function of the equivalence ratio ϕ. The temperatures, obtained with the chemical-equilibrium routine [1], have been evaluated for both equilibrium conditions and complete combustion to H_2O. As can bee seen, although tables represent data at different pressures p and initial temperatures T_u, the variation of the adiabatic temperature with pressure is negligible except at higher temperatures near stoichiometric equivalence ratios.

References

[1] W. C. Reynolds, The element potential method for chemical equilibrium analysis: Implementation in the interactive program stanjan [technical report], Tech. rep., Stanford University, Dept. of Mechanical Eng. (1986).

Table G.1: Adiabatic flame temperature for H_2-air at $p = 1$ atm and $T_u = 300$ K.

ϕ	T_∞^a [K]	T_∞^b [K]	ϕ	T_∞^a [K]	T_∞^b [K]	ϕ	T_∞^a [K]	T_∞^b [K]	ϕ	T_∞^a [K]	T_∞^b [K]
0.1	631.89	631.89	0.28	1139.20	1139.20	0.8	2178	2212	3	1772	1773
0.2	926.50	926.50	0.3	1189.60	1189.60	0.9	2307	2376	4	1562	1562
0.22	981.28	981.28	0.35	1312	1312	1	2390	2527	5	1400.60	1400.60
0.23	1008.30	1008.30	0.4	1428.97	1428.97	1.1	2416	2470	6	1280	1280
0.24	1035	1035	0.45	1540.38	1540.38	1.2	2374	2417	7	1180	1180
0.25	1061.48	1061.48	0.5	1648.26	1648.26	1.5	2251	2273	8	1098	1098
0.251	1064.13	1064.13	0.6	1845	1850	1.7	2171	2184	9	1030	1030
0.26	1087.65	1087.65	0.7	2023	2038	2	2062	2071	10	973.25	973.25

[a] From equilibrim conditions.

[b] From complete combustion.

Table G.2: Adiabatic flame temperature for H_2-air at $p = 1$ atm and $T_u = 200$ K.

ϕ	T_∞^a [K]	T_∞^b [K]	ϕ	T_∞^a [K]	T_∞^b [K]	ϕ	T_∞^a [K]	T_∞^b [K]	ϕ	T_∞^a [K]	T_∞^b [K]
0.2	834.55	834.55	0.29	1076.2	1076.2	0.4	1343.20	1343.20	0.6	1764.72	1767.55
0.25	971.66	971.66	0.3	1101.66	1101.66	0.45	1456.4	1456.4	0.7	1946.81	1954.78
0.26	998.21	998.21	0.35	1225.21	1225.21	0.5	1563.51	1564.17	0.8	2108.35	2124.8
0.28	1050.47	1050.47	0.38	1296.66	1296.66	0.55	1666.56	1668.04	0.9	2245	2271

[a] From equilibrim conditions.

[b] From complete combustion.

Table G.3: Adiabatic flame temperature for H_2-air at $p = 1$ atm and $T_u = 400$ K.

ϕ	T_∞^{a} [K]	T_∞^{b} [K]	ϕ	T_∞^{a} [K]	T_∞^{b} [K]	ϕ	T_∞^{a} [K]	T_∞^{b} [K]	ϕ	T_∞^{a} [K]	T_∞^{b} [K]
0.2	1017.11	1017.11	0.22	1071.31	1071.31	0.35	1398.48	1398.48	0.55	1830.2	1834
0.215	1057.86	1057.86	0.25	1150.48	1150.48	0.4	1514.16	1514.16	0.6	1925.3	1932.6
0.217	1063.24	1063.24	0.3	1277.45	1277.45	0.5	1730	1732.3	0.7	2098.48	2215.48

[a] From equilibrim conditions.

[b] From complete combustion.

Table G.4: Adiabatic flame temperature for H_2-air at $p = 10$ atm and $T_u = 580$ K.

ϕ	T_∞^{a} [K]	T_∞^{b} [K]	ϕ	T_∞^{a} [K]	T_∞^{b} [K]	ϕ	T_∞^{a} [K]	T_∞^{b} [K]	ϕ	T_∞^{a} [K]	T_∞^{b} [K]
0.2	1179.82	1179.82	0.55	1980.8	1980.8	1.5	2477.7	2501	8	1360.7	1360.7
0.25	1310.36	1310.63	0.6	2074.9	2084.1	2	2293	2303.4	9	1294	1294
0.28	1386.1	1386.1	0.7	2248	2269	3	2009.8	2012	10	1240	1240
0.3	1435.4	1435.4	0.8	2401	2444	4	1806	1806.7	11	1192.6	1192.6
0.4	1668.7	1668.7	0.9	2530	2602	5	1653	1653	12	1151.36	1151.36
0.45	1777.6	1777.6	1	2618.5	2753	6	1531.7	1537.7	13	1115.36	1115.36
0.5	1881	1881	1.2	2599.8	2644.5	7	1439	1439	14	1083.52	1083.52

[a] From equilibrim conditions.

[b] From complete combustion.

Table G.5: Adiabatic flame temperature for H_2-O_2 at $p = 1$ atm and $T_u = 300$ K.

ϕ	T_∞^{a} [K]	T_∞^{b} [K]	ϕ	T_∞^{a} [K]	T_∞^{b} [K]	ϕ	T_∞^{a} [K]	T_∞^{b} [K]	ϕ	T_∞^{a} [K]	T_∞^{b} [K]
0.03	746.17	746.17	0.06	1121.30	1121.30	0.075	1291.31	1291.31	0.15	1989.73	2009.3
0.04	877.13	877.13	0.065	1179.14	1179.14	0.08	1345.74	1345.74	0.2	2299.46	2387.68
0.05	1001.97	1001.97	0.07	1235.79	1235.79	0.09	1451.12	1451.52	0.25	2502.18	2686.22
0.056	1074.17	1074.17	0.074	1290.29	1280.29	0.1	1552.32	1553.32	0.3	2639	2906

[a] From equilibrim conditions.

[b] From complete combustion.